Molecular organisation of water and alcohols at solid-liquid interfaces

JOSEPH WILLIAM FOSTER

Durham University

Molecular organisation of water and alcohols at solid-liquid interfaces

Author:

J. William Foster

Primary Supervisors:

Dr. Kislon Voïtchovsky

Dr. Halim Kusumaatmaja

A thesis presented for the degree of

Doctor of Philosophy

Centre for Materials Physics

Department of Physics and Astronomy

Stockton Road

Durham

DH1 3LE

May 1, 2020

Abstract

The organisation and self-assembly of molecules at solid-liquid interfaces is central to numerous natural processes and can be used to create supramolecular architectures with functional applications. Historically, studies into surface-based self-assembly in liquids in ambient conditions are limited to molecules with significant surface interactions predisposed to durably reside at the surface. Outside of extreme conditions, such as low temperatures or under confinement, the self-assembly of small molecules (< 20 atoms) without significant surface interactions remains relatively unexplored.

Here, a joint approach involving atomic force microscopy and molecular dynamics simulations is used to explore the self-assembly of small alcohols and water into supramolecular structures on hydrophobic surfaces in ambient conditions. This self-assembly can occur because of the formation of extended hydrogen bonded networks between the assembling molecules at the interface, enabling the molecules to adsorb as a group. Investigations into this system has led to three, major, novel observations. The first is that graphite catalyses a reaction involving water and volatile organics to produce small quantities of methanol. This reaction is enhanced by applied electric fields and the methanol produced can subsequently self-assembly with the water, thus changing the behaviour of the interfacial liquid. The second is that at hydrophobic interfaces, the structure of small alcohol-water mixtures displays a strong concentration dependence; with alcohol molecules at the surface switching between states of hydrogen bonding with the bulk liquid and with other molecules in the same plane. The final result is that due to the weak molecular surface interactions, the hydrogen bond networks of these group-effect stabilised assemblies can be influenced through multiple approaches to create a wide variety of supramolecular structures. The generality and importance of group-effect self-assembly is demonstrated to be applicable to multiple hydrophobic interfaces.

Overall these results form the foundation for further investigations into small molecule self-assembly, along with having wider implications for other fields including the development of novel carbon-based catalytic materials, studies into transfer properties at electrodes as well as understanding friction and lubrication in many systems.

Acknowledgements

First of all, my deepest gratitude must go to both of my supervisors, Dr. Kislon Voïtchovsky and Dr. Halim Kusumaatmaja, who have continually provided excellent guidance throughout my project. I have learnt a significant amount from you both and I am undoubtedly a better scientist as a result.

I thoroughly enjoyable my time visiting the group led by Prof. Takeshi Fukuma at Kanazawa University and I am grateful to both Prof. Fukuma and Keisuke Miyazawa for making me feel welcome and for their help with my experiments. I also wish to thank Dr. Juan A. Aguilar Malavia from Durham Chemistry department for his help with the NMR experiments.

I have appreciated my time with both groups I have been a part of, however special mentions must go to Ethan Miller, Will Trewby, Miro Cafolla and Luca Piantanida for their support with the AFM, particularly during the early days of my project, as well as Raymond Christianto for his python help. I wish to show my gratitude to all my fellow PhD students and postdocs, who I have thoroughly enjoyed spending time with these last 4 years. Finally, I would like to thank Vanessa Woodhouse for her invaluable proofreading and assistance throughout my PhD.

Declaration

The work presented in this thesis has been developed under the supervision of Dr. Kislon Voïtchovsky and Dr. Halim Kusumaatmaja of the Department of Physics and Astronomy at Durham University. All text and figures are the work of the author, unless otherwise stated. The specific contributions of other researchers to the work presented is detailed in the next section. No part of this thesis has been presented for any other degree or qualification.

Contributions

- Section 3.3.2: J. A. Aguilar conducted the NMR measurements and assisted with their analysis, using samples provided by the author.
- Section 4.3.4: K. Voïtchovsky wrote and applied the gaussian fitting procedure to 3D-SFM data obtained by the author. K. Voïtchovsky also obtained the images in Figure 4.8a and b.
- Section 5.3.4: K. Miyazawa performed the average filtering process using the pattern matching algorithm.

Publications

- **W. Foster**, J. A. Aguilar, H. Kusumaatmaja and K. Voïtchovsky, "In Situ Molecular-Level Observation of Methanol Catalysis at the Water-Graphite Interface", *ACS Applied Materials and Interfaces*, 2018, *10*, 34265-34271. This work forms the basis of Chapter 3.

- **W. Foster**, K. Miyazawa, T. Fukuma, H. Kusumaatmaja and K. Voïtchovsky, "Self-Assembly of Small Molecules at Hydrophobic Interfaces Using Group Effect", *Nanoscale*, 2020, *9*, 5452-5463. This work forms the basis of Chapter 5.

- **W. Foster**, K. Voïtchovsky and H. Kusumaatmaja, "Concentration Dependent Local Structure of Alcohol and Water Mixtures at Hydrophobic Interfaces" [In preparation]. This work forms the basis of Chapter 4.

- C. Cafolla, **W. Foster** and K. Voïtchovsky, "Lubricated Friction Around Nano-Defects", *Science Advances*, 2020, *6*, 3673. I performed and analysed the molecular dynamics simulations for this paper and was involved in the subsequent commenting on the manuscript. This work involved studying large hydrocarbons and thus will not be discussed in this thesis.

Contents

1.0 Chapter 1: Introduction

1.1 Chapter Overview

This thesis concerns the self-assembly of small molecules at hydrophobic interfaces. The field of self-assembly is interdisciplinary and covers multiple length scales. Therefore, in this chapter I will give an overview of the field, with a focus on self-assembly at the molecular scale, to provide context for where the work presented herein fits.

I will start by explaining why studies involving self-assembly are important, including examples of how they can already provide solutions to existing problems. Then, the primary intermolecular interactions involved in promoting self-assembly will be outlined. Next, I will address the concept of self-assembly at interfaces, before discussing the difficulties of working with small molecules in interfacial self-assembly. Finally, I will introduce interfacial self-assembly relying on a group-effect, using the example of water and methanol on highly oriented pyrolytic graphite (HOPG).

1.2 Fundamentals of Self-assembly

Self assembly is the spontaneous formation of organised structures from components in a previously disordered state, driven by the interplay between inter-component interactions and their entropy. It is an inherent behaviour in systems at many different length scales including macroscopic colloids [1], microscopic crystals [2] and self-assembled monolayers at the nanoscale [3]. Some of the most common examples of self-assembly can be found in mixtures of water with amphiphilic molecules such

as those in soap. For example, the formation of soap bubbles is due to the hydrophilic and hydrophobic areas of the soap molecules becoming orientated in a manner which minimises the free energy of the system, in this case, forming a film. Self-assembly involving water as a solvent is also ubiquitous in natural processes, and is the driving force behind many biological systems at the center of life, such the formation of lipid membranes [4]. In these systems, particularly in biology, the self-assembly process is often not fully understood. Regularly the molecular assemblies form at such fast rates and with such high precision that researchers are struggling to explain the assembly mechanisms [5, 6], and therefore self-assembly at the molecular scale remains a key area of learning.

Despite the limits on our understanding of self-assembled processes in nature, they are still a source of inspiration for new strategies for building artificial systems. Many examples of bio-inspired self-assembly can be found in the field of DNA origami, whereby systems of DNA are encoded so that they can self-organise into pre-determined structures spanning several hundred nanometres [7].

More generally, the ability shown by self-assembly to exert high levels of control over the properties of materials at the nanoscale (1-10 nm) is also of significant interest to large industrial sectors, such as nano-electronics. The field of nano-electronics has long been reliant on 'top-down' material manufacturing techniques, where pre-existing materials are broken down by stencil-based techniques including photo, ion-beam and scanning probe lithography. The precision of these techniques is limited when approaching molecular scale features by the attainable resolution of the equipment. As early as 1965, a visionary paper by Moore [8] predicted that the rapidly growing demand for smaller, faster computers would inevitably be hindered by the size of the silicon electronics attainable with top-down lithographic techniques [9]. The advent of nanotechnology enabled a solution for this limitation. This involved the integration of functional molecular scale building blocks into the silicon devices in the form of nanoscale wires, switches and transistors. While other techniques exist for creating these nanoscale devices, it is generally recognised that 'bottom-up' approaches such as self-assembly are the most promising solution due to the potential for three-dimensional assemblies, cost-effective fabrication and the atomic precision to which the resulting structures can be designed. A key difference from top-down approaches, where nanostructures are created using external stimuli, is that bottom-up approaches have the final arrangement pre-encoded in the

assembling molecules. The most common approach to pre-encode the molecules is through tuning their molecular structure via chemical synthesis [10] which subsequently changes way they interact with one another through intermolecular interactions.

1.2.1 Principles driving self-assembly

The self-assembly of molecules is generally driven by non-covalent intermolecular interactions, each of which attempt to minimise the free energy of the system. There are some examples which utilise covalent bonds, such as alkanethiols on gold. However, even for these structures the features of the resulting assembly typically occur due to the intermolecular non-covalent interactions once the alkanethiols are bound to the surface (with a bond strength of the order of 100 k_bT per bond, discussed further in Section 1.3.2). Each type of non-covalent intermolecular interaction differs significantly in strength, length and direction. Therefore, by choosing the strength and location of each interaction (i.e. the number and location of chemical groups), the self-assembly process can be controlled. The properties of the most relevant interactions for this thesis will now be briefly discussed.

Electrostatics

Electrostatic forces arise due to charged groups. They are non-directional, but can be both attractive or repulsive depending on the charges of the two interacting groups. For two charged particles, the force acting between them is defined by

$$F(r) = \frac{Q_1 Q_2}{4\pi\epsilon_0\epsilon r^2} \tag{1.1}$$

where Q is the charge of the particles, ϵ_0 and ϵ are the dielectric permittivity of free space and the relative permittivity of the medium respectively and r is the particle separation. As can be seen from equation 1.1, electrostatic forces can in principle occur over long distance and can be influenced by the properties of the medium they are in, such as its dielectric constant. The strength of the interaction is also dependent on the charge of the particles themselves. To obtain an idea of the strength involved, one can consider a pair of isolated Na^+ and Cl^- ions. When in contact, the binding energy associated with the electrostatic force in a vacuum is of the order of 200 k_bT per ion [11], the same order of magnitude as that of a

covalent bond. For this example, the ions would need to have $r >> 50$ nm before the coulomb energy falls below k_bT. However, electrostatic interactions are also weakened when in media such as water, which has $\epsilon \sim 80$ compared with $\epsilon \sim 1$ for air at room temperature. This reduces the range over which the electrostatic interaction is significant for unit charges in water at room temperature to ~ 0.7 nm. Furthermore, when additional ions are present in a solution they can introduce a screening effect due to the ions being free to move and thus able to position themselves in a manner which may partially cancels the field. This can introduce an exponential decay factor to the strength of the interaction, as will be discussed further in Section 2.2.5.

Electrostatic interactions are particularly relevant for polar systems such as charged surfaces [12], or the self-assembly of larger building blocks such as colloidal particles [4]. At the molecular scale, however, these potentially strong interactions can be a limitation because they do not allow the interacting molecules to fully explore their conformational possibilities before settling [13]. This can leave the system in a meta-stable state, which makes obtaining reproducible well-ordered structures at the molecular level difficult.

Permanent dipole-based interactions

For individual molecules, permanent dipoles arise due to a non-symmetrical distribution of electrons within the molecule. Like electrostatic interactions, dipole-dipole interactions between molecules can also vary depending on the solvent they are in. However, permanent dipole-based interactions are typically weaker than the normal electrostatic interactions between particles, which makes them far more useful for predictable self-assembly [14]. The energy for a dipole-dipole interaction can be described by

$$U(r, \theta_1, \theta_2, \phi) = -\frac{u_1 u_2}{4\pi\epsilon_0\epsilon r^3}(2cos\theta_1 cos\theta_2 - sin\theta_1 sin\theta_2 cos\phi) \tag{1.2}$$

where u_1 and u_2 are the dipole moments and the definitions of θ_1, θ_2 and ϕ can be seen in Figure 1.1. Using equation 1.2 it can be seen that for two dipoles with equal moments of 1 D (comparable to that for HCl) the interaction energy in a vacuum is equal to k_bT at $r = 0.36$ nm when the dipoles are lined up. This is comparable to the diameter of molecules such as water and thus dipole-dipole bonds are considered to be short-ranged when compared with electrostatic interactions.

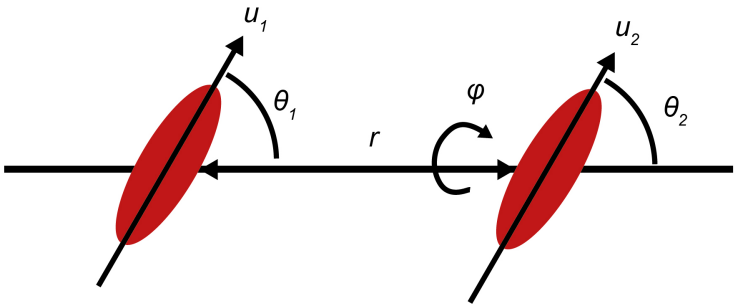

Fig. 1.1: Illustration of the angles used in equation 1.2. In this case the orientation of the molecule on the left is fixed.

Hydrogen bonds are a more selective version of the dipole-dipole interaction, which form between the positive dipole on a hydrogen atom and another electronegative atom. The small size and the single electron nature of the hydrogen atom mean that it has a significant unshielded positive charge. Therefore it is typically stronger than most dipole-dipole interactions with an energy of around 25-100 k_bT at room temperature [15]. Nonetheless, despite being stronger than other dipole-dipole interactions, hydrogen-bonds remain weak enough to allow the system to explore multiple configurations before settling on one of the most energetically favourable.

A further advantage of all dipole-dipole bonds is that, as can be seen from equation 1.2, they are inherently directional. When combined with the selectivity present for hydrogen-bonds, this encourages the formation of extended bonded networks which can help stabilise the assemblies, as will be outlined in Section 1.3.2. For this reason, hydrogen bonds are commonly used in self-assembly and will be the dominant interaction in the molecular self-assembly studied in this thesis.

Van der Waals interactions

Van der Waals (vdW) forces also arise from interactions due to electric dipoles. These dipoles can be permanent, or induced by either another permanent dipole or by thermal fluctuations. vdW forces are non-directional, can be effective over long ranges (greater than 10 nm) down to interatomic distances (around 0.2 nm). Many theoretical models exist to describe these interactions. One of the simplest of these is London's expression for the dispersion interaction energy between two identical atoms or molecules in a vacuum [16]:

$$U(r) = -\frac{C_{disp}}{r^6}, \tag{1.3}$$

where C_{disp} is a constant. However, this simple expression is not sufficient for describing interactions of anisotropic molecules and interactions when in a solvent, where the medium typically reduces strength of the interaction. For two small non-polar molecules, such as methane (CH_4), this interaction energy is $\sim$ 10 kJ/mol, one to two orders of magnitude weaker than covalent and ionic species and $< k_bT$. Experimentally it has been observed that increasing size of the carbon backbone for alcohols by one CH_2 group approximately increases the energy of the interaction by 6-7 kJ/mol [11]. This is why small non-branched alkanes are gaseous at room temperature until they reach the size of pentane (C_5H_{12}).

The vdW interaction is particularly influential when used in conjunction with surfaces to create two-dimensional structures or monolayers. In particular, they favour the formation of tightly packed structures with numerous interdigitation and therefore find use in organic systems, such as those containing long chain alkanes [9]. Alkane-based self-assembly on surfaces will be discussed in more detail in Section 1.3.2. In addition, studies have shown that despite being a relatively simple interaction, vdW forces can be easily be tailored using chemical modification to mediate in-plane interactions, inducing the spontaneous formation of ordered and disordered structures [17]. Furthermore, vdW forces are very important for so-called 2D materials such as graphene and MoS_2, which will be used in this thesis, because they are the dominant force in holding the stacked covalently bonded 2D sheets together [18].

Entropic Effects

Entropy effectively reflects the number of configurations within a thermodynamic system and can be defined by

$$S = k_b \, ln\Omega, \tag{1.4}$$

where Ω is the number of configurations or microstates in the system. The second law of thermodynamics states that for an isolated system, the total entropy can never decrease over time. The free energy of a system at constant volume which is allowed to exchange energy with its surroundings is defined as

$$F = U - TS, \tag{1.5}$$

where F is known as the Helmholtz free energy, U is the internal energy and T is the temperature. As can be seen from this equation, the entropic contribution to

the energy of the system is temperature dependent.

The self-assembly of molecules means an increase in order and thus is generally entropically unfavourable. Quantifying the entropic contribution to the thermodynamic equilibrium structure of a self-assembled system, as well as its influence on the path of the assembly process, is complicated and makes predicting such structures computationally challenging [19]. This is especially true for self-assembly at surfaces, where the end structure is a result of the subtle interplay between the energy gained from molecular interactions and adsorption, and entropy loss associated with the increased surface confinement. Recent studies have begun to address this by looking into the influence of entropic control (i.e. the impact of temperature) on the self-assembly process [20–22] as well as introducing models for the entropic component [19, 23]. However, these studies often still overlook key factors such as the impact of the solvent and thus the impact of entropy remains an active area of research.

It is worth noting that effects related to entropy can have as much of an impact on the self-assembly process as the other intermolecular forces previously discussed. This is particularity true for systems involving water, such as those in this thesis. This is due to what is known as the hydrophobic interaction. The hydrophobic interaction is a consequence of water forming three-dimensional hydrogen-bonded networks. When a non-hydrogen bonding molecule, or surface, is introduced the local water molecules re-arrange in order to remain involved in the extended hydrogen bonded networks. This re-arrangement corresponds to a decrease in entropy, i.e. the water is made more ordered as a result of the hydrophobic molecule/surface. The additional ordering is reduced if two hydrophobic molecules are brought close to each other, leading to an effective attractive interaction [15] known as the aforementioned hydrophobic interaction. This force is of entropic origin and thus is temperature dependent. One can get an idea of its strength by considering the free energy change associated with transferring one molecule of a hydrophobic alkane, such as butane (C_4H_{10}), from its pure liquid into water, which is 4.1 x 10^{-20}J or $\sim$ 10 k_bT [15]. For molecules such as methane, or butane, the distance over which the hydrophobic force is effective is reported to be 1.5 - 2.0 nm [11]. This is a significantly longer range than vdW forces for these hydrocarbons ($\sim$ 0.2 nm). Thus this comparatively long range means the hydrophobic force is an important consideration for self-assembly processes involving amphiphilic molecules, such as those found in biological sys-

tems (mentioned at the start of this Chapter). The hydrophobic force is also an important factor in understanding the interactions present during scanning probe measurements, one of the key methods in this thesis, and thus will be discussed further in Section 2.2.5.

Competition between intermolecule interactions

In practice, molecules are often complicated and interact via multiple types of intermolecular forces, with the resulting structure decided by the competition between them. For example, the influence of dipole-dipole and vdW interactions have been compared in a system of fluorene and fluorenone based molecules [24]. In this study two types of structures were observed, one linear and one cyclical, when using the same molecular components. In this system the dipole-dipole interactions were responsible for the cyclic network, whereas the vdW forces were the driving force behind the linear structures. Therefore, by controlling the functional groups and their location, the assembly pathway could be pre-defined (Figure 1.2). Reversible transitions between the two configurations could then be achieved by the application of an external electric field.

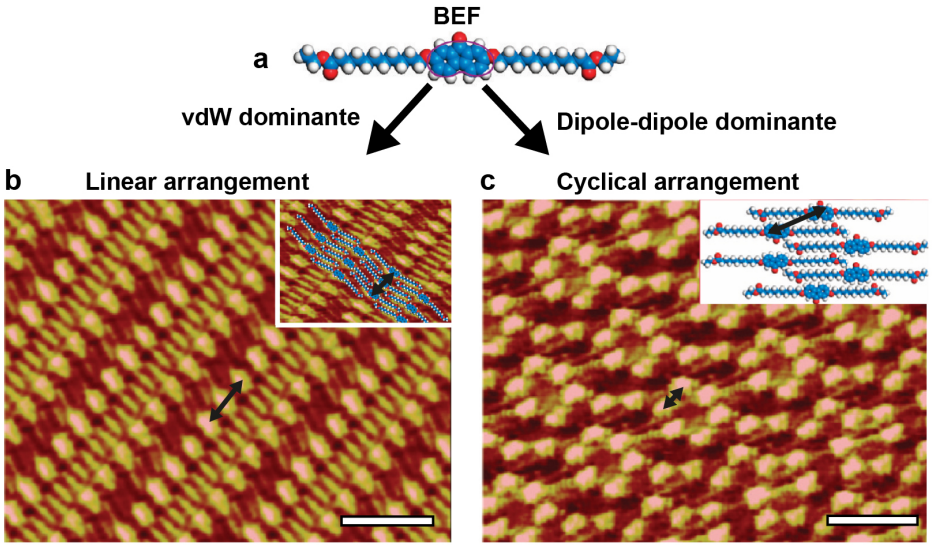

Fig. 1.2: Example of a system where one molecule has two different arrangements once self-assembled. One is dominated by the vdW interactions between the molecules and the other is dominated by the dipole-dipole interactions. (a) Chemical structure of a 2,7-bis(10-ethoxycarbonyl-decyloxy)- 9-fluorenone (BEF) molecule which has two potential dipole-bonding groups, one on the fluorone ring and the other on the alkoxy ester chains. (b) and (c) high resolution STM images of self-assembled monolayers on HOPG. The two different arrangements were shown to be due to the dominance of either the vdW interactions between the alkyl groups (linear structure, (b)) or the dipole-dipole interaction between the fluorone moeties and the alkoxyl group(cyclical structure, (c)). Cartoons of the two structure types are shown in the insets with the black arrows corresponding to features in the images. The scale bars are 4 nm. Figure adapted with permission from [24].

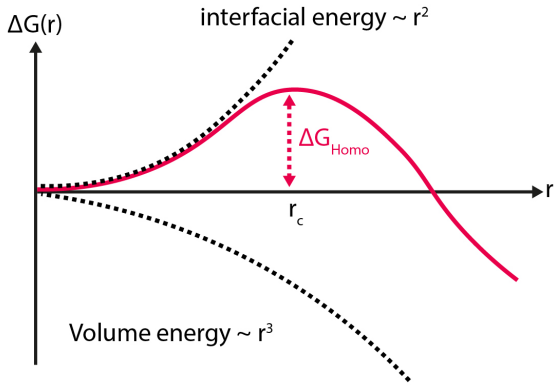

Fig. 1.3: Illustration of the principle behind homogeneous nucleation. The change in free energy (ΔG_{Homo}) associated with the formation of a new phase is related to two components, each of whom scale differently with the radius of the new phase (r). The interfacial term scales with r^2 and the volume term scales with r^3. This produces a curve with a single maximum at $r = r_c$. Therefore to allow the nucleation of a new phase to occur, this maximum needs to be overcome. This is typically achieved by the energy imparted through thermal fluctuations.

1.2.2 Structure Nucleation

The self-assembly of molecules is thermodynamically favoured due to the resulting phase having a lower free energy than the original phase. The transition between these phases often occurs through a nucleation event [25]. The nucleation process is an important concept within the field of self-assembly because it can determine the morphology of the resulting fully assembled structure. For this reason, understanding the nucleation pathway is the focus of many studies which have developed a basic theoretical framework.

Homogeneous Nucleation

Homogeneous nucleation occurs when thermal fluctuations transform a state in thermal equilibrium into a metastable state, without the influence of external surfaces [26]. This process can be described by the classical nucleation theory [27–29]. For homogeneous nucleation, classical nucleation theory predicts a free energy barrier for the formation of a new phase, whose value depends on the energy penalty for creating an interface between the new phases and the energy gain for enlarging the new phase [30]. In three-dimensional cases, the energy penalty scales with the nucleus surface area (r^2) whereas the energy gain scales with volume (r^3). Similarly, for the two-dimensional case the energy penalty scales with the nucleus circumference (r), whereas the energy gain scales with surface area (r^2). As a consequence when the nucleus is small and many molecules reside at the surface, the nucleus is unstable until it reaches a critical size, a feat achieved with the energy provided from the thermal fluctuations [31] (see Figure 1.3). This makes the nucleation process somewhat stochastic. A classic example of such nucleation can be found in the formation of liquid droplets from molecules in the gas phase [32].

While classical nucleation theory can successfully describe the qualitative nucleation behaviour in simple systems, it remains a phenomenological model based on empirical observations. Thus it is frequently challenged in more complicated situations, including cases involving alcohol water mixtures. For example, studies of the nucleation properties of alcohol water mixtures when transitioning from vapour to liquid droplets have reported large discrepancies between the theoretical and observed measurements [33–35]. This discrepancy may be due to the molecular scale liquid

nucleus being enriched with alcohols at its surface, reducing the surface tension and increasing the nucleation rate [36]. This effect is more pronounced the shorter the alcohol backbone [37]. Furthermore water and n-alcohols are reported to mutually enhance nucleation probability [37].

Heterogeneous Nucleation

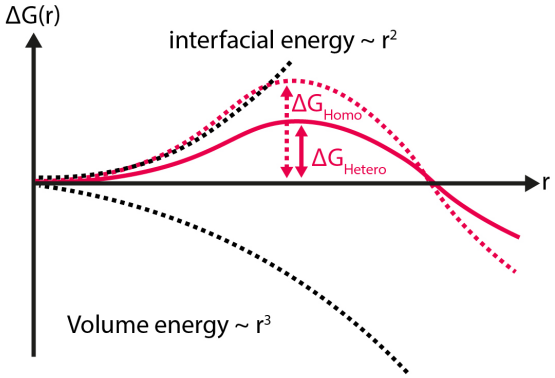

Fig. 1.4: Illustration of the principle behind heterogeneous nucleation. The presence of surface reduces the interfacial free energy term which also reduces ΔG_{Homo} to ΔG_{Hetero}. This lower energy barrier therefore increases the probability of nucleation occurring.

Despite being a relatively simple model, a fundamental principle of classical nucleation theory that is commonly experimentally observed is the concept of foreign surfaces altering the pathway to nucleation by reducing the energy barrier. The presence of a surface lowers the interfacial free energy, inducing a process known as heterogeneous nucleation, which is far more energetically favourable and therefore more common than homogeneous nucleation, Figure 1.4. Indeed, it has been reported that, for calcite crystals, the rate of heterogeneous nucleation on functionalised surfaces is 20 orders of magnitude higher than that of homogeneous nucleation of the crystals for solutions of calcium chloride dihydrate mixed with sodium carbonate [38].

While heterogeneous nucleation can be beneficial for inducing the nucleation of desired phase changes, it can also be a hindrance when the source of the heterogeneous nucleation is difficult to control. For the system of interest to this thesis, liquid droplets on surfaces, heterogeneous nucleation is both induced by intrinsic properties of the system and by external factors. Examples of the intrinsic properties include the solid surface itself as well as singularities such as step edges or

surface defects. These intrinsic properties can in principle be controled and their influence on the nucleation can be detected [39]. However, external factors, such as unavoidable containment particles, can be problematic because their influence on nucleation rates are more difficult to quantify.

1.3 Self-assembly at interfaces

The introduction of an interface can reduce the dimensionality of the system which can allow self-assembled structures to become more predictable. Furthermore, inherent properties of the interface can be utilised to act as a scaffold or template to control the component's self-assembly. In this section I will firstly give a brief description of self-assembly at liquid interfaces, before providing a more detailed overview of self-assembly at solid interfaces, due to the importance of solid surface in this thesis.

1.3.1 Interface with liquids

Liquid-Liquid interfaces

The macroscopic organisation of objects at the interface between immiscible liquids has been utilised for over a hundred years through systems known as Pickering Emulsions. Here, large particles (r >1 μm) can efficiently stabilize emulsions by adsorption to the fluid-fluid interface. Since then, the assembly of components at liquid interfaces has extended to nano-sized objects due to their potential applications [40]. One of the most commonly studied interfaces is that of water and amphiphilic molecules such as oils. Using such interfaces, various assemblies can be formed, including nanoparticles, nanorods and nanosheets. These in turn find uses in photovoltaic devices, coatings, detergents and pharmaceuticals to name but a few examples [41]. The key benefit of the liquid-liquid interface is that it encourages the assembly of particles to reduce the interfacial energy between the two liquids, particularly when the interfacial energy is high, as is the case for the oil-water interface. The value of the surface energy between the liquid interfaces can be altered by changing the chemical composition of the liquid. The preference for nanoparticles to reside at the interface can be altered by changing the particle radius [42].

This introduces further methods of control over the self-assembly process. Generally, the theory behind the liquid-liquid self-assembly is understood well enough that researchers' can predict the resulting features, although structures are still reported whose nature defies our understanding of colloidal forces [43]. This gap in our knowledge can be difficult to overcome, due to current limitations in techniques for characterising the end product of the self-assembly *in-situ* at the molecular level at liquid-liquid interfaces.

Liquid-Air interfaces

Methods for inducing self-assembly at the liquid-air interface have also been the focus of studies for many years. Perhaps the most of these significant studies involve Langmuir–Blodgett films, which originated early in the 20th century. The Langmuir-Blodgett process consists of two steps. The first step is the formation of a layer of particles at a liquid (usually water) air interface due to strong anisotropic interactions between the particles and the liquid, for example interactions due the amphiphilicity of the particles [40]. The properties of this particle layer can be controlled by evaporating the liquid, which reduces the surface area of liquid. This in turn compresses the particles at the interface. The second step is the deposition of this recently-formed monolayer onto a solid-surface. This process can be repeated to form well-defined multilayers of varying thicknesses. The properties of the deposited films can be further controlled by using specialised equipment such as Langmuir-Blodgett troughs which compress or expand the interfacial particles across the surface using moveable barriers [44]. Once deposited on a solid surface, such a film can be studied with scanning probe techniques. This allows them to be imaged at high resolution and the deposited assemblies to be mapped in-situ.

However, controlling the assembly formation using the Langmuir-Blodgett process requires well optimised deposition parameters, specialised equipment and only works for particles who like to reside at the liquid-air interface. This is limiting, as it undermines many of the great benefits of bottom-up self-assembly, including its simplicity and lack of dependence of external techniques. Furthermore, although the films can be characterised in-situ using scanning probe techniques, they are prone to distortion once transferred and therefore the measurements do not necessary relate to the liquid-air assembly [41].

1.3.2 Interface with solids

The presence of a solid surface introduces additional means of stabilising self-assemblies through surface-molecule interactions. The key difference between solid-liquid/air-based interfaces and liquid/air-based interfaces is the comparatively high shear strength of the solid, which allows it to support assembled structures through various interactions without yielding. The field of two-dimensional self assembly on solid surfaces has flourished over the last decade, due to the popularity of surface scanning probe microscopy techniques such as atomic force microscopy (AFM) and scanning tunnelling microscopy (STM), which can often reveal molecular level features within the assemblies [10]. The mapping of the assemblies is helped by the presence of the non-yielding surface, which gives an energetic benefit for forming two-dimensional bonded networks, meaning molecules prefer to form monolayers rather than three-dimensional assemblies. This in turn makes obtaining high resolution images of the structures easier and assists our understanding of the intermolecular behaviour. Arguably this gives surface-assisted self-assembly a significant benefit over bulk-liquid self-assembly, where the interaction network in complex assemblies is frequently still debated. Indeed, recent advances in scanning probe techniques have allowed for the imaging of individual hydrogen-bonds between self-assembled molecules [45] and the detection of their force [46]. As the scanning probe field continues to advance, further details will be discovered concerning the intermolecular interactions driving self-assembly, knowledge which will assist the design of highly organised and predictable functional assemblies.

The solid interfaces used in self-assembly tend to have expansive flat areas which enable the assembling components to form bonded networks over multiple μm. This can give them an advantage over liquid-liquid and liquid-gas interfaces, which are often curved on the macroscale. Such curvature can impose limits on any self-assembly process. Furthermore, despite the conformational limitations induced by the presence of a surface, self-assembly at the solid interface has been shown to retain flexibility and has been employed to fabricate clusters [47], one dimensional rows such as molecular wires [48] and porous networks [49]. Indeed, in Figure 1.2 in the previous section, we have already seen the formation of linear and cyclical structures on a surface dominated by networks of vdW and dipole-dipole interactions respectively. This principle can also be applied to molecules whose self-assembly is

driven by hydrogen bonding, an example of which can be seen in Figure 1.5. Here the directionality of hydrogen bonds is used to direct the self-assembly of different isomers of carboxylic acids into linear or zig-zag networks depending on the position of the hydroxyl and carbonyl groups [50]. Within this study, the authors observed that isomers which could not form extended hydrogen bonded networks due to steric effects are not capable of self-assembling into stable structures. This dependence on the formation of extended networks has been reported in numerous studies [10, 24, 47, 51] and indicates that the the surface is crucial.

It is worth noting that in hydrogen bonded networks, the resulting structure cannot always be predicted using a 'lego-block' method where hydrogen bond donors and acceptors can be simply matched up. Instead, the competition between the intermolecular hydrogen bonding, the inherent interactions between molecules and with the surface (discussed in Section 1.2.1) and the minimisation of the surface free energy results in the two-dimensional ordering being a compromise between the assembly inducing interactions. For example, hypothetically, should the molecules be in their closest packing arrangement to maximise vdW interactions, as is the case for pure alkanes on highly orientated pyrolytic graphite (HOPG), then no hydrogen bonding would be possible. On the other hand, configurations with molecules in their optimal hydrogen bonding positions would create voids. Instead, the experimentally observed packing is often a compromise between both factors, creating unexpected, yet intricate patterns [10].

The disparity between expected and observed arrangements is enhanced by the presence of the surface. For example, there have been reports of hydrogen bonding patterns, and distances between molecules, at surfaces which differ to those experimentally observed in 3D crystals or when theoretically modelled [10, 52–55]. This is attributed to the two-dimensional ordering existing as a result of the compromise between adsorbate–adsorbate, adsorbate–substrate interactions and the pseudo-confinement to two dimensions. The epitaxial effect, in particular, can increase the separation between hydrogen bonding molecules when the assembling molecules try to match the surface lattice. Epitaxial effects also often pack the molecules close together, with a large amount of interdigitation, allowing for more intermolecular interactions [56] as well as more interactions between the substrate and the assembling molecules [57], both of which further stabilise the structures. Generally, the stabilizing forces between assembling molecules and the surface can

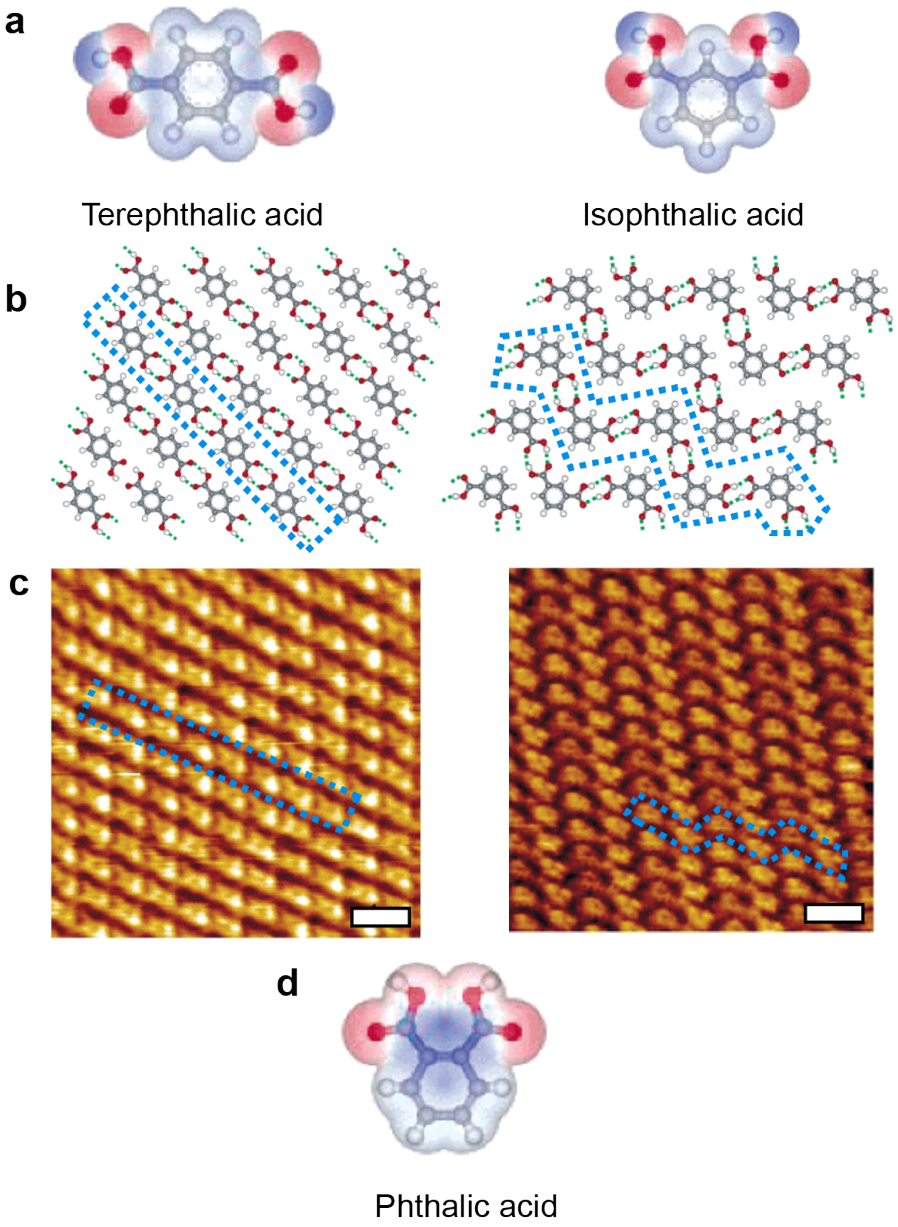

Fig. 1.5: Example of surface-assisted self assembly of extended chains of hydrogen bonding molecules. (a) shows to chemical structure of 2 isomers of benzene-dicarboxylic acid. Their arrangements on HOPG as predicted by molecular mechanics simulations can be seen in (b). These motifs are then visible in STM images as seen in (c). Both molecules are stabilized by extended networks of hydrogen bonds, whose topology differs depending on the location of the oxygen containing groups. In contrast, a further isomer, phthalic acid, (d) cannot form stable structures due to its topology inhibiting the formation of said extended hydrogen bonded networks. The scale bars are 1 nm. Figure adapted with permission from [50].

be put into two categories; those involving covalent bonds with the surface, known as chemisorption, and those involving non-covalent interactions, known as physisorption. Both cases will now be discussed briefly.

Chemisorption

Chemisorption is commonly used to stabilise molecules whose size (3-20 atoms) is comparable to those studied within this thesis, and therefore it is important to outline the process and its limitations.

Chemisorption involves a chemical reaction forming a bond between the adsorbate and the surface. Generally, chemisoprtion does not require any specialised equipment, such as UHV, or complex processes, such as using a Langmuir–Blodgett film, although it can benefit from the former. The most studied example of chemisorption in self-assembly is for alkylthiols on gold, where the covalent bonds forms between the sulphur group on the alkylthiol and the gold substrate with a bond strength of the order of 100 k_bT per bond. This sulfur-gold interaction dominates the molecular spacing at the surface, and the long alkyl chains are then stabilised by vdW interactions between each other, inducing further order. The covalent nature of the monolayer-surface bond mean chemisorped monolayers can couple the external environment to the electronic and optical properties of the metal [58], as well as influencing macroscopic properties ranging from metal corrosion protection to tunable wetability and friction of surfaces [10].

While there are benefits to chemisorption, it is ultimately hindered by the required use of covalent bonding chemicals which are limited to specific molecules and interactions (such as the aforementioned thio-alkanes on gold). Furthermore, the strength of the interactions involved makes the diffusion barriers very large when molecules are chemisorbed on the surface and therefore any ordered structure of chemisorbed molecules is usually not governed by intermolecular interactions, but solely by the strong chemisorption energy [9]. This negates one of the most promising methods of control over the resulting structures, the tuning of intermolecular interactions.

Physisorption

Intermolecular interactions are more important for physisorped structures. When a molecule is physisorped, it is defined as having a minimal perturbation to its electronic structure by the absorption site, such that the change in electronic states is difficult to detect experimentally. This corresponds to a far weaker interaction than

chemisorption (binding energies typically 1-20 kJ/mol for physisorption and 100-1000 kJ/mol for chemisorption [11, 59], although can vary greatly), mostly driven by either vdW forces or π-π interactions. Therefore, physisorption is a general phenomenon and can occur at any solid-liquid or solid-gas interface with none of the chemical specificity required for chemisorption. Furthermore, this removal of a dependence on specific chemical interactions means that physisorption can in principle support the formation of multiple layers of structures away from the surface, as well as reducing the activation energy barrier for their formation.

The weak interactions involved mean that, for systems driven by physisorption, either low temperatures or long molecular chains are usually required to ensure stability. However, this weak interaction also means that, upon deposition at a given temperature, the molecules are able to rotate and translate to 'find' each other and form the most stable supramolecular ordering, or a thermodynamic minimum. This is particularly useful for self-assembly at a solid-liquid interface, because it means that by definition the assembly process should naturally reject defects and therefore, in principle, it can induce highly ordered structures from highly disordered systems [44].

Surfaces used in this work

As mentioned at the start of this section, very flat surfaces with regular nanoscale periodicities are beneficial for self-assembled structures as they support the formation of extended bonded networks. For physisorped structures, flat surfaces also enable the re-organisation needed to create stable arrangements. In this thesis, the surfaces considered are highly oriented pyrolytic graphite (HOPG), graphite oxide (GrO) and molybdenum disulphide (MoS_2).

Organic surfaces, such as HOPG, are very commonly used to assist self-assembly of a wide variety of molecules [53, 60–62]. HOPG is a highly ordered, highly pure form of synthetic graphite with a large degree of alignment of the individual graphite crystallites. HOPG consists of layers of carbon atoms arranged in a honeycomb structure, a single layer of which is depicted in Figure 1.6a. The interactions between the individual graphite layers are weak, making HOPG easy to cleave. This results in stacked, atomically flat layers which are ideal for supporting self-assembly. Studies involving HOPG are particularly relevant at the present moment considering the

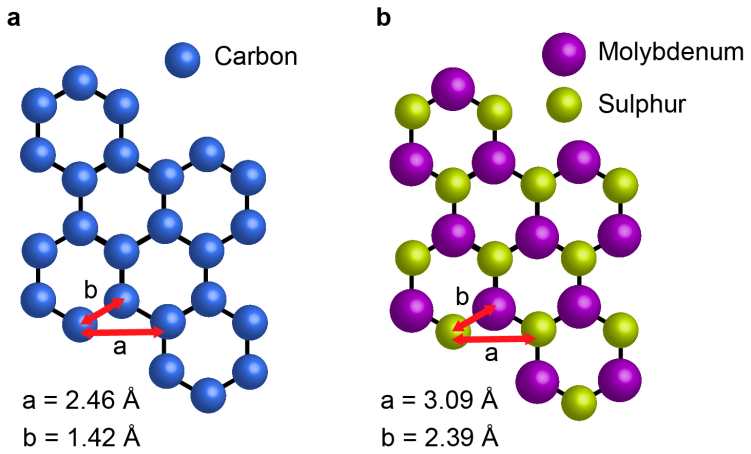

Fig. 1.6: Schematic of the lattice of (a) HOPG and (b) Molybdenum Disulphide with the relevant distances labelled. It is worth noting that MoS_2 has in fact a trilayer structure, with one of the sulphur atoms being hidden when viewed top-down. Nonetheless its two-dimensional structure is still very similar to that of HOPG.

emergence of graphene-based nanotechnology. Carbon interfaces are now finding themselves used for energy storage [63, 64] and photonics [65], to name just a few applications.

Graphite oxide (GrO) is the hydrophilic derivative of graphite. It is obtained by the replacement of single carbon atoms in the graphite sheets with oxygen containing functional groups, such as epoxy and methoxy groups. Thin sheets of GrO retain some of the unique electronic properties of graphene, but the presence of hydrophilic groups makes it soluble in water, opening new avenues for applications in water filtration and ion sieving [66].

MoS_2 is hydrophobic [67, 68] and, similar to HOPG, it can be cleaved to form large atomically flat areas. MoS_2 also exhibits a honeycomb pattern [67] in the lateral plane, with lattice parameters close to that of HOPG, as can be seen in Figure 1.6b. The lattice parameters of surfaces such as HOPG or MoS_2 mean that they are particularly effective in supporting the self-assembly of molecules with alkane backbones. This is due to the similarity between the carbon-carbon bond lengths of the alkanes and the periodicity of the surface lattice, which increases the shared atomic surface area and the adsorption energy (Figure 1.7) [69]. Generally, alkanes are well-suited to self-assembly due their simple synthesis and the fact that additional functional groups can easily be added at many different locations on the molecule. As detailed in Section 1.2.1, this high degree of molecular control in turn allows fine-tuning of the eventual self-assembled structures. The strength of

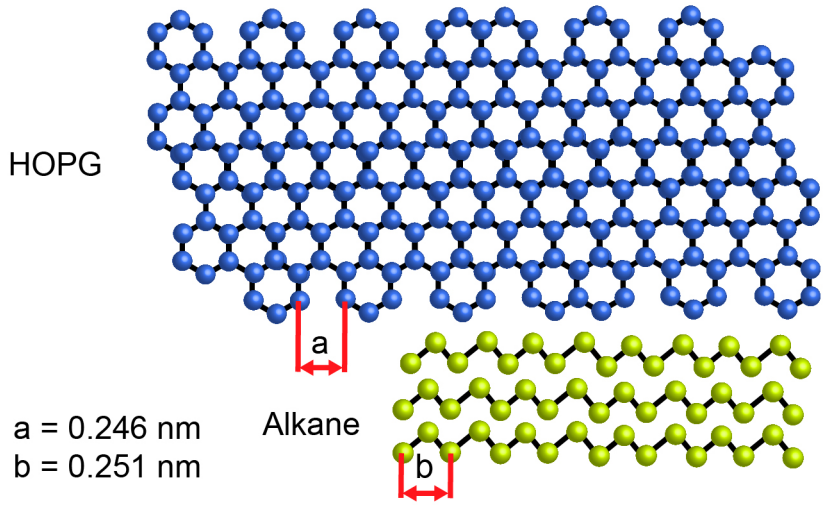

Fig. 1.7: Schematic of mismatch between alkane periodicity and that of HOPG. An example alkane ($C_{18}H_{38}$) is show in its most favourable arrangement, lying with its molecular backbone plane parallel to the graphite surface.

the monolayer-surface interaction for alkyl chain based self-assembly can also be tailored by altering the chain length. In many cases the alkyl chains are observed to orient themselves along one of the symmetry axes of the underlying graphite surface. This gives the system a degree of directionality despite the self-assembly mechanism being inherently non directional. This increased propensity for the molecules to pack in a certain direction promotes structures which are highly ordered over long distances, ideal for the self-assembly of functional interfaces.

1.4 The challenges in self-assembly of small molecules

In the field of self-assembly the term 'small molecules' is used ambiguously. Often the cause of this ambiguity is simply a matter of the relationship between the size of the assembling component and the system of interest. For example, biological studies have referred to molecules of around 50 - 70 atoms with bulky aromatic ring groups as being small [70, 71]. This is because, in biology, often the entities studied, such as lipid membranes or cells are on the scale of hundreds of nanometers to microns.

This work will study the self-assembly of some of the smallest possible molecules, which are generally < 20 atoms. In particular, the most used system is that of methanol and water molecules, which are only 6 and 3 atoms respectively. The

self-assembly of molecules this size in ambient conditions is rare. In the absence of restrictive tethers, such as in chemisorption, it is expected that the collective vdW physisorption effect and intermolecular bonds alone are not strong enough to stabilise extended structures.

This limitation has been overcome in the past by working at low temperatures with smaller thermal fluctuation. Investigations into low-temperature self-assembly of water on organic surfaces, such as HOPG, are frequent due to the emergence of carbon-based technologies, as well as a desire to better understand the nucleation of atmospheric ice, which has been shown to occur on organic aerosol particles [72, 73]. Performing electron crystallography on low temperature self-assembled ice on HOPG has previously revealed that close to step edges the water molecules prefer to form two-dimensional, ice due to similarities between the interplaner distance of two-dimensional ice and the carbon layer spacings [74].

There are also many organic molecules in low temperature environments in the atmosphere. Of these, methanol is the most common and thus has been subject to low temperature elastic helium and light scattering studies [73]. However, to date there are only a limited number of experimental studies which have obtained a molecular level understanding of methanol's structure on HOPG at temperatures < 200 K. Of these, none directly image the molecular structure *in-situ* [73, 75, 76]. Such data has been obtained, however, for methanol on gold and copper (111) surfaces using STM [77] at 30 K, where heating the surface to 160 K resulted in a full desorption of the structures. Herein lies the problem with low-temperature induced assemblies, their inability to be functional in ambient environments. For example, for a single methanol molecule the reported adsorption energy to HOPG (dominated by vdW interaction) can be as low as ~ 14 kJ/mol [78]. This is comparable to k_bT for $T = 300$ K. Water has an even lower value of ~ 7 kJ/mol [79]. Introducing additional lateral hydrogen bonds can increase this adsorption energy. For example a hydrogen bonded cluster of 5 methanol molecules has an adsorption energy of $\sim$ 35 kJ/mol [78]. However, experimentally it is observed that monolayers of larger alcohols, such as heptanol ($C_7H_{16}O$), formed from vapour in a sealed cell can still melt at ~ 290 K. The presence of further liquid introduces additional influential factors, such as the hydrophobic interaction (as discussed in Section 1.2.1). This makes small hydrogen bonding molecules, such as water, or methanol when mixed with water, even less likely to reside durably at hydrophobic interface due to the

energetic benefits of forming hydrogen bonds with the bulk liquid.

Alternatively, there have been many studies into the self-assembly of small molecules under two-dimensional confinement. Confined water is important in many research areas, such as geological and biological processes [80]; thus it has been subject to extensive experimental [74, 81–87] and computational [74, 88–91] studies. Furthermore, confinement of water mixed with small organic molecules between carbon surfaces is of high interest due to the potential use of graphene and graphene oxide nanopores in filtration [92, 93]. For example, the formation of room temperature stable ice has been observed using SEM to probe water confined between two graphene sheets [94]. In this study, the water was seen to form extended two-dimensional hydrogen-bonded networks, rather than the three-dimensional (tetrahedral) networks present in bulk ice [95]. Similar studies have been performed for mixtures of water and short chain length alcohols when confined between mica and graphene [96]. These revealed the room temperature crystallisation of the confined alcohols, although they did not provide any details regarding the molecular arrangements.

In the absence of the entropy-reducing effects of low temperature or confinement, a search of previous literature reported no cases of self-assembly of molecules < 20 atoms in the bulk or at an interface, other than the system studied in this work. This novelty therefore makes the results presented in this thesis of interest to the wider self-assembly community.

1.5 Self assembly of water with short chain length alcohols

As previously mentioned, the bulk of this thesis will involve the use of mixtures of water with short chain length alcohols. Methanol is the smallest and simplest alcohol. Other than the aforementioned confined cases, at room temperature both water and methanol remain liquid in the bulk [89, 94, 97] and at the interface with hydrophobic surfaces [97–99]. Indeed, when surface scanning techniques, such as AFM, are used to image hydrophobic surfaces, such as HOPG, in environments of pure water or pure methanol, only graphitic features are observed within the first couple of experimental hours. Example images from such experiments can be seen

in Figures 1.8a and b.

The situation changes significantly when a mixed droplet of equal parts of water and methanol is deposited on the HOPG (Figure 1.8c). Here the topographic image shows that raised patches have formed, as highlighted by the white dashed lines. The patches provide a strong contrast in the phase image, which indicates a change in energy dissipation when compared with the surrounding HOPG lattice. This phenomenon was first observed by Voïtchovsky et al. [51] and was attributed to the self-assembly of the water and methanol molecules into stable, solid-like structures on top of the HOPG. These structures typically formed on the order of minutes when a 50:50 water-methanol mixture was used. Once nucleated, the individual patches carry on growing until they covered the entire surface.

The core focus of the research presented within this thesis is to further our understanding of this novel self-assembly process involving aqueous mixtures of small molecules. To this end, it will be building on observations of the methanol-water assembly described in ref. [51]. Thus, it is important to understand the behaviour of this base system in detail. This section will provide a review of these structures based on the key observations raised in ref. [51].

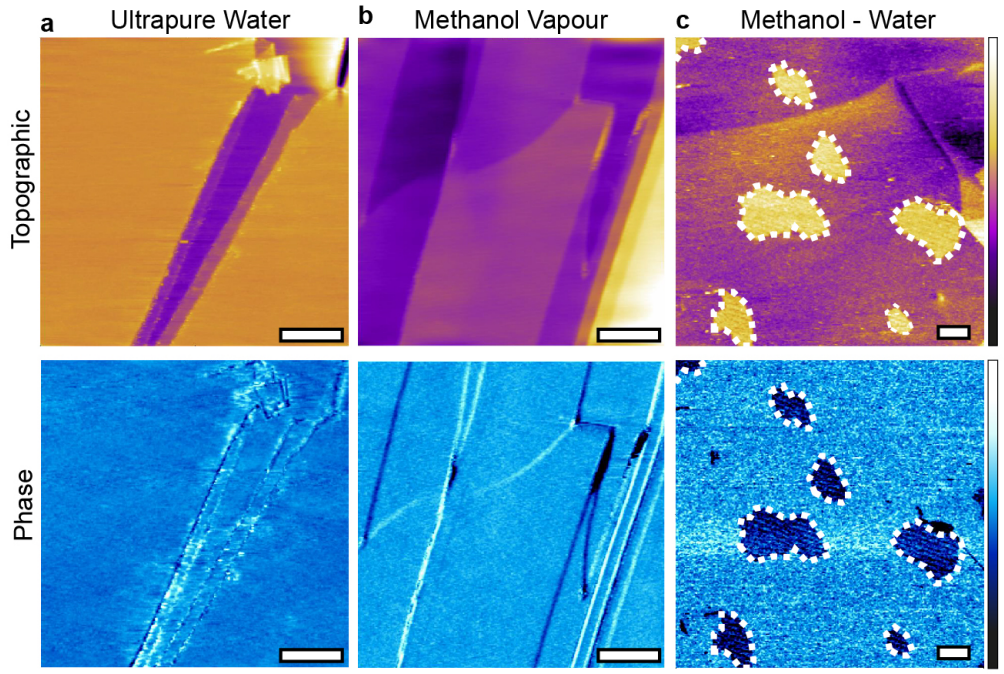

Fig. 1.8: Surface of HOPG imaged using amplitude modulation mode AFM (see Chapter 2 for details on the method) which shows no assemblies occur in pure water or methanol, but can nucleate when mixed. Panel (a) shows the case of pure water. Performing the same control experiments in pure methanol is challenging due to its high vapour pressure, which reduces the thermal stability and imposes a time limit on the experimental window. However, imaging of the HOPG surface in methanol can be achieved by dehydrating a sealed AFM cell with pure nitrogen before saturating the atmosphere with methanol vapour [51], (b). In contrast, when the two liquids are mixed, monolayers are observed growing across the surface, (c), outlined by the white dashed line. The blue scale bar represents a phase variation of 10 ^{o} in (a) and (b), and 4 ^{o} in (c). The purple scale bar represents a topographic variation of 6 nm in (a) and (b), and 1 nm in (c). The scale bars are 100 nm. Panel (a) and (c) are amplitude modulation-mode AFM measurements from this work obtained using the protocols outlined in Chapter 2. Panel (b) is adapted with permission from ref. [51].

1.5.1 Molecular structure of water-methanol assemblies on HOPG

Non-contact modes of AFM, such as those which will be described in Chapter 2, offer the ability to probe the molecular details of soft structures, such as the molecularly thin self-assemblies of water and methanol. Using non-contact AFM the methanol-water structures presented in Figure 1.8c have been imaged *in-situ*, revealing molecular-scale details. Figure 1.9a show a representative image for a 50:50 methanol water mixture. Here the molecular scale features observed are a series

of parallel wires which lie perpendicular to a larger well ordered supramolecular row-pattern. The molecular scale wires have a periodicity of 0.7 nm, while the supramolecular pattern is 5 nm. In ref. [51], it was observed that the incorporation of small amounts of ethanol into the mixture (<1%) allows the perpendicular Å scale sub-rows to be imaged with a higher resolution, revealing the intricate nature of the molecular-scale wires, as shown in Figure 1.9b. The exact mechanism resulting in the increased resolution was not clear, although it may be due to the incorporation of the larger ethanol molecules within the structures, pushing the distance between molecular features towards a resolvable resolution. A more detailed study into the impact of alcohols larger than methanol will be presented in Chapter 5. For the rest of this chapter the focus will remain on the row structures formed in methanol-water mixtures, which we will hereafter refer to as the 'basic methanol-water monolayer'.

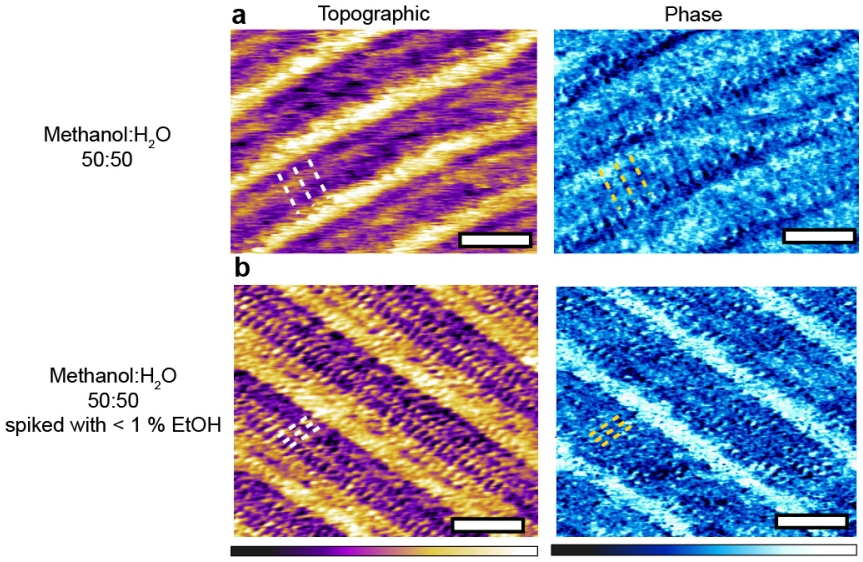

Fig. 1.9: Substructures in basic monolayers formed in a methanol-water mixture. Phase images of structures in a 50:50 methanol water mixture reveal ångström-scale perpendicular sub-features (dashed white/yellow lines) corresponding to water and methanol molecules forming correlated parallel 'wires' on the surface of HOPG. The scale bar represents 5 nm. The purple scale bar represents a topographic variation of 0.8 nm. The blue scale bar represents a phase variation of 10^o. Panel (a) is an amplitude modulation-mode AFM measurement from this work obtained using the protocols outlined in Chapter 2. Panel (b) is adapted with permission from [51]

Within a single domain the supramolecular row pattern observed in the basic methanol-water monolayer remains well ordered over larger scales. An example of this can be seen in Figure 1.10a, which shows the interface between two separately nucleated self-assembled patches. The direction of the main row patterns are consistently

observed to be at multiples of 60^o with respect to each other. The atomic lattice of HOPG is hexagonal with three symmetrical axes which indicates that the supramolecular pattern is epitaxially induced. This was confirmed by using contact mode AFM to scratch away the structure revealing the direction of the underlying HOPG lattice (Figure 1.10b) [51].

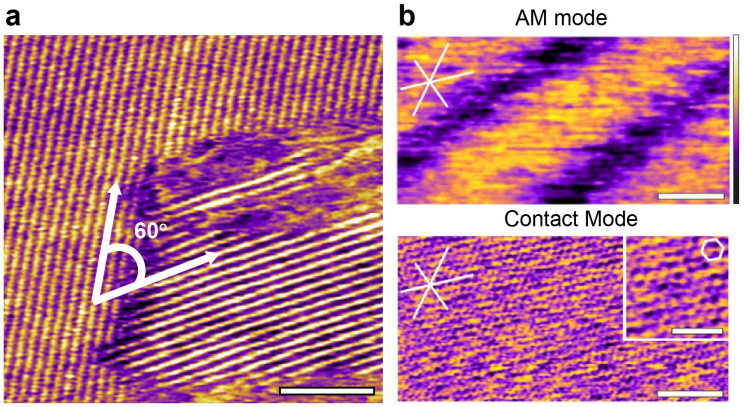

Fig. 1.10: A demonstration of the link between the supramolecular patterns of the monolayer and the underlying HOPG lattice. Panel (a) shows two independent monolayers whose row patterns are orientated at 120^o with respect to each other. (b) Switching from the soft amplitude modulation (AM) mode to contact mode allows the monolayer to be scratched away, revealing the underlying lattice with its 6-fold symmetry. The row pattern is perpendicular to one of the axis of symmetry which is consistent with an epitaxially induced effect. The scale bar is 50 nm in (a), 0.2 nm in (b), and 0.1 nm in the inset. The colour scale bar represents a variation of 0.4 nm. Panel (a) is an amplitude modulation-mode AFM measurement from this work obtained using the protocols outlined in Chapter 2. Panel (b) is adapted with permission from ref. [51]

To understand the source of the stabilisation of the methanol-water assemblies, it is important to gain molecular-level insights into the structures. The molecular level resolution provided by non-contact AFM cannot distinguish different types of molecules at this scale. Instead, computational simulations are needed to elucidate the details of the molecular organisation. The time-scales involved in the nucleation process eclipse those accessible by current simulation techniques (minutes compared with microseconds) [100–102]. Therefore in ref. [51], a multi-scale computational approach was used, consisting of *ab initio* density functional theory calculations to parametrize molecular interactions, followed by classical large scale molecular dynamics simulations. Over the course of a 100ns simulation, no long-lived stable structures were captured, consistent with the need for a nucleation event. Although they did not capture the formation of stable molecular patterns, the large scale simulations did provide hints towards the molecular behaviour. For

example, plotting how the free energy of methanol molecules at the surface changes reveals two-dimensional periodicities commensurate with the underlying HOPG lattice (Figure 1.11a). Furthermore, once close to the surface, both the methanol and water molecules had an enhanced local order. The in-plane oxygen-oxygen distribution function around a given methanol molecule is shown in Figure 1.11b. This distribution function shows that, close to the surface, the nearest neighbour of a methanol molecule is most likely a water molecule and the second neighbour tends to be another methanol molecule. An increase in longer range order was also observed. Figure 1.11c shows a plot of the probability of finding a methanol molecule in the hydrogen bonded chains of methanol and water (discussed in more detail in Chapter 4) for a 1:1 mixture in the bulk and at the HOPG interface. As can be seen from this Figure, every second bond has a higher probability and thus the most probable arrangement is an alternated network of methanol and water molecules. This arrangement has been previously reported for the bulk solution [103–105], but the effect is more pronounced at the interface with HOPG.

As part of the multi-scale simulation strategy in Voitchovsky *et al.*, smaller simulation boxes of sixteen by sixteen molecules were used in replica exchange simulations [106] coupled with a geometry optimization at regular intervals [51]. This method created hundreds of thousands of local energy minima which were classified using a non-linear dimensionality reduction technique to cluster similar arrangements together based on comparing atomic coordinates [107–110]. For full details regarding how the structural similarities were determined and quantified the reader is referred to the methods section in ref. [51]. With this approach they plotted the resulting configuration energy landscape, reproduced in Figure 1.12a, and identified a specific molecular arrangement that consistently exhibits lower energies. This arrangement involved two water and two methanol molecules forming a 'square motif', which can combine by either sharing a side, forming one-dimensional ribbons (Figure 1.12b), or by sharing corners (Figure 1.12c).

The experimentally observed molecular scale features in Figure 1.9 consisted of nanoscale stripes running perpendicular to a larger supramolecular row pattern. These nanoscale stripes can be explained by the low energy one-dimensional hydrogen bonded ribbon conformation shown in Figure 1.12d. Here, the proposed hypothetical spacing between the molecular ribbons is comparable to the stripe separation. The supramolecular row pattern was explained by an epitaxially-induced

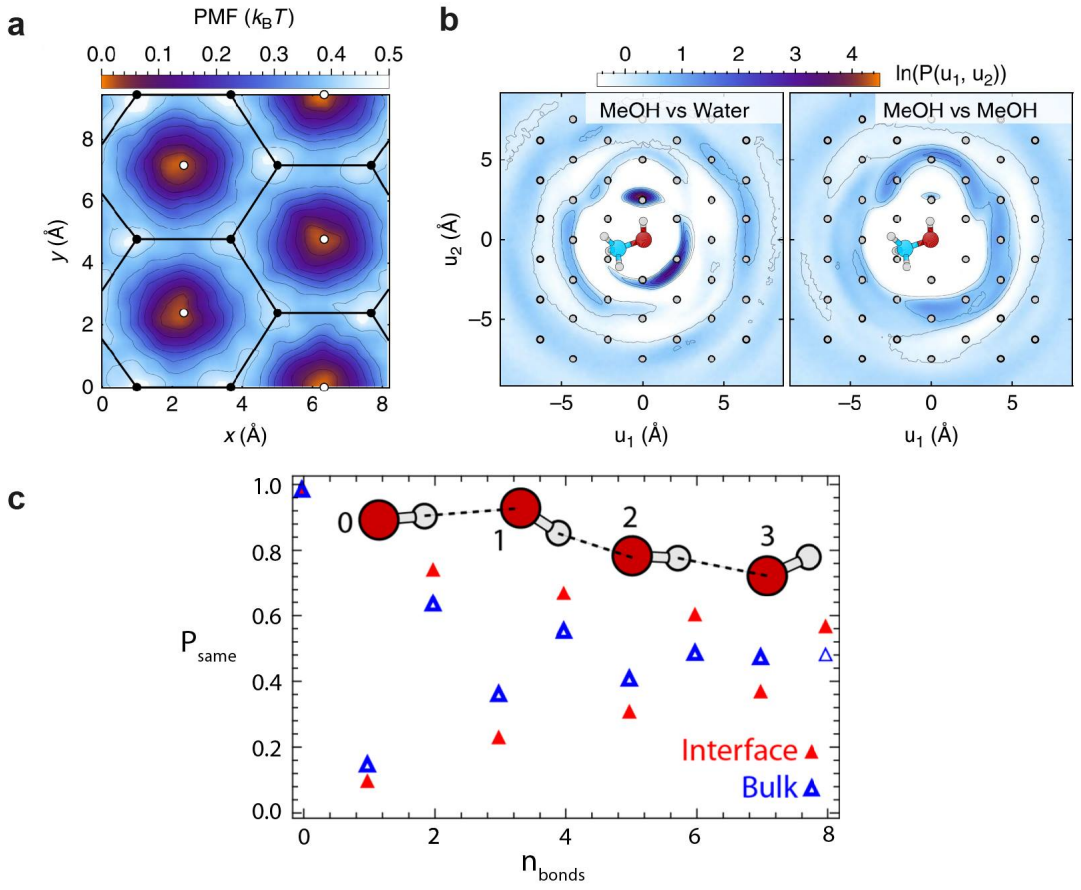

Fig. 1.11: Results from molecular dynamics simulations of a 50:50 methanol water mixture on top of HOPG performed in ref. [51]. (a) shows a plot of the potential of mean force in the xy plane for the methanol molecules on top of HOPG. The distribution of methanol is commensurate with the graphite lattice. In (b) the in-plane oxygen-oxygen distribution function between a reference methanol molecule close to the HOPG surface with another corresponding oxygen in water (left) and methanol (right) is plotted. The water showed an increased preference for being in the first coordination shell. Methanol sits mostly in the second coordination shell. The white dots represent the underlying graphite lattice. There is a small mismatch between the characteristic length scale of the water-methanol hydrogen bonded network and the periodicity of the HOPG surface. (c) presents the probability of finding a MeOH molecule after a distance of n bonds when moving along the hydrogen bond network. The cartoon provides an illustration of the analysed correlation. The points shown are both for the hydrogen bond network at the interface with HOPG (red solid triangles) and in the bulk liquid (blue open triangles). Figure adapted with permission from [51].

Moiré pattern due to the mismatch between the periodicity of the square motifs in the one dimensional ribbons (5.2 Å) and the periodicity of the top layer of the HOPG (2.46 Å). In ref. [51], they calculated the resulting Moiré periodicity to be around 45 Å, comparable to the row spacing found using AFM (typically 45 - 55

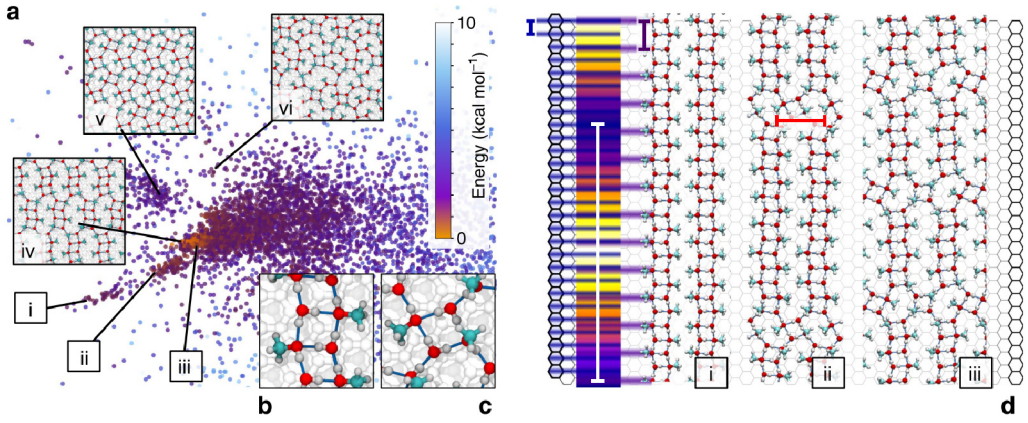

Fig. 1.12: Catalogue of stable two-dimensional structures obtained by replica-exchange simulations for a 50:50 methanol-water monolayer in ref. [51]. Every dot represents a certain molecular arrangement. The colour of the dot corresponds to the energy and therefore also its stability (see colour scale bar). The insets (i-vi) show six example structures. The most common feature in the arrangements is a water-methanol 'square' motif, (b) and (c). (d) The motifs can form elongated molecular ribbons which have a mismatched periodicity (5.20 Å, purple bar) with the HOPG underneath (2.46 Å, blue bar). This mismatch induces a Moiré pattern with a lengthscale of around 45 Å (white bar). The yellow-purple ribbon in (d) illustrates the degree of mismatch using the colour scale of AFM topographic images. The distance between adjacent ribbons is typically 8.2 Å (red bar). Figured adapted with permission from [51].

Å). The formation of Moiré patterns has previously been observed for self-assembled monolayers of large alcohols on HOPG [111].

Due to the presence of recurring motifs which form the segments of larger structures, the energy landscape presented in Figure 1.12 is rather flat, i.e. there are many molecular arrangements with similar energies. This principle of a flat energy landscape will be part of the foundation for the work in Chapter 5, where the small energy differences between configurations are utilised to easily alter existing monolayers.

Overall, these computational results strongly suggested that the basic methanol-water monolayer experimentally observed consists of hydrogen bonded chains of alternating methanol and water molecules. These monolayers are then capable of remaining stable at room temperature due to the extended hydrogen-bonded network involving many chains of molecules which allows them to adsorb as a group [51]. This principle will be subsequently referred to as 'group-effect' self-assembly. The subsequent frustration due to the small mismatch between the units within the monolayer and the graphite lattice gives rise to the supramolecular row-like patterns.

1.5.2 Evolution of monolayers with time

The well-ordered single monolayer with the global row pattern can evolve during the experimental window. When the system is studied for long timescales, second monolayers have been observed to nucleate on top of the original monolayer (Figure 1.13a). The height of this second layer is 0.3 nm, the same thickness as the first layer (Figure 1.13b). It exhibits a row pattern that follows the direction of the underlying monolayer, and thus also the symmetry of the HOPG. These second monolayers have never been observed to cover the whole surface. Instead, when the system is left for > 2 hours, the second layer growth eventually ceases, leaving well dispersed islands (Figure 1.13c).

The formation of a third monolayer was reported in ref. [51] although this occurs rarely. This may be explained in part by comparing with a study of 1-propanol monolayers on HOPG at low temperatures [112]. In ref. [112] they observed that the first three monolayers of 1-propanol molecules were all well ordered and orientated parallel to the surface due to weak surface-liquid van der Waals interactions, whereas the fourth and higher layers started to demonstrate inter-layer hydrogen bonding due to a diminished substrate potential. Similarly, the two-dimensional pattern of the second (and third) stacked layers are the same as the monolayer below, indicating that the epitaxial effect is capable of propagating through the first two monolayers.

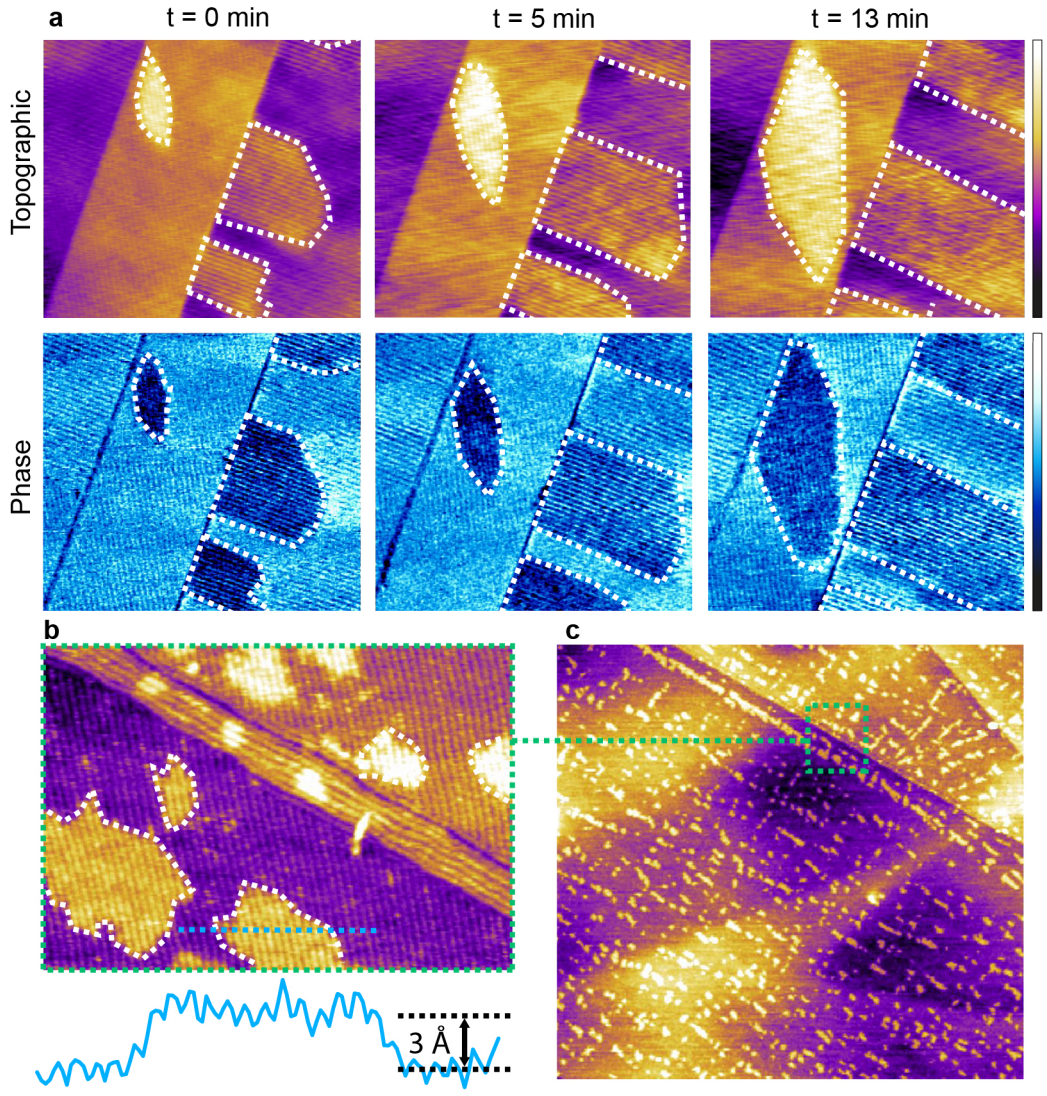

Fig. 1.13: (a) Examples of the growth of multiple second monolayers on top of the original. The second layer grows slower than the first and is never observed to cover the whole surface. (b) Higher resolution image of the multilayers with a line profile demonstrating their thickness is comparable to that of a molecular monolayer. (c) Large scale image showing the distribution of second layers across the surface. They are observed to nucleate and grow at increased rates close to HOPG step edges. The scale bars represent 50 nm in (a) and (b), and 200 nm in (c). The purple colour scale bar represents a height variation of 2 nm in (a) and (b), and 4 nm in (c). The blue scale bar represents a phase variation of 4 ^{o} in (a). These measurements were obtained using amplitude modulation-mode AFM measurements with the protocols outlined in Chapter 2.

1.6 Summary

Understanding and predicting the self-assembly of molecules into supramolecular structures at solid interfaces underpins modern materials science and is of paramount importance to nanotechnology. Applications range from crystal growth [113] and biomolecular function [114] to nanoscale electronics [115, 116], light harvesting [117], and the nano-functionalisation of interfaces [118] to name only a few examples. Interfacial self-assembly is also ubiquitous in nature, for example, in biological processes such as the formation of cell membranes [2, 4]. Generally, successful self-assembly requires some configurational flexibility for the assembling molecules to be able to probe multiple arrangements, and a stable support or template to assist and stabilise the self-organising molecules. The properties of the resulting assemblies are then determined by a complex interplay between the intermolecular interactions, kinetics, and entropic effects at the interface. This renders any comprehensive understanding of the self-assembly process highly challenging.

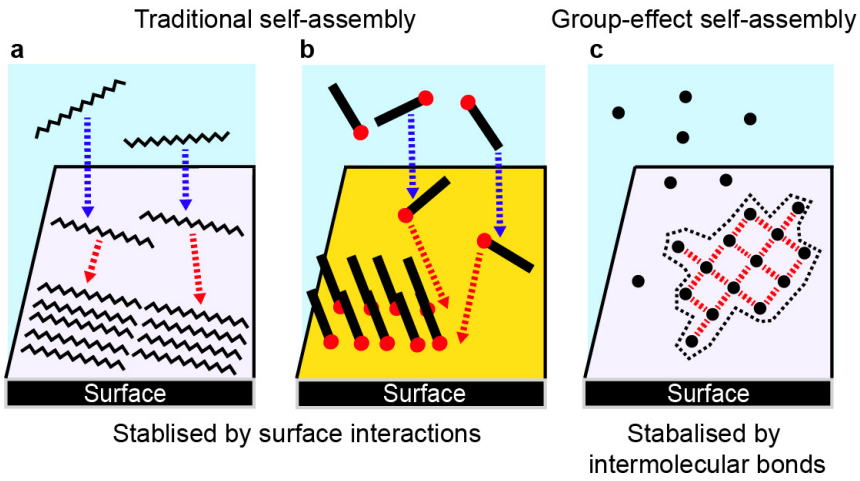

Fig. 1.14: Cartoon representation of strategies for molecular self-assembly at solid-liquid interfaces. The existing approaches typically involve a 2-step process where molecules are first stabilised at the interface either through van der Waal interactions for large molecules (a) or specific tethers for small molecules (b). In contrast, the process can occur in a single step through a group-effect self-assembly, (c). The molecules have weak interactions with the surface but are instead stabilised by extended networks of hydrogen bonds (red dashes).

The formation of self-assembled structures at solid-liquid or solid-gas interfaces typically occurs in a two-step process, whereby molecules first accumulate at the interface and subsequently self-organise into supramolecular structures [10]. During the first stage, the assembling molecules must reside at the interface for relatively

long periods of time, so as to meaningfully interact with neighbours and promote the relevant ordered structure. At solid-liquid interfaces this is typically made possible by significant interactions between the assembling molecules and the solid's surface. In systems comprising of large molecules, increased van der Waals interactions can overcome thermal fluctuations [119] and ensure a stable physisorption (Figure 1.14 a), as described in Sections 1.2.1 and 1.3.2. However, this becomes considerably more difficult for small molecules experiencing lower van der Waals forces. In principle, this problem can be overcome by using a mobile tether between the assembling molecules and the solid surface through a form of chemisorption. However, this strategy is inevitably limited to specific molecules and interactions, such as thio-alkanes on gold [3, 58, 120] (Figure 1.14 b), as outlined in Section 1.3.2. When specific tethers are excluded, the weak and non-specific surface interactions at play tend to render the self-assembly difficult to understand or predict. Molecular self-assembly in biological systems often rely on such relatively weak interactions in order to create soft or fluid structures that can evolve in response to changes in the environment [121, 122]. Yet, biological self-assembly can occurs at fast rates (for example, milliseconds for peptide self-assembly at a hydrophobic interface [123]) and with high precision, making it particularly interesting, although still poorly understood [5, 6].

To date, the self-assembly of small molecules has primarily been studied in extreme cases where systems are under confinement [95] or at low temperatures [77] (as described in Section 1.4), so as to force the molecules to remain long enough near the solid's surface for supramolecular structures to form. Examples in ambient conditions are scarce, with limited insights into the process. This gap is significant because the nanoscale arrangement of small molecules at solid-liquid interfaces is key to phenomena such as friction and lubrication [83], nanomembrane separation [124] and chemical reactivity [39]. Additionally, sophisticated or complex self-assembled structures are likely to involve small molecules as part of their building blocks. The weak dependence of small molecules on specific interactions could also increase the process robustness and flexibility while reducing costs for potential applications.

The aim of this thesis is to explore the new paradigm for small molecule self-assembly presented in Section 1.5. This is achieved using a base system of a mixture of short chain length alcohols and water on HOPG. Instead of relying on strong surface interactions, these monolayers are stabilised by a collective network of hydrogen-

bonds, in a process referred to as 'group-effect' self-assembly (Figure 1.14 c). These structures have the potential to impact multiple processes. For example, in recent years, the behaviour of aqueous mixtures at hydrophobic solid interfaces has been a key topic due to the surge in graphite or graphene based nano-technology. Examples involving alcohol and water mixtures can be found in filtration [125], catalysis [39] and fuel cells [126] to name just a few. Applications involving solid-liquid interfaces are generally heavily reliant on the structure and dynamics of the liquid component within the couple of molecular layers adjacent to the solid. Liquid structure at the interface has been shown to affect the transport of charge [127] as well as the adsorption of molecules [128], both of which are essential to the function of nanoscale devices.

As has been outlined within this introductory chapter, the self-assembly of small molecules, such as alcohols and water, at interfaces when at room temperature is rather novel. Therefore, it is important to fully understand the alcohol-water-HOPG base system. Investigations into this system will be presented in Chapters 3 and 4. Then, in Chapter 5, the behaviour of group-effect stabilised structures will be studied, including the response to external stimuli and methods of influencing the assembly. Thus, the rest of this thesis will be structured as follows:

Chapter 2 - Methods: This chapter will introduce the rationale and methodology behind the techniques used for investigations in this thesis. It will provide specific details for two-dimensional and three-dimensional atomic force microscopy and molecular dynamics simulations.

Chapter 3 - Methanol catalysis on HOPG: This chapter will address the production of methanol in-situ at the water-HOPG interface both in ambient conditions and when electric fields are applied. This phenomenon will be demonstrated using AFM with confirmation and quantitative analysis via NMR-spectroscopy. The catalysis mechanism will also be discussed.

Chapter 4 - Alcohol-water mixtures at hydrophobic interfaces: This chapter will provide a background on the behaviour of mixtures of alcohol and water in bulk. Then it will present novel molecular dynamics data regarding the concentration dependent arrangements of alcohol molecules at hydrophobic interfaces. Furthermore, comparisons will be made between computational data obtained and the concentration dependant structure of the alcohol-water assemblies observed ex-

perimentally.

Chapter 5 - Influencing the Small Molecule Assemblies: This chapter will present investigations into our ability to influence structures formed by group-effect self-assembly using the alcohol-water base system. The interplay between intermolecular and surface interactions will be investigated by adding small amounts of foreign molecules capable of interfering with the hydrogen bond network, and by systematically varying the length of the alcohol hydrocarbon chain. The generality of the self-assembly process will also be explored by replacing HOPG with other hydrophobic surfaces.

Chapter 6 - Conclusion and Outlook: This final chapter will summarise the key findings of the thesis and outline the pressing questions and experiments to be addressed in future work.

References: Chapter 1

[1] A. D. Dinsmore, J. C. Crocker, A. G. Yodh, "Self-assembly of colloidal crystals", *Current Opinion in Colloid and Interface Science* **1998**, *3*, 5–11.

[2] B. A. Grzybowski, C. E. Wilmer, J. Kim, K. P. Browne, K. J. Bishop, "Self-assembly: From crystals to cells", *Soft Matter* **2009**, *5*, 1110–1128.

[3] C. Vericat, M. E. Vela, G. Benitez, P. Carro, R. C. Salvarezza, "Self-assembled monolayers of thiols and dithiols on gold: New challenges for a well-known system", *Chemical Society Reviews* **2010**, *39*, 1805–1834.

[4] R. Thiruvengadathan, V. Korampally, A. Ghosh, N. Chanda, K. Gangopadhyay, S. Gangopadhyay, "Nanomaterial processing using self-assembly-bottom-up chemical and biological approaches", *Reports on Progress in Physics* **2013**, *76*.

[5] S. Petry, "Mechanisms of Mitotic Spindle Assembly Sabine", *Annu Rev Biochem.* **2016**, *85*, 659–683.

[6] A. Mogilner, E. Craig, "Towards a quantitative understanding of mitotic spindle assembly and mechanics", *Journal of Cell Science* **2010**, *123*, 3435–3445.

[7] J. Chen, J. J. De Yoreo, S. Zhang, E. Zhu, Y. Huang, J. Liu, H. Heinz, Z. Lin, X. Duan, "Building two-dimensional materials one row at a time: Avoiding the nucleation barrier", *Science* **2018**, *362*, 1135–1139.

[8] G. M. Moore, "Cramming more components onto integrated circuits", *Electronics* **1965**, *38*, 114.

[9] A. Kühnle, "Self-assembly of organic molecules at metal surfaces", *Current Opinion in Colloid and Interface Science* **2009**, *14*, 157–168.

[10] S. De Feyter, F. C. De Schryver, "Two-dimensional supramolecular self-assembly probed by scanning tunneling microscopy", *Chemical Society Reviews* **2003**, *32*, 139–150.

[11] J. Israelachvili, *Intermolecular and Surface Forces*, 2nd ed., Academic Press, **1991**.

[12] J. Tien, A. Terfort, G. M. Whitesides, "Microfabrication through electrostatic self-assembly", *Langmuir* **1997**, *13*, 5349–5355.

[13] K. J. Bishop, C. E. Wilmer, S. Soh, B. A. Grzybowski, "Nanoscale forces and their uses in self-assembly", *Small* **2009**, *5*, 1600–1630.

[14] T. Yokoyama, S. Yokoyama, T. Kamikado, Y. Okuno, S. Mashiko, "Selective assembly on a surface of supramolecular aggregates with controlled size and shape", *Nature* **2001**, *413*, 619–621.

[15] R. A. Jones, *Soft Condensed Matter*, 1st ed., Oxford University Press, **2002**.

[16] H. C. Hamaker, "The London-van der Waals attraction between spherical particles", *Physica* **1937**, *4*, 1058–1072.

[17] W. Gao, "The chemistry of graphene oxide", *Graphene Oxide: Reduction Recipes Spectroscopy and Applications* **2015**, 61–95.

[18] A. K. Geim, I. V. Grigorieva, "Van der Waals heterostructures", *Nature* **2013**, *499*, 419–425.

[19] S. Conti, M. Cecchini, "Predicting molecular self-assembly at surfaces: A statistical thermodynamics and modeling approach", *Physical Chemistry Chemical Physics* **2016**, *18*, 31480–31493.

[20] D. M. Packwood, P. Han, T. Hitosugi, "Chemical and entropic control on the molecular self-assembly process", *Nature Communications* **2017**, *8*, 1–8.

[21] R. Gutzler, T. Sirtl, J. F. Dienstmaier, K. Mahata, W. M. Heckl, M. Schmittel, M. Lackinger, "Reversible phase transitions in self-assembled monolayers at the liquid-solid interface: Temperature-controlled opening and closing of nanopores", *Journal of the American Chemical Society* **2010**, *132*, 5084–5090.

[22] J. F. Dienstmaier, K. Mahata, H. Walch, W. M. Heckl, M. Schmittel, M. Lackinger, "On the scalability of supramolecular networks - High packing density vs optimized hydrogen bonds in tricarboxylic acid monolayers", *Langmuir* **2010**, *26*, 10708–10716.

[23] M. Mammen, E. Shakhnovich, J. Deutch, G. Whitesides, "Estimating the Entropic Cost of Self-Assembly of Multiparticle Hydrogen-Bonded Aggregates Based on the Cyanuric Acid-Melamine Lattice", *J. Org. Chem* **1998**, *63*, 3821–3830.

[24] L. Xu, X. Miao, X. Ying, W. Deng, "Two-dimensional self-assembled molecular structures formed by the competition of van der Waals forces and dipole-dipole interactions", *Journal of Physical Chemistry C* **2012**, *116*, 1061–1069.

[25] S. Karthika, T. K. Radhakrishnan, P. Kalaichelvi, "A Review of Classical and Nonclassical Nucleation Theories", *Crystal Growth and Design* **2016**, *16*, 6663–6681.

[26] P. E. Wagner, R. Strey, "Measurements of homogeneous nucleation rates for n-nonane vapor using a two-piston expansion chamber", *The Journal of Chemical Physics* **1984**, *80*, 5266–5275.

[27] M. Volmer, A. Weber, "Nucleus Formation in Supersaturated Systems", *Zeitschrift für Physikalische Chemie* **1926**, *119*, 277–301.

[28] R. Becker, W. Döring, "Kinetische Behandlung der Keimbildung in übersättigten Dämpfen", *Annalen der Physik* **1935**, *416*, 719–752.

[29] J. Frenkel, "A general theory of heterophase fluctuations and pretransition phenomena", *The Journal of Chemical Physics* **1939**, *7*, 538–547.

[30] B. Kahr, M. D. Ward, "Barrier(less) islands", *Science* **2018**, *362*, 1111.

[31] J. J. De Yoreo, "Principles of Crystal Nucleation and Growth", *Reviews in Mineralogy and Geochemistry* **2005**, *54*, 57–93.

[32] R. Strey, Y. Viisanen, "Measurement of the molecular content of binary nuclei. Use of the nucleation rate surface for ethanol-hexanol", *The Journal of Chemical Physics* **1994**, *100*, 6062–6072.

[33] H. Flood, "Tropfchenbildung in ubersattigten Athylalkohol-Wasserdampfgemischen", *Zeitschrift für Physikalische Chemie* **1934**, *170A*, 286–294.

[34] P. Mirabel, J. L. Katz, "Condensaton of a supersaturated vapor. IV. The homogeneous nucleation of binary mixtures", *The Journal of Chemical Physics* **1977**, *67*, 1697–1704.

[35] R. A. Zahoransky, F. Peters, "Binary nucleation at low temperatures", *The Journal of Chemical Physics* **1985**, *83*, 6425–6431.

[36] Y. Viisanen, R. Strey, A. Laaksonen, M. Kulmalac, "Measurement of the molecular content of binary nuclei. II. Use of the nucleation rate surface for water–ethanol", *The Journal of Chemical Physics* **1994**, *103*, 4333–4345.

[37] R. Strey, Y. Viisanen, P. E. Wagner, "Measurement of the molecular content of binary nuclei. III. Use of the nucleation rate surfaces for the water-n-alcohol series", *The Journal of Chemical Physics* **1995**, *103*, 4333–4345.

[38] J. J. De Yoreo, P. U. Gilbert, N. A. Sommerdijk, R. L. Penn, S. Whitelam, D. Joester, H. Zhang, J. D. Rimer, A. Navrotsky, J. F. Banfield, A. F. Wallace, F. M. Michel, F. C. Meldrum, H. Cölfen, P. M. Dove, "Crystallization by particle attachment in synthetic, biogenic, and geologic environments", *Science* **2015**, *349*.

[39] W. Foster, J. A. Aguilar, H. Kusumaatmaja, K. Voïtchovsky, "In Situ Molecular-Level Observation of Methanol Catalysis at the Water-Graphite Interface", *ACS Applied Materials and Interfaces* **2018**, *10*, 34265–34271.

[40] W. H. Binder, "Supramolecular assembly of nanoparticles at liquid-liquid interfaces", *Angewandte Chemie - International Edition* **2005**, *44*, 5172–5175.

[41] A. Toor, T. Feng, T. P. Russell, "Self-assembly of nanomaterials at fluid interfaces", *European Physical Journal E* **2016**, *39*.

[42] C. N. Rao, K. P. Kalyanikutty, "The liquid-liquid interface as a medium to generate nanocrystalline films of inorganic materials", *Accounts of Chemical Research* **2008**, *41*, 489–499.

[43] R. McGorty, J. Fung, D. Kaz, V. N. Manoharan, "Colloidal self-assembly at an interface", *Materials Today* **2010**, *13*, 34–42.

[44] J. C. Huie, "Guided molecular self-assembly: A review of recent efforts", *Smart Materials and Structures* **2003**, *12*, 264–271.

[45] J. Zhang, P. Chen, B. Yuan, W. Ji, Z. Cheng, X. Qiu, "Real-space identification of intermolecular bonding with atomic force microscopy", *Science* **2013**, *342*, 611–614.

[46] S. Kawai, T. Nishiuchi, T. Kodama, P. Spijker, R. Pawlak, T. Meier, J. Tracey, T. Kubo, E. Meyer, A. S. Foster, "Direct quantitative measurement of the C==O···H-C bond by atomic force microscopy", *Science Advances* **2017**, *3*.

[47] M. Böhringer, K. Morgenstern, W.-D. Schneider, R. Berndt, F. Mauri, A. De Vita, R. Car, "Two-Dimensional Self-Assembly of Supramolecular Clusters and Chains", *Physical Review Letters* **1999**, *83*, 324–327.

[48] J. Weckesser, A. De Vita, J. V. Barth, C. Cai, K. Kern, "Mesoscopic correlation of supramolecular chirality in one-dimensional hydrogen-bonded assemblies", *Physical Review Letters* **2001**, *87*, 961011–961014.

[49] G. Pawin, K. L. Wong, K. Y. Kwon, L. Bartels, "A homomolecular porous network at a Cu(111) surface", *Science* **2006**, *313*, 961–962.

[50] M. Lackinger, S. Griessl, T. Markert, F. Jamitzky, W. M. Heckl, "Self-assembly of benzene-dicarboxylic acid isomers at the liquid solid interface: Steric aspects of hydrogen bonding", *Journal of Physical Chemistry B* **2004**, *108*, 13652–13655.

[51] K. Voitchovsky, D. Giofrè, J. J. Segura, F. Stellacci, M. Ceriotti, "Thermally-nucleated self-assembly of water and alcohol into stable structures at hydrophobic interfaces", *Nature Communications* **2016**, *7*, 13064.

[52] K. Eichhorst-gerner, A. Stabel, G. Moessner, D. Declerq, S. Valiyaveettil, V. Enkelmann, K. Mullen, J. P. Rabe, "Self-Assembly of a Two-Component Hydrogen-Bonded Network: Comparison of the Two-Dimensional Structure Observed by Scanning Tunneling Microscopy and the Three-Dimensional Crystal Lattice", *Angew. Chem. Int. Ed. Engl.* **1996**, *98*, 12–15.

[53] S. De Feyter, A. Gesquire, M. M. Abdel-Mottaleb, P. C. Grim, F. C. De Schryver, C. Meiners, M. Sieffert, S. Valiyaveettil, K. Mullen, "Scanning tunneling microscopy: A unique tool in the study of chirality, dynamics, and reactivity in physisorbed organic monolayers", *Accounts of Chemical Research* **2000**, *33*, 520–531.

[54] A. Dmitriev, N. Lin, J. Weckesser, J. V. Barth, K. Kern, "Supramolecular assemblies of trimesic acid on a Cu(100) surface", *Journal of Physical Chemistry B* **2002**, *106*, 6907–6912.

[55] Y. Ishikawa, A. Ohira, M. Sakata, C. Hirayama, M. Kunitake, "A two-dimensional molecular network structure of trimesic acid prepared by adsorption-induced self-organization", *Chemical Communications* **2002**, *2*, 2652–2653.

[56] S. Yin, C. Wang, X. Qiu, X. Bo, C. Bai, "Theoretical study of the effects of intermolecular interactions in self-assembled long-chain alkanes adsorbed on graphite surface", *Surface and Interface Analysis* **2001**, *32*, 248–252.

[57] T. Kudernac, S. Lei, J. A. Elemans, S. De Feyter, "Two-dimensional supramolecular self-assembly: Nanoporous networks on surfaces", *Chemical Society Reviews* **2009**, *38*, 402–421.

[58] J. C. Love, L. A. Estroff, J. K. Kriebel, R. G. Nuzzo, G. M. Whitesides, "Self-assembled monolayers of thiolates on metals as a form of nanotechnology", *Chemical Reviews* **2005**.

[59] F. Huber, J. Berwanger, S. Polesya, S. Mankovsky, H. Ebert, F. J. Giessibl, "Chemical bond formation showing a transition from physisorption to chemisorption", *Science* **2019**, *366*, 235–238.

[60] S. De Feyter, F. C. De Schryver, "Self-assembly at the liquid/solid interface: STM reveals", *Journal of Physical Chemistry B* **2005**, *109*, 4290–4302.

[61] M. Lackinger, S. Griessl, L. Kampschulte, F. Jamitzky, W. M. Heckl, "Dynamics of grain boundaries in two-dimensional hydrogen-bonded molecular networks", *Small* **2005**, *1*, 532–539.

[62] J. Adamcik, S. Tobenas, G. Di Santo, D. Klinov, G. Dietler, "Temperature-controlled assembly of high ordered/disordered dodecylamine layers on HOPG: Consequences for DNA patterning", *Langmuir* **2009**, *25*, 3159–3162.

[63] L. Qu, Y. Liu, J. B. Baek, L. Dai, "Nitrogen-Doped Graphene as Efficient Metal-Free Electrocatalyst for Oxygen Reduction in Fuel Cells", *Acs Nano* **2010**, *4*, 1321–1326.

[64] Y. Zhu, S. Murali, M. D. Stoller, K. J. Ganesh, W. Cai, P. J. Ferreira, A. Pirkle, R. M. Wallace, K. A. Cychosz, M. Thommes, D. Su, E. A. Stach, R. S. Ruoff, "Carbon-Based Supercapacitors Produced by Activation of Graphene", *Science* **2011**, *332*, 1537–1542.

[65] S. Le Liepvre, P. Du, D. Kreher, F. Mathevet, A. J. Attias, C. Fiorini-Debuisschert, L. Douillard, F. Charra, "Fluorescent Self-Assembled Molecular Monolayer on Graphene", *ACS Photonics* **2016**, *3*, 2291–2296.

[66] B. Mi, "Graphene Oxide Membranes for Ionic and Molecular Sieving", *Science* **2014**, *343*, 740–742.

[67] A. P. S. Gaur, S. Sahoo, M. Ahmadi, S. P. Dash, M. J. F. Guinel, R. S. Katiyar, "Surface energy engineering for tunable wettability through controlled synthesis of MoS2", *Nano Letters* **2014**, *14*, 4314–4321.

[68] J. Lee, P. Dak, Y. Lee, H. Park, W. Choi, M. A. Alam, S. Kim, "Two-dimensional layered MoS_2 biosensors enable highly sensitive detection of biomolecules", *Scientific Reports* **2014**, *4*, 1–7.

[69] A. J. Gellman, K. R. Paserba, "Kinetics and mechanism of oligomer desorption from surfaces: n-alkanes on graphite", *Journal of Physical Chemistry B* **2002**, *106*, 13231–13241.

[70] Y. Gao, C. Berciu, Y. Kuang, J. Shi, D. Nicastro, B. Xu, "Probing nanoscale self-assembly of nonfluorescent small molecules inside live mammalian cells", *ACS Nano* **2013**, *7*, 9055–9063.

[71] A. Roy, A. Gautam, J. A. Malla, S. Sarkar, A. Mukherjee, P. Talukdar, "Self-assembly of small-molecule fumaramides allows transmembrane chloride channel formation", *Chemical Communications* **2018**, *54*, 2024–2027.

[72] L. Lupi, A. Hudait, V. Molinero, "Heterogeneous nucleation of ice on carbon surfaces", *Journal of the American Chemical Society* **2014**, *136*, 3156–3164.

[73] X. Kong, P. U. Andersson, E. S. Thomson, J. B. Pettersson, "Ice formation via deposition mode nucleation on bare and alcohol-covered graphite surfaces", *Journal of Physical Chemistry C* **2012**, *116*, 8964–8974.

[74] D. Yang, A. H. Zewail, "Ordered water structure at hydrophobic graphite interfaces observed by 4D, ultrafast electron crystallography", *PNAS* **2009**, *106*, 4112–4126.

[75] K. Morishige, K. Kawamura, A. Kose, "X-ray diffraction study of the structure of a monolayer methanol film adsorbed on graphite", *The Journal of Chemical Physics* **1990**, *93*, 5267–5270.

[76] T. Ohkubo, K. Kaneko, "Oriented structures of alcohol hidden in carbon micropores with ERDF analysis", *Colloids and Surfaces A: Physicochemical and Engineering Aspects* **2001**, *187-188*, 177–185.

[77] A. E. Baber, T. J. Lawton, E. C. H. Sykes, "Hydrogen-bonded networks in surface-bound methanol", *Journal of Physical Chemistry C* **2011**, *115*, 9157–9163.

[78] E. Schröder, "Methanol adsorption on graphene", *Journal of Nanomaterials* **2013**, *2013*.

[79] P. Pršlja, E. Lomba, P. Gómez-Álvarez, T. Urbič, E. G. Noya, "Adsorption of water, methanol, and their mixtures in slit graphite pores", *Journal of Chemical Physics* **2019**, *150*.

[80] Q. Li, J. Song, F. Besenbacher, M. Dong, "Two-dimensional material confined water published as part of the accounts of chemical research special issue "2d nanomaterials beyond Graphene"", *Accounts of Chemical Research* **2015**, *48*, 119–127.

[81] A. I. Kolesnikov, J. M. Zanotti, C. K. Loong, P. Thiyagarajan, A. P. Moravsky, R. O. Loutfy, C. J. Burnham, "Anomalously soft dynamics of water in a nanotube: A revelation of nanoscale confinement", *Physical Review Letters* **2004**, *93*, 035503–1.

[82] G. A. Kimmel, J. Matthiesen, M. Baer, C. J. Mundy, N. G. Petrik, R. S. Smith, Z. Dohnálek, B. D. Kay, "No confinement needed: Observation of a metastable hydrophobic wetting two-layer ice on graphene", *Journal of the American Chemical Society* **2009**, *131*, 12838–12844.

[83] T. D. Li, J. Gao, R. Szoszkiewicz, U. Landman, E. Riedo, "Structured and viscous water in subnanometer gaps", *Physical Review B - Condensed Matter and Materials Physics* **2007**, *75*, 1–6.

[84] S. Granick, S. Bae, S. Kumar, C. Yu, "Confined liquid controversies near closure?", *Physics* **2010**, *3*, 18–21.

[85] S. Liu, D. Guo, G. Xie, "Water film confined in a nanoscale gap: Surface polarity and hydration effects", *Journal of Applied Physics* **2010**, *108*.

[86] E. Tombari, G. Salvetti, C. Ferrari, G. P. Johari, "Thermodynamic functions of water and ice confined to 2 nm radius pores", *Journal of Chemical Physics* **2005**, *122*.

[87] C. Cafolla, K. Voïtchovsky, "Lubricating properties of single metal ions at interfaces", *Nanoscale* **2018**, *10*, 11831–11840.

[88] A. Kalra, S. Garde, G. Hummer, "Osmotic water transport through carbon nanotube membranes", *Proceedings of the National Academy of Sciences of the United States of America* **2003**, *100*, 10175–10180.

[89] J. Song, Q. Li, X. Wang, J. Li, S. Zhang, J. Kjems, F. Besenbacher, M. Dong, "Evidence of Stranski-Krastanov growth at the initial stage of atmospheric water condensation", *Nature Communications* **2014**, *5*, 1–8.

[90] N. Giovambattista, P. J. Rossky, P. G. Debenedetti, "Phase transitions induced by nanoconfinement in liquid water", *Physical Review Letters* **2009**, *102*, 6–9.

[91] R. Zangi, "Water confined to a slab geometry : a review of recent", *Journal of Physics: Condensed Matter* **2004**, *16*, S5371–S5388.

[92] N. Severin, J. Gienger, V. Scenev, P. Lange, I. M. Sokolov, J. P. Rabe, "Nanophase separation in monomolecularly thin water-ethanol films controlled by graphene", *Nano Letters* **2015**, *15*, 1171–1176.

[93] S. You, J. Yu, B. Sundqvist, L. A. Belyaeva, N. V. Avramenko, M. V. Korobov, A. V. Talyzin, "Selective intercalation of graphite oxide by methanol in water/methanol mixtures", *Journal of Physical Chemistry C* **2013**, *117*, 1963–1968.

[94] G. Algara-Siller, O. Lehtinen, F. C. Wang, R. R. Nair, U. Kaiser, H. a. Wu, a. K. Geim, I. V. Grigorieva, "Square ice in graphene nanocapillaries.", *Nature* **2015**.

[95] R. Zangi, D. Roccatano, "Strings-to-Rings Transition and Antiparallel Dipole Alignment in Two-Dimensional Methanols", *Nano Letters* **2016**, *16*, 3142–3147.

[96] P. Bampoulis, J. P. Witteveen, E. S. Kooij, D. Lohse, B. Poelsema, H. J. W. Zandvliet, "Structure and Dynamics of Confined Alcohol-Water Mixtures", *ACS Nano* **2016**, *10*, 6762–6768.

[97] R. S. Smith, J. Matthiesen, B. D. Kay, "Desorption kinetics of methanol, ethanol, and water from graphene", *Journal of Physical Chemistry A* **2014**, *118*, 8242–8250.

[98] J. Sung, K. Park, D. Kim, "Surfaces of Alcohol-Water Mixtures Studied by Sum-Frequency Generation Vibrational Spectroscopy", *The Journal of Physical Chemistry B* **2005**, *109*, 18507–18514.

[99] K. H. *. Yoichi Kanda, Tomonobu Nakamura, "AFM studies of interaction forces between surfaces in alcohol–water solutions", *Colloids and Surfaces A: Physicochemical and Engineering Aspects* **1998**, *139*, 55–62.

[100] J. A. B. da Silva, F. G. B. Moreira, V. M. L. dos Santos, R. L. Longo, "On the hydrogen bond networks in the water-methanol mixtures: topology, percolation and small-world.", *Physical Chemistry Chemical Physics* **2011**, *13*, 6452–6461.

[101] D. Surblys, Y. Yamaguchi, K. Kuroda, M. Kagawa, T. Nakajima, H. Fujimura, "Molecular dynamics analysis on wetting and interfacial properties of water-alcohol mixture droplets on a solid surface", *Journal of Chemical Physics* **2014**, *140*.

[102] E. J. W. Wensink, A. C. Hoffmann, P. J. Van Maaren, D. Van Der Spoel, "Dynamic properties of water/alcohol mixtures studied by computer simulation", *Journal of Chemical Physics* **2003**, *119*, 7308–7317.

[103] S. Dixit, J. Crain, W. C. K. Poon, J. L. Finney, A. K. Soper, "Molecular segregation observed in a concentrated alcohol-water solution", *Nature* **2002**, *416*, 829–832.

[104] M. Nagasaka, K. Mochizuki, V. Leloup, N. Kosugi, "Local structures of methanol-water binary solutions studied by soft X-ray absorption spectroscopy", *Journal of Physical Chemistry B* **2014**, *118*, 4388–4396.

[105] C. Corsaro, J. Spooren, C. Branca, N. Leone, M. Broccio, C. Kim, S. H. Chen, H. E. Stanley, F. Mallamace, "Clustering dynamics in water/methanol mixtures: A nuclear magnetic resonance study at 205 K ¡ T ¡ 295 K", *Journal of Physical Chemistry B* **2008**, *112*, 10449–10454.

[106] D. J. Earl, M. W. Deem, "Parallel tempering: Theory, applications, and new perspectives", *Physical chemistry chemical physics : PCCP* **2005**, *7*, 3910.

[107] M. Ceriotti, G. A. Tribello, M. Parrinello, "Simplifying the representation of complex free-energy landscapes using sketch-map", *Proceedings of the National Academy of Sciences* **2011**, *108*, 13023–13028.

[108] S. De, A. P. Bartók, G. Csányi, M. Ceriotti, "Comparing molecules and solids across structural and alchemical space", *Physical Chemistry Chemical Physics* **2016**, *18*, 13754–13769.

[109] G. A. Tribello, M. Ceriotti, M. Parrinello, "Using sketch-map coordinates to analyze and bias molecular dynamics simulations", *Proceedings of the National Academy of Sciences* **2012**, *109*, 5196–5201.

[110] A. P. Bartók, R. Kondor, G. Csányi, "On representing chemical environments", *Physical Review B - Condensed Matter and Materials Physics* **2013**, *87*, 1–19.

[111] F. Silly, "Moiré pattern induced by the electronic coupling between 1-octanol self-assembled monolayers and graphite surface.", *Nanotechnology* **2012**, *23*, 225603.

[112] M. Wolff, F. Kruchten, P. Huber, K. Knorr, U. G. Volkmann, "Transition from van der waals to h bond dominated interaction in n-propanol physisorbed on graphite", *Physical Review Letters* **2011**, *106*, 1–4.

[113] P. R. Singh, X. Zeng, "Size-dependent intercalation of ions into highly oriented pyrolytic graphite in ionic liquids: An electrochemical atomic force microscopy study", *Journal of Physical Chemistry C* **2011**, *115*, 17429–17439.

[114] D. Mandal, A. Nasrolahi Shirazi, K. Parang, "Self-assembly of peptides to nanostructures", *Organic and Biomolecular Chemistry* **2014**, *12*, 3544–3561.

[115] X. Zhang, T. Chen, H.-j. Yan, D. Wang, Q.-h. Fan, L.-j. Wan, K. G. Hai-, B. Yang, P. J. Stang, "Engineering of Linear Molecular Mediated Modular and Flexible Host Guest Assembly", *ACS Nano* **2010**, *4*, 5685–5692.

[116] J. Puigmartí-Luis, A. Minoia, S. Lei, V. Geskin, B. Li, R. Lazzaroni, S. De Feyter, D. B. Amabilino, "Self-assembly of supramolecular wires and cross-junctions and efficient electron tunnelling across them", *Chemical Science* **2011**, *2*, 1945–1951.

[117] L. Dordevic, N. Demitri, D. Bonifazi, "Solvent-dependent moulding of porphyrin-based nanostructures: solid state, solution and on surface self-assembly", *Supramolecular Chemistry* **2016**, *28*, 753–761.

[118] K. Ariga, M. Nishikawa, T. Mori, J. Takeya, L. K. Shrestha, J. P. Hill, "Self-assembly as a key player for materials nanoarchitectonics", *Science and Technology of Advanced Materials* **2019**, *20*, 51–95.

[119] K. Morishige, T. Kato, "Chain-length dependence of melting of n-alcohol monolayers adsorbed on graphite: n-hexanol, n-heptanol, n-octanol, and n-nonanol", *Journal of Chemical Physics* **1999**, *111*, 7095–7102.

[120] K. Tahara, T. Ishikawa, B. E. Hirsch, Y. Kubo, A. Brown, S. Eyley, L. Daukiya, W. Thielemans, Z. Li, P. Walke, S. Hirose, S. Hashimoto, S. De Feyter, Y. Tobe, "Self-Assembled Monolayers as Templates for Linearly Nanopatterned Covalent Chemical Functionalization of Graphite and Graphene Surfaces", *ACS Nano* **2018**, *12*, 11520–11528.

[121] E. J. Miller, K. Voïtchovsky, M. Staykova, "Substrate-led cholesterol extraction from supported lipid membranes", *Nanoscale* **2018**, *10*, 16332–16342.

[122] D. A. Los, N. Murata, "Membrane fluidity and its roles in the perception of environmental signals", *Biochimica et Biophysica Acta - Biomembranes* **2004**, *1666*, 142–157.

[123] S. Auer, A. Trovato, M. Vendruscolo, "A condensation-ordering mechanism in nanoparticle-catalyzed peptide aggregation", *PLoS Computational Biology* **2009**, *5*, 1–7.

[124] D.-Y. Wang, C.-Y. Wei, M.-C. Lin, C.-J. Pan, H.-L. Chou, H.-A. Chen, M. Gong, Y. Wu, C. Yuan, M. Angell, Y.-J. Hsieh, Y.-H. Chen, C.-Y. Wen, C.-W. Chen, B.-J. Hwang, C.-C. Chen, H. Dai, "Advanced rechargeable aluminium ion battery with a high-quality natural graphite cathode", *Nature Communications* **2017**, *8*, 14283.

[125] D. Damasceno Borges, C. F. Woellner, P. A. Autreto, D. S. Galvao, "Insights on the mechanism of water-alcohol separation in multilayer graphene oxide membranes: Entropic versus enthalpic factors", *Carbon* **2018**, *127*, 280–286.

[126] H. Liu, C. Song, L. Zhang, J. Zhang, H. Wang, D. P. Wilkinson, "A review of anode catalysis in the direct methanol fuel cell", *Journal of Power Sources* **2006**, *155*, 95–110.

[127] L. V. Protsailo, W. R. Fawcett, "Studies of electron transfer through self-assembled monolayers using impedance spectroscopy", *Electrochimica Acta* **2000**, *45*, 3497–3505.

[128] W. Beckner, Y. He, J. Pfaendtner, "Chain Flexibility in Self-Assembled Monolayers Affects Protein Adsorption and Surface Hydration: A Molecular Dynamics Study", *The Journal of Physical Chemistry B* **2016**, *120*, 10423–10432.

2.0 Chapter 2: Methods

2.1 Chapter Overview

This chapter will provide details of the two key methods used in this thesis to explore the properties of the water and alcohol based self-assemblies at solid liquid interfaces: atomic force microscopy (AFM) and molecular dynamics (MD) simulations. It will start with an overview of the experimental techniques typically used in this context, before focussing on why AFM was chosen for this work and explaining its basic function. Then, the computational technique, MD, will be described, with details regarding the models used to study alcohol and water mixtures. As will become clear within the chapter, the combination of AFM with MD is rapidly becoming the norm in the field of self-assembly at solid-liquid interfaces. This is due to the ability of both techniques to provide details at a similar scale, allowing for a comparison of the experimental observations with the theoretical prediction.

2.2 Experimental Techniques

To be used in applications, self-assembled structures often need to be highly sophisticated with complicated patterns such as clusters, pores, wires etc., or to possess well defined chemical properties when used in surface coatings to control e.g. adhesion and wetting. Forming such assemblies requires the molecules to be decorated with multiple chemical groups who interact in different ways [1–3], as outlined in detail in Chapter 1. This makes predicting the end product difficult, especially for self-assembly at solid-liquid interfaces, due to the presence of additional substrate-liquid interactions. Computational techniques, such as those which will be introduced in

Section 2.3, offer an approach to predicting the resulting self-assembly, although they are ultimately limited by the accuracy of the models used. Furthermore they can struggle with complex systems of small molecules where the magnitudes of the interaction potentials between the liquid molecules and that between liquid molecules and the surface become comparable. Therefore, developing an understanding of the self-assembly mechanism often needs to be iterative with the information derived about the impact of small changes to assembling molecules on the resulting structure fed back to the molecular design stage. Thus an accurate characterisation of self-assembled structures is essential. This can be achieved using multiple experimental techniques at different length scales.

2.2.1 Overview of the main experimental techniques used to study self-assembly

For characterising self-assembly occurring in the bulk liquid, the preferred methods are often scattering or absorption techniques such as neutron scattering or X-ray absorption. The benefits of such techniques are that they can study the properties of the assemblies in a non-invasive manner. Due to the X-rays ability to penetrate deep into the liquid, scattering techniques such as X-ray diffraction can also be used to study assemblies at solid-liquid interfaces. These techniques can be used to great effect, obtaining details pertaining to the separation of atoms and molecules. However, they tend to rely on averaging over large areas of the sample (μms) creating an average picture of the equilibrium structures. Therefore gaining local information, such as the formation of defects or the presence of multiple co-existing domains, is highly challenging and often simply not possible. Nonetheless, they remain useful for studying self-assembly in the bulk. A review of the information obtained by such techniques regarding the behaviour of mixtures of water and short chain length alcohols will be presented in Chapter 4.

The limitations of scatterings techniques can in principle be overcome by mapping the local structure *in-situ* using microscopy techniques such as scanning probe microscopy (SPM) and scanning electron microscopy (SEM). Of these, the SPM technique atomic force microscopy(AFM) [4] is arguably the most versatile, being able to scan a variety of surfaces in a vacuum [5], in air [6] and in a liquid [7, 8] without any

specific sample constraint other than the transparency of the liquid. This gives it a significant advantage over other techniques, such as scanning tunnelling microscopy (STM), which can only be used on conductive materials. AFM has been used to study many interfacial processes such as electrochemistry [9–11], filtration [12, 13], friction [14] and lubrication [15] as well as the real-time behaviour of molecules on surfaces [16]. Furthermore, AFM already has an extensive history of sucessfully obtaining molecular details of the assemblies of molecules at solid-interfaces [7, 8, 11, 17–20].

2.2.2 Atomic force microscopy principles

In general, AFM utilises an atomically-sharp tip to probe local forces at an interface. The tip is mounted on a cantilever which is mechanically driven so that the position of the tip and its distance from the interface can be controlled. Interactions between the tip and the interface are then monitored through the behaviour of the cantilever, such as its deflection, amplitude, frequency or phase, to name a few examples. By controlling the desired properties of the cantilever using a feedback loop while raster-scanning the tip over a given area, information about the interface can then be mapped, such as its topography, chemistry as well as its physical properties. The

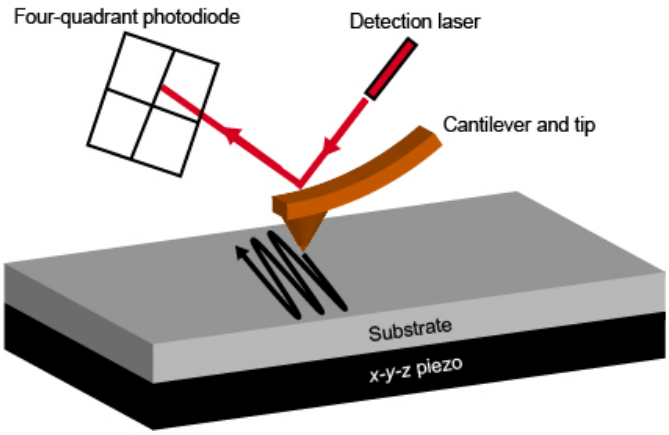

Fig. 2.1: Diagram of the working principles of an AFM. As the tip is raster-scanned across the surface, the deflection (contact mode) or the dynamic properties (AM or FM mode) of the cantilever are detected by a laser beam reflected onto a four-quadrant photodiode. A feedback loop alters in real time the distance between the base of the cantilever and the surface so as to keep constant either the deflection (contact), amplitude (AM) or frequency (FM) as the tip experiences interactions with the interface being imaged.

original design for AFM had the tip be in mechanical contact with the sample surface and was aptly named 'contact-mode AFM' [4]. In this mode, the deflection of the cantilever is maintained by changing the tip-sample distance via adjustments of the z-height of the sample using an x-y-z piezo. Any changes in the deflection of the cantilever due to tip-interface interactions are usually recorded via the movement of a laser beam reflected of the back of the cantilever onto a four-quadrant photodiode, Figure 2.1. A schematic of the typical deflection versus piezo z-height curve for this situation can be seen in Figure 2.2. Once the tip is in contact with the surface, the tip-sample force exerted on the surface (F_{ts}) can be considered a Hookean spring for small displacements (ΔD) and therefore:

$$F_{ts} = k_c \Delta D, \tag{2.1}$$

where k_c is the flexural spring constant of the lever.

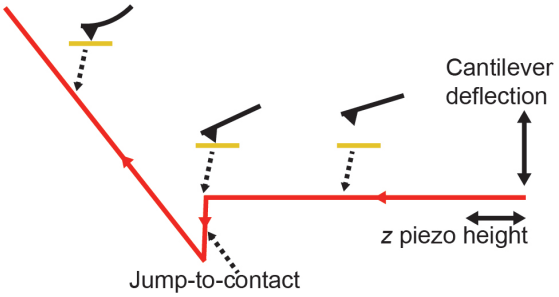

Fig. 2.2: A typical deflection versus piezo z-height plot for cantilever approaching the surface in contact mode-AFM.

The cantilevers used in contact-mode tend be soft with a low spring constant and thus are prone to an effect known as 'jump-to-contact', as seen in Figure 2.2. This effect is due to the attractive force gradient in the z-direction exceeding the spring constant of the cantilever as the probe approaches the surface ($k_c > dF_{ts}/dz$), which causes the tip to suddenly snap into contact with the surface. Therefore the jump-to-contact effect limits the control over the vertical tip-position and can further degrade the attainable resolution of the tip, as well as damage the interface being imaged [21, 22]. While it is possible to overcome this limitation by using stiffer cantilevers, this reduces the sensitivity of the measurement because ΔD is less for the same force. Furthermore, the general contact between the tip apex and the surface in contact-mode AFM can damage and deform samples, making unsuitable

for the imaging of soft interfaces.

As a response to the aforementioned problems associated with contact-mode AFM, dynamic-mode AFM was invented. In dynamic-mode AFM the cantilever is oscillated, often near its resonant frequency. The dynamics of the cantilever in this case can be described by using equation 2.2 [23]:

$$m\ddot{z} + \frac{m\omega_0}{Q}\dot{z} + kz = F_0 cos(\omega t) + F_{ts}(d), \tag{2.2}$$

where F_0 and ω are the amplitude and angular frequency of the driving force respectively, m, Q, ω_0, k and d are the effective mass, quality factor, angular natural frequency (undamped), force constant and tip-sample separation respectively. Provided that the amplitude (A) of the oscillation is sufficiently small with respect to its equilibrium position, the tip-sample interaction force can be expressed by a first order Taylor expansion:

$$F_{ts}(z) = F_{ts}(0) + \left(\frac{dF_{ts}}{dz}\right)_0 z. \tag{2.3}$$

For this approximation it is the gradient of the force which is the relevant factor influencing the motion of the tip and thus the interaction can be characterised by an effective spring constant k_{ts},

$$k_{ts} = -\left(\frac{dF_{ts}}{dz}\right)_0, \tag{2.4}$$

which is also known as the interaction stiffness. Substituting equation 2.4 into equation 2.2 then leads to the equation of a forced damped harmonic oscillator with an effective spring constant k_{eff},

$$k_{eff} = k_c - \left(\frac{dF_{ts}}{dz}\right)_0, \tag{2.5}$$

with an effective resonance frequency

$$\omega_{eff} = \left(\frac{k_{eff}}{m}\right)^{1/2}, \tag{2.6}$$

and the difference $\Delta\omega = \omega_{eff} - \omega_0$ can be approximated by

$$\Delta\omega \approx \frac{\omega_0 k_{ts}}{k_c}, \tag{2.7}$$

valid for $k_{ts} << k_c$ and a constant force gradient over the oscillation range [23]. Therefore for this case, the value of the resonance frequency is related to force gradient. This is typically more short-ranged than the net force and hence can increase the maximum obtainable resolution of dynamic-mode AFM because it enables the last few atoms of the tip to participate in the interaction. Usually for dynamic-mode AFM, the key interaction for the force gradient is the solvation force, which will be discussed in more detail in Section 2.2.5.

When operated close to the resonance frequency, the enhanced force sensitivity allows the cantilevers used in dynamic-mode AFM to be stiffer than those used in contact-mode and thus do not suffer from the jump-to-contact effect. Furthermore, the oscillation of the tip reduces the lateral friction forces and can allow the surface to be investigated without or in semi-contact. This causes less damage to the interface being imaged and thus dynamic-mode AFM can be used to probe softer samples consisting of molecules held together by weaker, non-covalent interactions, such as the water and alcohol assemblies studied within this thesis.

Operating in liquid, as will be the case throughout this work, introduces damping to the vibration of the cantilever due to being in a higher viscosity environment. This damping induces energy dissipation for the vibrating cantilever which reduces its force sensitivity and reduces the signal to noise ratio. Thus multiple technological advancements have been needed to increase the sensitivity of dynamic-mode AFM in liquid by reducing the noise in the deflection sensor as well as improving the methods of exciting the cantilever [24–28]. The summation of these efforts allows dynamic-mode AFM to to map surfaces in liquid with atomic-level resolution [29, 30].

Historically, the cantilever excitation is induced by applying an AC voltage signal to a piezoactuator close to the base of the cantilever. This approach introduces many unwanted resonances in the cantilever as well as the local components, such as the substrate holder, which ultimately makes finding the actual resonance of the cantilever difficult. Furthermore it also means that the response of the cantilever to the driving force is dependant on where its resonance frequency lies within the many piezoactuator-induced peaks [31]. This is further complicated by the fact that the position of the peaks can vary with time as the location of the mechanical contact between the components changes. In the case of AFM in liquid, even contact between the components and the liquid itself can induce unwanted peaks. Therefore,

due to the need for high resolution imaging, the experiments within this work use a cantilever excitation method known as the 'photothermal method'. Here a second laser is focussed on the reflective coating of the cantilever. This induces a rapid and controllable photothermal expansion of the illuminated area of the coating when the laser is on, causing the cantilever itself to bend. In this situation, there is no physical contact needed which reduces the amount of unwanted peaks.

In this thesis two different approaches to dynamic-mode AFM will be used; amplitude-modulation mode and frequency-modulation mode. Both modes of operation have been shown to offer comparable resolutions for liquid-solid interfaces [7, 32]. Their workings will now be discussed.

2.2.3 Amplitude-modulation AFM

In amplitude-modulation mode AFM (AM-AFM) the cantilever is excited with a fixed driving amplitude at a fixed frequency close to its resonance frequency. As demonstrated by equation 2.4, once vibrating, the resonant frequency and hence the amplitude of the cantilever oscillation is dependent upon interactions between the tip and the surface. These interactions are themselves then a function of the tip-surface separation. For AM-AFM, the change in amplitude of the cantilever oscillation is detected (ΔA). As its name suggests, in AM-AFM the minimum separation between the tip and the surface is modulated so that to maintain a constant oscillation amplitude. The tip-sample separation is typically adjusted by using an $x-y-z$ piezo. In addition to ΔA, the phase difference between the driving signal and the actual oscillation ($\Delta\theta$) is also recorded. However, while ΔA is fixed, $\Delta\theta$ is allowed to vary and therefore can be used to construct an image of the phase-lag. Phase-lag images (or just phase images) are related to the energy dissipation, itself sensitive to different mechanical properties of the interface. Therefore they can often provide an enhanced contrast [33], especially for structures whose height is comparable to the substrate features [34]. This can be used to good effect when studying monolayers such as the alcohol water structures discussed herein [7, 8].

One disadvantage of AM-AFM is the response time of the mode, which behaves as $\tau = 2Q/\omega_0$ [35]. In the case if imagining in air or in vacuum Q can exceed 10,000 which can limit the bandwidth for feedback. However, when imaging in liquid and

using soft cantilevers Q can be reduced to a value (typically < 5) where the response time is fast enough to remove this obstacle. Furthermore, in standard AM-AFM the fact that the cantilever is not oscillated at its resonance frequency means that conservative forces (which do not dissipate any vibration energy of the cantilever) and dissipative forces (which do dissipate it) cannot be measured independently and thus a quantitative interpretation of the forces measured is highly difficult [22] and remains an active area of research [36, 37].

2.2.4 Frequency-modulation AFM

Frequency-modulation mode (FM-AFM) relies on changes in the resonant frequency of the oscillating tip ($\Delta\omega$ as defined in equation 2.7). For FM-AFM imaging, the resonant frequency, the amplitude and the phase of the oscillation are all maintained at a constant value to map the properties of the surface. Therefore, more feedback loops are required than was the case for AM-AFM, which makes FM-AFM more complicated. The feedback signal in FM-AFM is provided by a phase-locked loop (PLL), which keeps the phase constant at 90^o. The PLL also relies on the cantilever deflection signal to generate the cantilever excitation signal [22], therefore should the tip crash into the surface at any point, both factors become distorted which can create an instability [22], potentially further damaging the tip and the sample. However, because in FM-AFM the cantilever is always excited at resonance with a constant amplitude, the imaging is not limited by the time taken for the cantilever to decay to a new oscillation frequency or amplitude and thus can achieve a high scanning speed when in air.

A further benefit of FM-AFM is that oscillating the cantilever at its resonance frequency and maintaining the phase at 90^o allows the conservative forces and dissipative forces experienced by the tip to be measured in a decoupled manner. Here the conservative forces varying $\Delta\omega$ and then the dissipative forces can be inferred from the drive amplitude. Having both values allows the measured frequency shifts to be easily converted into values for the force between the tip and the sample [38, 39]. Obtaining such values from AM-AFM is more difficult and thus is still an ongoing area of research [37, 40, 41]. The simple conversion required to map out force profile of interfaces is particularly beneficial for studying solid-liquid interfaces such as those in this work, because it means the values can be directly compared

with parameters extracted from molecular dynamics simulations [42–44]. This also makes FM-AFM the mode of choice for the recently developed technique known as three-dimensional scanning force microscopy (3D-SFM), which maps properties of the interfacial liquid away from the surface. This is the reason FM-AFM is also used in this work. The background and details of 3D-SFM will be discussed in Section 2.2.6.

Ultimately, the effectiveness of both AM-AFM and FM-AFM hinges on the ability to obtain high resolution details of the interface. As mentioned within this section, this resolution is based on the interactions between the oscillating tip and the liquid it is displacing, along with the surface itself. A comprehensive understanding of how these interactions are linked is highly complicated due to the coupling between the individual factors. For example, the mechanism by which any liquid is displaced is linked to the both the chemistry of the surface, the tip and the inherent properties of the liquid itself. Nonetheless, to operate any mode of AFM efficiently and with high resolution, it is important to understand the main forces at play.

2.2.5 Tip-surface interactions

When imaging in air the dominant forces on an AFM tip are van der Waals interactions, short range repulsive interactions, electrostatic interactions and adhesion and capillary forces [23]. Immersing the cantilever in liquid removes capillary forces but also introduces additional effects. Most notably, the tip is no longer simply experiencing interactions due do the surface, it also experiences interactions arising from the surrounding liquid molecules.

Viscous dissipation

The mechanical behaviour of the AFM cantilever and tip is influenced by the hydrodynamic drag force due to viscous friction with the liquid. The amount of energy dissipated for the cantilever and tip due to this friction depends on multiple factors, including the density and viscosity of the medium. For ultrapure water in ambient conditions, the density is 999.615 kg/m^3 and the dynamic viscosity is 1.009 x 10^{-3} Pa s, compared with 1.204 kg/m^3 and 1.814 x 10^{-5} Pa s for air [45]. It is known that the introduction of confinement effects due to solid surfaces further alters the structure and viscosity of liquids compared with their bulk values [46]. However,

the extent of this alteration is still under debate. For example, in ref. [47] the viscosity of water under confinement was investigated using off-resonance AM-AFM and concluded that damping variation is oscillatory as a function of the confined film thickness. Alternatively, in ref. [48] FM-AFM was used to observe monotonic damping. These differing results are currently attributed to changes in the geometry of the confinement, i.e. factors such as tip radii and curvature [49]. While the exact workings of liquid damping effects are still unclear, it is important they be taken into consideration because of their impact on the oscillating cantilever's ω_0 and Q (as mentioned in Section 2.2.3).

Forces due to charged surfaces

The majority of surfaces become charged when they are submerged in polar solvents such as water [23] which can cause any ions in the liquid to re-arrange. The ionic species tend to accumulate near to the surface so as to neutralise it resulting in what is known as an electrical double layer (EDL). The exact organisation of these ions at the interface is is complex and its size can vary from ~ 0.2 nm to tens or hundreds of nanometres depending on the concentration and valence of the ions, as well as the dielectric constant of the solution and the temperature of the system [23]. Generally there are two distinguished regions, the first consisting of counterions directly bound to the surface, which is known as the Stern layer, the second consisting of counterions in thermal motion extending further from the surface, known as the Gouy–Chapman layer [50] (see Figure 2.3a). When two surfaces are close to each other, for example an AFM tip and a substrate, this ion rearrangement can lead to an interaction between the tip and surface. These are known as electric double layer forces. Electric double layer forces are repulsive for similarly charged surfaces. The distance at which this interaction begins to occur is characterised by what is known as the Debye length. For dynamic-mode AFM these potentially long-range interactions can be screened by varying the ionic composition, which in turn can improve spatial resolution [23]. However, in the system studied in this thesis the small concentration of ions in the solution means the we expect to see only minimal double layer forces.

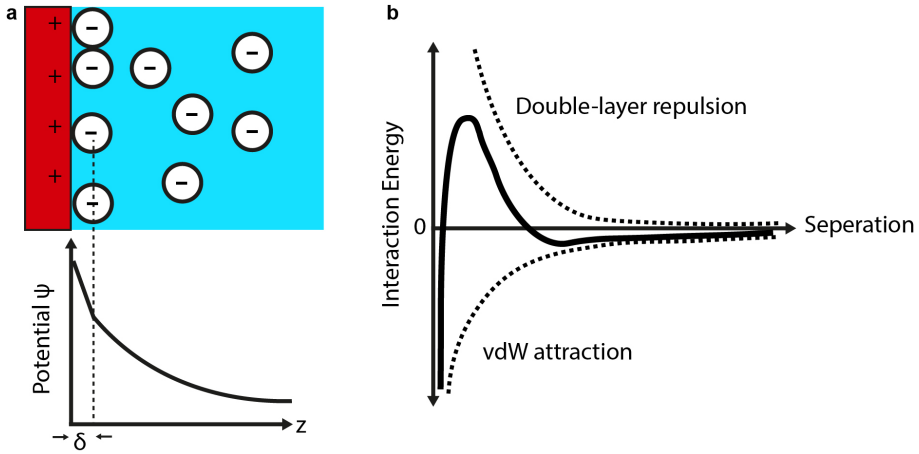

Fig. 2.3: In (a) a schematic is shown which demonstrates a simple description of the ion behaviour in solvent at a positively charged interface. Here δ defines the location of the Stern layer of counterions (also known as the outer Helmholtz plane), after which is the Gouy-Chapman layer of mobile ions. As demonstrated on the corresponding plot, the potential drops off roughly linearly in the Stern layer and then exponentially through the Gouy-Chapman layer. (b) is a schematic of the interaction energy versus distance for the DLVO interaction. The attractive vdW and the repulsive electrostatic potentials (dashed lines) form the total interaction energy (solid line). At short ranges, the vdW attractive interaction dominates. Panel (a) is adapted with permission from ref. [50]

The combination of the double layer force and the van der Waals force (discussed in Chapter 1) are important components of the Derjaguin-Landau-Verwey-Overbeek (DLVO) theory [51]. DLVO theory is commonly referenced in surface-liquid science, especially AFM. For a spherical tip and a flat surface the DLVO force can be approximated [52] as:

$$F_{DLVO} = \frac{4\pi R}{\epsilon\epsilon_0}\sigma_t\sigma_s\lambda_D e^{-\frac{d}{\lambda_D}} - \frac{HR}{6d^2}, \tag{2.8}$$

valid for $d << \lambda_D$ where λ_D, d, ϵ_0 and ϵ are the Debye length, tip-surface separation, the dielectric permittivity of free space respectively and the relative permittivity of the medium, and σ_t and σ_s are the surface charge densities of the tip and sample surface respectively and finally H and R are the Hamaker constant and tip radius respectively. As can be seen in equation 2.8, for small separations the van der Waals attraction overcomes the double layer repulsion ($1/d^2$ compared with $exp(-d/\lambda_D)$, see Figure 2.3b). However, theories such as DLVO also begin to break down when the gap between the AFM tip and the surface approaches the molecular scale. For this reason they shall be considered no further and for details interested readers are referred to textbooks such as that by Israelachvili [51] or Jones [53].

Solvation forces

The most important tip-related force to be considered in the context of this thesis pertains to the re-arrangement of the liquid molecules close to the interface as the tip-surface separation decreases. These are known as solvation forces. Solvation forces usually come into effect for surface separations less than a few nanometers. They depend on both the properties of the intervening liquid, such as the shape of the molecule, and the properties of surface of interest e.g. its hydrophilicity [54, 55] hydrophobicity [56, 57], roughness [58], whether the surface is atomically structured or amorphous and whether the surface is rigid or fluid-like [51]. This coupling arises due to the liquid properties themselves being defined by not only the interactions between liquid molecules, but also the interactions between the liquid and the surface. Furthermore these liquid-surface interactions can be due to both direct forces and indirect effects [59]. This makes understanding the nature of the solvation force difficult, as well as their modelling. As a result, solvation forces have been studied using empirical force measurements, such as surface force apparatus (SFA) [60–62]. Using such approaches allows the detection of forces close to flat surfaces such as mica which are repulsive overall, but also oscillate at the nanoscale corresponding to molecular layering close to surfaces [63, 64]. These are known as solvation layers and are most pronounced in single component liquids, although can occur in mixtures [65]. For an atomically flat wall the oscillatory solvation force can be described empirically by [51]

$$F = f_0 cos\left(\frac{2\pi d}{\sigma}\right) e^{-\frac{d}{\lambda}} \tag{2.9}$$

where f_0 is the prefactor, d is the thickness of the confined film, σ is the periodicity and λ is the decay length. For rougher or more flexible surfaces a monotonic repulsive force is also detected [66, 67] for small surface separations which is also well-modelled by an exponential decay in the z direction. However, techniques such as SFA give little information pertaining to the influence of liquid-liquid and liquid-surface interactions and instead only provide an average picture.

Generally solvation forces exceed the van der Waals force for separations below 5-10 molecular diameters [68]. This strength, compared with the other longer ranged interactions, is significant for AFM imaging because of its impact on the motion of the cantilever. The vertical resolution of scanning probe techniques is limited by

the noise in the measured height (δh), which can be defined as [69]:

$$\delta h = \frac{\delta A}{|dA/dz|}, \tag{2.10}$$

where δA is the noise in the oscillation amplitude, which is associated with the tip-sample interaction. In principle the same relationship also holds for any physical observable related to the tip-sample interaction [70]. As can be seen here, the resolution fundamentally depends upon the gradient of the interaction, $|dA/dz|$. Solvation forces impact $A(z)$ and induce a comparable exponential drop off, which therefore typically permits vertical resolutions of $\sim$ 0.01 - 0.1 nm [23].

Advances in AFM technology have allowed a greater understanding of the solvation force at molecular level [36, 71–73]. An example of a direct interaction can be found in atomically flat hydrophilic surfaces such as mica or calcite. These surface have polar groups and thus can directly interact with molecules such as water. Studies have shown this interaction can structure the interfacial water [55, 73, 74]. This creates an energy penalty to remove the molecules from the interface which leads to a so-called 'hydration force'. This hydrated layer at the interface is typically $\sim$ 0.2 - 0.4 nm in thickness [75]. It is worth noting, however, the these hydration forces are not limited to just water and can be observed in other systems where there is a significant interaction between the surface and solvent [76].

Most AFM tips are made of hydrophilic materials, such as silica, and thus obtaining an understanding of the hydration landscape close to the tip has been the focus of multiple studies combining molecular dynamics simulations and AFM experiments [42, 77, 78]. There is a general consensus regarding the importance of well ordered hydration peaks adjacent to both the tip and the substrate, with the coupling between hydration peaks predominantly contributing to the short-range force variations which enable high resolution imaging. Thus high resolution imaging is assisted by well defined hydration sites at the point of the tip. This can be achieved by tip-modification techniques, such as silicon or argon sputtering and UV/O_3. Of these, silicon sputtering has been shown to be the most effective [79, 80] and will be utilised within this work when performing 3D-SFM.

Hydrophobic forces

Hydrophobic surfaces are defined by their inability to form hydrogen bonds or in-

teract via polar groups. Thus the hydrophobic substrates used within this thesis, such as HOPG or MoS_2, have a less well defined lateral solvation landscape compared to their hydrophilic counterparts [56, 57] and hence obtaining high resolution of the interface using dynamic mode AFM is very difficult. Hydrophobic surface do, however, induce indirect interactions with the interfacial liquid. For example, when a molecule such as water is in the vicinity of a hydrophobic surface, its prefers to bond with another water molecule to minimise the number of dangling hydrogen bonds. Hence, when the gap between the hydrophobic surface and an oscillating tip decreases, the water molecules prefer to escape the gap, creating an entropic (and thus strongly temperature dependent) attractive force between the tip and the surface. This is known as the hydrophobic force, which was discussed in detail in Section 1.2.1. This hydrophobic force can also apply at the molecular level for molecules with hydrophobic groups, such as the short chain length alcohols discussed within this thesis. As will be shown in Chapter 4, at hydrophobic interfaces, alcohol and water mixtures demonstrate a concentration gradient with the alcohol molecules existing at higher concentrations close to a HOPG surface than they do in the corresponding bulk solution. This is due to hydrophobic forces.

2.2.6 *Three-dimensional SFM*

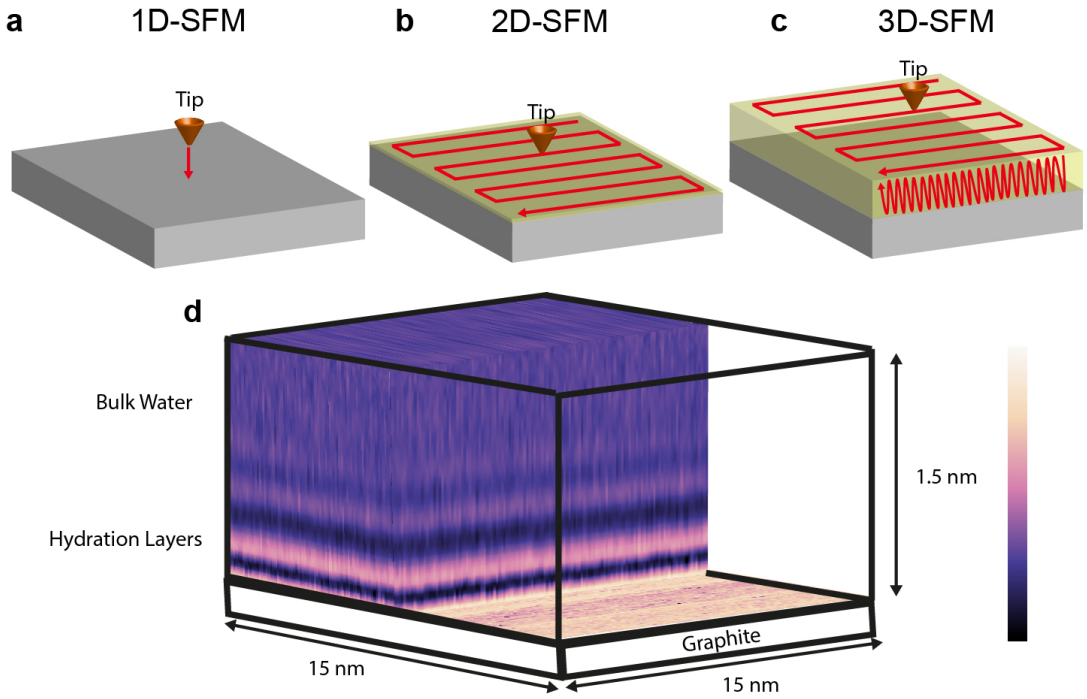

Fig. 2.4: (a-c) Illustrations of the principles behind 1D, 2D and 3D SFM. (d) Example 3D-SFM scan obtained for a system of ultrapure water on HOPG. The colour scale bar represents a $\Delta\omega$ variation of 3 Hz.

As previously mentioned, when operating in FM mode, the AFM tip can be used to probe the force interaction between the tip and the surface by recording the variations in $\Delta\omega$ and mathematically converting $\Delta\omega$ into force using the method of Sader and Jarvis [81]. Such a method is commonly implemented in AFM by scanning the tip in the z-direction only, to create what is known as a force curve, or one-dimensional scanning force microscopy (1D-SFM, Figure 2.4a). Similarly, it is possible to perform the same analysis in two-dimensions to analyse the lateral force profile, or an 'isosurface' of the interaction force between the tip and the surface (2D-SFM, Figure 2.4b) [82]. However, at the solid-liquid interface the force profiles of interest often extend up to several molecular layers away for the surface and thus cannot be mapped using 2D-SFM. 1D-SFM can detect force variations away from the surface, but suffers from no lateral resolution. This is a severe limitation considering that the behaviour of solvating molecules is inherently three-dimensional at the nanoscale. Thus, to address this limitation, the technique of three-dimensional scanning force microscopy was developed (3D-SFM, Figure 2.4c) [55].

In 3D-SFM, an additional sinusoidal motion of a few nanometres is applied to the tip in the vertical direction which has a frequency far lower than that that of oscillating tip. While scanning, the average tip-position in the z-direction is kept constant by a feedback regulation to prevent the tip crashing into the surface. Using this approach creates a three-dimensional plot of $\Delta\omega$ values, which can then converted into a quantitative three-dimensional force image using the method mentioned above. An example of such a data-set can be seen in Figure 2.5a for a system of water on top of HOPG. In this case, clear hydration layers are visible above the surface, consistent with previous experimental studies [56, 72]. These hydration layers show little detail at the atomic level. This is due to the lack of interactions between the water molecules and the hydrophobic interface, which both makes the force required to displace them weak as well as meaning that the water molecules have a high mobility and thus are difficult to resolve using 3D-SFM.

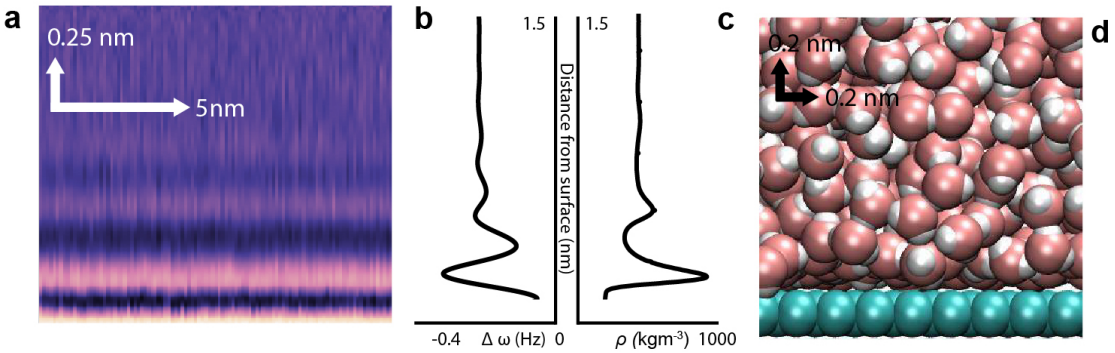

Fig. 2.5: An example of how 3D-SFM and MD simulations can complement each other. (a) A xz cross section of a 3D-SFM scan of ultrapure water on HOPG with the average frequency shift ($\Delta\omega$ as defined in Section 2.2.4) profile plotted in (b). (c) show a density plot from a MD simulation of the same system, a snapshot of which can be seen in (d). The density plot and the frequency shift profile show a good agreement of the peak positions, thus validating the interpretation of the 3D-SFM data. Full details of the parameters and how the experimental and computational data is obtained is presented in Chapter 4.

High resolution data has, however, been obtained for hydrophilic surfaces which have clear hydration sites, such as mica [55], fluorite [54] and calcite [42]. However, the interpretation of forces observed in 3D-SFM images is not simple due to the impact of the physical and chemical heterogeneities of the tip. This effect is pronounced when studying systems without electrolytes, such as pure water [54, 56, 57]. Thus, currently there is a need to understand these tip-effects using atomic-scale simulations of AFM in liquid. As previously mentioned, computational studies have revealed that in the case of a calcite-water interface, the sub-nanometre contrasts can mostly

be attributed to a direction interaction between the apex atom of the tip and a hydration peak (a region of enhanced density) [74, 79]. However, this result remains specific to a certain tip chemistry and a defined framework for interpretation of general three-dimensional force distributions has yet to be achieved. Thus, often there is a need to compare features observed using 3D-SFM to computational simulations to validate the force images. For example, the results from a molecular dynamics simulation of water on HOPG is shown in Figure 2.5d, where the water density layers observed match up with the hydration layers seen in the 3D-SFM measurement. Such approaches have already been used to successfully study the hydration of solid surfaces [54–56] and will become essential for image interpretation in the future [83].

2.2.7 Equipment and protocols used within this thesis

In this final experimental section the specific details of the equipment, chemicals and experimental protocol used for this thesis will be described.

AM-AFM

AM-AFM data was obtained using a commercial Cypher ES AFM (Asylum Research, Santa Barbara, USA) equipped with temperature control and a photothermal drive. The imaging cell was sealed to prevent alcohol evaporation. Hydrophobic surface are prone to contamination and the alcohol-water structures are highly sensitive to additional molecules (Chapter 5). Therefore to reduce the chance of cross-contamination, the cantilever holder used for this work was not shared with other AFM operators.

The cantilevers (Arrow UHF-AUD, Nanoworld, Neuchatel, Switzerland) had a spring constant of 1.95 nN/nm (from thermal spectrum calibration) and a resonance frequency of 430 kHz in liquid. They were cleaned by immersion in ultrapure water before imaging. All parts of the AFM in direct and indirect contact with the solution (cantilever holder, imaging chamber) were cleaned thoroughly with ultrapure water prior to imaging. After washing, the stage was heated to 120 ^{o}C in air for 20 minutes to evaporate possible substances from previous experiments.

FM-AFM and 3D-SFM

The FM-AFM measurements were taken using a system built by the Fukuma group

in Kanazawa University [55] with an ultra-low noise cantilever deflection system [26, 84]. The AFM head is controlled by a commercially available AFM controller (ARC2, Asylum Research). The tips used were usually AC-55 (Olympus, Tokyo, Japan) with 15 nm of silicon coating (K575XD, Emitech) to improve the stability and reproducibility of the images [79]. The tip quality factor, resonance frequency and spring constant were approximately Q ≈ 12, fo ≈ 1.2 MHz and k ≈ 85 N/m respectively. A softer cantilever, 15 nm Si coated NCH-AUD (Nanoworld), was needed to obtain stable 3D-SFM images for some of the softer systems in Chapter 5, where Q ≈ 7, fo ≈ 150 kHz and k ≈ 13.5 N/m. No temperature control was possible using this system so all samples were at room temperature.

Sample Preparation

All the solutions used in this thesis were prepared with ultrapure water (AnalaR NORMAPUR ISO 3696 Grade 3, VWR Chemicals, Leicestershire, UK). The alcohols used were: HPLC-grade methanol with a purity of ≥99 %, HPLC absolute ethanol without additive A15 o1 with a purity of ≥99.8 %, 1-propanol anhydrous with a purity of ≥99.7 %, 2-propanol anhydrous with a purity of ≥99.5 % and 1-hexanol anhydrous with a purity of ≥99 % (all from Sigma-Aldrich, Dorset, UK). The sodium chloride, potassium chloride, disodium phosphate and PBS used all had a purity of ≥99 % (all from Sigma-Aldrich, Dorset, UK). In a typical experiment, a liquid droplet (200 µL) of solution was deposited on a freshly cleaved HOPG substrate (from SPI supplies, West Chester, PA, USA) mounted on a stainless steel disk. In all cases the substrates was baked at >120 ^{o}C for 20 minutes to remove any contaminants before immediately depositing the droplet.

2.3 Molecular Dynamics Simulations

2.3.1 Introduction

The almost universal access modern researchers have to powerful computers has in many ways re-invented how we approach self-assembly. Prior to computational simulations, only average properties could be predicted using theories based on approximate descriptions of systems. Now, well-established models can be used to

help predict the molecular structure of self-assemblies [85]. Within this thesis, the computational work will utilise molecular dynamics simulations (MD) to provide details about the molecular properties near the graphite interface.

As a technique, MD is perhaps one of the best examples of a so-called computational experiment. A system of model particles is prepared based on a prior theoretical, or experimental observation, before solving Newton's equations of motion to observe how the system evolves in time. The key benefit of MD simulations is the ability to obtain atomic-scale details of the system. Obtaining atomic-level information using experimental methods can be difficult and time-consuming, as discussed in Section 2.2. Thus, for the level of molecular details they provide, MD simulations can be comparatively inexpensive in terms of time and materials. Furthermore, MD easily allows simulations of hundreds of thousands of atoms for microseconds with current computing power. This is advantageous for comparison with experiments, compared to more accurate techniques such as density functional theory. DFT simulations can typically account for a hundred atoms run for the order of picoseconds [86].

The use of MD and AFM is highly complementary. In particular, AFM-based techniques are now approaching the stage where they almost routinely obtain atomic resolution in liquids, and can even map smaller properties, such as hydrogen bonds. In this context of this development, MD simulations are now routinely harnessed for direct comparisons with experiments, so as to rule out possible tip-effects, including confinement effects, the presence of a slight charge on the AFM tip or the physical disturbance of the liquid as the cantilever oscillates.

It is nonetheless important to be aware of the limitations of MD simulations. The quality of the results depends on the accuracy of the models (force fields), and correspondingly there is a significant and continuous effort in the community to develop better models. In addition, the time scales and size accessible by MD simulations are still significantly smaller than many experimental systems. This can be problematic [7], as discussed in Chapter 1.

2.3.2 Simulation Geometry

To avoid edge effects and make computational simulations comparable to real physical systems, simulation boxes with periodic boundary conditions (PBC) are typically

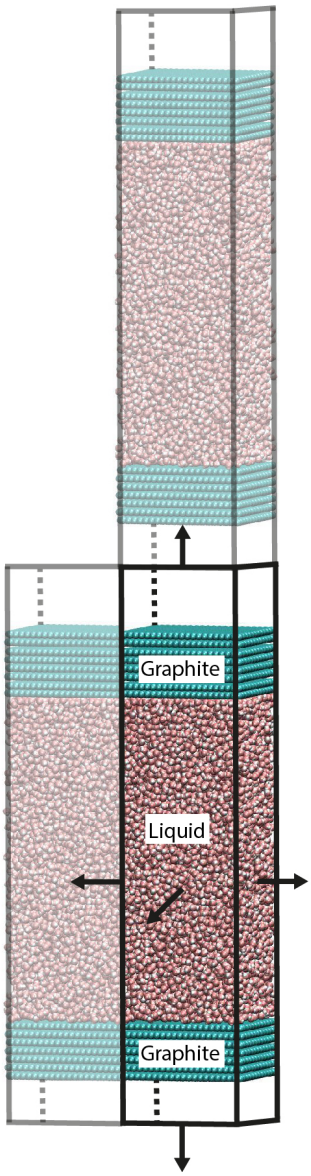

Fig. 2.6: An example of the typical PBC simulation box used for this thesis. A region of liquid (pink) is placed between two stacks of HOPG (cyan). Periodic boundary conditions are applied in all directions (although for simplicity, only two periodic images are shown). There is a vacuum region between the periodic images of the two HOPG stacks so as to ensure computational artefacts do not arise due to intermolecular interactions between periodic images of liquid molecules on the either side of the graphite stack.

used. In PBC, when a molecule moves out of the simulation box, it simply re-appears at the corresponding opposite side. Equally, interaction potentials are also allowed to transfer across these periodic boundaries to mimic an infinite system. Using such an approach means that care needs to be taken when defining the size of the simulation box so that it is larger than twice the cut-off distance of the interactions, due to what is known as the minimum image convention [87]. An example simulation

box set up can be seen in Figure 2.6. Two sets of 7 graphite layers are placed along the $x-y$ plane in a rectangular box of a chosen size with liquid inbetween them. In this work simulations were performed using xyz periodic boundary conditions.

2.3.3 Solving the equations of motion

Classical MD simulations calculate how the properties of a system of particles evolves in time by numerically integrating Newton's equations of motion for each atom:

$$\boldsymbol{f_i} = m_i \boldsymbol{a}_i, i = 1...N \tag{2.11}$$

where N is the number of interacting atoms, $\boldsymbol{f}_i$ is the force exerted on the i^{th} atom, $\boldsymbol{r}_i$ is its position, m_i is its mass, $\boldsymbol{a}_i$ is its acceleration. The forces are given by equation 2.12 and are the negative derivatives of a potential function, $U(\boldsymbol{r}_1, \boldsymbol{r}_2, ..., \boldsymbol{r}_N)$

$$\boldsymbol{f_i} = -\frac{\partial U_i}{\partial \boldsymbol{r}_i} \tag{2.12}$$

These equations of motion are commonly solved using the Verlet-leapfrog scheme [88], which uses an initial set of positions $\boldsymbol{r}_i$ at time t_i and velocities $\boldsymbol{v}_i$ at time $t_i - \frac{1}{2}\Delta t$ to update the positions using the following equations:

$$\boldsymbol{v}_i(t_i + \frac{1}{2}\Delta t) = \boldsymbol{v}_i(t_i - \frac{1}{2}\Delta t) + \frac{\Delta t}{m_i}\boldsymbol{f}_i \tag{2.13}$$

$$\boldsymbol{r}_i(t_i + \Delta t) = \boldsymbol{r}(t_i) + \boldsymbol{v}(t_i + \frac{1}{2}\Delta t)\Delta t. \tag{2.14}$$

Using this algorithm, the positions are calculated and updated at each time step. The choice of the value of the time step is important as it needs to be short enough to capture the shortest time scales of the interaction [89], typically bond vibrations involving hydrogen atoms, which limits the time step to $\sim$ 1 fs [90]. To enable a larger time step of 2 fs, all bonds were constrained for the simulations in this thesis using the Linear Constraint Solver (LINCS) algorithm [91]. For this thesis the calculations are performed using the simulation package GROMACS version 2016 [92]. The principles of molecular dynamics as implemented in GROMACS are well documented in the package manual [93] along with other sources [94]. Therefore

only a brief overview of the key features is presented in the remainder of this section.

2.3.4 Atomic interaction potentials

Within Equation 2.12, U can generally be decomposed into two groups, bonded and nonbonded interactions:

$$U = U_{bonded} + U_{nonbonded}. \tag{2.15}$$

U_{bonded} is defined as:

$$U_{bonded} = U_{bonds} + U_{angles} + U_{dihedral}, \tag{2.16}$$

where U_{bonds} represents covalent bond-stretching (2-body interaction), U_{angles} represents angle-bending (3-body interaction) and $U_{dihedral}$ represents proper and improper dihedrals or torsions (4 body interactions). The improper dihedral exists to force planar groups (e.g. aromatic rings) to remain planar and to prevent transitions to configurations of opposing chirality [93]. U_{bond}, U_{angles} and the improper dihedrals are modelled by harmonic potentials. Proper dihedrals, defined as the rotations of molecular groups, are usually modelled by sinusoidal functions. U_{bonded} typically acts between atoms separated by less than three covalent bonds [95].

$U_{nonbonded}$ is defined as:

$$U_{nonbonded} = U_{electrostatic} + U_{Lennard-Jones}. \tag{2.17}$$

$U_{electrostatic}$ is the electrostatic potential, caused by uneven charge distributions in molecules. It is usually described by the Coulomb potential:

$$U_{Coulomb} = \sum_{ij} \frac{1}{4\pi} \frac{q_i q_j}{\epsilon_0 r_{ij}}, \tag{2.18}$$

where q_i and q_j are point charges, ϵ_0 the permittivity of free space and r_{ij} the point charge separation. $U_{Coulomb}$ terms can be troublesome due to their long range and the fact that they cannot be truncated with inducing inaccuracies and artefacts [96]. There are multiple possible means to solving this problem. Of these, the particle mesh Ewald (PME) approach is used in this work. The PME method introduces a cut-off to the electrostatic interaction, which splits it into its short-ranged and long-

ranged parts. The short-range parts behave as a direct sum using equation 2.18 and the long-range contributions are calculated by a summation in Fourier space [97, 98]. For a detailed description of the workings of PME the reader is referred to the book by Frenkel and Smit [94].

The other repulsive (Pauli exclusion principle) and dispersion (London) nonbonded interactions are usually described by the Lennard-Jones potential:

$$U_{Lennard-Jones} = \sum_{i<j} \frac{A_{ij}}{r_{ij}^{12}} - \frac{C_{ij}}{r_{ij}^{6}} \tag{2.19}$$

where A_{ij} and C_{ij} are interaction dependent constants and r_{ij} is again the atomic separation. All the nonbonded interactions are pair additive, i.e. they act as an effective sum.

The forms of the bonded potentials and values of the constants are defined by the 'force field' chosen by the researcher. The choice of these parameters is essential to ensuring reliable results. The simulations in this work use the Optimized Potentials for Liquid Simulations - All Atom [99] (OPLS-AA) force field because of its well established alcohol models that provides a good description of their phase diagrams [100] as well their mixing with water [101]. The graphite is also modelled using OPLS-AA force field parameters. The 2005 transferable interatomic potential with four points (TIP4P) model is used to model the water [102] due to the quality of its phase diagram and its previous successes at modelling the properties of water and alcohol mixtures [103–107].

2.3.5 Controlling the temperature and pressure

The fundamental ensemble of MD involves a constant number of particles (N) at constant volume (V) and a constant energy (E). This is known as a constant-NVE ensemble. Alternative ensembles in MD include constant-NVT and constant-NPT, where T is the temperature and P is the pressure. To create such ensembles, some form of regulations on T and P are needed. This is achieved by using what are known as thermostats or barostats for the temperature and pressure respectively.

Thermostats

Following the equipartition theorem, the temperature of a system is related to the average kinetic energy of its atoms by:

$$\frac{1}{2}\sum_{i}^{N} m\langle v_i\rangle^2 = \frac{3}{2}Nk_BT, \tag{2.20}$$

where k_B is the Boltzmann constant and the initial velocities are generated using the Maxwell-Boltzman distribution. Thermostats utilise this relationship to control the temperature of the system by controlling the velocities of the particles. In this work two thermostats are used, the Berendsen [108] and the Nosé - Hoover thermostat [109, 110].

The Berendsen thermostat scales the velocities of all the particles in the system by the same factor, λ, using the following expression:

$$\lambda = \sqrt{1 + \frac{\Delta t}{\tau_T}\left(\frac{T_0}{T} - 1\right)}, \tag{2.21}$$

where T is the current temperature, T_0 is the reference temperature and τ_T is the temperature coupling constant. In this method, the velocities are scaled to maintain a constant average total kinetic energy, and thus also an average temperature. Since the velocities are all scaled by a constant, the Berendsen thermostat does not generate a Boltzmann distribution of the velocities and hence does not produce a correct canonical ensemble. However, the Berendsen thermostat is a very fast and efficient way to reach the desired temperature, and so is used within this work for the initial equilibration of the systems.

In contrast, the Nosé - Hoover thermostat does generate the correct canonical ensemble and therefore is used in the NPT and NVT simulations where data is recorded. In this method the equations of motion are modified with a friction variable, ζ:

$$\frac{d^2\boldsymbol{r}_i}{dt_i^2} = \frac{\boldsymbol{f}_i}{m_i} - \zeta\boldsymbol{v}_i, \tag{2.22}$$

$$\frac{d\zeta(t)}{dt} = \frac{1}{Q}\left[\sum_{i}^{N} m_i v_i^2 - (X+1)k_BT_0\right], \tag{2.23}$$

where Q is known as the coupling strength factor and X is the number of degrees of freedom in the system. Using this approach, when the the target temperature has been reached, the two components on the right hand side of the equation become equal and thus

$$\frac{d\zeta(t)}{dt} = 0. \tag{2.24}$$

This equation is used to find the value of ζ required to maintain a pre-defined temperature.

Barostats

In an NPT ensemble the pressure of the system is kept constant by allowing the volume of the box to fluctuate. This is enabled by using a barostat; the two most common of which are the Berendsen [108] and the Parrinello-Rahman [111] barostats.

The Berendsen barostat follows a similar principle to that of the thermostat where the pressure is defined by the virial formula:

$$P_{vir} = \frac{1}{V}\left(Nk_BT + \frac{1}{3}\left\langle \sum_i^N \boldsymbol{r_i} \cdot \boldsymbol{f_i} \right\rangle\right). \tag{2.25}$$

Here the pressure is inversely proportional to the volume and thus a scaling factor can be introduced:

$$\mu = 1 - \frac{\kappa_T \Delta t}{3\tau_p}(P_0 - P), \tag{2.26}$$

where τ_P is the pressure coupling constant, P_0 is the reference pressure and κ_T is the approximate isothermal compressibility of the system. Using this approach the box dimensions can be scaled by the factor μ to achieve a predefined pressure, P_0. In a similar manner to the Berendsen thermostat, the Berendsen barostat is only used for the equilibration of the box. It is efficient but inherently inaccurate.

Instead, for the production runs the Parrinello-Rahman barostat is used. It generates accurate pressure fluctuations, albeit at the cost of computational efficiency. In the Parrinello-Rahman barostat, the matrix of simulation box vectors, $\boldsymbol{b}$ follows the equation of motion:

$$\frac{d^2\boldsymbol{b}}{dt^2} = V\boldsymbol{W}^{-1}\boldsymbol{b}^{\top-1}(\boldsymbol{P} - \boldsymbol{P}_0), \tag{2.27}$$

where $\boldsymbol{W}$ is the coupling strength, $\boldsymbol{P}$ and $\boldsymbol{P_0}$ are the current and target pressure

tensors respectively. The equation of motion for the atoms is then modified as follows:

$$\frac{d^2\boldsymbol{r}_i}{dt^2} = \frac{\boldsymbol{f}_i}{m_i} - \boldsymbol{M}\boldsymbol{v}_i, \tag{2.28}$$

where

$$\boldsymbol{M} = \boldsymbol{b}^{-1}\left[\boldsymbol{b}\frac{d\boldsymbol{b}^\top}{dt} + \frac{d\boldsymbol{b}}{dt}\boldsymbol{b}^\top\right]\boldsymbol{b}^{\top-1}. \tag{2.29}$$

2.3.6 Analysis of MD simulations

Once the MD simulations have completed, there are multiple forms of analysis that can be performed on the data obtained. This data includes the trajectory of the molecules in the system, the various energy components of the system and average parameters such as the density, pressure and temperature. Analysis related to these parameters as well as spatial information such as the radial distribution function (RDF), were performed using in-built functions in the GROMACS software [92]. Furthermore, the greatest asset of MD simulations is the ability to continually observe the arrangements the molecules take during a simulation. In this work the software Visual Molecular Dynamics (VMD) was used for this purpose [112].

2.4 Summary

This chapter has introduced the two key methods used to obtain the scientific data for this thesis, namely dynamic mode AFM and MD simulations, along with the rationale behind the choice of these techniques. As will be seen in the subsequent Chapters, these two methods complement each other well, with the atomistic simulations providing valuable insight into the experimentally observed features which would have been otherwise unobtainable using a solely AFM-based approach. The overall effectiveness of these techniques will be re-visited and discussed at the end of the thesis in Chapter 6.

References: Chapter 2

[1] G. Pawin, K. L. Wong, K. Y. Kwon, L. Bartels, "A homomolecular porous network at a Cu(111) surface", *Science* **2006**, *313*, 961–962.

[2] M. Böhringer, K. Morgenstern, W.-D. Schneider, R. Berndt, F. Mauri, A. De Vita, R. Car, "Two-Dimensional Self-Assembly of Supramolecular Clusters and Chains", *Physical Review Letters* **1999**, *83*, 324–327.

[3] L. Xu, X. Miao, X. Ying, W. Deng, "Two-dimensional self-assembled molecular structures formed by the competition of van der Waals forces and dipole-dipole interactions", *Journal of Physical Chemistry C* **2012**, *116*, 1061–1069.

[4] G. Binning, C. F. Quate, C. Gerber, "Atomic Force Microscope", *Physical Review Letters* **1986**, *56*, 930–934.

[5] F. J. Giessibl, S. Hembacher, H. Bielefeldt, J. Mannhart, "Subatomic features on the silicon (111)-(7x7) surface observed by atomic force microscopy", *Science* **2000**, *289*, 422–425.

[6] R. A. Oliver, "Advances in AFM for the electrical characterization of semiconductors", *Reports on Progress in Physics* **2008**, *71*.

[7] K. Voitchovsky, D. Giofrè, J. J. Segura, F. Stellacci, M. Ceriotti, "Thermally-nucleated self-assembly of water and alcohol into stable structures at hydrophobic interfaces", *Nature Communications* **2016**, *7*, 13064.

[8] W. Foster, J. A. Aguilar, H. Kusumaatmaja, K. Voïtchovsky, "In Situ Molecular-Level Observation of Methanol Catalysis at the Water-Graphite Interface", *ACS Applied Materials and Interfaces* **2018**, *10*, 34265–34271.

[9] K. Voïtchovsky, N. Ashari-Astani, I. Tavernelli, N. Tétreault, U. Rothlisberger, F. Stellacci, M. Grätzel, H. A. Harms, "In Situ Mapping of the Molecular Arrangement of Amphiphilic Dye Molecules at the TiO¡inf¿2¡/inf¿ Surface of Dye-Sensitized Solar Cells", *ACS Applied Materials and Interfaces* **2015**, *7*, 10834–10842.

[10] J. J. Segura, A. Elbourne, E. J. Wanless, G. G. Warr, K. Voïtchovsky, R. Atkin, "Adsorbed and near surface structure of ionic liquids at a solid interface", *Physical Chemistry Chemical Physics* **2013**, *15*, 3320–3328.

[11] R. Hayes, G. G. Warr, R. Atkin, "Structure and Nanostructure in Ionic Liquids", *Chemical Reviews* **2015**, *115*, 6357–6426.

[12] K. Voïtchovsky, "Effect of temperature on the viscoelastic properties of nano-confined liquid mixtures", *Nanoscale* **2016**, *8*, 17472–17482.

[13] P. Bampoulis, J. P. Witteveen, E. S. Kooij, D. Lohse, B. Poelsema, H. J. W. Zandvliet, "Structure and Dynamics of Confined Alcohol-Water Mixtures", *ACS Nano* **2016**, *10*, 6762–6768.

[14] M. Urbakh, E. Meyer, "Nanotribology: The renaissance of friction", *Nature Materials* **2010**, *9*, 8–10.

[15] T. D. Li, E. Riedo, "Nonlinear viscoelastic dynamics of nanoconfined wetting liquids", *Physical Review Letters* **2008**, *100*, 6–9.

[16] D. J. Muller, D. A. Helenius, F. Dufrene, Yves, "Force probing surfaces of living cells to molecular resolution", *Nature Chemical Biology* **2009**, *5*, 383–390.

[17] J. C. Love, L. A. Estroff, J. K. Kriebel, R. G. Nuzzo, G. M. Whitesides, "Self-assembled monolayers of thiolates on metals as a form of nanotechnology", *Chemical Reviews* **2005**.

[18] M. Schreiber, M. Eckardt, S. Klassen, H. Adam, M. Nalbach, L. Greifenstein, F. Kling, M. Kittelmann, R. Bechstein, A. Kühnle, "How deprotonation changes molecular self-assembly-an AFM study in liquid environment", *Soft Matter* **2013**, *9*, 7145–7149.

[19] T. Kudernac, S. Lei, J. A. Elemans, S. De Feyter, "Two-dimensional supramolecular self-assembly: Nanoporous networks on surfaces", *Chemical Society Reviews* **2009**, *38*, 402–421.

[20] J. Chen, J. J. De Yoreo, S. Zhang, E. Zhu, Y. Huang, J. Liu, H. Heinz, Z. Lin, X. Duan, "Building two-dimensional materials one row at a time: Avoiding the nucleation barrier", *Science* **2018**, *362*, 1135–1139.

[21] F. J. Giessibl, "AFM's path to atomic resolution", *Materials Today* **2005**, *8*, 32–41.

[22] A. M. Baro, R. G. Reifenberger, *Atomic Force Microscopy in Liquid - Biological Applications*, Wiley-Vch, **2012**.

[23] R. Garcia, *Amplitude Modulation Atomic Force Microscopy*, 1st ed., Wiley-VCH Verlag and Co. KGaA, **2010**.

[24] N. Umeda, Ishizaki, H. Uwai, "Scanning attractive force microscope using photothermal vibration", *Journal of Vacuum Science and Technology B* **1991**, *9*.

[25] S. P. Jarvis, A. Oral, T. P. Weihs, J. B. Pethica, "A novel force microscope and point contact probe", *Review of Scientific Instruments* **1993**, *64*, 3515–3520.

[26] T. Fukuma, K. Kimura, K. Kobayashi, K. Matsushige, H. Yamada, "Frequency-modulation atomic force microscopy at high cantilever resonance frequencies using the heterodyne optical beam deflection method", *Review of Scientific Instruments* **2005**, *76*, 1–3.

[27] H. Asakawa, T. Fukuma, "Spurious-free cantilever excitation in liquid by piezoactuator with flexure drive mechanism", *Review of Scientific Instruments* **2009**, *80*, 1–4.

[28] F. L. Degertekin, B. Hadimioglu, T. Sulchek, C. F. Quate, "Actuation and characterization of atomic force microscope cantilevers in fluids by acoustic radiation pressure", *Applied Physics Letters* **2001**, *78*, 1628–1630.

[29] T. Fukuma, K. Kobayashi, K. Matsushige, H. Yamada, T. Fukuma, "True atomic resolution in liquid by frequency-modulation atomic force microscopy True atomic resolution in liquid by frequency-modulation atomic force microscopy", *Appl. Phys. Lett* **2005**, *87*, 3–6.

[30] T. Fukuma, K. Kobayashi, K. Matsushige, H. Yamada, "True molecular resolution in liquid by frequency-modulation atomic force microscopy", *Applied Physics Letters* **2005**, *86*, 1–3.

[31] T. E. Schäffer, J. P. Cleveland, F. Ohnesorge, D. A. Walters, P. K. Hansma, "Studies of vibrating atomic force microscope cantilevers in liquid", *Journal of Applied Physics* **1996**, *80*, 3622–3627.

[32] T. Fukuma, M. Kimura, K. Kobayashi, K. Matsushige, H. Yamada, "Development of low noise cantilever deflection sensor for multienvironment frequency-modulation atomic force microscopy", *Review of Scientific Instruments* **2005**, *76*.

[33] R. García, R. Magerle, R. Perez, "Nanoscale compositional mapping with gentle forces", *Nature Materials* **2007**, *6*, 405–411.

[34] N. F. Martínez, R. García, "Measuring phase shifts and energy dissipation with amplitude modulation atomic force microscopy", *Nanotechnology* **2006**, *17*, 167–172.

[35] T. R. Albrecht, P. Grütter, D. Horne, D. Rugar, "Frequency modulation detection using high-Q cantilevers for enhanced force microscope sensitivity", *Journal of Applied Physics* **1991**, *69*, 668–673.

[36] H. Söngen, C. Marutschke, P. Spijker, E. Holmgren, I. Hermes, R. Bechstein, S. Klassen, J. Tracey, A. S. Foster, A. Kühnle, "Chemical Identification at the Solid-Liquid Interface", *Langmuir : the ACS journal of surfaces and colloids* **2017**, *33*, 125–129.

[37] A. F. Payam, D. Martin-Jimenez, R. Garcia, "Force reconstruction from tapping mode force microscopy experiments", *Nanotechnology* **2015**, *26*, 1–12.

[38] J. E. Sader, T. Uchihashi, M. J. Higgins, A. Farrell, Y. Nakayama, S. P. Jarvis, "Quantitative force measurements using frequency modulation atomic force microscopy - Theoretical foundations", *Nanotechnology* **2005**, *16*.

[39] B. W. Hoogenboom, H. J. Hug, Y. Pellmont, S. Martin, P. L. Frederix, D. Fotiadis, A. Engel, "Quantitative dynamic-mode scanning force microscopy in liquid", *Applied Physics Letters* **2006**, *88*, 23–26.

[40] M. Lee, W. Jhe, "General theory of amplitude-modulation atomic force microscopy", *Physical Review Letters* **2006**, *97*, 1–4.

[41] A. J. Katan, M. H. Van Es, T. H. Oosterkamp, "Quantitative force versus distance measurements in amplitude modulation AFM: A novel force inversion technique", *Nanotechnology* **2009**, *20*.

[42] T. Fukuma, B. Reischl, N. Kobayashi, P. Spijker, F. F. Canova, K. Miyazawa, A. S. Foster, "Mechanism of atomic force microscopy imaging of three-dimensional hydration structures at a solid-liquid interface", *Physical Review B* **2015**, *92*, 155412.

[43] K. Miyazawa, N. Kobayashi, M. Watkins, A. L. Shluger, K. I. Amano, T. Fukuma, "A relationship between three-dimensional surface hydration structures and force distribution measured by atomic force microscopy", *Nanoscale* **2016**, *8*, 7334–7342.

[44] K. Umeda, L. Zivanovic, K. Kobayashi, J. Ritala, H. Kominami, P. Spijker, A. S. Foster, H. Yamada, "Atomic-resolution three-dimensional hydration structures on a heterogeneously charged surface", *Nature Communications* **2017**, *8*, 1–9.

[45] T. Berthold, G. Benstetter, W. Frammelsberger, R. Rodríguez, M. Nafría, "Numerical study of hydrodynamic forces for AFM operations in liquid", *Scanning* **2017**, *2017*, DOI 10.1155/2017/6286595.

[46] R. Zangi, "Water confined to a slab geometry : a review of recent", *Journal of Physics: Condensed Matter* **2004**, *16*, S5371–S5388.

[47] S. H. Khan, G. Matei, S. Patil, P. M. Hoffmann, "Dynamic solidification in nanoconfined water films", *Physical Review Letters* **2010**, *105*, 1–4.

[48] A. Labuda, K. Kobayashi, K. Suzuki, H. Yamada, P. Grütter, "Monotonic damping in nanoscopic hydration experiments", *Physical Review Letters* **2013**, *110*, 1–5.

[49] S. de Beer, W. K. den Otter, D. van den Ende, W. J. Briels, F. Mugele, "Non-monotonic variation of viscous dissipation in confined liquid films: A reconciliation", *EPL (Europhysics Letters)* **2012**, *97*, 46001.

[50] H. J. Butt, K. Graf, M. Kappl, *Physics and Chemistry of Interfaces*, **2003**.

[51] J. Israelachvili, *Intermolecular and Surface Forces*, 2nd ed., Academic Press, **1991**.

[52] H. J. Butt, B. Cappella, M. Kappl, "Force measurements with the atomic force microscope: Technique, interpretation and applications", *Surface Science Reports* **2005**, *59*, 1–152.

[53] R. A. Jones, *Soft Condensed Matter*, 1st ed., Oxford University Press, **2002**.

[54] K. Miyazawa, M. Watkins, A. L. Shluger, T. Fukuma, "Influence of ions on two-dimensional and three-dimensional atomic force microscopy at fluorite-water interfaces", *Nanotechnology* **2017**, *28*.

[55] T. Fukuma, Y. Ueda, S. Yoshioka, H. Asakawa, "Atomic-Scale distribution of water molecules at the mica-Water interface visualized by three-Dimensional scanning force microscopy", *Physical Review Letters* **2010**, *104*, 2–5.

[56] I. Schlesinger, U. Sivan, "Three-Dimensional Characterization of Layers of Condensed Gas Molecules Forming Universally on Hydrophobic Surfaces", *Journal of the American Chemical Society* **2018**, *140*, 10473–10481.

[57] M. R. Uhlig, D. Martin-Jimenez, R. Garcia, "Atomic-scale mapping of hydrophobic layers on graphene and few-layer MoS2 and WSe2 in water", *Nature Communications* **2019**, *10*, 2606.

[58] K. Yang, Y. Lin, X. Lu, A. V. Neimark, "Solvation forces between molecularly rough surfaces", *Journal of Colloid and Interface Science* **2011**, *362*, 382–388.

[59] J. N. Israelachvili, "Forces between hydrophobic surfaces in aqueous elect.ro- lyte and surfaczant solutions containing common air- borne impuhities", **1981**, *2*, 287–291.

[60] R. M. Pashley, "DLVO and hydration forces between mica surfaces in Li+, Na+, K+, and Cs+ electrolyte solutions: A correlation of double-layer and hydration forces with surface cation exchange properties", *Journal of Colloid and Interface Science* **1981**, *83*, 531–546.

[61] J. N. Israelachvili, "Measurement of forces between surfaces immersed in electrolyte solutions", *Faraday Discussions of the Chemical Society* **1978**, *65*, 20–24.

[62] D. Tabor, R. H. S. Winterton, "Surface forces: Direct measurement of normal and retarded van der waals forces", *Nature* **1968**, *219*, 1120–1121.

[63] J. N. Israelachvili, P. M. McGuiggan, "Forces Between Surfaces in Liquids", *Science* **1988**, *241*, 795–800.

[64] J. N. Israelachvili, R. M. Pashley, "Molecular layering of water at surfaces and origin of repulsive hydration forces", *Nature* **1983**, *306*, 249–250.

[65] R. G. Horn, D. F. Evans, B. W. Ninham, "Double-layer and solvation forces measured in a molten salt and its mixtures with water", *Journal of Physical Chemistry* **1988**, *92*, 3531–3537.

[66] J. J. Valle-Delgado, J. A. Molina-Bolívar, F. Galisteo-González, M. J. Gálvez-Ruiz, "Evidence of hydration forces between proteins", *Current Opinion in Colloid and Interface Science* **2011**, *16*, 572–578.

[67] M. Kanduč, A. Schlaich, E. Schneck, R. R. Netz, "Water-Mediated Interactions between Hydrophilic and Hydrophobic Surfaces", *Langmuir* **2016**, *32*, 8767–8782.

[68] H. K. Christenson, V. V. Yaminsky, "Adhesion and Solvation Forces between Surfaces in Liquids Studied by Vapor-Phase Experiments", *Langmuir* **1993**, *9*, 2448–2454.

[69] F. J. Giessibl, "Advances in atomic force microscopy", *Rev. Mod. Phys.* **2003**, *75*, 949–983.

[70] R. Pérez, R. García, *Dynamic atomic force microscopy methods - Surface Science Reports.pdf*, *Vol. 47*, **2002**, pp. 197–301.

[71] S. De Beer, D. D. Van Ende, F. Mugele, "Dissipation and oscillatory solvation forces in confined liquids studied by small-amplitude atomic force spectroscopy", *Nanotechnology* **2010**, *21*.

[72] D. Martin-Jimenez, E. Chacon, P. Tarazona, R. Garcia, "Atomically resolved three-dimensional structures of electrolyte aqueous solutions near a solid surface", *Nature Communications* **2016**, *7*, 1–7.

[73] T. D. Li, J. Gao, R. Szoszkiewicz, U. Landman, E. Riedo, "Structured and viscous water in subnanometer gaps", *Physical Review B - Condensed Matter and Materials Physics* **2007**, *75*, 1–6.

[74] T. Fukuma, "Water distribution at solid/liquid interfaces visualized by frequency modulation atomic force microscopy", *Science and Technology of Advanced Materials* **2010**, *11*, 033003.

[75] V. A. Parsegian, T. Zemb, "Hydration forces: Observations, explanations, expectations, questions", *Current Opinion in Colloid and Interface Science* **2011**, *16*, 618–624.

[76] K. Voïtchovsky, J. J. Kuna, S. A. Contera, E. Tosatti, F. Stellacci, "Direct mapping of the solid-liquid adhesion energy with subnanometre resolution", *Nature Nanotechnology* **2010**, *5*, 401–405.

[77] K. Kobayashi, Y. Liang, K. I. Amano, S. Murata, T. Matsuoka, S. Takahashi, N. Nishi, T. Sakka, "Molecular Dynamics Simulation of Atomic Force Microscopy at the Water-Muscovite Interface: Hydration Layer Structure and Force Analysis", *Langmuir* **2016**, *32*, 3608–3616.

[78] X. Hu, P. Egberts, Y. Dong, A. Martini, "Molecular dynamics simulation of amplitude modulation atomic force microscopy", *Nanotechnology* **2015**, *26*.

[79] S. M. Akrami, H. Nakayachi, T. Watanabe-Nakayama, H. Asakawa, T. Fukuma, "Significant improvements in stability and reproducibility of atomic-scale atomic force microscopy in liquid", *Nanotechnology* **2014**, *25*.

[80] K. Miyata, K. Miyazawa, S. M. R. Akrami, T. Fukuma, "Improvements in fundamental performance of liquid-environment atomic force microscopy with true atomic resolution", *Japanese Journal of Applied Physics* **2015**, *54*.

[81] J. E. Sader, S. P. Jarvis, "Accurate formulas for interaction force and energy in frequency modulation force spectroscopy", *Applied Physics Letters* **2004**, *84*, 1801–1803.

[82] T. Fukuma, M. J. Higgins, S. P. Jarvis, "Direct imaging of individual intrinsic hydration layers on lipid bilayers at Ångstrom resolution", *Biophysical Journal* **2007**, *92*, 3603–3609.

[83] T. Fukuma, R. Garcia, "Atomic- and Molecular-Resolution Mapping of Solid-Liquid Interfaces by 3D Atomic Force Microscopy", *ACS Nano* **2018**, *12*, 11785–11797.

[84] T. Fukuma, S. P. Jarvis, "Development of liquid-environment frequency modulation atomic force microscope with low noise deflection sensor for cantilevers of various dimensions", *Review of Scientific Instruments* **2006**, *77*.

[85] A. Ciesielski, P. J. Szabelski, W. Rz??ysko, A. Cadeddu, T. R. Cook, P. J. Stang, P. Samor??, "Concentration-dependent supramolecular engineering of hydrogen-bonded nanostructures at surfaces: Predicting self-assembly in 2D", *Journal of the American Chemical Society* **2013**.

[86] J. Dziedzic, S. J. Fox, T. Fox, C. S. Tautermann, C. K. Skylaris, "Large-scale DFT calculations in implicit solvent - A case study on the T4 lysozyme L99A/M102Q protein", *International Journal of Quantum Chemistry* **2013**, *113*, 771–785.

[87] A. R. Leach, *Molecular modelling: principles and applications*, Longman, **1996**.

[88] R. W. Hockney, S. P. Goel, J. W. Eastwood, "Quiet high-resolution computer models of a plasma", *Journal of Computational Physics* **1974**, *14*, 148–158.

[89] D. Fincham, "Choice of timestep in molecular dynamics simulation", *Computer Physics Communications* **1986**, *40*, 263–269.

[90] C. W. Hopkins, S. Le Grand, R. C. Walker, A. E. Roitberg, "Long-time-step molecular dynamics through hydrogen mass repartitioning", *Journal of Chemical Theory and Computation* **2015**, *11*, 1864–1874.

[91] B. Hess, H. Bekker, H. J. Berendsen, J. G. Fraaije, "LINCS: A Linear Constraint Solver for molecular simulations", *Journal of Computational Chemistry* **1997**, *18*, 1463–1472.

[92] M. J. Abraham, T. Murtola, R. Schulz, S. Páll, J. C. Smith, B. Hess, E. Lindah, "Gromacs: High performance molecular simulations through multi-level parallelism from laptops to supercomputers", *SoftwareX* **2015**, *1-2*, 19–25.

[93] M. Abraham, D. van der Spoel, B. H. E. Lindahl, "GROMACS User Manual version 2016", **2016**.

[94] D. Frenkel, B. Smit, *Understanding Molecular Simulation*, 2nd, Academic Press, Inc., Orlando, FL, USA, **2001**.

[95] A. Pineiro, "Introduction to Molecular Dynamics Simulations of Monolayers at Liquid/Air Interfaces", **2009**, 1–18.

[96] P. J. Steinbach, B. R. Brooks, "New spherical-cutoff methods for long-range forces in macromolecular simulation", *Journal of Computational Chemistry* **1994**, *15*, 667–683.

[97] U. Essmann, L. Perera, M. L. Berkowitz, T. Darden, H. Lee, L. G. Pedersen, "A smooth particle mesh Ewald method", *The Journal of Chemical Physics* **1995**, *103*, 8577–8593.

[98] T. Darden, D. York, L. Pedersen, "Particle mesh Ewald: An N·log(N) method for Ewald sums in large systems", *The Journal of Chemical Physics* **1993**, *98*, 10089–10092.

[99] J. Jorgensen, W. Tirado-Rives, "Potential energy functions for atomic-level simulations of water and organic and biomolecular systems", *PNAS* **2005**, *102*, 6667–6670.

[100] W. Jorgensen, J. Madura, C. Swenson, "Optimized Intermolecular Potential Functions for Liquid Hydrocarbons", *J. Am. Chem. Soc.* **1984**, 6638–6646.

[101] H. Tanaka, K. E. Gubbins, "Structure and thermodynamic properties of water-methanol mixtures: Role of the water-water interaction", *The Journal of Chemical Physics* **1992**, *97*, 2626–2634.

[102] J. L. Abascal, C. Vega, "A general purpose model for the condensed phases of water: TIP4P/2005.", *The Journal of chemical physics* **2005**, *123*, 234505.

[103] E. J. W. Wensink, A. C. Hoffmann, P. J. Van Maaren, D. Van Der Spoel, "Dynamic properties of water/alcohol mixtures studied by computer simulation", *Journal of Chemical Physics* **2003**, *119*, 7308–7317.

[104] D. Surblys, Y. Yamaguchi, K. Kuroda, M. Kagawa, T. Nakajima, H. Fujimura, "Molecular dynamics analysis on wetting and interfacial properties of water-alcohol mixture droplets on a solid surface", *Journal of Chemical Physics* **2014**, *140*.

[105] E. Galicia-Andrés, L. Pusztai, L. Temleitner, O. Pizio, "Microscopic structure of methanol-water mixtures: Synchrotron X-ray diffraction experiments and molecular dynamics simulations over the entire composition range", *Journal of Molecular Liquids* **2015**, *209*, 586–595.

[106] S. Fias, S. V. Damme, P. Bultinck, "Multidimensionality of delocalization indices and nucleus independent chemical shifts in polycyclic aromatic hydrocarbons", *... of Computational Chemistry* **2008**, *29*, 358–366.

[107] P. Pršlja, E. Lomba, P. Gómez-Álvarez, T. Urbič, E. G. Noya, "Adsorption of water, methanol, and their mixtures in slit graphite pores", *Journal of Chemical Physics* **2019**, *150*.

[108] H. J. Berendsen, J. P. Postma, W. F. Van Gunsteren, A. Dinola, J. R. Haak, "Molecular dynamics with coupling to an external bath", *The Journal of Chemical Physics* **1984**, *81*, 3684–3690.

[109] S. Nosé, M. L. Klein, "Constant pressure molecular dynamics for molecular systems", *Molecular Physics* **1983**, *50*, 1055–1076.

[110] W. G. Hoover, "Canonical Dynamics Equilibrium Phase Space Distributions", **1985**, *31*, 1695–1697.

[111] M. Parrinello, A. Rahman, "Polymorphic transitions in single crystals: A new molecular dynamics method", *Journal of Applied Physics* **1981**, *52*, 7182–7190.

[112] W. Humphrey, A. Dalke, K. Schulten, "VMD – Visual Molecular Dynamics", *Journal of Molecular Graphics* **1996**, *14*, 33–38.

3.0 Chapter 3: Methanol catalysis on HOPG

3.1 Chapter Overview

Methanol occupies a central role in chemical synthesis and is considered an ideal candidate for cleaner fuel storage and transportation, as will be discussed in Section 3.2.1. It can be catalyzed from water and volatile organic compounds, such as carbon dioxide, thereby offering an attractive solution for limiting carbon emissions. However, molecular-level experimental observations of the catalytic process are scarce, and most existing catalysts tend to rely on empirically optimized, expensive, and complex nanocomposite materials. This lack of molecular-level insights has precluded the development of simpler, more cost-effective alternatives.

In this chapter I will show that graphite immersed in ultrapure water is able to spontaneously catalyse methanol from volatile organic compounds in ambient conditions. I will start by giving a brief overview of the importance of the conversion of such compounds to methanol as well as the benefits of understanding catalytic reactions involving graphite. Then, using single-molecule resolution atomic force microscopy (AFM) in liquid, I will show that it is possible to directly observe the formation and evolution of methanol-water nanostructures at the surface of graphite. These molecularly ordered structures nucleate near catalytically active surface features, such as atomic step edges, and grow progressively as further methanol is being catalysed. Complementary nuclear magnetic resonance analysis of the liquid confirms the formation of methanol and quantifies its concentration. Finally, I will show that electric fields significantly enhance the catalysis rate, even when as small as that induced by the natural surface potential of the silicon AFM tip. While the amount of methanol

produced by this mechanism is comparatively small, these findings could have a significant impact on the development of organic catalysts and on the function of nanoscale carbon devices.

3.2 Introduction

3.2.1 Importance of the catalytic production of methanol

The production of methanol is a key contemporary topic given the need for alternative energy sources to fossil fuel [1] as well as methanol being an important platform molecule for chemical synthesis [2]. Hypothetical long term replacements for fossil fuels have been proposed, the most significant of which were the hydrogen and ethanol fuel economies. In the 1990s the idea of a methanol fuel economy started to gain traction, leading to the publication of an essay by nobel laureate George Olah in 2005 [3] outlining the growing problem regarding fossil fuels, the limitations of the currently proposed alternative energy source and finally the potential for using methanol for cleaner energy storage and transportation. One of the main benefits of using methanol as a fuel is that methanol can be stored safely as a liquid at room temperature, similar to current popular fuels such as petrol, and therefore minimal changes would be needed to the existing fuel transportation infrastructure. Furthermore, many popular reactions for producing methanol involve using synthetic gases produced via the catalytic reformation of fossil fuels. Thus a key benefit of a methanol fuel economy would be the use of volatile organics such as carbon dioxide as a feedstock. The problem of greenhouse gasses in the environment is well documented and is one of the most important problems we face as a society. The conversion of unwanted volatile organics to methanol is reported to have the potential to significantly reduce these carbon emissions [3]. The negatives of using methanol include it having a lower energy density than than current fuel (e.g. petrol) and alternatives such as ethanol [3] as well as methanol being highly toxic.

3.2.2 *Overview of current catalytic processes for methanol production*

The purpose of a catalyst is to chemically activate an otherwise unreactive reagent and reduce the energy required to transform it into a useful chemical under accessible conditions. The most common methanol production process via the conversion of CO_2 involves flowing the CO_2 and H_2 gas over catalysts at increased temperatures (200-350 ^oC) and pressures (50-250 bar) (known as thermocatalysis), or by reacting CO_2 dissolved in electrolytes at an electrode, usually at ambient temperatures [4] (known as electrocatalysis). Electrocatalysts are frequently studied for their potential uses in methanol production due the benefits of ambient catalysis [5–7]. However, currently electrocatalysis is not commonly used on the industrial scale due to a lower product yield compared with their thermocatalytic counterparts [8]. For the thermocatalytic process the reaction is:

$$CO_2 + 3H_2 \rightleftharpoons CH_3OH + H_2O \quad \Delta H_{298K} = -49.4\,\text{kJ/mol} \tag{3.1}$$

where ΔH is the change in enthalpy. This reaction is exothermic and leads to a reduction in the number of molecules. Therefore, according to Le Chatelier's principle, increasing the pressure and decreasing the temperature favours product formation [9]. However, CO_2 is a chemically inert molecule the reaction can produce numerous unwanted by-products and hence there remains a need for a catalyst to reduce energy barrier and increase the specificity of the reaction.

At the present time, the catalysts used in thermocatalytic processes are made of complex composite materials comprising active metal nanoparticles in an oxide support [10–12]. The complexity of these composites means their catalytic behaviour is still not fully understood, although the synergy between the constituent components has been shown to be one of the key elements [13]. Significantly, composites usually require a specific nanoscale arrangement, making them expensive and highly sensitive to even slight structural changes. Indeed, the first demonstration of an effective homogeneous catalysts for the conversion of CO_2 to methanol was only reported recently [14] and remains an active area of research [15].

Organic materials, such as graphite derivatives, are obvious candidates for alternative catalysts due to their low cost and stability compared to metals [16]. However,

they do still suffer from currently being difficult to produce in bulk quantities [17]. Due to their rich quantities of uncoordinated atoms and large surface areas, doped two-dimensional nanosheets, such as graphene, are frequently studied for use in electrocatalysis [18]. Furthermore, they have been shown to have good catalytic activity, particularly when simple modifications are made such as the replacement of single carbon atoms with oxygen containing functional groups such as epoxy and methoxy groups [19]. As detailed in Chapter 1, this type of modified graphene is known as graphene oxide (GrO). GrO is one of the most commonly used graphene derivatives in the field of catalysis [20, 21] and recent results suggest that the graphene oxide can act as a photocatalyst for the conversion of water and carbon dioxide to methanol [22]. This behaviour is attributed to the presence of the hydrophilic functional groups that stretch the bandgap of GrO. This in turn allows the photo-generated electrons and holes to serve as oxidation and reduction sites. Such catalytic effects have never been observed for pure graphene where the absence of chemical singularities does not favour localized electrons.

The surface of bulk multi-layered graphite presents singularities at exposed atomic steps and edges. These singularities have long been known to make the edges of graphite electrochemically active [23]. The study of such singularities is currently a flourishing field due to advances in technology which allow the measurement of electrochemical properties at the molecular level [24]. Of these, the scanning micropipet contact method [25] has been particularly successful [26]. Using this technique researchers have demonstrated that graphite's basal plane, previously considered electrochemically inert, has an activity comparable to that of noble metal electrodes such as platinum [26]. These findings suggest that graphite may offer a suitable alternative to metal electrodes given the fact that it can be readily immersed in aqueous solutions, unlike graphene.

This chapter demonstrates the catalytic production of methanol at the surface of immersed highly orientated pyrolytic graphite (HOPG) in ambient conditions. The process occurs spontaneously with the thermal energy available, but is stimulated in the presence of an applied electric field. The amount of methanol produced will be quantified using ^{1}H NMR spectroscopy of the resulting solution. However, the chapter will start with *in-situ* observations of the methanol production using single-molecule resolution atomic force microscopy (AFM) in liquid.

3.3 Observing methanol production

3.3.1 AFM

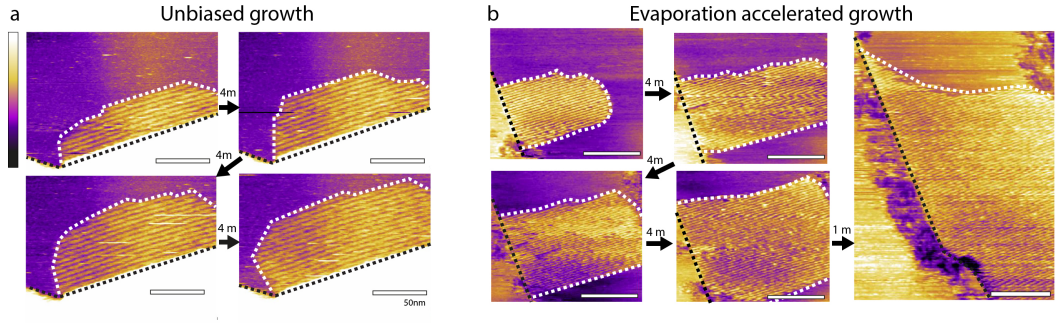

Fig. 3.1: High resolution amplitude modulation AFM imaging (using conditions described in Chapter 2) of HOPG immersed in initially ultrapure water. (a) A solid-like assembly of molecules (dashed white outline) nucleates from an atomic step (dashed black line) at the HOPG surface. The assembly, observed here *in situ*, progressively grows across the surface over a period of 16 minutes with its front moving away from the step. Row-like structures are visible with a periodicity of 4.71 ± 0.30 nm. (b) Small patches were observed in repeated experiments. Here the receding contact line of the droplet reached the area being scanned during the final frame, causing a spike in monolayer growth rate consistent with an instantaneous increase in methanol concentration due to alcohols existing at higher concentrations at the droplet-air/surface interface [27–29]. The white scale bars are 50 nm in (a) and 100 nm in (b). The purple color scale bar represents a height variation of 0.2 nm in (a) and (b).

The detection of small quantities of methanol being produced on the surface of HOPG immersed in ultrapure water occurred after scanning the surface for extended periods of time with amplitude-modulation mode AFM (AM-AFM). The process was followed via the resulting self-assembly of water and alcohol molecules at the HOPG-water interface. Representative examples of this self-assembly are seen in Figure 3.1a, where a molecularly structured patch is slowly growing in a system that initially consisted only of ultrapure water at the surface of HOPG. Consistent with a catalytic reaction, the nucleating structures are seen predominantly at the more electrochemically active edges of HOPG. Pure liquid water itself cannot form long-lived structures on HOPG at room temperature [30] indicating that the observed patch must contain molecules formed *in situ*. Furthermore, the molecular assemblies developing at the interface with HOPG in ultrapure water appear to be the same as those reported in Chapter 1, suggesting that HOPG-induced catalysis of water into methanol is occurring. Regarding the source of the carbon for the reaction,

the HOPG surface was not seen to evolve in time, ruling out any loss of material. Carbon dioxide, however, is the main source of volatile carbon in the experiment and is responsible for the slight acidity of ultrapure water in ambient conditions (pH 5.8) and hence is the most probable provider of the carbon. NMR measurements presented in the next section will confirm this methanol production at the interface between ultrapure water and HOPG, as well as providing further evidence for CO_2 being the carbon source. As will be shown in Chapter 5, when performing the same experiment in a system of ultrapure water on molybdenum disulfide, no structures are observed over several hours of scanning, indicating this effect requires the specific properties of HOPG.

While the monolayers may physically resemble those formed in methanol-water mixtures, their nucleation and growth characteristics differ when forming in systems of ultrapure water. Along with the long time-scales needed to observe their nucleation (1-2 hours minimum), they are also unable to cover the entirety of the visible surface. Furthermore, the growth rate of the monolayer in Figure 3.1a is 9.57 ± 0.50 nm^2/s, an order of magnitude slower than reported for systems with a methanol concentration of >5% [27]. Considering the structures most likely involve alternating methanol and water molecules present in equal parts, a slower growth rate is reasonable given the expected low concentrations of methanol. Indeed, there were multiple observations of rapidly increased monolayer growth rates when nucleated patches came into proximity with the receding droplet contact line, where the amphiphilic alcohols have been shown to exist at higher concentrations (Figure 3.1b) [27–29]. This corroborates the methanol concentration being the critical factor.

3.3.2 NMR

To independently confirm the formation of methanol, it was important to use a technique with chemical identification capabilities. Mass spectrometry and Raman spectroscopy were tried, but both lacked the sensitivity needed to detect the small concentrations (∼ µM) of methanol in this system. This high resolution was achieved with NMR spectroscopy. NMR analysis was performed on the solution in direct contact with the HOPG before and after the monolayer nucleation timescale. Practically, the NMR measurement was challenging because it requires observing typically sub-millimolar quantities of methanol in the presence of a signal (due to

water) that is five orders of magnitude larger. Therefore the water signal had to be very efficiently suppressed to allow for unambiguous identification of the methanol produced. This was achieved using the recently reported Robust-5 pulse sequence [31] (see experimental section for details). As mentioned in the introduction, there have been many results pertaining to electrocatalyic processes on HOPG, especially in the region of singularities such as step edges. Therefore in order to test the impact of applied electric fields, the experiment was adapted so that a DC potential could be applied between the HOPG surface and an immersed platinum electrode (see experimental section). The value of the applied voltage was selected to be +1 V, to avoid any significant chemical modification of the surface [32].

The results, presented in Figure 3.2, compare three sets of measurements: (i) ultrapure water placed for 5 seconds in contact with the surface of HOPG, (ii) ultrapure water placed for 2 hours in contact with the surface of HOPG, and (iii) ultrapure water placed for 2 hours in contact with the surface of HOPG while applying a DC potential of +1 V to the HOPG surface with respect to the electrode placed directly in the water. All the samples were collected in identical conditions, at room temperature, in contact with air and over HOPG previously heated above 120 ^{o}C to evaporate any historical contaminant (see experimental section) [33]. 50 µL of the solution from the bulk liquid was taken as the sample for analysis (see methods section). To obtain estimates of the methanol concentration, and to have a marker for comparison between different experiments, the system needed to be doped with a tracer. Methylsulfonylmethane ($DMSO_2$) was chosen due to it being relatively chemically inert and producing a ^{1}H NMR peak close to that of methanol [34]. Therefore the samples were all doped with 2µM of $DMSO_2$.

Sample (i) act as an immediate control for possible contaminants since no supramolecular structures could be observed by AFM on such short timescale. The 5 second water-HOPG contact time was chosen simply because it was the shortest timescale in which the sample could be prepared. No detectable level of methanol is expected and this is indeed confirmed (Figure 3.2a (i)), demonstrating that the methanol present in the solution originates from catalytic activity and is not due to any form of external contamination.

Sample (ii) represents the timescale typically necessary for the nucleation of supramolecular structures at the HOPG-water interfaces, 2 hours, as observed with AFM. A distinctive methanol peak is present (Figure 3.2a (ii)), confirming catalysis of water

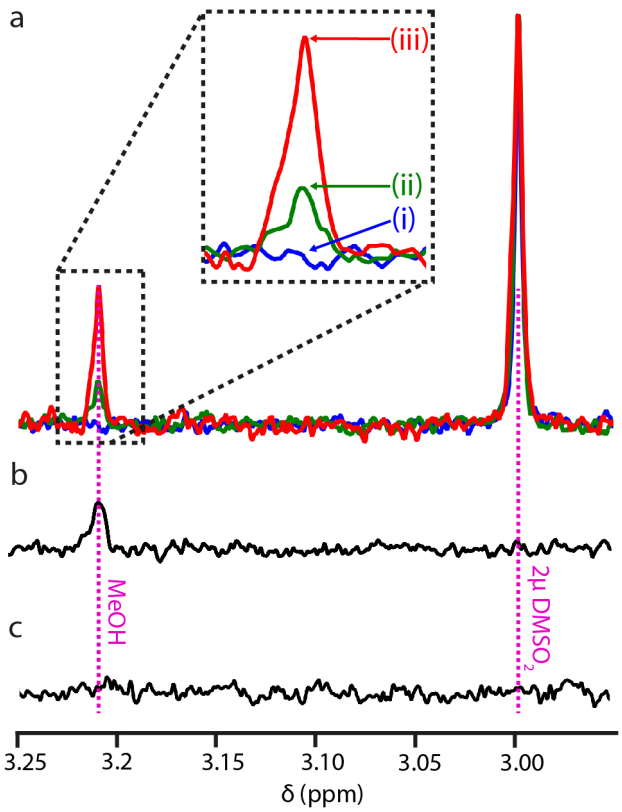

Fig. 3.2: ^{1}H NMR analysis for the methanol (MeOH) content of the ultrapure water solution after catalysis has occurred at the surface.(a) Spectra quantitatively comparing: (i) ultrapure water placed for 5 seconds in contact with the surface of HOPG, (ii) ultrapure water placed for 2 hours in contact with the surface of HOPG, and (iii) ultrapure water placed for 2 hours in contact with the surface of HOPG while applying a DC potential of +1 V to the HOPG. The peak at 3.21 ± 0.01 ppm is associated with the presence of methanol and the tracer peak ($DMSO_2$, peak just below 3 ppm) was used to adjust the relative magnitude of the curves. The determined concentrations of methanol are 0.000 ± 0.010 µM (i), 0.464 ± 0.010 µM (ii) and 1.180 ± 0.010 µM (iii). For comparison with samples (i-iii), spectra were also collected in a 1 µM solution of methanol (b) and in ultrapure water exposed to air for 2 hours (c). All samples were prepared in identical conditions (see methods for experimental details).

to methanol at the surface of HOPG immersed in water in ambient conditions. Comparing the area of the methanol peak with that of the $DMSO_2$ indicates a methanol concentration of 0.464 ± 0.010 µM in the solution. This is an underestimate since it excludes any methanol that remained at the HOPG surface after the solution was removed for analysis. Indeed, a significantly higher alcohol concentration is expected to remain at the interface with the hydrophobic HOPG surface where alcohol preferentially resides (as will be demonstrated in Chapter 4) [28, 29].

Sample (iii) demonstrates that there is a clear observed enhancement of the catalytic

activity under an electrical potential. When a potential of +1V ± 0.01 V was applied for 2 hours, 1.180 ± 0.010 µM of methanol was detected (Figure 3.2a (iii)), more than twice the amount formed without the electric potential. This further confirms the expected electrocatalytic activity of the HOPG, both at atomic steps and edges where the existence of additional functional groups may serve as oxidizing and reduction sites, similar to hydrophilic groups in GrO, and in the basal plane where fast electron transfer under applied fields is expected [26].

To further ensure there was no contamination from the glassware and equipment used or from the atmosphere, measurements were also taken for a vial of ultrapure water exposed to the laboratory environment for 2 hours (Figure 3.2c). This did not show any peak in the methanol region confirming the methanol catalysis is occurring during the experiment.

3.4 Importance for SPM investigations

3.4.1 Time-delayed nucleation

Overall, the NMR results confirm spontaneous methanol catalysis, with the process being enhanced by the presence of an electric field. Interestingly, the electrocatalytic result from the NMR spectroscopy suggests that the scanning AFM tip may also have an influence on the rate of methanol production at the HOPG surface. Composite nanomaterials involving oxides are widely used in methanol catalysis [8, 35–37] and the silicon oxide AFM tips such as those used in the present study have been shown to develop a negative surface potential of typically -60 mV [38, 39] when immersed in ultrapure water (pH of 5.8 in our experimental conditions). Furthermore, the tips are designed to have a highly curved apex (radius >10 nm) which can significantly enhance the resulting local electric field and therefore any electrocatalytic effects. Experimentally, it was observed that when water is placed in contact with the HOPG surface for several hours prior to imaging, ordered structures do not appear immediately at the start of imaging. Instead these structures appear to be stimulated by the presence of the scanning tip, as can be seen in Figure 3.3.

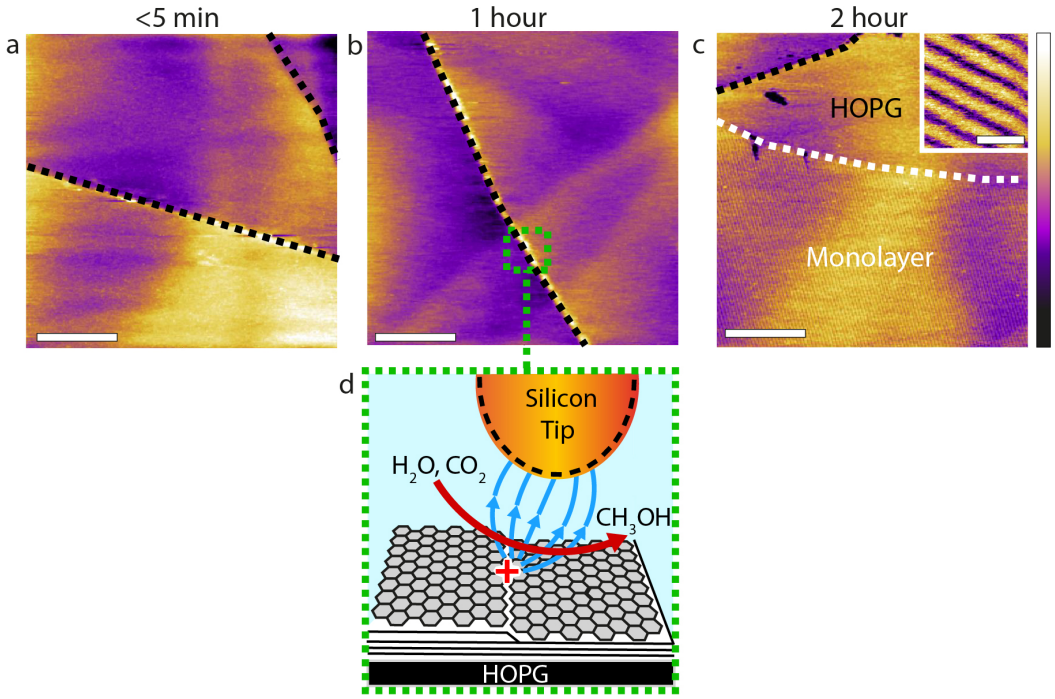

Fig. 3.3: AFM images of a sample pre-conditioned for 24 hours with no applied electric field. (a-b) During < 5 min and 1 hour of imaging, no structures are observed in a system of ultrapure water on HOPG. (c) After an hour the interfacial structures nucleate and cover a significant amount of the accessible area and show the characteristic row features (inset). (d) The hour long delay in nucleation between (a) and (c), despite the 24 hours of contact beforehand, suggests the methanol production is electrocatalysed by the silicon AFM tip. This tip has a surface potential of around -60 mV and is not grounded . The white scale bars are 500 nm in the main images and 10 nm in the inset. The color scale bar represents a height variation of 1.5 nm in the main images and 1.2 nm in the inset.

3.4.2 Replicating tip induced charge

Due the observations regarding the time-delayed nucleation and the impact of the the AFM tip present, further investigations were performed into the effect of small voltages, comparable in magnitude to the surface potential of typical oxides. Here the evolution of samples exposed to 50 ± 1 mV or in open circuit for 24h were compared. Applying the electric field in the AFM chamber was not possible due to spatial restrictions. Therefore, in both cases, it was necessary to de-wet the HOPG surface in order to transfer a pre-conditioned sample to the AFM chamber; thereby leaving a thin interfacial liquid layer containing the produced methanol. More ultrapure water is then deposited ontop of liquid layer and the imaging starts within minutes. While necessary, this procedure makes it difficult to rule out any disassembly/reassembly of the interfacial structures during the transfer. Nonetheless the differences between the two samples are obvious (Figure 3.4).

Figure 3.4a shows that no features other than the characteristic graphite steps are initially visible in the absence of electrical pre-conditioning. After one hour of continuous imaging, small raised patches about 100 nm in diameter begin to nucleate near step-edges (Figure 3.4b). The patches exhibit supramolecular row patterns, comparable to those shown in Figure 3.1. The assembly of these rows proceeds at a slow rate, here 54.3 ± 1.0 nm^2/s for the patch in Figure 3.4b, suggesting growth is limited by the rate of methanol catalysis. Interestingly this rate is almost an order of magnitude larger than the one reported for the structures in Figure 3.1. This is consistent with a larger concentration of methanol due to the 24 hours of preconditioning. Additionally, structures never fully cover the surface over the time-scale of the experiment (several hours) with the largest patch observed with a diameter of 1.2 µm.

When the 50mV external potential is applied for 4 hours after 20 hours of open circuit (an elongated version of the hypothetical scenario presented in Figure 3.3) the monolayers still take approximately an hour to nucleate, Figures 3.4d and e. However, they subsequently grow at a rate of 275 ± 2.5 nm^2/s, significantly faster than in the open circuit case. This increased growth rate indicates a larger amount of alcohol being presented due the electrocatalytic assisted production of methanol.

Finally, when a 50 mV external potential is applied for the full 24 hours prior to

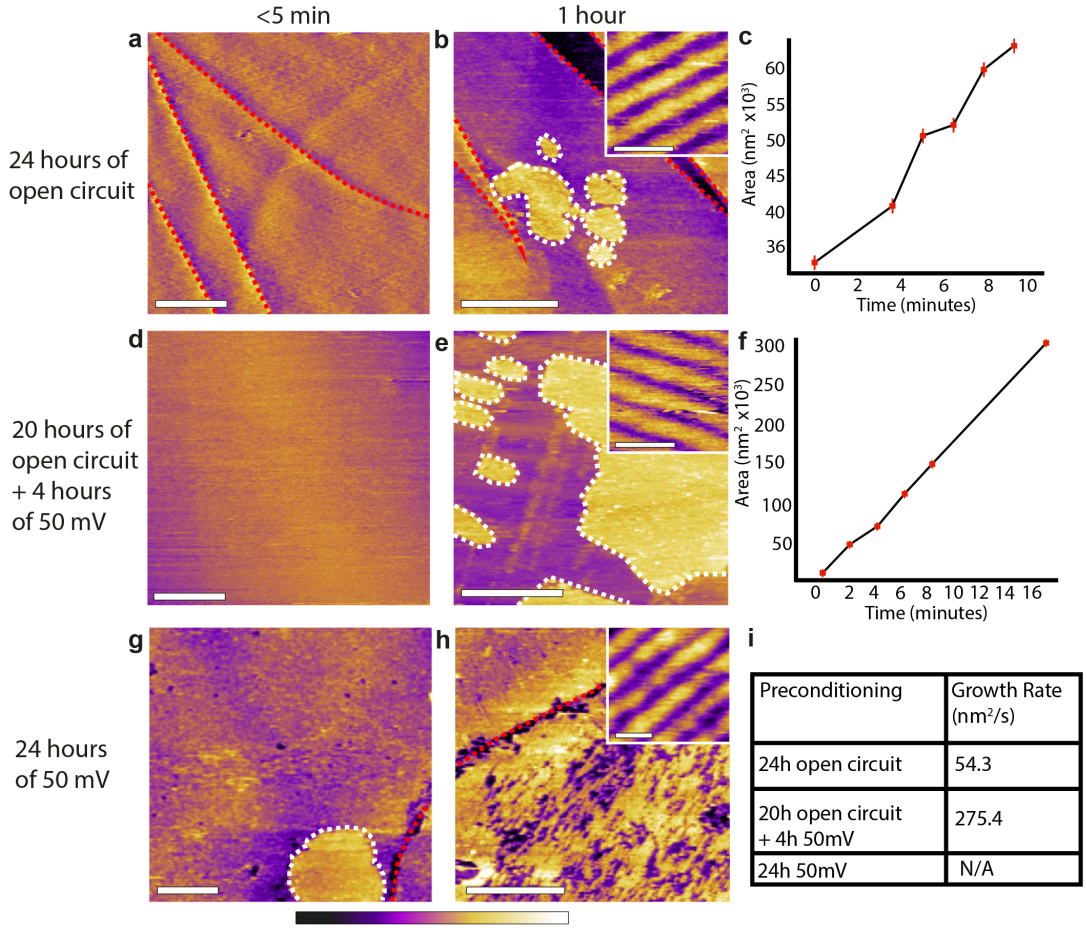

Fig. 3.4: Influence of small electric potentials on the evolution of the methanol-water interfacial structures observed by AFM. (a) Image taken immediately after a sample that has been pre-conditioned for 24h in ultrapure water has been transferred into the AFM chamber, and (b) after 1 hour of imaging. Interfacial structures with row features (inset) outlined by the white dashes begin to appear near atomic steps (highlighted with red dashed lines). (c) The area of the growing patch after nucleation as a function of time. (d,e,f) Similar set of data for a system where there has been 20 hours of open circuit followed by 4 hours of an applied 50mV electric field. No structures are immediately visible, although after an hour, structures begin to nucleate and grow at a faster rate than for the 24 hours of open circuit. (g-h) are images taken immediately after a sample pre-conditioned for 24h in ultrapure water with an applied 50 mV DC potential was transferred into the AFM chamber. Some unstructured patches are already present on the surface. After 1 hour of imaging the interfacial structures cover all the accessible area and also show the characteristic row features (inset). Here the structures grew at a rate faster than could be imaged. (i) A table comparing the growth rates for the 3 cases. The white scale bars are 500 nm in the main images and 10 nm in the insets. The color scale bar represents a height variation of 1.5 nm in the main images and 1.2 nm in the insets.

imaging, patches of structures are immediately visible on the HOPG surface (Figure 3.4g). The patches rapidly develop into ordered structures resembling those of the

methanol-water monolayers. Significantly, within an hour of imaging the structures have almost completely covered the surface of the graphite (Figure 3.4h). Moreover, this increase in methanol concentration induced the occasional observation of multiple monolayers, Figure 3.5, consistent with higher concentrations of methanol. While there are still nucleation sites near surface features, such as in Figure 3.4e, nucleation is also observed deep into the basal plane (see Figure 3.6) indicating that the electrical pre-conditioning has caused electrocatalysis across all of the HOPG, instead of being limited to just surface singularities.

The results in this section all support the existence of a significantly larger quantity of methanol at the interface when compared to the sample prepared without any applied electric field. Furthermore, the hour long delay in nucleation between Figure 3.4a and Figure 3.4b despite the 24 hours of contact beforehand is consistent with the idea that while there is initially methanol present in the solution (as shown in the NMR data, Figure 3.2a (ii)), the local concentration is initially too low for nucleation, but the presence of the charged tip with a surface potential comparable to the electric field applied in Figure 3.4d-h, helps overcome this barrier and nucleation eventually takes place.

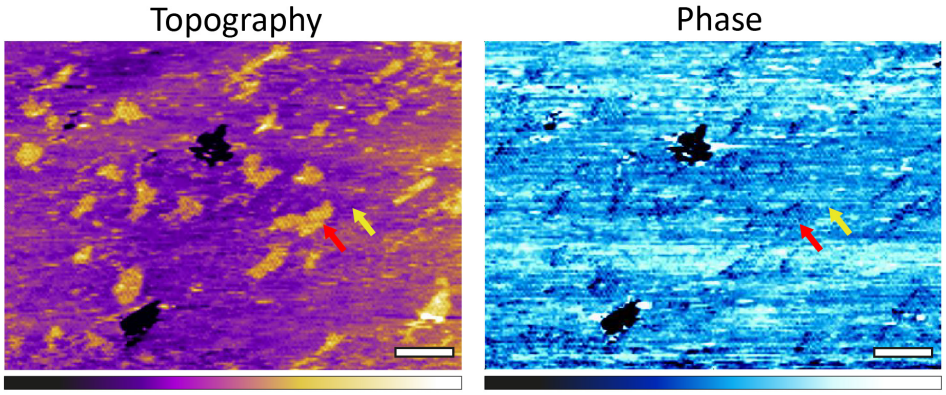

Fig. 3.5: AFM imaging of the graphite surface preconditioned in a water droplet with a 50 mV electrical potential applied for 24 hours. The whole surface is covered with a structured monolayer (yellow arrow). A second layer can develop directly atop the first layer (red arrow). The nucleation of multiple layers suggests a higher concentration of methanol than when no electric field is applied where the structures exist only as monolayers. The white scale bars represent 100 nm. The purple scale bar represents a variation of 1.5 nm in the main images and blue scale bar represents a phase variation of 10^o.

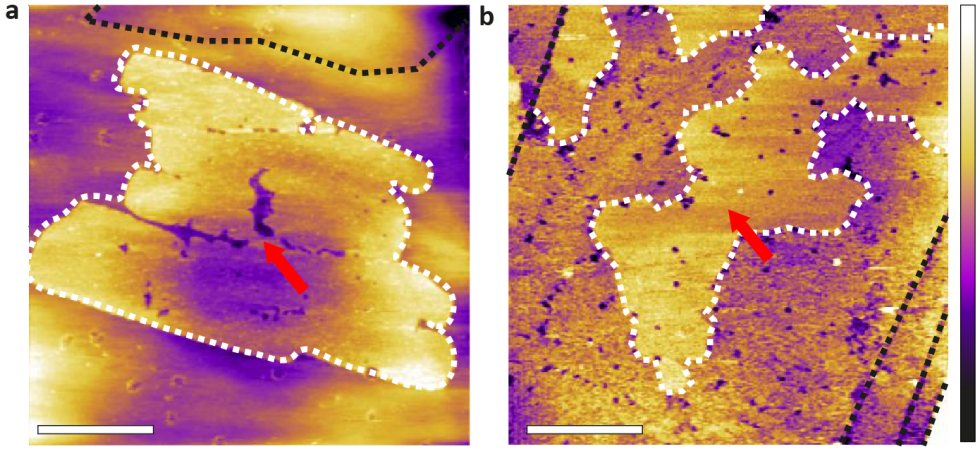

Fig. 3.6: Topographic images of HOPG pre-conditioned for (a) 4h and (b) 24h in ultrapure water with an external 50mV DC potential. The sample was immediately transferred to AFM chamber. In contrast to samples with no applied potential, nucleation sites can be found several microns away from step edges (red arrows), indicating the electrocatalytic activity is no longer limited to surface defects. The structures are outlined by white dashed line and the step edges highlighted with black dashed lines. The white scale bars represent 1 µm. The purple scale bar represents a variation of 4 nm.

3.5 Catalysis mechanism

AFM and NMR experiments consistently demonstrate catalysis of methanol at the surface of immersed graphite in ambient conditions. The mechanism allowing the methanol synthesized at the surface of graphite to be released in the bulk liquid is not immediately obvious from the data. The results show that the water-methanol assembly is fully stable when directly in contact with the surface of graphite, but becomes progressively less stable as new layers form on top of the first layer. Additional layers could occasionally be observed (Figure 3.8) but are only partially formed and exhibit many defects, suggesting a transition from stable assembly to bulk liquid. A single release mechanism is however unlikely and the methanol produced may be dispensed directly into the bulk liquid at catalytically active surface features where the water-methanol network is disrupted.

The results suggested that the carbon source of the material converted into alcohol is primarily the carbon dioxide naturally dissolved in the ultrapure water. Experiments run in a sealed atmosphere for 2 hours (comparable in duration to sample (ii) in Figure 3.2) revealed no detectable concentration of methanol upon subsequent NMR analysis of the liquid, as shown in Figure 3.7, supporting the hypothesis of carbon

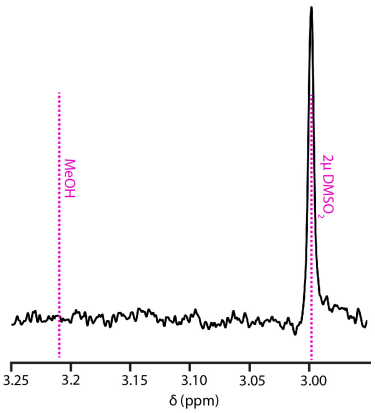

Fig. 3.7: NMR spectrum for a droplet of ultrapure water left on HOPG for 2 hours in a sealed environment. The sample is doped with 2μM of Methylsulfonylmethane, consistent with the data in Figure 2. Here no methanol is detected, indicating the reaction most likely involves volatile organics that dissolve in the ultrapure water from the air.

dioxide as a reagent. However, the C-O dissociation energy for carbon dioxide is 526.1 kJ mol^{-1} [40], far larger than the energy associated with thermal fluctuations ($\approx$ 2.479 kJ mol^{-1}) and thus the HOPG surface must be playing a role. There have been no previous cases of HOPG demonstrating the catalytic capability to reduce the C-O disassociation energy $\sim$ kT. Furthermore the process can occur in an open circuit, indicating that it is not solely due to electrocatalysis. This leaves the possibility of photocatalysis.

As mentioned in Section 3.2.2, it has been shown that photogenerated electrons and holes from stimulating graphene oxide with white light can convert water and carbon dioxide into methanol at room temperatures [22]. In this reaction, the photogenerated electrons and holes to serve as oxidation and reduction sites for absorbed reagents. Ref. [22] estimated that the reduction potential of the electrons (e^-) excited to the graphene oxide conduction band was -0.79 V (vs. the normal hydrogen electrode value, NHE), which is lower than the potential of CO_2/CH_3OH (-0.38 V vs. NHE) which means that it can act as a donor. Similarly, the oxidation potential of the holes (h^+) in the graphene oxide valance band was estimated to be 4 V (vs. NHE) which is higher than the potential of H_2O/O_2, H^+ (0.82 V vs. NHE) and thus they can act as acceptors. Therefore the photogenerated holes and electrons on the illuminated graphene oxide could react with the adsorbed CO_2 and H_2O to produce

CH_3OH through the following reaction:

$$\begin{aligned} H_2O + 2h^+ &\rightarrow 2H^+ + 1/2O_2 \\ CO_2 + 6H^+ + 6e^- &\rightarrow CH_3OH + H_2O \end{aligned} \tag{3.2}$$

In this case, each methanol molecule produced involves the transfer of six electrons with the reactive intermediates (for example formic acid and formaldehyde [41]) being required to diffuse across the surface to obtain electrons. For the work presented in this chapter, it is possible that the reported presence of oxygen containing groups on the edge plane of HOPG steps may be inducing a similar catalytic reaction. Initial experiments indicate no appreciable catalytic increase under illumination (see Figure 3.8). This may be due to the reported low number of functional groups on HOPG and hence a low number of possible 'photo-excitable' electrons, which would mean that the system could become saturated when additional illumination is present. Therefore the next stage of this research should be to perform ^{1}H NMR on samples which have had no exposure to light. Unfortunately this was not possible to achieve with the equipment available for this study and thus shall be consigned to further work.

It has been noted that a degree of atmospheric contamination of the HOPG [33, 42] is expected despite all the steps taken to minimize contamination. However, the consistent and reproducible trends observed indicate that possible contaminants do not dominate the results. Furthermore, the typical HOPG contaminants [33, 42] are molecules far larger than methanol, and so they would not interfere with the AFM observations of its catalytic production.

3.6 Discussion

The exact molecular mechanism underlying the catalytic process cannot by deduced from the present results alone, partly because the exact chemical details of the graphite are not known. Surface groups at the edge plane [23] could significantly alter graphite's catalytic behaviour by modifying the local electron accepting/donating abilities and inducing charge delocalization that would in turn impact chemisorption [16]. The results presented in this chapter suggest that the methanol production is caused by multiple factors, all involving the HOPG surface, that are difficult to

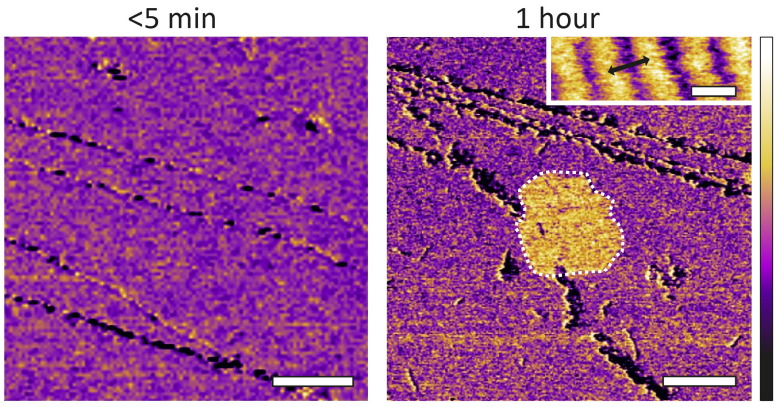

Fig. 3.8: Amplitude modulation AFM phase images of HOPG pre-conditioned for 24h in ultrapure water with an external 60 W incandescent light bulb. The sample was immediately transferred to AFM chamber (left). The structures (outlined with the white dashed line) with a periodicity of 4.3 nm (black arrow) were only observed nucleating after an hour (right), consistent with the results in Figure 3.2 (a) and (b) indicating that no observable photo-catalysis of water to methanol has occurred. The inset is a height image using the same color scale. The white scale bars represent 500 nm in the main image and 4 nm in the inset. The purple scale bar represents a variation of 5^o in the main images and 1.5 nm in the inset.

disentangle. The AFM results provide consistent evidence of the AFM tip influencing the catalysis, likely through a tip field-effect [43] electrochemical reaction when in proximity to the HOPG surface (Figures 3.3 and 3.4). However, catalysis also occurs in the absence of an applied electric potential (Figure 3.2), through a mechanism dominated by step edges. Oxygen containing functional groups unique to multi-layered graphite could also be at play, inducing absorption via bonded and non-bonded interactions with the liquid molecules and serving as active sites [44]. In any case, the catalytic activity benefits from a positive polarization of the HOPG under an external electrical potential. This could be due to both a further enhancement of the chemical reaction at the step edges or to induced electron transfer occurring elsewhere. Indeed, recent studies have shown that doped graphene is able to reduce carbon dioxide in ambient conditions, when submitted to an electric potentials [45].

When considering practical applications, the catalytic process reported here is far from optimized. It occurs slowly and could be temperature dependent. In ambient conditions, the catalytic production rate is estimated to be 4.6 $\mathrm{mgh^{-1}m^{-2}}$, far smaller than the best reported catalysis rates [13]. However, since singularities in the potential landscape such as atomic step-edges or the proximity of an AFM tip can significantly enhance the rate of catalysis, there is much scope for improvement.

Additionally, the relatively low cost of graphite, its outstanding stability and the fact that material of technically lower quality (more defects) is catalytically more efficient should enable device geometries that maximize the catalytically active area without significant challenges. Furthermore a recent report has stated that for any reduction process of carbon dioxide to methanol to be overall carbon neutral it will need to be a hybrid of both thermocatalysis and electrocatalysis [8]. Thus studies into hybrid processes such as the case presented here are becoming increasingly important.

From an electrochemical perspective, the results suggest that a graphite electrode immersed into an aqueous solution progressively develops an interfacial 'passivation' layer formed by a solid self-assembled layer of water and methanol molecules produced in-situ. While relatively easy to destroy, this layer reforms spontaneously and may significantly affect interfacial processes such as charge exchange [46] and molecular adsorption [47] as well as the catalysis of other molecules [23]. Interestingly, this result also suggests that local probe investigations of graphitic materials in aqueous solution may be prone to tip induced catalysis effects.

3.7 Conclusion

In conclusion, the combined AFM and NMR results consistently show that graphite is able to spontaneously catalyse methanol at room temperature. The amount of methanol produced is relatively modest (∼µM concentrations) and catalysis appears to occur almost exclusively at surface singularities on the graphite such as atomic steps and in the absence of any external input of energy. The underlying molecular mechanism remains unclear due uncertainties over the chemical composition of the graphite, but applying an external electrical potential across the interface considerably enhances the catalysis rate, even when due to the surface potential of nano-objects located near the interface. This findings could have a significant impact on the development and understanding of novel carbon-based catalytic materials as well as devices highly sensitive to interfacial liquids. Furthermore the unpreventable presence of low concentrations of methanol will be important to consider in work later in this thesis when non-methanol-based mixtures are used.

3.8 Experimental Section

Sample preparation

All the solutions were prepared using the chemicals outlined in Chapter 2. In a typical experiment, a liquid droplet (around 200 µL) of water was deposited on a freshly cleaved HOPG substrate (SPI supplies, West Chester, PA, USA) mounted on a stainless steel disk using silver paint (Ted Pella Inc, Redding, CA, USA). In all cases the HOPG was baked to $> 120\ ^{o}$C for 15 minutes to remove any contaminants [33] before depositing the droplet. When required, the droplet was then left for a set period (5 seconds to 24 hours) inside a partially sealed glass container at room temperature (20 ± 1 °C). The container was thoroughly cleaned with ultrapure water beforehand and protected from the light throughout the incubation. The same procedure was used for the electric field experiments, except for a platinum wire (Sigma-Aldrich) is immersed in the droplet. The wire and HOPG sample were connected to a DC power supply (Aim-TTi, Cambridgeshire, UK) with a positive voltage applied to the HOPG with respect to the platinum.

NMR

After the determined incubation period, 50 µL the droplet was pipetted from the HOPG into a clean NMR tube. The solution was then diluted with deuterium oxide (purity 99.9%, Cambridge Isotope Laboratories, Inc., MA, USA) as needed and the $DMSO_2$ (Sigma-Aldrich, Dorset, UK) tracer added before conducting the measurement. The intense water signal was attenuated using the Robust-5 pulse sequence using a Varian (CA, USA) 600 MHz spectrometer equipped with an Agilent (CA, USA) probe able to deliver a maximum pulsed field gradient of 62 Gcm^{-1}. Nine thousand two hundred and forty-eight scans were collected, each comprising 32728 complex data points and a spectral width of 10 kHz. The repetition time was 3.6 s, of which 1.6 s comprised the acquisition time. The W5 inter-pulse delay was set to 287 µs. Rectangular 1 ms pulsed field gradients were used with a strength of G =4.8 Gcm^{-1} [31]. The gradient stabilization delay was 1 ms. The error associated with estimating the quantity of methanol produced is dominated by the error in measuring the volume of liquid for NMR analysis leading to an overall uncertainty on the concentrations of ± 0.01 µM. The contribution to this error from the NMR procedure itself was negligible.

AFM

Imaging was conducted using the methodology described in Chapter 2. The cantilevers were cleaned by immersion in ultrapure water before imaging. All parts of the AFM in direct and indirect contact with the solution (cantilever holder, imaging chamber) where thoroughly cleaned with ultrapure water prior to imaging. After washing, the stage was heated to 105 °C for 20 minutes in air to evaporate possible substances from previous experiments. In order to nucleate the structures all the samples were imaged at 40 ^{o}C, although all the preconditioning occurred at room temperature.

References: Chapter 3

[1] W. Wang, S. Wang, X. Ma, J. Gong, "Recent advances in catalytic hydrogenation of carbon dioxide", *Chemical Society Reviews* **2011**, *40*, 3703–3727.

[2] C. T. Wu, K. M. K. Yu, F. Liao, N. Young, P. Nellist, A. Dent, A. Kroner, S. C. E. Tsang, "A non-syn-gas catalytic route to methanol production", *Nature Communications* **2012**, *3*, 1050–1058.

[3] G. A. Olah, A. Goeppert, G. K. Prakash, "Beyond Oil and Gas: The Methanol Economy: Second Edition", *Beyond Oil and Gas: The Methanol Economy: Second Edition* **2005**, 1–334.

[4] G. W. Huber, S. Iborra, A. Corma, "Synthesis of transportation fuels from biomass: Chemistry, catalysts, and engineering", *Chemical Reviews* **2006**, *106*, 4044–4098.

[5] E. Barton Cole, P. S. Lakkaraju, D. M. Rampulla, A. J. Morris, E. Abelev, A. B. Bocarsly, "Using a one-electron shuttle for the multielectron reduction of CO 2 to methanol: Kinetic, mechanistic, and structural insights", *Journal of the American Chemical Society* **2010**, *132*, 11539–11551.

[6] L. Arnarson, P. S. Schmidt, M. Pandey, A. Bagger, K. S. Thygesen, I. E. Stephens, J. Rossmeisl, "Fundamental limitation of electrocatalytic methane conversion to methanol", *Physical Chemistry Chemical Physics* **2018**, *20*, 11152–11159.

[7] D. Yang, Q. Zhu, C. Chen, H. Liu, Z. Liu, Z. Zhao, X. Zhang, S. Liu, B. Han, "Selective electroreduction of carbon dioxide to methanol on copper selenide nanocatalysts", *Nature Communications* **2019**, *10*, 1–9.

[8] B. M. Tackett, E. Gomez, J. G. Chen, "Net reduction of CO 2 via its thermocatalytic and electrocatalytic transformation reactions in standard and hybrid processes", *Nature Catalysis* **2019**, *2*, 381–386.

[9] M. Stawowy, R. Ciesielski, T. Maniecki, K. Matus, R. Łużny, J. Trawczynski, J. Silvestre-Albero, A. Łamacz, "CO2 hydrogenation to methanol over Ce and Zr containing UiO-66 and Cu/UiO-66", *Catalysts* **2020**, *10*, 1–17.

[10] B. A. Peppley, J. C. Amphlett, L. M. Kearns, R. F. Mann, "Methanol–steam reforming on Cu/ZnO/Al2O3. Part 1: the reaction network", *Applied Catalysis A: General* **1999**, *179*, 21–29.

[11] A. Dhakshinamoorthy, H. Garcia, "Catalysis by metal nanoparticles embedded on metal–organic frameworks", *Chemical Society Reviews* **2012**, *41*, 5262–5284.

[12] J. Graciani, K. Mudiyanselage, F. Xu, A. Baber, J. Evans, S. D. Senanayake, D. J. Stacchiola, P. Liu, J. Hrbek, J. Sanz, J. A. Rodriguez, "Highly active copper-ceria and copper-ceria-titania catalysts for methanol synthesis from CO", *Science* **2014**, *345*, 546–550.

[13] F. Studt, M. Behrens, E. L. Kunkes, N. Thomas, S. Zander, A. Tarasov, J. Schumann, E. Frei, J. B. Varley, F. Abild-Pedersen, J. K. Nørskov, R. Schlögl, "The Mechanism of CO and CO2 Hydrogenation to Methanol over Cu-Based Catalysts", *ChemCatChem* **2015**, *7*, 1105–1111.

[14] S. Wesselbaum, T. Vom Stein, J. Klankermayer, W. Leitner, "Hydrogenation of carbon dioxide to methanol by using a homogeneous ruthenium-phosphine catalyst", *Angewandte Chemie - International Edition* **2012**, *51*, 7499–7502.

[15] J. Klankermayer, S. Wesselbaum, K. Beydoun, W. Leitner, "Selective Catalytic Synthesis Using the Combination of Carbon Dioxide and Hydrogen: Catalytic Chess at the Interface of Energy and Chemistry", *Angewandte Chemie - International Edition* **2016**, *55*, 7296–7343.

[16] D. Yu, E. Nagelli, F. Du, L. Dai, "Metal-free carbon nanomaterials become more active than metal catalysts and last longer", *Journal of Physical Chemistry Letters* **2010**, *1*, 2165–2173.

[17] M. Xu, T. Liang, M. Shi, H. Chen, "Graphene-like two-dimensional materials", *Chemical Reviews* **2013**, *113*, 3766–3798.

[18] Z. Sun, T. Ma, H. Tao, Q. Fan, B. Han, "Fundamentals and Challenges of Electrochemical CO 2 Reduction Using Two-Dimensional Materials", *Chem* **2017**, *3*, 560–587.

[19] N. Guo, Y. Xi, S. Liu, C. Zhang, "Greatly enhancing catalytic activity of graphene by doping the underlying metal substrate", *Scientific Reports* **2015**, *5*, 1–7.

[20] O. Mohammadi, M. Golestanzadeh, M. Abdouss, "Recent advances in organic reactions catalyzed by graphene oxide and sulfonated graphene as heterogeneous nanocatalysts: A review", *New Journal of Chemistry* **2017**, *41*, 11471–11497.

[21] M. F. R. Hanifah, J. Jaafar, M. H. Othman, A. F. Ismail, M. A. Rahman, N. Yusof, F. Aziz, N. A. Rahman, "One-pot synthesis of efficient reduced graphene oxide supported binary Pt-Pd alloy nanoparticles as superior electro-catalyst and its electro-catalytic performance toward methanol electro-oxidation reaction in direct methanol fuel cell", *Journal of Alloys and Compounds* **2019**, *793*, 232–246.

[22] H. Hsu, I. Shown, H. Wei, Y. Chang, H. Du, Y. Lin, C. Tseng, C. Wang, L. Chen, Y. Lin, K. Chen, "Graphene oxide as a promising photocatalyst for CO 2 to methanol conversion", *Nanoscale* **2013**, *5*, 262–268.

[23] R. L. McCreery, "Advanced carbon electrode materials for molecular electrochemistry", *Chemical Reviews* **2008**, *108*, 2646–2687.

[24] S. Lemay, H. White, "Electrochemistry at the Nanoscale: Tackling old questions, posing new ones", *Accounts of Chemical Research* **2016**, *49*, 2371.

[25] C. G. Williams, M. A. Edwards, A. L. Colley, J. V. Macpherson, P. R. Unwin, "Scanning micropipet contact method for high-resolution imaging of electrode surface redox activity", *Analytical Chemistry* **2009**, *81*, 2486–2495.

[26] P. R. Unwin, A. G. Güell, G. Zhang, "Nanoscale Electrochemistry of sp 2 Carbon Materials: From Graphite and Graphene to Carbon Nanotubes", *Accounts of Chemical Research* **2016**, *49*, 2041–2048.

[27] K. Voitchovsky, D. Giofrè, J. J. Segura, F. Stellacci, M. Ceriotti, "Thermally-nucleated self-assembly of water and alcohol into stable structures at hydrophobic interfaces", *Nature Communications* **2016**, *7*, 13064.

[28] J. Sung, K. Park, D. Kim, "Surfaces of Alcohol-Water Mixtures Studied by Sum-Frequency Generation Vibrational Spectroscopy", *The Journal of Physical Chemistry B* **2005**, *109*, 18507–18514.

[29] M. Lundgren, N. L. Allan, T. Cosgrove, "Wetting of water and water/ethanol Droplets on a non polar surface: A Molecular Dynamics Study.", *Langmuir* **2002**, *18*, 10462–10466.

[30] D. Yang, A. H. Zewail, "Ordered water structure at hydrophobic graphite interfaces observed by 4D, ultrafast electron crystallography", *PNAS* **2009**, *106*, 4112–4126.

[31] J. A. Aguilar, S. J. Kenwright, "Robust NMR water signal suppression for demanding analytical applications", *The Analyst* **2016**, *141*, 236–242.

[32] S. Kondo, M. Lutwyche, Y. Wada, "Nanofabrication of layered materials with the scanning tunneling microscope", *Applied Surface Science* **1994**, *75*, 39–44.

[33] D. Martinez-Martin, R. Longuinhos, J. G. Izquierdo, A. Marele, S. S. Alexandre, M. Jaafar, J. M. Gómez-Rodríguez, L. Bañares, J. M. Soler, J. Gomez-Herrero, "Atmospheric contaminants on graphitic surfaces", *Carbon* **2013**, *61*, 33–39.

[34] H. E. Gottlieb, V. Kotlyar, A. Nudelman, "NMR chemical shifts of common laboratory solvents as trace impurities", *Journal of Organic Chemistry* **1997**, *62*, 7512–7515.

[35] M. Ravi, V. L. Sushkevich, A. J. Knorpp, M. A. Newton, D. Palagin, A. B. Pinar, M. Ranocchiari, J. A. van Bokhoven, "Misconceptions and challenges in methane-to-methanol over transition-metal-exchanged zeolites", *Nature Catalysis* **2019**, *2*, 485–494.

[36] J. Xie, R. Jin, A. Li, Y. Bi, Q. Ruan, Y. Deng, Y. Zhang, S. Yao, G. Sankar, D. Ma, J. Tang, "Highly selective oxidation of methane to methanol at ambient conditions by titanium dioxide-supported iron species", *Nature Catalysis* **2018**, *1*, 889–896.

[37] H. Mistry, A. S. Varela, S. Kühl, P. Strasser, B. R. Cuenya, "Nanostructured electrocatalysts with tunable activity and selectivity", *Nature Reviews Materials* **2016**, *1*.

[38] S. I. Raider, R. Flitsch, M. J. Palmer, "Oxide Growth on Etched Silicon in Air at Room Temperature", *Journal of The Electrochemical Society* **1975**, *122*, 413–418.

[39] A. M. Shaw, T. E. Hannon, F. Li, R. N. Zare, "Adsorption of Crystal Violet to the Silica-Water Interface Monitored by Evanescent Wave Cavity Ring-Down Spectroscopy", *The Journal of Physical Chemistry B* **2003**, *107*, 7070–7075.

[40] Y. Izumi, "Selective ethanol synthesis from carbon dioxide: Roles of rhodium catalytic sites", *Platinum Metals Review* **1997**, *41*, 166–170.

[41] N. Manzoor, M. Sadiq, M. Naqvi, S. R. Naqvi, U. Sikandar, "Experimental study of CO2 conversion into methanol by synthesized photocatalyst (ZnFe2O4/TiO2) using visible light as an energy source", *Catalysts* **2020**, *10*, 1–17.

[42] Z. Li, Y. Wang, A. Kozbial, G. Shenoy, F. Zhou, R. McGinley, P. Ireland, B. Morganstein, A. Kunkel, S. P. Surwade, L. Li, H. Liu, "Effect of airborne contaminants on the wettability of supported graphene and graphite", *Nature Materials* **2013**, *12*, 925–931.

[43] J. Huang, B. G. Sumpter, V. Meunier, G. Yushin, C. Portet, Y. Gogotsi, "Curvature effects in carbon nanomaterials: Exohedral versus endohedral supercapacitors", *Journal of Materials Research* **2010**, *25*, 1525–1531.

[44] A. Sims, M. Jeffers, S. Talapatra, K. Mondal, S. Pokhrel, L. Liang, X. Zhang, A. L. Elias, B. G. Sumpter, V. Meunier, M. Terrones, "Hydro-deoxygenation of CO on functionalized carbon nanotubes for liquid fuels production", *Carbon* **2017**, *121*, 274–284.

[45] Y. Song, R. Peng, D. K. Hensley, P. V. Bonnesen, L. Liang, Z. Wu, H. M. Meyer, M. Chi, C. Ma, B. G. Sumpter, A. J. Rondinone, "High-Selectivity Electrochemical Conversion of CO2to Ethanol using a Copper Nanoparticle/N-Doped Graphene Electrode", *ChemistrySelect* **2016**, *1*, 6055–6061.

[46] L. V. Protsailo, W. R. Fawcett, "Studies of electron transfer through self-assembled monolayers using impedance spectroscopy", *Electrochimica Acta* **2000**, *45*, 3497–3505.

[47] W. Beckner, Y. He, J. Pfaendtner, "Chain Flexibility in Self-Assembled Monolayers Affects Protein Adsorption and Surface Hydration: A Molecular Dynamics Study", *The Journal of Physical Chemistry B* **2016**, *120*, 10423–10432.

4.0 Chapter 4: Alcohol-water mixtures at hydrophobic interfaces

4.1 Chapter Overview

The behaviour of mixtures of alcohol and water at hydrophobic interfaces is central to this thesis. However, despite the importance of alcohol-water mixtures in both industrial and natural processes, their behaviour at hydrophobic interfaces is still poorly understood with only a few studies available. In this chapter I will present a computational molecular dynamics (MD) study of the structure of mixture of water with methanol, ethanol and 1-propanol at the interface with highly orientated pyrolytic graphite. I will demonstrate that the hydrogen-bonded networks forming at the interface have a strong concentration dependence. This dependence will be characterised and then linked to experimental observations obtained using three dimensional scanning force microscopy. Finally, the concentration dependant behaviour of the alcohol-water mixtures at the interface prior to any group-effect based self-assembly occurring will be compared with resulting structures.

4.2 Introduction

Mixtures of alcohols and water are commonplace in industry where they find use as solvents [1] and reagents [2] in chemical synthesis and in separation processes [3, 4]. Furthermore, aqueous alcohols are important in biological processes [5, 6].

For example, ethanol-water mixtures have been shown to induce concentration dependant structural transitions in DNA molecules [7]. More broadly, alcohols are amphiphilic with both non-polar (hydrophobic, CH_3) and polar (hydrophilic, OH) regions. Their simple structure thus also makes them an attractive model for more complex amphiphilic molecules [8]. Understanding the behaviour of complex amphiphilic molecules in water has significant consequences for biological processes such as the structure [9, 10], dynamics and self-assembly of proteins [5], the formation of membranes and the transport of ions and cosolutes [11, 12].

Due to their plethora of uses, the properties of alcohol and water mixtures in the bulk have been extensively studied, revealing a mixing behaviour which deviates from that of an ideal solution of randomly mixed molecules [13]. This is typically characterised by a large negative excess entropy [14]. The anomalous mixing behaviour of alcohol with water is attributed to the impact of the alcohol's hydrophobic group on both the local and extended hydrogen bonded networks forming between the constituent molecules. For methanol, the simplest alcohol, studies originally proposed that this unusual behaviour was due to an enhanced water order around the methanol's hydrophobic group. However this explanation remains under debate and contradicts multiple experimental and computational studies [15–19]. More recent updates on the model explain the behaviour by partial segregation of the alcohol and water molecules at the molecular level [20].

Regardless of the origin of the unexpected behaviour, the properties of alcohol and water mixtures show a strong concentration dependence. Mass spectrometry and X-ray diffraction [21] and absorption [22] results show, that for methanol and water mixtures, at room temperature this concentration dependence can be split into three regions. The boundaries between these regions lie at methanol molar fractions (x_m) of $x_m \approx 0.3$ and $x_m \approx 0.7$. The concentration dependence has been attributed to the different hydrogen bonding capabilities of the two components. Water has two hydrogen donating sites and two hydrogen accepting sites. Therefore, it has a preference to form three-dimensional tetrahedrally coordinated hydrogen bond networks, which dominate at low alcohol concentrations. Primary alcohols, such as methanol, have just one donor and acceptor site. Alcohols-rich solutions prefer to form one-dimensional (1D) and two-dimensional (2D) networks of chains, rings and clusters [23]. A similar behaviour and explanation has also been obtained using spectroscopic techniques including Raman spectroscopy [24]. Computational studies

of methanol-water mixtures also report comparable structural properties with a strong concentration dependence [18, 22, 25], in good agreement with experimental observations.

Larger alcohols such as ethanol and 1-propanol have been subject to many experimental [26–29] and computational [30–33] investigations where they show a different behaviour to methanol due to their larger hydrophobic regions. Significantly, X-ray scattering [27], infrared absorption spectroscopy and mass spectrometry [34] reveal that at room temperature binary mixtures of both ethanol and 1-propanol with water display a sharper concentration dependent structural transition close to $x_e \approx 0.2$ and $x_p \approx 0.1$ respectively. These sharper transition at lower molar fractions are attributed to larger hydrophobic group disturbing the tetrahedral-like structure of water more rapidly as the alcohol molar fraction increases [27].

In recent years, the behaviour of aqueous mixtures at hydrophobic solid interfaces has been a key topic due to the surge in graphite or graphene based nano-technology. Examples involving alcohol and water mixtures can be found in filtration [35], catalysis [36] and fuel cells [37] to name just a few. Applications involving solid-liquid interfaces are generally heavily reliant on the structure and dynamics of the liquid component within the couple of molecular layers adjacent to the solid. Liquid structure at the interface has been shown to affect the transport of charge [38] as well as the adsorption of molecules [39], both of which are essential to the function of nanoscale devices. Thus, there is an interest in obtaining molecular level details regarding the local structure of alcohol-water mixtures at hydrophobic interfaces.

The amphiphilicity of the alcohol molecules makes their concentration dependent behaviour at hydrophobic surfaces interesting due to the surface-liquid hydrophobic interactions. However, despite their common use, aqueous alcohol mixtures at hydrophobic interfaces remain a relatively unexplored area. Previous studies of these systems tend to focus on droplet behaviour such contact angles [40–42] or interfacial tension [43] and are limited in their molecular level insight. Studies into the molecular level behaviour of alcohol-water mixtures at interfaces have previously been limited to either the vapour-liquid interface [31, 44, 45] or alcohol-water mixtures under confinement [46–48]. This represents a serious limitation in our understanding because concentration dependent molecular scale structure of alcohol-water mixtures at hydrophobic interfaces, such as hydrophobic regions of ribonuclease [49], is reported to play a role in the stability of proteins [50] and is expected to influence

properties such as the dielectric constant of the interfacial liquid [51].

Regarding the self-assembled methanol-water structures central to this thesis, MD simulations have previously been used to gain insights into the spatial arrangements of the fully formed monolayers. This work is presented in ref. [52] and was summarised in Section 1.5.1. To recap, using MD simulations it was not possible to capture the nucleation and subsequent arrangement of the alcohol and water molecules into stable long-lived structures. This was true even when using custom parameters derived from *ab initio* density functional theory calculations. This is attributed to the experimentally observed long nucleation time associated with the formation of the structures (usually at least several minutes) compared with the time-scales computationally accessible with MD simulations (e.g. 100 ns in ref. [52]). However, in ref. [52] the authors observe that it was still possible to obtain insight into the hydrogen bonding behaviour of the methanol water mixture in its liquid phase at the interface with HOPG with the use of replica exchange MD coupled with geometry optimisation. Most notably, the authors found that at the HOPG interface, the hydrogen bonded networks of methanol and water had an increased preference to alternate molecules than in the bulk mixtures. Furthermore they found the system to be glassy with many local energy minima and further structural classification was need using a dimensionality reduction technique, details of which can be seen in ref. [53].

Due to the inaccessible nucleation times-scales, the presence of many structural local energy minima and the subsequent need for customised analysis techniques to obtain spatial details of the stable monolayer structure, the majority of this Chapter will instead focus on measurements of alcohol water mixtures in their mobile state, rather than their self-assembled state. However, as will be seen in Section 4.4, this approach will still provide valuable details regarding the subsequent self-assembled spatial arrangements which matches up well with experimental observations.

In this chapter I will investigate the concentration dependent structure of mixtures of short chain length alcohols (methanol, ethanol and 1-propanol) with water at the interface with hydrophobic highly orientated pyrolythic graphite (HOPG). This is achieved using molecular dynamics (MD) simulations of 18, 14 and 13 aqueous mixtures of methanol, ethanol and 1-propanol respectively at various concentrations. The composition of these simulation boxes can be seen in the methods section at the end of this Chapter. In addition, three-dimensional scanning force microscopy

(3D-SFM) is used to obtain an experimental molecular scale map of the density of a methanol-water mixture at the HOPG interface which matches the computational observations.

4.3 Results

In alcohol-water mixtures it is well known that the composition of the liquid at the surface is significantly different to that in the bulk, due to the hydrophobic forces between the alcohols and the surface [41, 52, 54]. To characterise the local composition of the alcohol-water mixtures at the hydrophobic interface, the time-averaged number density of the water oxygen (O_w) and the alcohol carbon closest to the hydroxyl group (C_m, C_e or C_p for methanol, ethanol or 1-propanol respectively) was plotted as a function of the distance from the top layer of the HOPG (d). An example of the C_m and O_w plot can be seen in Figure 4.1a for a bulk methanol molar fraction of 0.5, which shows two clear peaks for C_m. These two peaks correspond to regions of high density due to surface induced effects related to the discrete nature of the liquid molecules and hydrophobic attraction between the methanol and the surface [55, 56].

As evident from the molecular dynamics snapshot, the two peaks arise due to two molecular layers of alcohol. Molecules are defined as being at the surface in the simulations when they are within the region of first two alcohol molecular layers. For example, for methanol the surface molar fraction $x_m = N_m \,/\, (N_m + N_w)$, where N_m and N_w are the number of methanol and water molecules with $d < 0.9$ nm (as defined in Figure 4.1a). The same approach was used for ethanol and 1-propanol whose molecular layer definitions can be seen in Figure 4.1b and c. Using this protocol, the surface alcohol molar fraction as a function of the corresponding bulk alcohol molar fraction was plotted for the three alcohols of interest, methanol (Figure 4.1d), ethanol (Figure 4.1e) and 1-propanol (Figure 4.1f). Interestingly, the multiple peaks for the ethanol and 1-propanol carbon plots indicate multiple preferential configurations. This is likely due to geometric restrictions arising from the larger carbon backbones, which alters the number of possible atomic configurations and thus induces additional entropic effects (as discussed in Chapter 1). Furthermore, for ethanol, these preferential configurations induce a slight inflection point in the

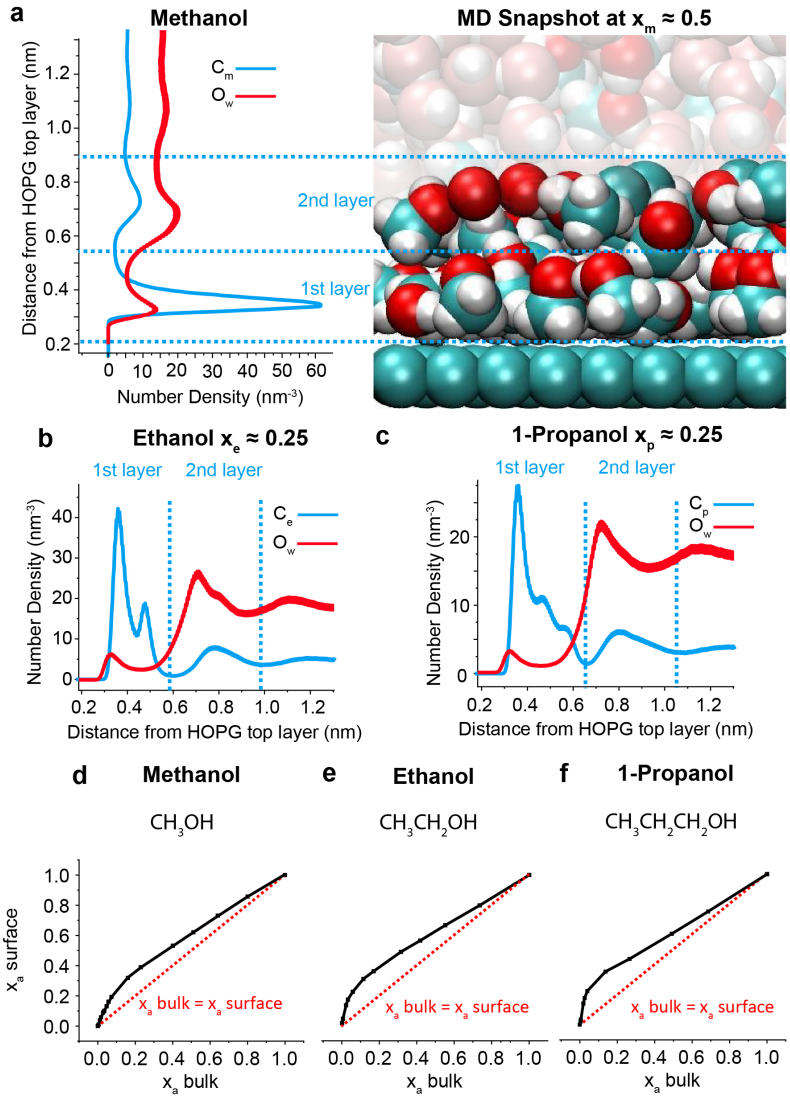

Fig. 4.1: Molecular layering of the alcohol molecules at the interface between HOPG and alcohol-water mixtures. In (a) a plot of the carbon number density and oxygen water density is shown as a function of the distance d from the top layer of HOPG for $x_m \approx 0.5$. Two maxima are visible for the carbon between 0.2 nm $< d <$ 0.52 nm and 0.52 nm $< d <$ 0.90 nm which correspond to the first two molecular layers of alcohol. These can be seen in the corresponding MD snapshot. (b-c) show the equivalent data for ethanol and 1-propanol, with the boundaries defined at 0.2 nm $< d <$ 0.59 nm and 0.59 nm $< d <$ 0.99 nm and 0.2 nm $< d <$ 0.64 nm and 0.64 nm $< d <$ 1.05 nm for the first and second layers of ethanol and 1-propanol respectively. (d-f) show how the surface molar fraction (defined as within the first two molecular layers shown in (a-c)) varies as a function of the bulk molar fraction for methanol (d), ethanol (e) and 1-propanol (f). In (d-f) x_a is the surface molar fraction of the alcohol under consideration.

second water solvation layer (Figure 4.1b). However, no such feature is seen for the 1-propanol case. This may be due to 1-propanol having more preferential configurations than ethanol, which in turn smooths out the water solvation peaks. Exper-

imental evidence of ethanol having more preferential configurations than methanol when self-assembled with water will be presented in Chapter 5.

The surface molar fraction deviates significantly from that of the bulk for all the alcohols. The largest deviation occurs at low molar-fractions and this deviation becomes more significant as the size of the hydrophobic group increases. To provide an accurate description of the molecular distribution local to the alcohol molecules at the hydrophobic interface, the remaining data presented will be plotted as a function of the surface molar fraction. Hereafter, the surface molar fraction will simply be referred to as x_a unless stated, where a represents the alcohol under consideration, e.g. x_m is the surface molar fraction of methanol to water. This also enables better comparisons with the concentration dependent bulk behaviour of alcohol-water mixtures.

4.3.1 Methanol

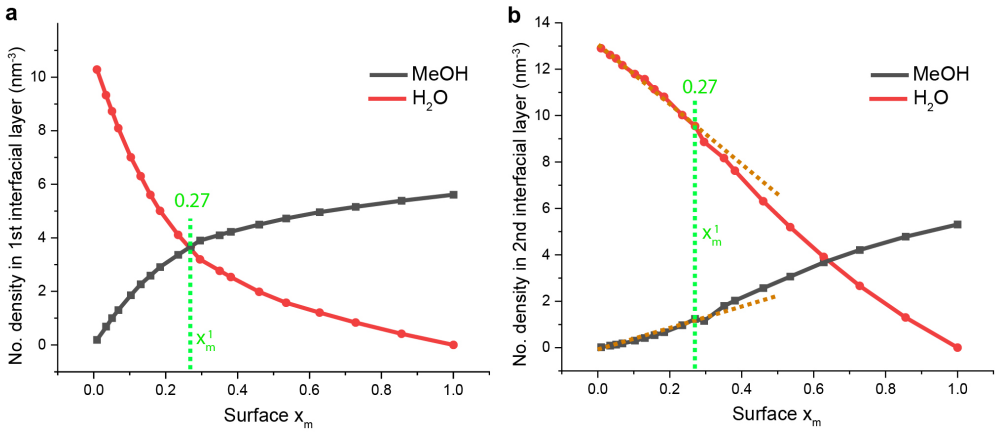

Fig. 4.2: Composition of the first two molecular layers in a methanol-water mixture at the interface with HOPG as a function of x_m. The number density of methanol (black) and water (red) molecules in the first (a) and second (b) molecular layer is shown. The molar fraction at which the number of methanol molecules surpasses the number of water molecules in the first layer is denoted by the green dashed line at $x_m = 0.27$, hereafter referred to as x_m^1. In (b), linear fits were applied to the data prior to this point and extrapolated to provide a visual aid of an inflection point.

When considering aqueous mixtures of alcohols at hydrophobic interfaces, the behaviour of the first couple of molecular layers is highly important because individual layers have significant structural differences depending on their proximity to the

interface [31, 46, 57]. For a methanol-water system on HOPG, the time-averaged composition of the first and second molecular layers (as defined in Figure 4.1a) as a function of x_m can be seen in Figure 4.2a and b respectively. These plots show that the local molecular composition is non-linear and highly concentration dependent. In the first molecular layer at low x_m the methanol demonstrates a strong ability to displace the water (Figure 4.2a). This is because of the hydrophobic attraction between the methanol and the surface. The rate of exchange of water and methanol subsequently decreases as x_m increases due to saturation effects. The molar ratio where the number of methanol molecules surpasses the number of water molecules in the first molecular layer occurs at $x_m \approx 0.27$ and is denoted by the green dashed line on Figure 4.2a. This value will hereafter be referred to as x_m^1. The composition of the second molecular layer exhibits a more linear behaviour as a function of x_m (Figure 4.2b) due to a reduction in the influence of the surface-induced hydrophobic attraction. However, there is an inflection point close to x_m^1, corresponding to a reduction in the number of water molecules and an increase in the number of methanol molecules, indicating a structural transition has occurred. The hydrophobic attraction to the surface induces local concentration gradients (Figure 4.2) which make defining boundaries for the potential transitions between the different concentration dependent regimes of the methanol difficult. Therefore values such as x_m^1 should only be regarded as guidelines.

To gain further insight into the concentration dependent interfacial structure of the methanol-water mixture, the time-averaged orientation of the methanol molecules within the first molecular layer was studied. Figure 4.3a shows a number density plot for the oxygen group of methanol (O_m) as a function of d. Here two clear maxima can be seen at values of $d = 0.35$ and 0.46 nm. As demonstrated by the corresponding MD snapshot, these peaks represent two preferential configurations for the methanol molecules; either with the alcohol lying flat and the oxygen group next to the surface (corresponding to an inclination to be involved in 1D/2D hydrogen-bonded networks parallel to the plane of surface) or the oxygen group facing away from the surface, indicating the methanol is upright (corresponding to an inclination to bond away from the surface).

The distribution of methanol molecules in the two configurations ($N_{upright}$ and N_{flat}) as a function of x_m can be seen in Figure 4.3b. To prevent methanol molecules in the second molecular layer influencing the result, molecules whose centre of mass is

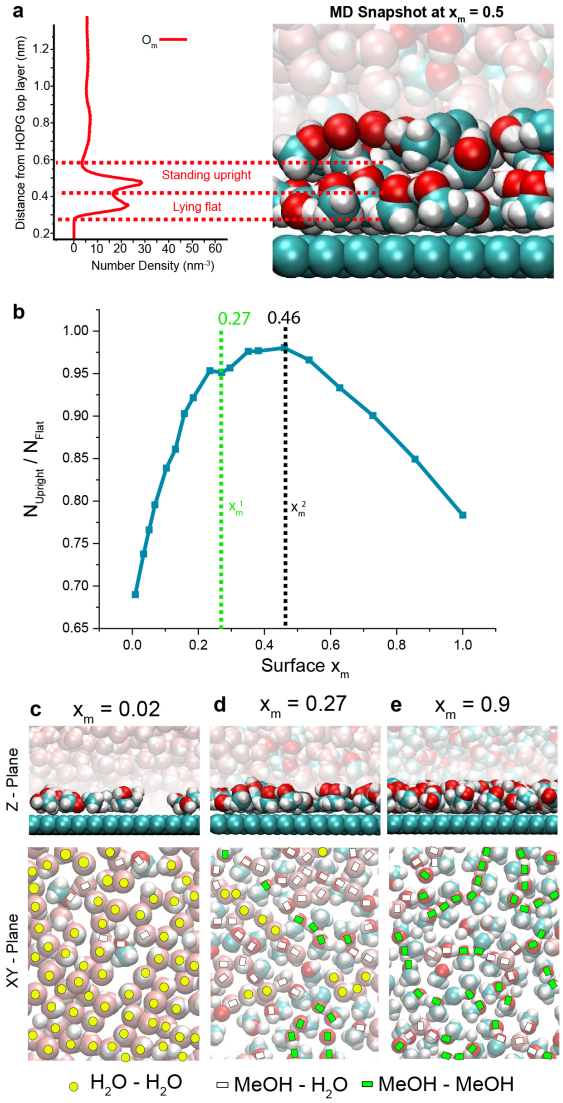

Fig. 4.3: The behaviour of methanol molecules at the interface with HOPG. In (a) an example number density plot for the oxygen group of methanol as a function d is shown for $x_m = 0.5$. Two clear maxima are visible between $0.2 < d < 0.402$ nm and $0.402 < \mathrm{d} < 0.6$ nm. These two maxima correspond to the methanol molecule either lying flat with its carbon-oxygen bond parallel to the surface, or standing upright, with its carbon-oxygen bond perpendicular to the surface. This can be seen in the corresponding MD snapshot. (b) shows the number of methanol molecules in the first molecular layer in the upright and flat configurations as a function of x_m. As was the case in Figure 4.2, x_m^1 is marked by the green dashed line. The black dashed line denotes the location where the $\mathrm{N}_{upright}/\mathrm{N}_{flat}$ begins decreasing. (c-e) shows MD snapshots in the z-plane and xy-plane at $x_m = 0.02$, 0.27 and 0.9 respectively. To provide a visual aid, the nature of the molecules hydrogen bonded to each individual molecule (obtained by visual inspection) is represented by either a yellow circle (water-water), a white rectangle (methanol-water) or a green rectangle (methanol-methanol).

further away than the position of the peak of the upright configuration in Figure 4.3a ($d = 0.46$ nm) were excluded from the analysis. Across all surface molar fractions

$N_{upright}/N_{flat} < 1$, which indicates a preference for the methanol to lie flat. This is different to the methanol-water liquid-vapour interface where the methanol C-O axis is reported to prefer to be orientated perpendicular to the interface [57].

As can be seen in Figure 4.3b, $N_{upright}/N_{flat}$ has a strong concentration dependence. At low methanol concentrations, $x_m < x_m^1$, increasing the amount of methanol increases $N_{upright}/N_{flat}$. Then for $0.27 < x_m < 0.46$ the rate of change decreases, before $x_m > 0.46$ where $N_{upright}/N_{flat}$ starts to decrease. $x_m = 0.46$ will hereafter be referred to as x_m^2. MD snapshots of the hydrogen bonded networks at the HOPG interface at $x_m = 0.02$, 0.27 and 0.9 indicate the low concentration region is dominated by the 3D tetrahedral network common to water molecular (Figure 4.3c) whereas in the methanol rich region 1D/2D chains of methanol dominate(Figure 4.3e). This suggests the orientation of the methanol molecules next to the interface is linked to the nature of the local hydrogen bonded networks forming both at the interface and in the immediate vicinity.

The amount of hydrogen bonding interactions between a methanol molecule in the first molecular layer and water or methanol molecules in the second molecular layer can be seen in Figure 4.4a. To hydrogen bond between the molecular layers, the C-O axis of the methanol molecules must be perpendicular to the interface, and thus the molecule must be in the upright configuration (defined in Figure 4.3). For $x_m < x_m^1$, the number of hydrogen bonds per molecule between methanol and either a water or another methanol in the second layer increases. This is despite the decreasing number of water molecules, which can form more hydrogen bonds. Then, for $x_m > x_m^1$, the average number of hydrogen bonds forming between methanol in the first layer and molecules in the second layer gradually begins to decrease. The 3D hydrogen bonded networks present in the bulk of methanol-water mixtures at low concentrations would favour the upright configuration. Thus, this decreasing region of the total number of interactions suggests the methanol molecules at the interface become less involved in the 3D hydrogen-bond networks away from the surface.

Figure 4.4b shows a similar plot for methanol molecules in the flat configuration (i.e. only involving hydrogen bonds parallel to the surface). In Figure 4.4b, for $x_m < x_m^2$, as x_m increase the total amount of in-plane hydrogen bonds the methanol decreases at a high rate due to methanol (who can only donate/accept 1 hydrogen bond) replacing water (who can donate/accept 2 hydrogen bonds). For $x_m > x_m^2$ the total number of hydrogen bonds per methanol molecule begins to plateau, indicating

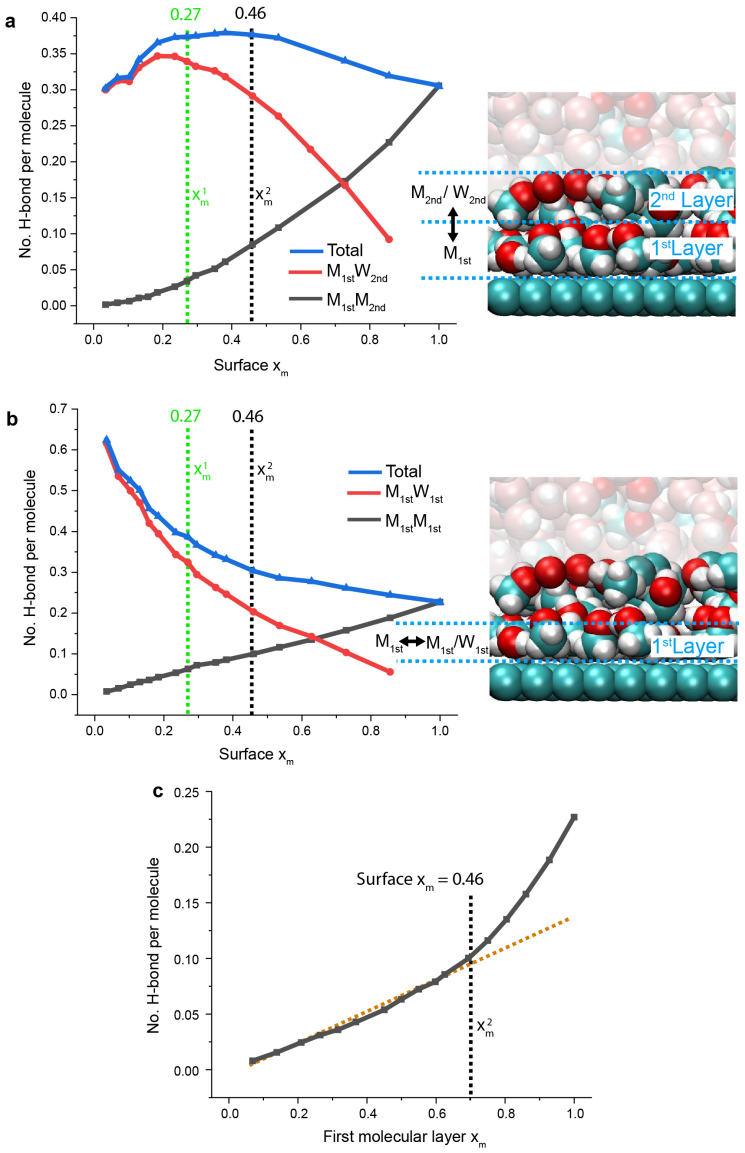

Fig. 4.4: Hydrogen bonding behaviour of methanol molecules at the interface with HOPG. The number of hydrogen bonds per molecule between a methanol molecule in the first molecular layer with either water of another methanol molecule in the second molecular layer (a) or with either a water or another methanol molecule in the first molecular layer (b) is plotted as a function of x_m. Then, (c) shows the number of hydrogen bonds per methanol molecule with other methanol molecules in the first molecular layer as a function of the methanol molar fraction of the first molecular layer, with the value corresponding a surface x_m^2 shown by the black dashed line. This coincides with a value of 0.7 on the x-axis. A linear fit has been applied for values of the first layer methanol molar fraction smaller than this value to provide a visual aid for an inflection point.

in this concentration regime the methanol molecules replace the water molecules at the surface without significantly decreasing the total amount of intermolecular hydrogen bonds. For this to occur, the structure at the interface must be dominated by 1D and 2D hydrogen bonded networks which only require one hydrogen-bond

donor/acceptor. The transition to methanol dominated 1D/2D hydrogen-bonded networks is supported by plotting the number of hydrogen bonds per methanol molecule with other molecules in the first molecular layer as a function of the molar fraction within the first molecular layer, Figure 4.4c. This produces an inflection point at $x_m \approx x_m^2$, after which an increase in the number of hydrogen bonds is observed. Interestingly, x_m^2 corresponds to a methanol molar fraction in the first molecular layer of 0.7, where the transition into 1D/2D methanol dominated hydrogen bonded networks occurs for bulk methanol-water mixtures[21, 22]. As was the case with x_m^1, while x_m^2 appears to effectively model a transition in the system behaviour, it should only be regarded as a guideline value.

Overall, using the information obtained from the preferential intermolecular interactions (Figure 4.4) along with the composition of the first two interfacial layers (Figure 4.2), a basic interpretation of the concentration dependent orientation of the methanol molecules at the interface with HOPG (Figure 4.3) can be formulated. At low molar fractions, the methanol rapidly displaces the water in the first molecular layer. Water can form more hydrogen bonds than methanol. Thus, as more water is displaced, the methanol becomes more inclined to have its C-O bond perpendicular to the surface, joining the water dominated 3D hydrogen-bond network. This is amplified by the increasing presence of other methanol molecules within the first interfacial layer, which are less favourable to bond with. This behaviour is consistent with previous studies regarding the interface between vapour and liquid, where a region of enhanced water density is observed just outside of a methanol rich region next to the interface [57].

Between $x_m^1 < x_m < x_m^2$ the system enters a transitional regime where the rate of change decreases. In this region, the behaviour of the mixture is complicated with a kink appearing near x_m^1. The physical cause of this kink is not entirely clear, although x_m^1 corresponds to the point where the number of methanol molecules first exceeds the number of water molecules, which may be significant. Furthermore, anomalous behaviour close to x_m^1 is also reported in other studies in the bulk [25, 58, 59] and has been attributed to the formation of percolation networks of both components [18]. The reason for the ratio of upright to flat methanol molecules remaining relatively constant within this region is also uncertain. One plausible explanation is that at this stage individual mixed 1D/2D hydrogen bonded chains start to form, but are too few and far between to link up and form extended hydrogen

bonded networks.

For $x_m > x_m^2$, the ratio of methanol becomes high enough to enable the formation of extended 1D/2D hydrogen bonded chains (exemplified in Figure 4.3e). At this point, the inclination to form 1D/2D structures, combined with the additional support provided by the 2D solid surface, gradually makes more methanol molecules become involved in 1D/2D networks and thus lie flat, so as to hydrogen-bond parallel to the surface, corresponding to a decrease in $N_{upright}/N_{flat}$.

4.3.2 Ethanol

Ethanol has the same number of hydrogen bonding sites as methanol with a larger hydrophobic region and thus experiences a greater hydrophobic attraction to HOPG and to the other ethanol molecules. Results obtained using the same analysis procedure and boundary definition for the methanol-water mixture can be seen in Figure 4.5 for an ethanol-water mixture. Generally, as the surface molar fractions of ethanol (x_e) increases, the ethanol molecules undergo a similar transition from flat to upright to that of methanol (Figure 4.5a). However, the larger hydrophobic group does induces behavioural changes. In contrast to methanol, $N_{upright}/N_{flat} > 1$ for all ethanol surface molar fractions, indicating a general preference for the hydroxyl group to face away from the hydrophobic interface. This may be due to steric restrictions imposed by ethanol's longer alkyl chain making forming hydrogen-bonds parallel to the surface more difficult.

The increased hydrophobic attraction due to this longer alkyl chain also shifts the transition point towards lower values of surface molar fractions when compared with methanol. The point where the number of ethanol molecules surpasses the number of water molecules in the first molecular layer occurs at $x_e = 0.2$ (hereafter referred to as x_e^1, Figure 4.5b).

At this value the number of additional ethanol molecules begins to plateau. Close to this transition point there is an inflection point in the number of each respective molecule in the second molecular layer (Figure 4.5c), corresponding to the ethanol molecules starting to fill up the second layer at an increased rate. As was the case with methanol, the transition point between the most common molecules in the first layer marks a kink in the plot of $N_{upright}/N_{flat}$ as a function of x_e. Significant

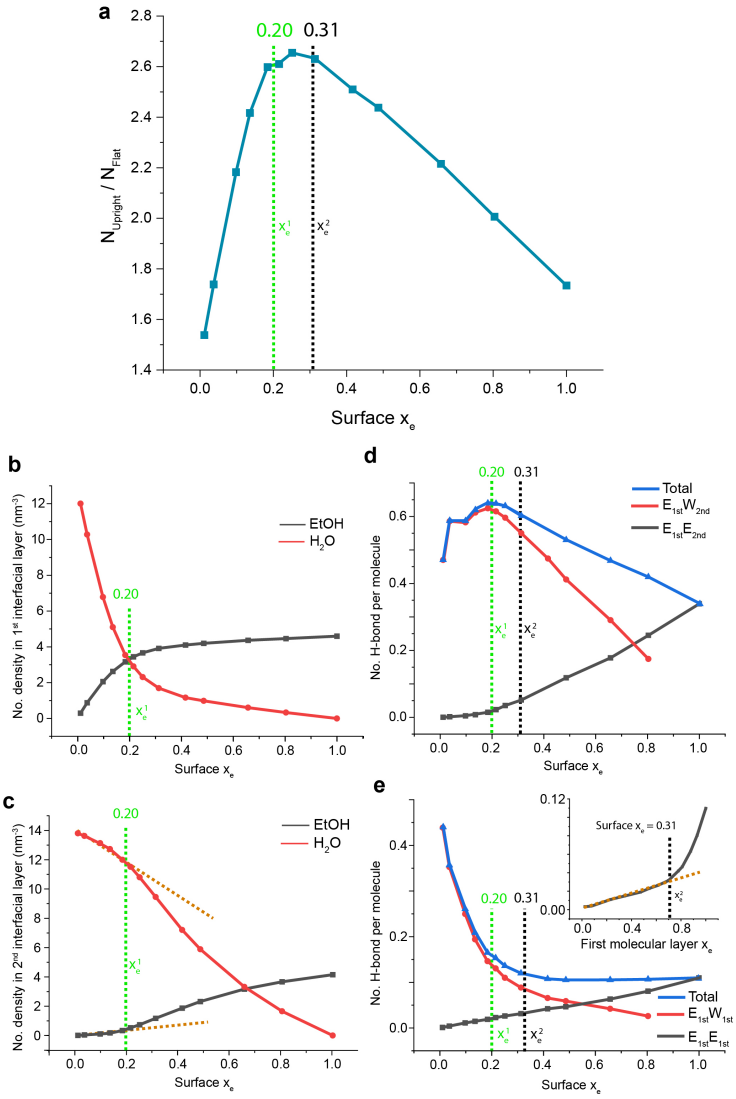

Fig. 4.5: The behaviour of ethanol-water mixtures at the interface with HOPG as a function of x_e. In (a) the number of ethanol molecules in the flat and upright configurations is shown, as defined in Figure 4.3. (b-c) show the molecular composition of the first and second molecular layers, as defined in Figure 4.1. For visual aid, a linear fit has been applied in (c) for all the points with $x_e < 0.2$ and extrapolated afterwards. (d-e) show the average number of hydrogen bonds experienced by the ethanol molecule in the first molecule layer using the same definitions outlined in Figure 4.4. The inset of (e) shows the number of hydrogen bonds per molecule as a function of the ethanol molar fraction in the first molecular layer. As was the case in Figures 4.1, 4.2 and 4.3, the green line denotes the value of x_e the number of ethanol molecules surpasses the number of water molecules in the first molecular layer (x_e^1) and the black dashed line denotes the x_e where the inflection point is observed in the inset of (e) (x_e^2).

changes in the properties and structure in bulk ethanol-water mixtures have been reported to occur at $x_e = 0.2$ [21, 34, 60, 61]. Furthermore, in the bulk $x_e = 0.2$ is the value where there is the optimum number of water molecules to solvate each

ethanol molecule, and corresponds to a minimum in the mobility of the ethanol molecules [62]. This offers a possible explanation for the anomalous behaviour.

The transition to a decrease in $N_{upright}/N_{flat}$ occurs at $x_e \approx 0.31$ (hereafter referred to as x_e^2). Interestingly, prior to this value, increasing the molecular fraction of ethanol to water also increases the hydration of ethanol in the upright configuration (Figure 4.5d). This is consistent with the concept of the alcohol molecules preferring to hydrogen bond with the water molecules that they have been displacing from the interface. After x_e^2, total amount of hydrogen bonds experienced by flat ethanol molecules plateaus, indicating a transition involving an increase in the formation of 1D/2D alcohol dominated networks. As was the case with methanol, this transition is accompanied by an increase in the number of alcohol-alcohol hydrogen bonds between flat molecules (inset, Figure 4.5e), indicating a propensity for 1D/2D hydrogen bonded networks. In the bulk it has been reported that at high ethanol concentrations the majority of the hydrogen bonding networks involving the ethanol are linear [63], suggesting the 1D hydrogen-bonded chains previously discussed must dominate the molecular arrangements next to HOPG surface. Furthermore, x_e^2 also corresponds to an ethanol molar fraction in the first molecular layer of ≈ 0.7, where transitions to chain-like structures for ethanol have been reported [62].

It is interesting to note that the flatter region of $N_{upright}/N_{flat}$ around $x_e^1 < x_e < x_e^2$ is smaller for ethanol than it was for methanol next to the surface. This may be attributed to the methanol clusters ability to accommodate a large amount of water molecules, which leads to a more moderate change from the tetrahedral-like structure of water to the chain-like structure of methanol as the methanol concentration increases. This is also consistent with previous observations of sharper concentration dependent transitions in ethanol-water mixtures in the bulk when compared with methanol water mixtures [21, 34]. Furthermore, the carbon chains of linear alkanes and alcohols prefer to lie parallel to the HOPG interface due to similarities between the C-C bond lengths of the backbone and the periodicity of the surface lattice [64]. This will induce additional steric effects for the ethanol compared with methanol due to the longer carbon backbone. The shorter transition region is thus likely due to a combination of ethanol's greater water exclusion ability and the greater steric effects it experiences.

4.3.3 1-Propanol

The larger hydrophobic carbon backbone on 1-propanol is reported to disrupt the tetrahedral-like structure of the water more rapidly than methanol and ethanol with increasing alcohol concentration [27]. Thus, at the interface between mixtures of 1-propanol and water and HOPG, there is a sharper concentration dependent transition, Figure 4.6a. As was the case with methanol and ethanol, in Figure 4.6a the two boundaries marked correspond to the transition between the most common molecule in the first molecular layer ($x_p = 0.17 = x_p^1$, Figure 4.6b) and the location of the inflection point corresponding to an increase in the number of alcohol-alcohol interactions between flat 1-propanol molecules ($x_p = 0.27 = x_p^2$, Figure 4.6e inset). Both boundaries are again lower than the case for ethanol-water mixtures and methanol-water mixtures. However they no longer accurately define notable points on the curve. This indicates that the steric effects and increased hydrophobic attraction associated with the larger carbon chain makes the description formulated for the methanol-water system less applicable. Nonetheless, the general trend observed in Figure 4.6a remains very similar to that of the aqueous methanol and ethanol mixtures.

A behaviour comparable to the smaller alcohols continues with the filling of the first two molecular layers (Figure 4.6b-c), where it is clear that at concentrations slightly higher than x_p^1, the first molecular layer begins to saturate with 1-propanol. This causes the inflection point in the number of both types of molecules in the second molecular layer as a function of x_p. Furthermore, like the ethanol-water mixture, for $x_p < x_p^2$ there is an increase in the number of hydrogen bonds between the 1-propanol molecules in the upright configuration in the first molecular layer and the water molecules above them (Figure 4.6d). As was the case with the aqueous methanol and ethanol mixtures, after this transition point the total number of hydrogen bonds between 1-propanol molecules in the flat configuration and other 1-propanol or water molecules remains relatively constant as x_p increases. However, unlike the ethanol-water mixture, it does exhibit a small increase as as x_p increases, indicating that increasing the molar fraction of 1-propanol molecules allows the formation of more hydrogen bonds parallel to the surface. This is potentially due to more efficient packing of the carbon chains resulting from to increased intermolecular van der Waals interactions. The inflection point x_p^2 in Figure 4.6e occurs at a

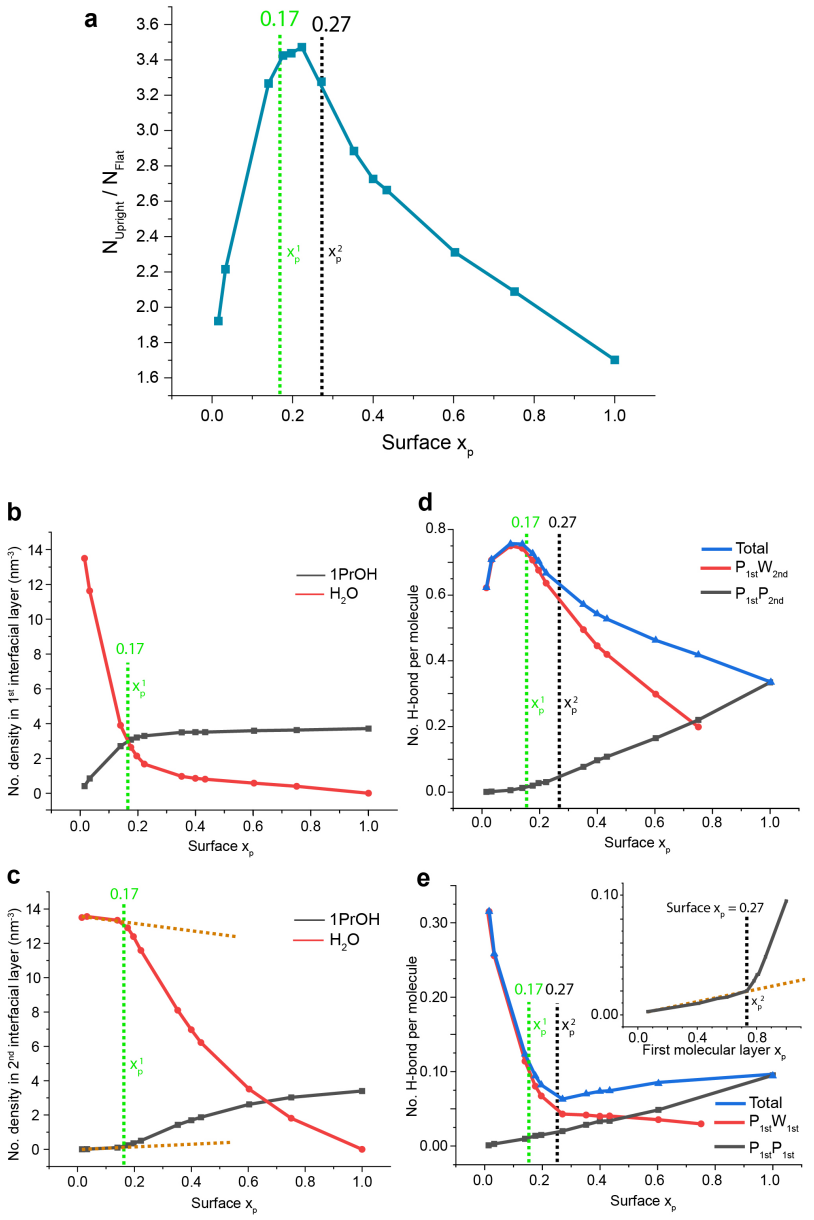

Fig. 4.6: The behaviour of 1-propanol-water mixtures at the interface with HOPG as a function of the x_p. (a) Shows the variance of the number of 1-propanol molecules in the flat and upright configurations, as defined in Figure 4.2 (b-c) shows the molecular composition of the first and second molecular layers, as defined in Figure 4.1. For visual aid, a linear fit has been applied in (c) for all the points with $x_p < 0.2$ and extrapolated afterwards. (d-e) show the average number of hydrogen bonds experienced by the 1-propanol molecule in the first molecule layer using the same definitions outlined in Figure 4.4 and 4.5. The inset of (e) shows the number of hydrogen bonds per molecule as a function of the 1-propanol molar fraction in the first molecular layer. As was the case in Figures 4.2, 4.3 and 4.5, the green line denotes the surface molar fraction where more 1-propanol molecules are present in the first molecular layer than water molecules (x_p^1) and the black dashed line denotes the x_p=x_p^2 where the inflection point is observed in the inset of (e).

1-propanol molar fraction in the first molecular layer ≈ 0.73, close to the molar fraction reported in bulk 1-propanol-water mixtures where 1-propanol hydrogen-bonded chains dominate [27].

4.3.4 *Experimental observation of concentration dependant interfacial structure*

The computational results demonstrate the interfacial structure of the alcohol-water mixtures at the HOPG interface has a clear concentration dependence. Experimentally, small alcohols evaporate at high rates in ambient conditions. Due to this high volatility, one should expect to be able to experimentally observe the effect of the concentration dependant structures reported here for a binary alcohol-water mixture over the time-scale of minutes. To test this, three-dimensional scanning force microscopy (3D-SFM) was used. 3D-SFM enables precise 3-dimensional mapping of the liquid density near the interface [65–67] using individual frequency shift profiles (corresponding to force [68]) as a function of the distance from the interface (as described in detail in Chapter 2).

A 200 µL droplet consisting of a methanol-water mixture with a surface $x_m \approx x_m^1$ (the location of the peak of $N_{upright}/N_{flat}$ in Figure 4.3) was deposited freshly cleaved HOPG. The droplet was then left to evaporate freely while the 3D-SFM measurement took place. Methanol evaporates quicker than water [69, 70] leading to a decrease of x_m with time. Over a period of 4 minutes, 16640 consecutive frequency profiles were acquired at the interface, the results of which can be seen in Figure 4.7a-b. From these frequency profiles, the position of the maxima and minima were tracked using an automated Gaussian fitting procedure (see methods section at the end of this chapter). This allows the evolution of the profiles to be observed over time, revealing a decrease in the distance between the peaks. This supports the theoretical prediction.

The magnitude of the change observed over 4 minutes is 0.07 nm. The peaks in Figure 4.7a-b correspond to regions where the force required to displace the liquid (which is linked to the liquid properties such as its density, viscosity and structure) is at a maximum. Modelling this spatial force distribution using MD is not trivial due to tip-effects. Instead, the peaks were compared with plots of atomic number

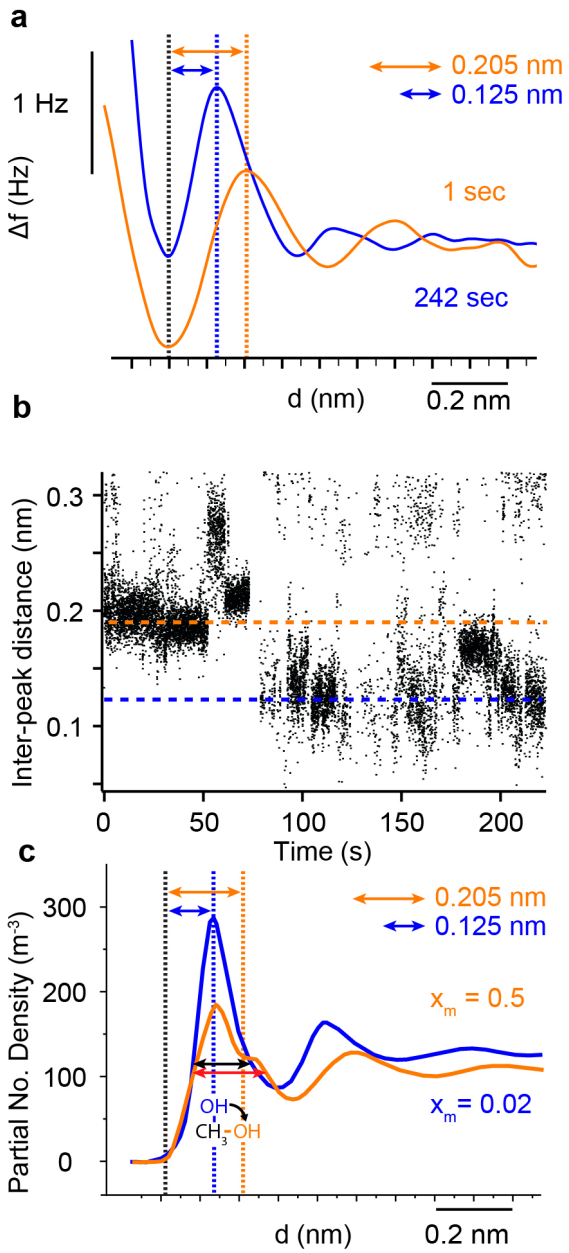

Fig. 4.7: 3D-SFM measurements corresponding to the the liquid density (as discussed in Section 2.2.6) of a methanol-water mixture at the interface with HOPG. In (a) two example frequency shift curves can be seen corresponding to t = 1s (orange) and 242s (blue). Over this time period, the position of the first density peak has shifted (yellow dashed line to blue dashed line). (b) shows the full set of data points corresponding to the inter-peak distances as a function of time, with the yellow and blue dashed lines corresponding to the same positions presented in (a). (c) MD simulations of two different concentrations ($x_m = 0.5$ and $x_m = 0.02$) show a comparable shift in the peaks of number density plots for all liquid atoms. In (c) the yellow and blue dashed lines correspond to the same location as (a-b). The decreasing width of the peak (represented by the black and red arrows) is due to the methanol molecules transition to lying parallel to the interface, as previously discussed. An illustration of a methanol molecule in the two configurations is shown to provide visual assistance.

density from the MD simulations for $x_m = 0.5$ and $x_m = 0.02$ (Figure 4.7c). In Figure 4.7c, the location of the two peaks from Figure 4.7a-b are superimposed, demonstrating that the experimentally observed shift is comparable to the shift in the middle of number density peaks. The broadening of the number density peaks is a result of the methanol molecules transition between being flat and standing upright, indicating this is likely the cause of the experimentally observed shift. However, the full set of peak positions presented in Figure 4.7b suggest that experimentally, the transition occurs as a jump, rather than the gradual change predicted by the simulations (Figure 4.3a). This inconsistency in the time-scale is likely due to confinement effects imposed by the AFM tip. Furthermore, the interpretation of the experimental results still generally require caution due to other potential effects at play, such as the tip experiencing physical and chemical changes, as discussed in Chapter 2. This result could nonetheless help rationalise the fact that experiments involving solvophobic interfaces are considerably more difficult to reproduce than those at solvophilic interfaces where water always dominates the measured solvation forces [71, 72].

4.4 Discussion

The molecular explanation for the concentration-dependent behaviour of the methanol in methanol-water mixtures at hydrophobic interfaces generally also applied to the alcohol molecule in both the aqueous ethanol and 1-propanol mixtures. The low concentrations regimes are dominated by the alcohols preference to be involved in the 3D tetrahedral hydrogen-bonded networks characteristic of the water molecules, which are more populous away from the hydrophobic surface. The increasing hydration of the upright alcohol molecules at low alcohol concentrations despite the ratio of water decreasing supports this concept (Figures 4.4a, 4.5e and 4.6e). There is then a transitional region, which covers a smaller alcohol molar fraction as the alcohol hydrophobic group gets larger, due to a greater ability to disrupt the water-induced hydrogen-bond structure. The final regime is then dominated by 2D alcohol hydrogen-bonded arrangements and the lateral layering of 1D hydrogen-bonded chains lying largely parallel to the solid interface, a configuration commonly reported for the pure alcohols on HOPG [73, 74].

As can be seen in Figure 4.6, the method for marking the boundaries used for methanol and ethanol are not wholly sufficient for 1-propanol. This may be in part explained by comparisons with a previous X-ray scattering study [27], where it was shown that the enthalpy of mixing for both bulk methanol-water and ethanol-water mixtures remains negative for all molar fractions, however for 1-propanol it becomes positive for molar fractions > 0.34. This was attributed to the hydrophobic group on 1-propanol being large enough that the enthalpic gain for hydrogen-bonding between the alcohol molecules being insufficient to cancel the enthalpic loss associated with the disruption of the water structure [27]. Thus the break-down of our methanol-based description, which fitted ethanol, may be due these increased hydrophobic effects for 1-propanol. Furthermore, larger alcohols such as 1-propanol will generally have larger steric effects which methanol does not suffer from. This will include the carbon backbone belonging to one alcohol molecule being long enough to span and influence multiple interfacial molecular layers.

While the fundamental concentration dependent structures of the alcohol-water mixtures at the HOPG interface have similarities to that of the bulk mixtures, the presence of the surface has a clear impact. The hydrophobic attraction with the surface induces local concentration variations which depend on the distance from the surface. This impacts the molar fraction at which the transitions occur. The transition point corresponding to a shift away from involvement in 3D hydrogen-bonded networks close to the interface occurs at a comparable values for methanol ($x_m = 0.3$ in bulk and $x_m^1 \approx 0.27$ at the surface) and ethanol ($x_e = 0.2$ in bulk and $x_e^1 \approx 0.2$ at the surface). However the deviation becomes larger for 1-propanol ($x_p = 0.1$ in bulk and $x_p^1 \approx 0.17$ at the surface), indicating the hydrophobic effects are becoming significant. The transition point denoting the start of a regime dominated by the 1D/2D alcohol hydrogen bonded networks occurs at a significantly lower value than in the bulk ($x_m = 0.7$ in bulk and $x_m^1 \approx 0.46$ at the surface for methanol and $x_e = 0.7$ in bulk and $x_e^1 \approx 0.31$ for ethanol). Interestingly, a surface x_m^1 also corresponds to molar fraction of 0.7 within the first molecular layer, and thus this value seems reasonable considering the 1D/2D nature of the hydrogen-bonded networks and the confinement effects of the surface. As was the case with the first transition point, for 1-propanol the most significant deviation from the bulk values is also observed (first layer $x_p = 0.73$ compared with $x_p = 0.70$ in bulk).

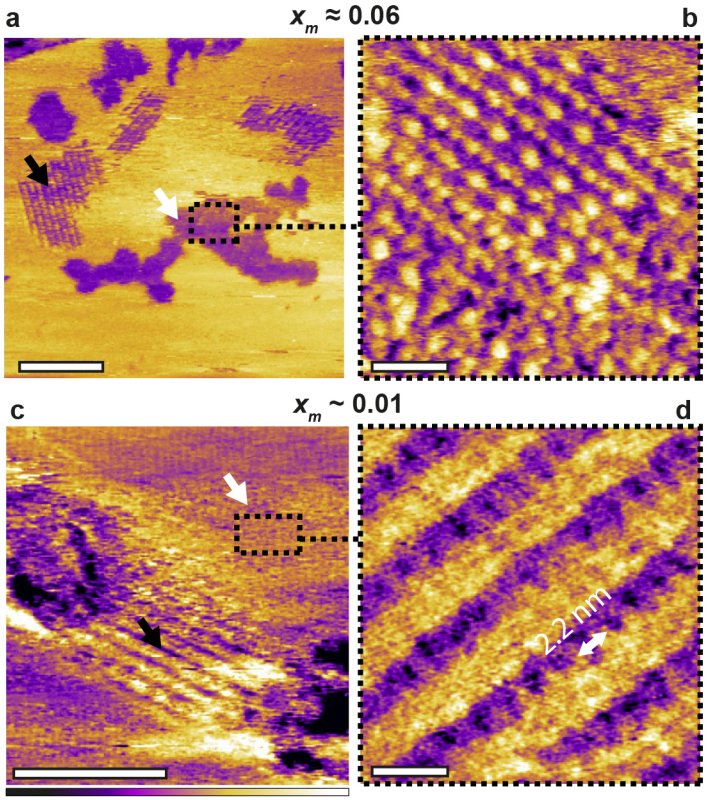

Fig. 4.8: (a) shows the surface of HOPG in a methanol-water mixture with $x_m \approx 0.06$. Here two domain types are visible as denoted by the black and white arrows. The structures denoted by the black arrows have the same properties as the rows formed in e.g. a $x_m = 0.5$ mixture (see Chapter 1). (b) High resolution images of the newly observed features demonstrate they have a different morphology with a complex 2D pattern. (c-d) show similar results for a mixture with $x_m \sim 0.01$ where two domains have formed with significantly different row-periodicities. As was the case for the $x_m \approx 0.06$ mixture, these new structures (white arrow) co-exist alongside the larger row features (black arrow). The scale bars are 50 nm in (a) and (c) and 2.5 nm in (b) and (d). The purple scale bar represents a height variation of 2 nm in (a) and 0.8 nm in (b-d).

The reduced dimensionality imposed by the surface also allows the hydrogen bonded networks present in the bulk of the mixture to induce a concentration dependent anisotropy in the alcohol molecules. This last aspect is key because molecular arrangement at the interface has been shown to be highly influential [38, 39]. These results may also offer explanations for observations related to the self-assembly of water and methanol molecules at hydrophobic interfaces central to this thesis. For these assemblies, a degree of concentration dependence exists. Methanol-water assemblies formed at high methanol concentrations (bulk $x_m \sim 0.5$) exist as monolayers with very linear features (see Chapter 1). However, at lower methanol concentrations (bulk $x_m \approx 0.06$), structures which exhibit tetrahedral-like features can co-

exist alongside the linear monolayers (Figure 4.8a and b) [52]. As will be shown in Chapter 5, these low concentration structures show a greater propensity for forming hydrogen-bonds pointing away from the surface compared to the monolayers characteristic of higher methanol concentrations. Furthermore, lowering the methanol concentration further to $x_m \sim 0.01$ causes a re-emergence of highly linear features (Figure 4.8c and d). An exact comparison between the values of the bulk x_m and surface x_m in experiments is difficult due to the methanol evaporation, as discussed in the previous section. However, there remains clear parallels between the general trends observed in the preferential orientation of the methanol at the interface, and the type of self-assembled structure produced.

Regarding the spatial organisation of the liquid molecules when at the interface, the hydrogen bond analysis performed in this Chapter builds upon MD simulations of methanol-water mixtures in ref. [52] (presented in Chapter 1 and mentioned in the introduction to this Chapter). In this work the authors observed that for an equal parts mixture ($x_m = 0.5$) the preferential lateral arrangement of methanol and water molecules at the interface was for them to alternate. This is consistent with the preferential hydrogen bond data presented Figure 4.4b, where for $x_m = 0.5$ the methanol molecule is almost twice as likely to form an in-plane hydrogen bond with a water molecule than another methanol molecule. As can be seen in Figure 4.4b, this changes for $x_m > 0.65$ where methanol-methanol hydrogen bonds become more probable. Experimentally it is difficult to perform measurements for $x_m > 0.65$ due to alcohol evaporation. However, this observation does suggest that working at high methanol concentrations (potentially facilitated by using low temperatures) may reveal new methanol-water self-assembled arrangements. Furthermore, in this work the self-assembled structures of aqueous ethanol and 1-propanol mixtures have only been studied for one or two different concentrations (presented in Chapter 5). The difference between the lateral hydrogen bonding behaviour for different concentrations of aqueous ethanol and 1-propanol mixtures (Figures 4.5e and 4.6e) compared with aqueous methanol mixtures (Figure 4.4b) indicates that changing the ethanol and 1-propanol concentrations may be an interesting area to experimentally explore in future work, especially considering the evidence of multiple preferential arrangements for ethanol in Figure 4.1b.

It is interesting to note that Figure 4.4b demonstrates that the relationship between the in-plane hydrogen bonding partners of a methanol molecule with x_m is non-

linear. This may in-part explain why, experimentally, it has not been possible to observe changes in the morphology of the self-assembled methanol-water structures when small concentration variations are made [52] (as opposed to large concentration variations such as that presented in Figure 4.8).

One final implication of the concentration dependent alcohol orientation is that it may also influence its molecular exchange at the interface. At lower concentrations, when the alcohol is preferentially hydrogen-bonding with the bulk liquid, its involvement with the bulk liquid may allow it to be displaced from the interface more easily. This would in principle reduce its residence time at the interface, which may impact both the mechanism of the self-assembly as well other aforementioned interfacial processes.

4.5 Conclusion

This chapter has studied the molecular level behaviour of three alcohols with increasingly large hydrophobic chains when mixed with water at the interface with HOPG. The local structure show a strong concentration dependence, which is linked to the nature of the hydrogen-bonded networks formed at the interface. It has been possible to generate a general description for the nature of the interfacial hydrogen-bonded networks and to approximately mark molar fractions where transitions between different regimes occur. In the low concentration regime, increasing the amount of alcohol increases the alcohol molecules preference to form hydrogen bonds away from the surface, until there is enough alcohol at the interface for the formation of extended 1D/2D hydrogen bonded networks. After this point, the alcohols prefer to lie flat with the hydrogen-bonds forming parallel to the surface. Increasing the length of the hydrophobic alkyl chain (by using aqueous ethanol and 1-propanol mixtures) introduces additional steric and hydrophobic interactions, rendering a simple description more challenging. Nonetheless, generally, the reduced configurational entropy imposed by the interface and the presence of hydrophobic interactions induce a concentration-dependent anisotropy in the alcohol molecules. Experimentally, the impact of this concentration dependence can be observed through both the density of the interfacial mixture and the morphology of the self-assembled methanol-water structures. Furthermore, the results presented for ethanol and 1-propanol mixtures

indicate that further structural changes may be observed should their respective concentrations be varied, a task beyond this current work. It is expected that this concentration dependant behaviour will also apply at other hydrophobic interfaces. Examples include large hydrophobic groups found on biomolecules and hydrophobic surfaces, such as those used in the drying of droplets.

4.6 Methods

Atomic force microscopy

The image taken in Figure 4.8 was using AM-AFM mode. The temperature was 25^{o}C. No temperature control was possible using the 3D-SFM system and thus the sample was at room temperature. For full details regarding both AM-AFM and 3D-SFM, the reader is referred to Chapter 2.

The automated Gaussian fitting procedure was performed by K. Voïtchovsky. The basics of the procedure were as follows: Each frequency shift curve was divided into intervals, each encompassing a different maximum/minimum throughout the whole set of data. Then each interval is fitted with a Gaussian to determine the actual position of the extremum. The error associated with each fit is taken as half the full width at half maximum (FWHM) of the Gaussian. Due to noise in the curves, not all fits converged properly or gave meaningful results. If the fit did not converge, or the results are unphysical (e.g. a minimum found instead of an expected maximum, FWHM too narrow or too wide) the result is rejected and ignored. The key aspect of the procedure is to determine an interval as broad as possible for a given extremum, so that all the frequency shift curves are included despite a potential shift in the location of this extremum. However, a too large interval would include several extrema which would make the fit unreliable.

Molecular dynamics simulations

The liquid boxes of varying alcohol/water concentrations were allowed to equilibrate without HOPG for 1 ns in an NPT ensemble before being placed between two slabs of 7 graphite layers (a configuration previously successfully used in ref. [52]). Periodic boundary conditions were used, with a 10 nm vacuum region inserted between the periodic images of the graphite layers to ensure no artefacts occurred due to long

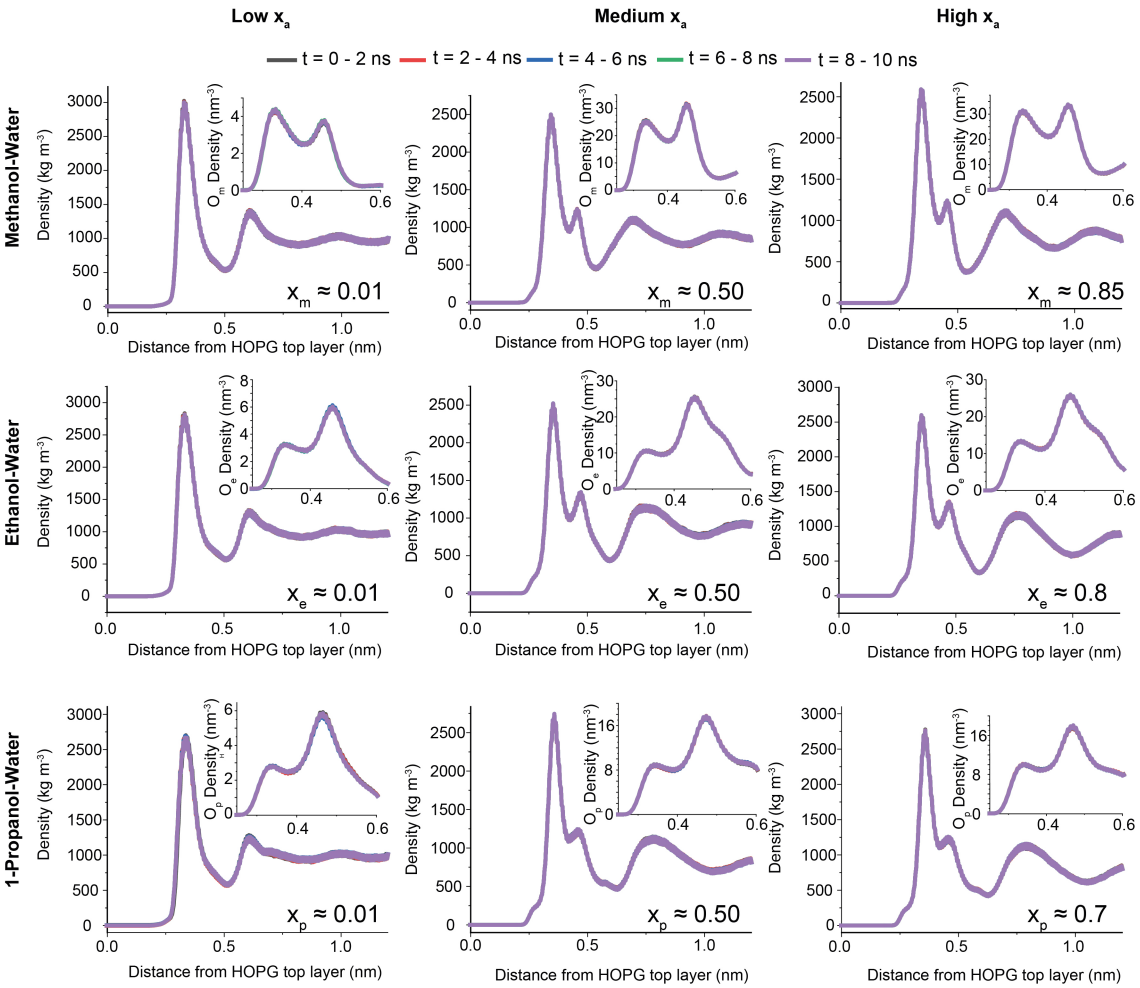

Fig. 4.9: Plots demonstrating convergence in the MD simulations. The graphs correspond to 3 different concentrations of the methanol-water, ethanol-water and 1-propanol-water mixtures studied in this work. For each of these cases both the average linear density of the liquid, and the O_a number density (such as was shown in Figure 4.3a), over 5 subsequent 2 ns periods (starting from the end of the equilibration period) is superimposed. As can be seen from these graphs, the average linear density, and the oxygen distribution, does not change with time indicating the system has successfully converged.

range interactions between liquid molecules across the graphite layers [75]. However, it is noted that this vacuum may not be required due to the choice of cut-off scheme for long ranged electrostatics (discussed in Chapter 2). There were no covalent bonds across the period boundary for the graphite layers and the graphite atoms were not allowed to move during the simulation (achieved using the freeze setting in GROMACS [76]). It is not recommended to combine frozen atoms with pressure-coupling, due to frozen co-ordinates being unaffected by pressure scaling [77]. Therefore the next equilibration step was a further 10 ns in a NVT ensemble

(i.e. no pressure coupling). The data was then taken over the next 50 ns using the same settings as the previous equilibration step. Proof of system convergence can be seen in Figure 4.9.

Using a NVT ensemble requires the graphite layers to be manually positioned at the top and bottom of the liquid box. This introduces a potential inaccuracy in the liquid density. Plots of the change of liquid density ($\Delta\rho$) between the bulk liquid simulation (ρ_{liquid}) and the simulation with the graphite layer ($\rho_{confined}$), where:

$$\Delta\rho = \frac{\rho_{liquid} - \rho_{confined}}{\rho_{liquid}} \tag{4.1}$$

can be seen in Figure 4.10 for all the simulation boxes used. As can be seen from this figure, the change in density due to this method is generally low and shows little correlation with the concentration dependent behaviour observed in this Chapter. However, the change in liquid density does exhibit an increase at high alcohol concentrations, which is amplified as the alcohol size increases. This is likely due to a combination of the overall density of the liquid decreasing, as well as the difficulties arising from larger alcohol backbones extending across periodic boundaries. Therefore for future studies, especially those using high alcohol concentrations or larger alcohols, the simulations may be improved by introducing semi-isotropic pressure coupling with the graphite layers fixed in the center of the simulation box. The time-step used was 2 fs and thus all bonds were constrained using the Linear Constraint Solver (LINCS) algorithm [78]. All analysis was performed using tools included in the GROMACS package [76]. The temperature of the system was 300 K and the pressure was 1 bar when applicable. Further details regarding the simulations are provided in Chapter 2.

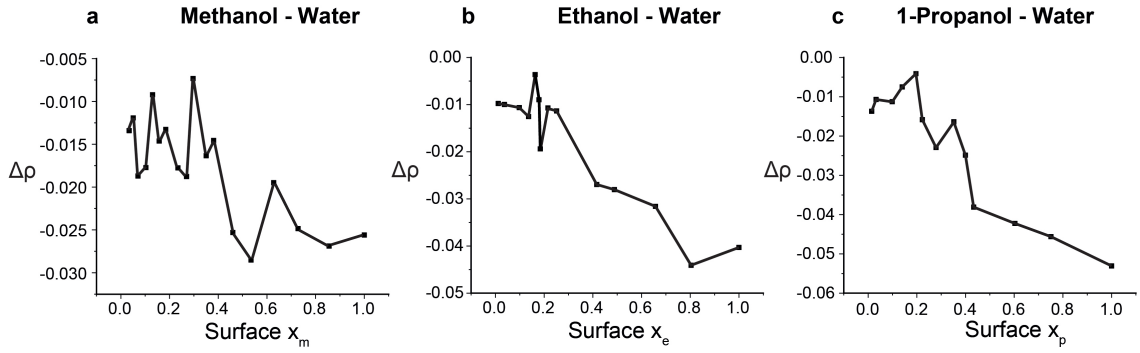

Fig. 4.10: Plots of the change in density, $\Delta\rho$, as a function of the surface molar fraction for the methanol-water (a), ethanol-water (b) and 1-propanol-water (c) systems studied in this chapter.

Composition of simulation boxes The compositions of the simulation boxes were chosen based on an increasing alcohol volume fraction, so as to offer a better comparison with the experimental systems studied in Chapter 5. However, for comparison with literature in this Chapter, the corresponding molar fraction is used. The composition of the methanol, ethanol and 1-propanol mixtures with water can be seen in Tables 4.1, 4.2 and 4.3 respectively.

MeOH Vol. Frac.	No. MeOH Mols.	No. H_2O Mols.	MeOH Mol. Frac.
0.0250	125	10935	0.0113
0.0375	188	10794	0.0171
0.0500	251	10654	0.0230
0.0750	376	10374	0.0350
0.1000	501	10094	0.0473
0.1250	601	9869	0.0574
0.1500	752	9533	0.0731
0.2000	1002	8972	0.1005
0.2500	1253	8411	0.1296
0.3000	1503	7851	0.1607
0.3500	1754	7290	0.1939
0.4000	2004	6729	0.2295
0.5000	2505	5608	0.3088
0.6000	3006	4486	0.4012
0.7000	3507	3365	0.5104
0.8000	4008	2243	0.6412
0.9000	4509	1122	0.8008
1.0000	5010	0	1

Tab. 4.1: Composition of the methanol-water simulation boxes studied in this chapter.

EtOH Vol. Frac.	No. EtOH Mols.	No. H_2O Mols.	EtOH Mol. Frac.
0.0100	35	11088	0.0031
0.0250	87	10920	0.0079
0.0500	173	10640	0.0160
0.0750	260	10360	0.0245
0.1000	347	10080	0.0333
0.1250	416	9856	0.0405
0.1500	520	9520	0.0518
0.2000	694	8960	0.0718
0.3000	1040	7840	0.1171
0.5000	1734	5600	0.2364
0.6000	2081	4480	0.3171
0.8000	2774	2240	0.5533
0.9000	3121	1120	0.7359
1.0000	3468	0	1

Tab. 4.2: Composition of the ethanol-water simulation boxes studied in this chapter.

1PrOH Vol. Frac.	No. 1PrOH Mols.	No. H_2O Mols.	1PrOH Mol. Frac.
0.0100	27	11088	0.0031
0.0250	68	10920	0.0079
0.0750	203	10360	0.0245
0.1000	270	10080	0.0333
0.1250	324	9856	0.0405
0.1500	405	9520	0.0518
0.2000	541	8960	0.0718
0.4000	1081	6720	0.1171
0.5000	1352	5600	0.2364
0.6000	1622	4480	0.3171
0.8000	2162	2240	0.5533
0.9000	2433	1120	0.7359
1.0000	2703	0	1

Tab. 4.3: Composition of the 1-propanol-water simulation boxes studied in this chapter.

References: Chapter 4

[1] X. Jiang, Y. Wang, M. Li, "Selecting water-alcohol mixed solvent for synthesis of polydopamine nanospheres using solubility parameter", *Scientific Reports* **2014**, *4*, 1–6.

[2] C. P. Rodrigues, P. d. C. Zonetti, L. G. Appel, "Chemicals from ethanol: The acetone synthesis from ethanol employing Ce0.75Zr0.25O2, ZrO2 and Cu/ZnO/Al2O3", *Chemistry Central Journal* **2017**, *11*, 1–11.

[3] S. Gravelle, H. Yoshida, L. Joly, C. Ybert, L. Bocquet, "Carbon membranes for efficient water-ethanol separation", *Journal of Chemical Physics* **2016**, *145*.

[4] Q. Kang, J. Huybrechts, B. Van Der Bruggen, J. Baeyens, T. Tan, R. Dewil, "Hydrophilic membranes to replace molecular sieves in dewatering the bio-ethanol/water azeotropic mixture", *Separation and Purification Technology* **2014**, *136*, 144–149.

[5] S. K. Pal, A. H. Zewail, "Dynamics of water in biological recognition", *Chemical Reviews* **2004**, *104*, 2099–2123.

[6] Q. L. Zhou, Q. Zhou, S. A. Forman, "The n-alcohol site in the nicotinic receptor pore is a hydrophobic patch", *Biochemistry* **2000**, *39*, 14920–14926.

[7] Y. Fang, T. S. Spisz, J. H. Hoh, "Ethanol-induced structural transitions of DNA on mica", *Nucleic Acids Research* **1999**, *27*, 1943–1949.

[8] L. Dougan, J. Crain, J. L. Finney, A. K. Soper, "Molecular self-assembly in a model amphiphile system", *Physical Chemistry Chemical Physics* **2010**, *12*, 10221–10229.

[9] A. Stradner, H. Sedgwick, F. Cardinaux, W. C. Poon, S. U. Egelhaaf, P. Schurtenberger, "Equilibrium cluster formation in concentrated protein solutions and colloids", *Nature* **2004**, *432*, 492–495.

[10] P. Schurtenberger, R. A. Chamberlin, G. M. Thurston, J. A. Thomson, G. B. Benedek, "Observation of critical phenomena in a protein-water solution", *Physical Review Letters* **1989**, *63*, 2064–2067.

[11] J. Yu, A. J. Yool, K. Schulten, E. Tajkhorshid, "Mechanism of Gating and Ion Conductivity of a Possible Tetrameric Pore in Aquaporin-1", *Structure* **2006**, *14*, 1411–1423.

[12] P. Ball, "Water as a biomolecule", *ChemPhysChem* **2008**, *9*, 2677–2685.

[13] H. S. Frank, M. W. Evans, "Free Volume and Entropy in Condensed Systems III. Entropy in Binary Liquid Mixtures; Partial Molal Entropy in Dilute Solutions; Structure and Thermodynamics in Aqueous Electrolytes", *The Journal of Chemical Physics* **1945**, *13*, 507.

[14] S. Dixit, J. Crain, W. C. K. Poon, J. L. Finney, A. K. Soper, "Molecular segregation observed in a concentrated alcohol-water solution", *Nature* **2002**, *416*, 829–832.

[15] J. Fidler, P. M. Rodger, "Solvation structure around aqueous alcohols", *Journal of Physical Chemistry B* **1999**, *103*, 7695–7703.

[16] D. T. Bowron, J. L. Finney, A. K. Soper, "Structural investigation of solute-solute interactions in aqueous solutions of tertiary butanol", *Journal of Physical Chemistry B* **1998**, *102*, 3551–3563.

[17] D. T. Bowron, A. K. Soper, J. L. Finney, "Temperature dependence of the structure of a 0.06 mole fraction tertiary butanol-water solution", *Journal of Chemical Physics* **2001**, *114*, 6203–6219.

[18] L. Dougan, S. P. Bates, R. Hargreaves, J. P. Fox, J. Crain, J. L. Finney, V. Réat, A. K. Soper, "Methanol-water solutions: A bi-percolating liquid mixture", *Journal of Chemical Physics* **2004**, *121*, 6456–6462.

[19] A. K. Soper, J. L. Finney, "Hydration of methanol in aqueous solution", *Physical Review Letters* **1993**, *71*, 4346–4349.

[20] A. K. Soper, L. Dougan, J. Crain, J. L. Finney, "Excess entropy in alcohol-water solutions: A simple clustering explanation", *Journal of Physical Chemistry B* **2006**, *110*, 3472–3476.

[21] T. Takamuku, T. Yamaguchi, M. Asato, M. Matsumoto, N. Nishi, "Structure of clusters in methanol-water binary solutions studied by mass spectrometry and X-ray diffraction", *Zeitschrift fur Naturforschung - Section A Journal of Physical Sciences* **2000**, *55*, 513–525.

[22] M. Nagasaka, K. Mochizuki, V. Leloup, N. Kosugi, "Local structures of methanol-water binary solutions studied by soft X-ray absorption spectroscopy", *Journal of Physical Chemistry B* **2014**, *118*, 4388–4396.

[23] I. Bako, T. Megyes, S. Balint, T. Grosza, V. Chihaiab, "Water–methanol mixtures: topology of hydrogen bonded network", *Physical Chemistry Chemical Physics* **2008**, *10*, 4968–4974.

[24] S. Dixit, W. C. Poon, J. Crain, "Hydration of methanol in aqueous solutions: A Raman spectroscopic study", *Journal of Physics Condensed Matter* **2000**, *12*.

[25] J. A. B. da Silva, F. G. B. Moreira, V. M. L. dos Santos, R. L. Longo, "On the hydrogen bond networks in the water-methanol mixtures: topology, percolation and small-world.", *Physical Chemistry Chemical Physics* **2011**, *13*, 6452–6461.

[26] C. Dethlefsen, P. G. Sorensen, A. Hvidt, "Excess Volumes of Propanol-Water Mixtures", *Journal of Solution Chemistry* **1984**, *13*.

[27] T. Takamuku, H. Maruyama, K. Watanabe, T. Yamaguchi, "Structure of 1-propanol-water mixtures investigated by large-angle X-ray scattering technique", *Journal of Solution Chemistry* **2004**, *33*, 641–660.

[28] K. Yoshida, M. Misawa, K. Maruyama, M. Imai, M. Furusaka, "Small angle neutron scattering study on the salt-induced phase separation of 1-propanol aqueous solution", *Journal of Chemical Physics* **2000**, *113*, 2343–2348.

[29] H. Hayashi, K. Nishikawa, T. Iijima, "Small-Angle X-ray Scattering Study of Fluctuations in 1-Propanol-Water and 2-Propanol-Water Systems", *J. Phys. Chem.* **1990**, *94*, 8334–8338.

[30] O. Gereben, L. Pusztai, "Investigation of the structure of ethanol-water mixtures by molecular dynamics simulation I: Analyses concerning the hydrogen-bonded pairs", *Journal of Physical Chemistry B* **2015**, *119*, 3070–3084.

[31] M. Tarek, D. J. Tobias, M. L. Klein, "Molecular dynamics investigation of the surface/bulk equilibrium in an ethanol-water solution", *Journal of the Chemical Society - Faraday Transactions* **1996**, *92*, 559–563.

[32] E. J. W. Wensink, A. C. Hoffmann, P. J. Van Maaren, D. Van Der Spoel, "Dynamic properties of water/alcohol mixtures studied by computer simulation", *Journal of Chemical Physics* **2003**, *119*, 7308–7317.

[33] C. Zhang, X. Yang, "Molecular dynamics simulation of ethanol/water mixtures for structure and diffusion properties", *Fluid Phase Equilibria* **2005**, *231*, 1–10.

[34] N. Nishi, S. Takahashi, M. Matsumoto, A. Tanaka, K. Muraya, T. Takamuku, T. Yamaguchi, "Hydrogen bonding cluster formation and hydrophobic solute association in aqueous solution of ethanol", *Journal of Physical Chemistry* **1995**, *99*, 462–468.

[35] D. Damasceno Borges, C. F. Woellner, P. A. Autreto, D. S. Galvao, "Insights on the mechanism of water-alcohol separation in multilayer graphene oxide membranes: Entropic versus enthalpic factors", *Carbon* **2018**, *127*, 280–286.

[36] W. Foster, J. A. Aguilar, H. Kusumaatmaja, K. Voïtchovsky, "In Situ Molecular-Level Observation of Methanol Catalysis at the Water-Graphite Interface", *ACS Applied Materials and Interfaces* **2018**, *10*, 34265–34271.

[37] H. Liu, C. Song, L. Zhang, J. Zhang, H. Wang, D. P. Wilkinson, "A review of anode catalysis in the direct methanol fuel cell", *Journal of Power Sources* **2006**, *155*, 95–110.

[38] L. V. Protsailo, W. R. Fawcett, "Studies of electron transfer through self-assembled monolayers using impedance spectroscopy", *Electrochimica Acta* **2000**, *45*, 3497–3505.

[39] W. Beckner, Y. He, J. Pfaendtner, "Chain Flexibility in Self-Assembled Monolayers Affects Protein Adsorption and Surface Hydration: A Molecular Dynamics Study", *The Journal of Physical Chemistry B* **2016**, *120*, 10423–10432.

[40] M. Lundgren, N. L. Allan, T. Cosgrove, "Wetting of water and water/ethanol Droplets on a non polar surface: A Molecular Dynamics Study.", *Langmuir* **2002**, *18*, 10462–10466.

[41] L. Zhai, M. C. Berg, F. Ç. Cebeci, Y. Kim, J. M. Milwid, M. F. Rubner, R. E. Cohen, "Patterned superhydrophobic surfaces: Toward a synthetic mimic of the namib desert beetle", *Nano Letters* **2006**, *6*, 1213–1217.

[42] T. Soeno, K. Inokuchi, S. Shiratori, "Ultra-water-repellent surface: Fabrication of complicated structure of SiO 2 nanoparticles by electrostatic self-assembled films", *Applied Surface Science* **2004**, *237*, 539–543.

[43] D. Ballal, W. G. Chapman, "Hydrophobic and hydrophilic interactions in aqueous mixtures of alcohols at a hydrophobic surface", *Journal of Chemical Physics* **2013**, *139*.

[44] F. Biscay, A. Ghoufi, P. Malfreyt, "Surface tension of water-alcohol mixtures from Monte Carlo simulations", *Journal of Chemical Physics* **2011**, *134*.

[45] M. Matsumoto, Y. Takaoka, Y. Kataoka, "Liquid-vapor interface of water-methanol mixture. I. Computer simulation", *The Journal of Chemical Physics* **1993**, *98*, 1464–1472.

[46] M. Zhao, X. Yang, "Segregation Structures and Miscellaneous Diffusions for Ethanol/Water Mixtures in Graphene-Based Nanoscale Pores", *Journal of Physical Chemistry C* **2015**, *119*, 21664–21673.

[47] S. You, J. Yu, B. Sundqvist, L. A. Belyaeva, N. V. Avramenko, M. V. Korobov, A. V. Talyzin, "Selective intercalation of graphite oxide by methanol in water/methanol mixtures", *Journal of Physical Chemistry C* **2013**, *117*, 1963–1968.

[48] N. Severin, I. M. Sokolov, J. P. Rabe, "Dynamics of ethanol and water mixtures observed in a self-Adjusting molecularly thin slit pore", *Langmuir* **2014**, *30*, 3455–3459.

[49] J. F. Brandts, L. Hunt, "The Thermodynamics of Protein Denaturation. III. The Denaturation of Ribonuclease in Water and in Aqueous Urea and Aqueous Ethanol Mixtures", *Journal of the American Chemical Society* **1967**, *89*, 4826–4838.

[50] G. Onori, A. Santucci, "Dynamical and structural properties of water/alcohol mixtures", *Journal of Molecular Liquids* **1996**, *69*, 161–181.

[51] L. Fumagalli, A. Esfandiar, R. Fabregas, S. Hu, P. Ares, A. Janardanan, Q. Yang, B. Radha, T. Taniguchi, K. Watanabe, G. Gomila, K. S. Novoselov, A. K. Geim, "Anomalously low dielectric constant of confined water", *Science* **2018**, *360*, 1339–1342.

[52] K. Voitchovsky, D. Giofrè, J. J. Segura, F. Stellacci, M. Ceriotti, "Thermally-nucleated self-assembly of water and alcohol into stable structures at hydrophobic interfaces", *Nature Communications* **2016**, *7*, 13064.

[53] M. Ceriotti, G. A. Tribello, M. Parrinello, "Simplifying the representation of complex free-energy landscapes using sketch-map", *Proceedings of the National Academy of Sciences* **2011**, *108*, 13023–13028.

[54] J. Sung, K. Park, D. Kim, "Surfaces of Alcohol-Water Mixtures Studied by Sum-Frequency Generation Vibrational Spectroscopy", *The Journal of Physical Chemistry B* **2005**, *109*, 18507–18514.

[55] J. N. Israelachvili, R. M. Pashley, "Molecular layering of water at surfaces and origin of repulsive hydration forces", *Nature* **1983**, *306*, 249–250.

[56] J. N. Israelachvili, P. M. McGuiggan, "Forces Between Surfaces in Liquids", *Science* **1988**, *241*, 795–800.

[57] M. Matsumoto, Y. Kataoka, "Molecular orientation near liquid-vapor interface of methanol: Simulational study", *The Journal of Chemical Physics* **1989**, *90*, 2398–2407.

[58] I. L. Shulgin, E. Ruckenstein, "Excess around a central molecule with application to binary mixtures", *Physical Chemistry Chemical Physics* **2008**, *10*, 1097–1105.

[59] Y. Marcus, "Preferential solvation in mixed solvents", *Phys. Chem. Chem. Phys.* **1999**, *1*, 2975.

[60] F. Franks, D. J. G. Ives, "The structural properties of alcohol-water mixtures", *Q. Rev. Chem. Soc.* **1966**, *20*, 1–43.

[61] M. Matsumoto, N. Nishi, T. Furusawa, M. Saita, T. Takamuku, M. Yamagami, T. Yamaguchi, Structure of Clusters in Ethanol–Water Binary Solutions Studied by Mass Spectrometry and X-Ray Diffraction, **1995**.

[62] G. L. Sergei Yu. Noskov, B. Roux, "Molecular Dynamics Study of Hydration in Ethanol-Water Mixtures Using a Polarizable Force Field†", *J. Phys. Chem. B* **2004**, *109*, 6705–6713.

[63] A. Ghoufi, F. Artzner, P. Malfreyt, "Physical Properties and Hydrogen-Bonding Network of Water-Ethanol Mixtures from Molecular Dynamics Simulations", *Journal of Physical Chemistry B* **2016**, *120*, 793–802.

[64] A. J. Gellman, K. R. Paserba, "Kinetics and mechanism of oligomer desorption from surfaces: n-alkanes on graphite", *Journal of Physical Chemistry B* **2002**, *106*, 13231–13241.

[65] T. Fukuma, Y. Ueda, S. Yoshioka, H. Asakawa, "Atomic-Scale distribution of water molecules at the mica-Water interface visualized by three-Dimensional scanning force microscopy", *Physical Review Letters* **2010**, *104*, 2–5.

[66] T. Fukuma, "Water distribution at solid/liquid interfaces visualized by frequency modulation atomic force microscopy", *Science and Technology of Advanced Materials* **2010**, *11*, 033003.

[67] K. Miyazawa, N. Kobayashi, M. Watkins, A. L. Shluger, K. I. Amano, T. Fukuma, "A relationship between three-dimensional surface hydration structures and force distribution measured by atomic force microscopy", *Nanoscale* **2016**, *8*, 7334–7342.

[68] T. Fukuma, R. Garcia, "Atomic- and Molecular-Resolution Mapping of Solid-Liquid Interfaces by 3D Atomic Force Microscopy", *ACS Nano* **2018**, *12*, 11785–11797.

[69] E. Hoffmann, D. Pfenning, E. Philippsen, P. Schwahn, M. Sieber, R. Wehn, D. Woermann, G. Wiedner, "Evaporation of alcohol/water mixtures through hydrophobic porous membranes", *Journal of Membrane Science* **1987**, *34*, 199–206.

[70] C. K. Chiang, Y. W. Lu, "Evaporation phase change processes of water/methanol mixtures on superhydrophobic nanostructured surfaces", *Journal of Micromechanics and Microengineering* **2011**, *21*.

[71] I. Schlesinger, U. Sivan, "Three-Dimensional Characterization of Layers of Condensed Gas Molecules Forming Universally on Hydrophobic Surfaces", *Journal of the American Chemical Society* **2018**, *140*, 10473–10481.

[72] M. R. Uhlig, D. Martin-Jimenez, R. Garcia, "Atomic-scale mapping of hydrophobic layers on graphene and few-layer MoS2 and WSe2 in water", *Nature Communications* **2019**, *10*, 2606.

[73] R. Zangi, D. Roccatano, "Strings-to-Rings Transition and Antiparallel Dipole Alignment in Two-Dimensional Methanols", *Nano Letters* **2016**, *16*, 3142–3147.

[74] K. Morishige, T. Kato, "Chain-length dependence of melting of n-alcohol monolayers adsorbed on graphite: n-hexanol, n-heptanol, n-octanol, and n-nonanol", *Journal of Chemical Physics* **1999**, *111*, 7095–7102.

[75] R. Zangi, "Self-Assembly of Alcohols Adsorbed on Graphene", *Journal of Physical Chemistry C* **2019**, *123*, 16902–16910.

[76] M. J. Abraham, T. Murtola, R. Schulz, S. Páll, J. C. Smith, B. Hess, E. Lindah, "Gromacs: High performance molecular simulations through multi-level parallelism from laptops to supercomputers", *SoftwareX* **2015**, *1-2*, 19–25.

[77] M. Abraham, D. van der Spoel, B. H. E. Lindahl, "GROMACS User Manual version 2016", **2016**.

[78] B. Hess, H. Bekker, H. J. Berendsen, J. G. Fraaije, "LINCS: A Linear Constraint Solver for molecular simulations", *Journal of Computational Chemistry* **1997**, *18*, 1463–1472.

5.0 Chapter 5: Influencing the small molecule assemblies

5.1 Chapter Overview

Small hydrogen bonding molecules exhibiting weak interactions with surfaces can self-assemble at hydrophobic interfaces via the formation of extended hydrogen bonded networks enabling the molecules to adsorb as a group. In this group-effect self-assembly, the weak molecular interactions with the surface should make it possible to influence the supramolecular structures formed by small changes in the interfacial hydrogen bond network. This potentially opens the possibility for creating a wide variety of supramolecular structures. In this chapter, the ability to influence group-effect self-assembly will be explored using a base system of alcohol-water mixtures at the interface with graphite. The interplay between intermolecular and surface interactions will be investigated by adding small amounts of foreign molecules able to interfere with the hydrogen bond network and systematically varying the length of the alcohol hydrocarbon chain. The generality of the self-assembly process is explored by replacing highly oriented pyrolytic graphite (HOPG) with partially hydrophobic graphene oxide (GrO) and hydrophobic molybdenum disulphide (MoS_2).

5.2 Introduction

To date, the self-assembly of small molecules ($<$ 20 atoms) has primarily been studied in extreme cases where systems are under confinement or at low temper-

atures so as to force the molecules to remain long enough near the solid's surface for supramolecular structures to form (see Chapter 1). Examples in ambient conditions are scarce, with limited insights into the process. This gap is significant because the nanoscale arrangement of small molecules at solid-liquid interfaces is key to phenomena such as friction and lubrication [1], nanomembrane separation [2] and chemical reactivity [3]. Additionally, sophisticated or complex self-assembled structure are likely to involve small molecules as part of their building blocks. The weak dependence of small molecules on specific interactions could also increase the process robustness and flexibility while reducing costs for potential applications.

As outlined in Chapter 1, when mixed together, water and methanol, both small molecules, spontaneously form organised stable supramolecular structures at the surface of HOPG at room temperature. This is remarkable because both water and methanol only interact weakly with the hydrophobic HOPG and neither pure solvent can form any stable structure at room temperature. Instead, large heterogeneous self-assembled structures can nucleate thanks to an extended hydrogen bond network that stabilises the assembly by a 'group effect' [3, 4]. This result suggests a very different approach to molecular self-assembly: molecules weakly interacting with a solid can be stabilised at the interface by a network of inter-molecular interactions already existing in the liquid [5] albeit transiently (as outlined in Chapter 4). In this framework, the surface mainly serves to reduce the configurational entropy and mobility of the molecules for the self-assembly to begin. This approach is particularly well-suited to small molecules able to form hydrogen bonds.

This chapter will exploit the alcohol-water platform to explore some of the main factors influencing group-based self-assembly, in particular the interplay between molecule-molecule and molecule-surface interactions. First, the fact that weak solid-liquid interactions are at play should allow added molecules able to interfere with the molecule-molecule interactions to affect the resulting self-assembled structures. In principle, only trace amounts of these added molecules could already have a significant impact if the assembly relies on group-effect. Second, the self-assembly process should not strongly depend on the choice of solid, hence increasing the generality and applicability of this self-assembly mechanism. Here, these effects are explored systematically: (1) Starting with a simple water-methanol system at the interface with HOPG, the methanol-water interactions are modified by adding small amounts of foreign molecules able to locally modify the hydrogen bond network. (2) The ratio

of methanol to water is then changed, also in conjunction with foreign molecules. (3) The methanol is then replaced with primary alcohols exhibiting progressively longer backbones to increase the relative importance of interactions with the substrate in the self-assembly process otherwise dominated by the interfacial hydrogen bond network. (4) The generality of the self-assembly process is demonstrated by replacing HOPG with molybdenum disulphide (MoS_2) and graphene oxide (GrO). MoS_2 is a non-organic hydrophobic solid whereas GrO is weakly hydrophilic and has a less regular surface than HOPG.

5.3 Adjunction of small 'influencers' molecules

To begin with we explore the ability of added charged foreign molecules -hereafter referred to as 'influencers' for simplicity- to modulate the molecular arrangement of methanol-water structures at the interface with HOPG. In principle, countless molecules can be used as influencers. For this study the constitutive molecules and ions at the concentrations present in the standard laboratory buffering agent for biological systems, phosphate buffered saline (PBS), were chosen due to their relevance to biological systems and other self-assembly studies [6, 7]. Systems containing the pure solvents were compared with that doped with small amounts of PBS, or its main components in isolation, namely disodium phosphate (Na_2HPO_4), sodium chloride (NaCl) and potassium chloride (KCl). Thus five aqueous solutions are explored: (i) ultrapure water, (ii) a PBS solution comprising 10 mM Na_2HPO_4, 137 mM NaCl and 2.7 mM KCl (hereafter simply referred to as PBS solution), (iii) a 10 mM Na_2HPO_4 aqueous solution, (iv) a 137 mM NaCl aqueous solution and (v) a 2.7 mM KCl aqueous solution. In all cases, the aqueous solution is mixed 50:50 by volume ratio with methanol and the resulting mixture placed in contact with HOPG.

High-resolution amplitude modulation atomic force microscopy (AFM) in liquid [8] is used to explore in-situ the sub-nanometre details of the resulting interfacial molecular assemblies. The AFM results include simultaneously acquired topographic and phase images of the interface. For each system, the experiment was conducted both with and without the methanol in order to ensure that any molecular assembly observed does indeed involve both types of molecules. Additionally, the AFM data

was always collected within an hour of the liquid deposition onto the surface. This is because of the micromolar quantities of methanol produced directly at the HOPG-water interface as outlined in Chapter 3. By restricting the observations to less than an hour, the influence of methanol produced in-situ can be ignored, as will be confirmed by the control measurements.

5.3.1 PBS

When water and methanol are both present in the solution, molecularly ordered monolayers nucleate as expected, consisting of ordered row-like features with an inter-row periodicity of 5.30 ± 0.20 nm. This structure will hereafter be referred to as the 'basic methanol-water monolayer'. Control experiments show that ultrapure water itself is unable to form stable structures on HOPG at room temperature (Figure 5.1).

Using the PBS solution as an influencer induces the co-existence of two different structural domains: the basic methanol-water monolayer (Figure 5.1, blue arrow) and regions presenting a new type of ribbon-like structures (black arrow). Over the course of a typical experiment, both structures occupy a comparable area, and remain unperturbed by the scanning AFM tip. The ribbon-like features exhibit similarities with the basic structure suggesting the presence of methanol in the assembly. However, the irregular periodicity (black arrow) point to a significant impact of the influencers on the assembling methanol and water structures. Understanding the precise role of the influencers is however challenging due to the PBS solution containing three types of molecules at different concentrations. To better assess the role of these components, each was investigated separately at the same concentration present in PBS.

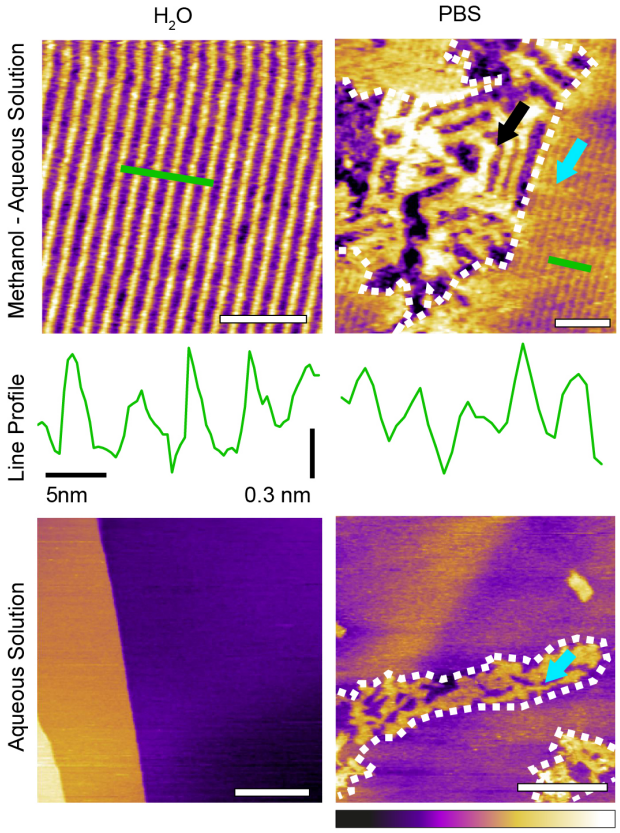

Fig. 5.1: Representative AM-AFM images of the HOPG-liquid interface in solutions of a 50:50 volume ratio mixture of methanol and the aqueous component (water or PBS) or just the aqueous component (controls). When methanol is present in the solution (top), characteristic methanol-water longitudinal rows can be observed with inter-row periodicities of 5.30 ± 0.20 nm, as shown by the corresponding line profiles beneath each figure. The green bars on the images represent the location of the line profile. Swapping the pure water with PBS creates complex domains comprising the row-like structures (light blue arrow) and individual ribbon-like structures (black arrow). Control experiments conducted in the absence of methanol exhibit no clear assemblies, with only transient features visible for the PBS mixture (blue arrow). The scale bars represent 25 nm (top) and 100 nm (controls). All images are topographic images. The colour scale bars represent a height variation of 0.5 nm for top left panel, 1 nm for the top right and 3 nm for the bottom panels.

5.3.2 *Individual components of PBS*

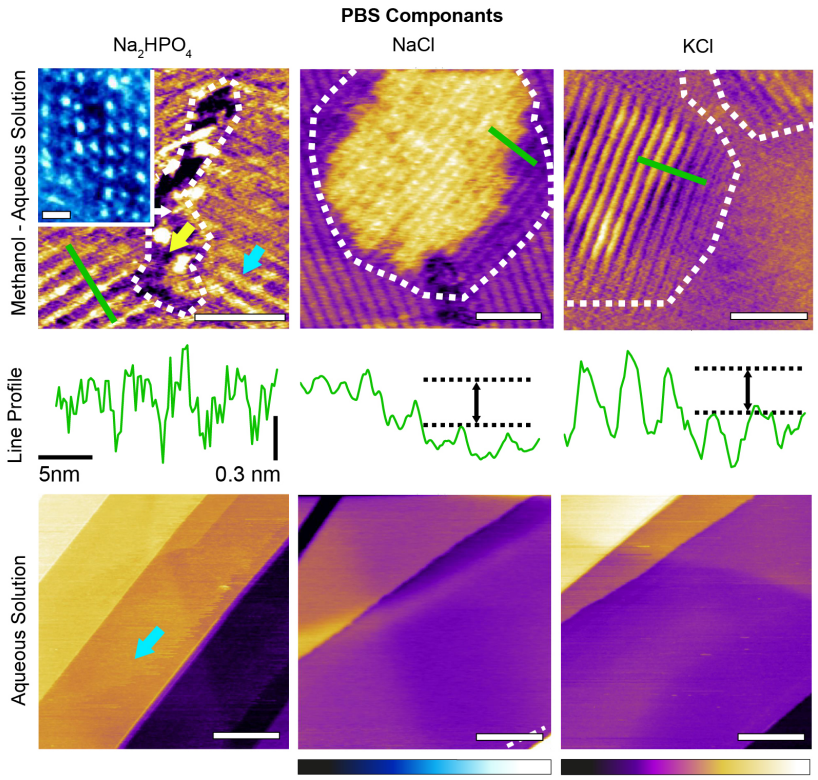

Fig. 5.2: Representative AM-AFM images of the HOPG-liquid interface in solutions containing the individual components of PBS. The solutions contain a 50:50 volume ratio mixture of methanol and the aqueous component (see text), except for the controls that contain only the aqueous component. The green bars on the images represent the location of the line profile which demonstrates when methanol is present, rows with a periodicity of 5.30 ± 0.20 nm form. When the buffering agent (10mM Na_2HPO_4) is mixed with methanol different structures can co-exist (yellow and light blue arrows) with new features covering only a small area. The inset shows a magnified phase image over these new structures. When only the metal ions (137 mM NaCl or 2.7 mM KCl) are present in the aqueous solution mixed with methanol, the longitudinal rows visible in the methanol-water mixture re-appear, but some exhibit an altered z-profile with an upward shift of the rows by 0.30 ± 0.06 nm (black arrow). Control experiments conducted in the absence of methanol exhibit no clear assemblies, with only transient features visible in Na_2HPO_4(blue arrows). The scale bars represent 25 nm (top), 2.5 nm (inset) and 100 nm (controls). All images are topographic images except for the inset (phase). The colour scale bars represent 1 nm for the top row, and 3 nm for the bottom row. The blue scale bar represents a phase variation 10^o.

Disodium Phosphate

When only the buffering agent, Na_2HPO_4, is present in the aqueous solution, fine rectangular patterns appear at the boundary between basic methanol-water monolayer domains (Figure 5.2 inset). The area covered by these features is comparatively small and the pattern is easily deformed or damaged by the scanning AFM tip (Figure 5.3a and b). This indicates weakly bound structures compared to the basic water-methanol motif. When dissolved in water, Na_2HPO_4 disassociates into sodium (Na^+) and phosphate (HPO_4^{2-} and $H_2PO_4^-$) ions, the latter being able to form multiple hydrogen bonds. Here the fine structures observed suggest phosphate ions to have been incorporated within the methanol-water assembly. Molecular Dynamics (MD) simulations cannot provide detail insights into the self-assembled molecular arrangement at the interface given the weak interactions at play which makes the nucleation times-scale inaccessible (minutes compared with $\sim$ 100 ns simulated in ref. [4], as discussed in Chapters 2 and 4). However, bulk MD simulations suggest that the phosphate and sodium ions form clusters with their hydrogen bonding groups facing outwards towards the surrounding liquid (Figure 5.3c), and should therefore be able to be incorporated into the basic structures. A similar behaviour has been previously reported for calcium diphosphate [9]. At very low concentrations these clusters are comparable in size to the dotted features observed (inset) which may be explained by hydrated ionic clumps incorporated into the basic monolayer. This would also be consistent with recent reports of long residence times for metal ions at hydrophilic interfaces, here the monolayer [10, 11].

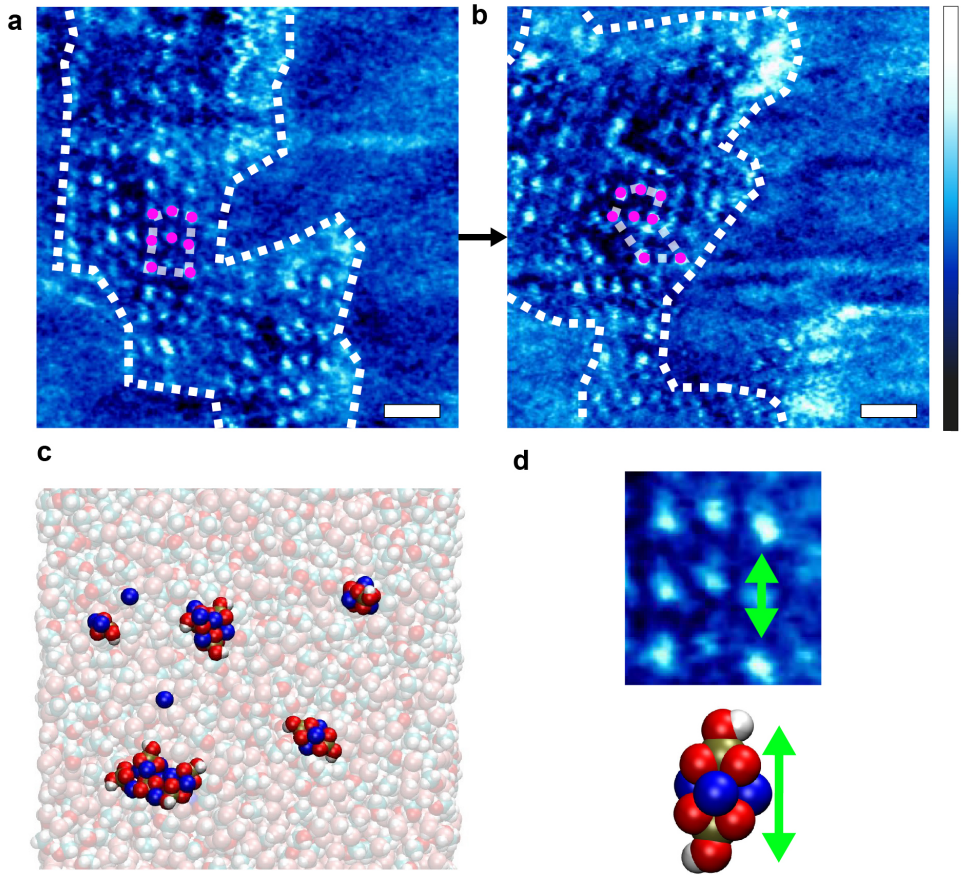

Fig. 5.3: High resolution images of some of the unique features observed in a methanol-disodium phosphate mixture. (a-b) The two consecutive images were taken within approx. 1 minute of each other. The pink dots denote example features (potentially molecules) that undergo a translational shift, indicating that the assembly is not stable under imaging conditions. The images are phase images for their better contrast. The scale bars represent 2 nm. The blue colour scale bar represents a phase variation of 12^o. (c) MD simulations of Na^+ and HPO_4^{2-} ions in a 50:50 water-methanol mixture. The ions concentration corresponds to a weight percentage of 1%. The simulations demonstrate that the charged molecules all cluster together with their hydroxyl group facing outwards and the sodium ions (dark blue) coordinating to the phosphate ions (where the phosphate atom is yellow). Only a snapshot of the simulation is shown and by the end of the simulation all of the ions are permanently clumped, consistent with results reported for the very similar molecule calcium diphosphate [9]. The water and methanol molecules have been made partially transparent for better visibility of the Na^+ and HPO_4^{2-} ions. All the ions in the simulation are visible in the snapshot. (d) The size of clusters involving two HPO_4^{2-} ions is comparable in size to the features observed in (a-b). The green arrow is 1.5 nm. Full details of the simulation can be seen in the methods section at the end of this chapter.

Metal Salts

Using only the metallic salts (NaCl or KCl) does not impact the lateral order of the basic methanol-water monolayer. Instead the metal ions appear to induce an upward shift of the rows by 0.30 ± 0.06 nm from the average height of the basic methanol-water structure (black arrow on line profile, Figure 5.2). A similar vertical displacement could also be observed for the system containing the Na^+ ions from Na_2HPO_4 (see Figure 5.4). Vertical stacking of multiple basic methanol-water monolayers has previously been observed in pure water-methanol mixtures (Chapter 1), but this is unlikely to be the case here as evident from the continuity of the rows in the profiles. The features observed for both the 137 mM NaCl and 2.7 mM KCl cases are very similar, indicating changes in the ionic strength of the solutions appear to have no significant effect. This is consistent with a previous computational study into the influence of the ionic strength of NaCl in methanol-water-NaCl mixtures. In this study it was observed that changing the number of ions in the solution had little impact on the co-ordination numbers or local distribution of the water and methanol molecules [12]. Enhanced resolution images on the raised structures in the NaCl experiment show features that can be interpreted as molecular clusters involving the metal ions and residing on top of a basic row structure (see Figure 5.5). These clusters tend to follow the pattern of the underling rows. This view is compatible with previous experiments where electric fields were used to reversibly adsorb metal cations or anions on top of the basic structures [4], thereby inducing raised row-like structure in registry with the underlying methanol-water assembly. The metal ions themselves cannot directly form hydrogen bonds (although can still interact with hydrogen bonding molecules) and sitting atop the assembly would allow them to remain fully hydrated while altering the local hydrogen bonding properties. The raised patches therefore likely result from this perturbation to the local hydrogen bond network. The non-raised regions in Figure 5.5 appears smooth and regular, with no evidence of clusters.

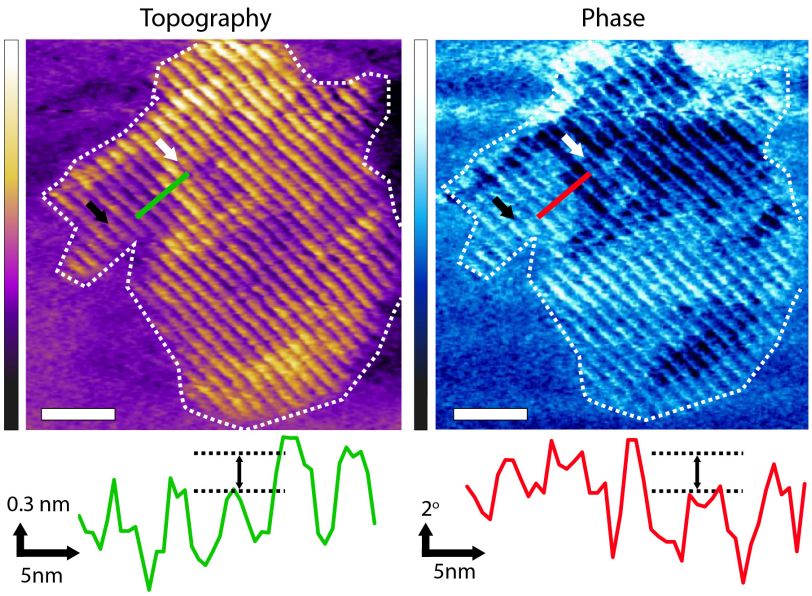

Fig. 5.4: Impact of disodium phosphate on the basic monolayers formed in a methanol-water mixture observed using AM-AFM. The white and black arrows denote the two different parts of the monolayer, with the raised parts (white arrow) appearing on average 0.32 ± 0.06 nm higher than the surface of the basic monolayer (green topographic profile). This is identical to the effect observed in NaCl and KCl within error. The phase also shows a contrast between the two types of layer (red profile) The scale bar represents 25 nm. The purple scale bar represents a height variation of 1.5 nm. The blue scale bar represents a phase variation of 6^o.

Interestingly, changes to basic methanol-water structure in the presence of multiple influencer molecules (PBS) appear significantly more pronounced than could be expected from a simple addition of changes observed in the individual components at equivalent concentrations (Na_2HPO_4, NaCl and KCl). This points towards a complex interplay between the influencers and the hydrogen bonded networks stabilising the system. Experiments conducted with the individual molecules suggest the incorporation of the phosphate ions into the basic monolayer assembly, and the ability of the metal ions to shift the monolayers despite their lack of direct hydrogen bond. One plausible explanation for this cooperative behaviour of the influencers is that once the phosphate ions become involved in the hydrogen bonded networks of the monolayers, their charged nature encourages interaction with metal ions, allowing the latter to have a larger influence on the resulting structures.

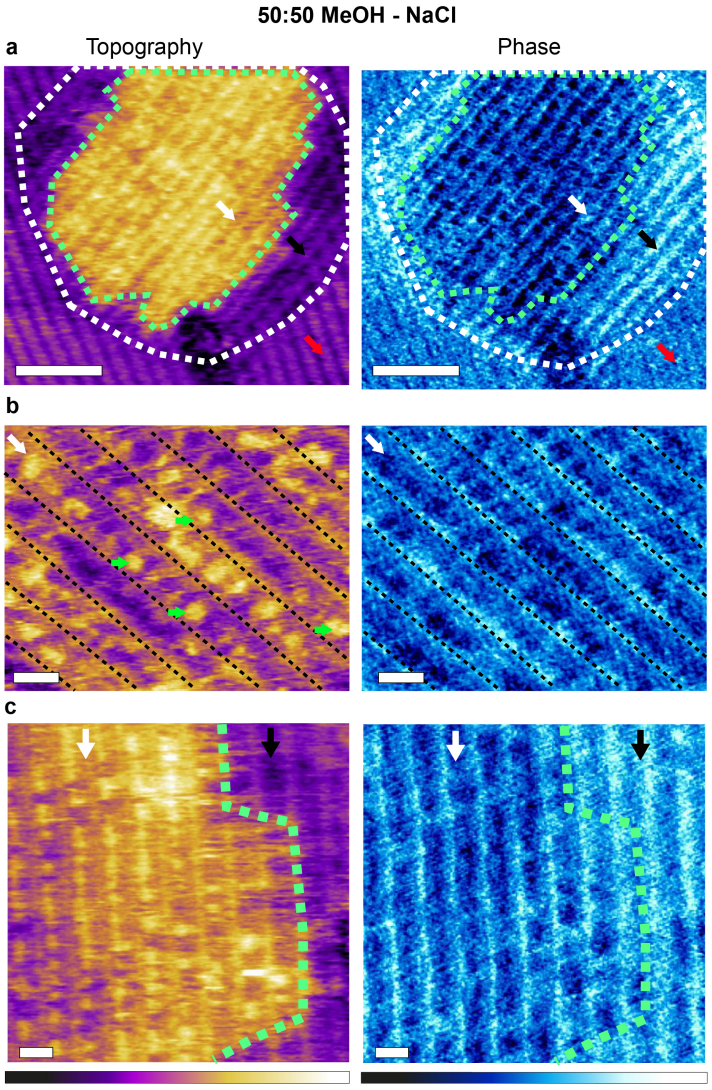

Fig. 5.5: Impact of NaCl on the basic monolayers formed in a methanol-water mixture. (a) Topographic and phase images of raised areas formed in a 50:50 mixture of methanol with 137mM NaCl. The white and black arrows point to two different domains of a single structure (white dashed outline), with the green dashed line marking the boundary between the domains. The red arrow points to a region covered by the basic methanol-water monolayer unchanged by the presence of the metallic salt ions. (b) High resolution images of the raised structures (white arrow) show small localised features sitting on top of the row structures and lying in registry with them (rows highlighted by the dashed black lines). The features are presumably molecular clusters involving the metal ions. (c) The non-raised regions (black arrow) do not show any of these 'clusters', indicating standard basic methanol-water monolayer. The scale bar is 25 nm in (a), 5 nm in (b-c). The purple scale bar represents a height variation of 1 nm in (a) and 0.5 nm in (b-c). The blue scale bar represents a phase variation of 8^o in (a) and (c) and 6^o in (b). The direction of the patterns in (a-c) differ due to changes in the angle of scanning to obtain optimum resolution.

5.3.3 *Solvation properties of PBS-induced structures*

To gain further insights into the hydration properties of the stable new structures observed in PBS, experiments were repeated using small-amplitude frequency-modulation AFM. This operating mode, while potentially more challenging on soft samples, enables precise three dimensional mapping of the liquid density near the interface [13–15]. This makes it possible to derive *in situ* local quantification of the structures' thickness and shape in three dimensions, when moving away from the HOPG surface. The technique is often referred to as three dimensional scanning force microscopy or 3D-SFM (as outlined in detail in Chapter 2). The size of the domains formed in PBS and their stability under imaging conditions makes the system suitable for investigations with 3D-SFM.

Frequency modulation AFM is able to resolve both the basic methanol-water assemblies and the PBS-specific longitudinal domains in solution (Figure 5.6a). The former structures are characteristically highly ordered and periodic, whereas the latter exhibit a significant degree of variability in the periodicity of the features (see also Figure 5.7). Higher resolution images of the PBS-induced structures (Figure 5.6b) reveal molecular-level features running parallel to the main rows. A representative 3D-SFM section taken over the PBS-specific interfacial domains (Figure 5.6c) shows no clear solvation features other than the rows themselves. In contrast, when the same analysis is performed on the basic methanol-water rows formed in the pure solvents (Figure 5.6d and e), intricate solvation features extend in the bulk solution, with multiple well-defined hydration layers (spacing of 0.30 ± 0.05 nm) visible directly above the basic monolayer. The inter-layer spacing is similar to that reported for the HOPG-degassed water interface [16] and simulations of a HOPG-water-methanol interface (Chapter 4), suggesting little direct interaction between the basic methanol-water monolayer and the interfacial liquid. This is consistent with the molecular model of the basic monolayer where all the available hydrogen bonds are engaged within the layer (described in Chapter 1), leaving little to interact with the surrounding solvent. Interestingly, the layer spacing is smaller than the 0.5 nm spacing reported for hydration layers at the non-degassed water-HOPG interface [16, 17]. This larger spacing was attributed to dissolved molecules displacing the water from the interface with HOPG. The present observations suggests that the structured basic monolayers prevent such a displacement of water occurring.

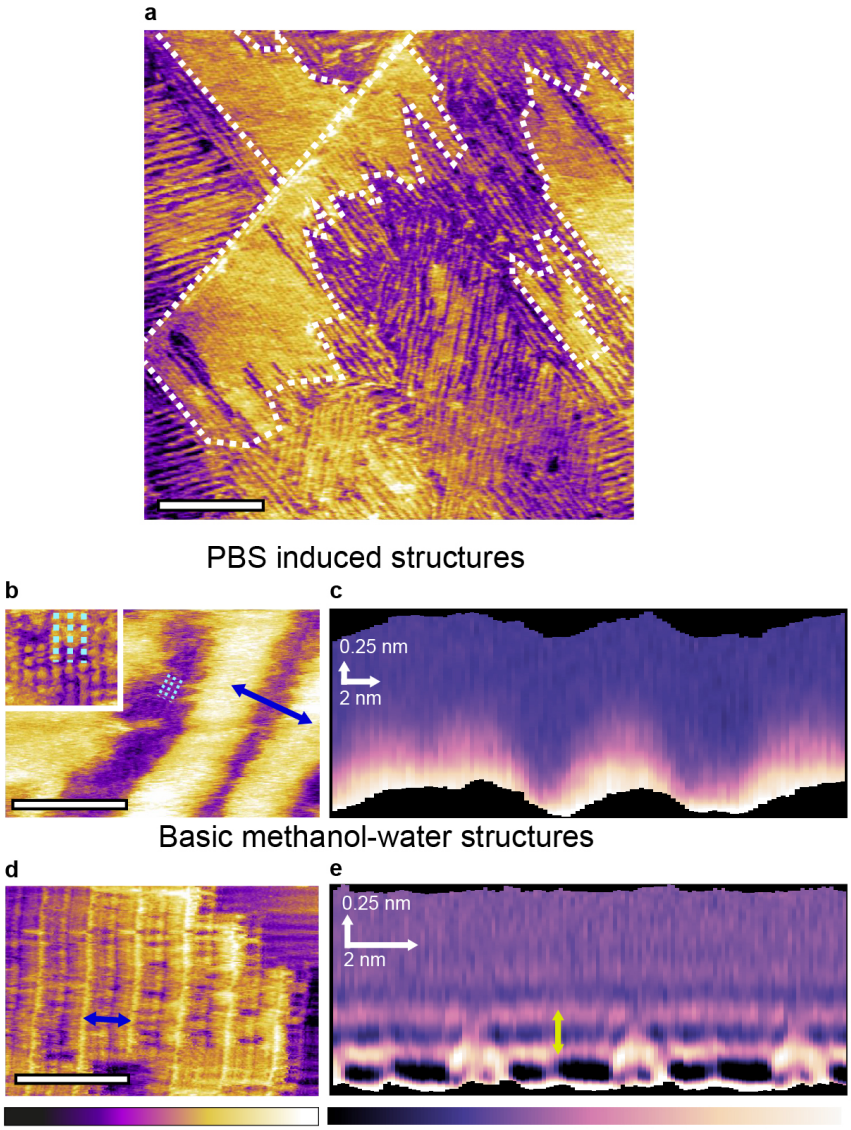

Fig. 5.6: Influence of PBS on the 3-dimensional self-assembly of water-methanol structures at the interface with HOPG. Frequency modulation imaging of the interface between HOPG and a 50:50 mixture of methanol and PBS solution shows the two types of domains visible in Figure 5.2 (a) (domain boundary denoted by white dashed line). At higher magnification, domains unique to the methanol PBS mixture exhibit features running parallel to the rows (inset and dashed lines) (b). These fine features exhibit a periodicity of 0.94 ± 0.06 nm. Taking a 3D SFM cross-section horizontally across the taller rows in (b) does not reveal any particular solvation features when moving vertically away from the interface (c). For comparison, the same analysis conducted in a 50:50 mixture of methanol and ultrapure water yields the basic monolayer, here with a row spacing of 4.65 ± 0.08 nm (d). A 3D SFM cross-section analysis (e) reveals clear hydration layers with a vertical periodicity of 0.30 ± 0.05 nm (yellow arrow). The scale bars are 100 nm in (a) and 10 nm in (b) and (d). The purple-yellow colour scale bar represents a height variation of 0.5 nm in (a), 0.6 nm in (b) and 0.3 nm in the inset and 0.4 nm in (d). The purple-white scale bar represents a frequency shift variation of 2 kHz in (c) and 3 kHz in (e).

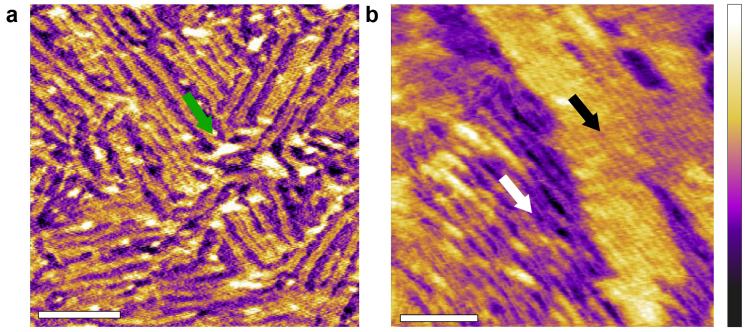

Fig. 5.7: High-resolution structures observed in a 50:50 methanol:PBS solution mixture. Distinct longitudinal structures with no well-defined periodicity are formed (a). Multiple round features (green arrow) can also be observed, likely due to the incorporation or clumping of the salt ions. The features of this assembly may be due to the incorporation of hydrogen bonding diphosphate molecules into the extended hydrogen bonded network of square methanol-water motifs (introduced in Chapter 1). The subsequent interactions between the charged diphosphate molecules and the surrounding sodium and phosphate ions would disrupt the previously well-ordered linear features, producing the more irregular periodicities visible here. Some regions (b) exhibit co-existence of PBS induced structures (white arrow) and structures resembling the well-ordered basic methanol water monolayers (black arrow). The scale bars are 50 nm. The purple colour scale bar represents a height variation of 0.5 nm in (a) and 1 nm in (b).

5.3.4 Changes in the alcohol-water ratio

The data presented so far in this section demonstrates that influencer molecules can alter the self-assembly, leading to a variety of different structures that can differ substantially from the basic methanol-water monolayer, both in morphology and in their local interaction with the surrounding interfacial liquid. In all cases, water and methanol are both needed for well-ordered structures to nucleate. However, their respective molecular proportions can be changed, offering an additional route to influence the interfacial self-assembly, especially when in the presence of influencers. To illustrate this point, the methanol-PBS ratio was varied from Figure 5.6a, reducing the methanol concentration down to 5%. This results in the formation of intricate, highly ordered structures with a rectangular lattice (Figure 5.8a). These structures are reminiscent of those visible in a 5:95 mixture of methanol and ultrapure water (Figure 5.8b, as previously discussed in Chapter 4), but the respective unit cell in each system differs in shape and size, once again highlighting the specific role played by PBS in the interfacial molecular organisation.

Three-dimensional SFM mapping of the interface between HOPG and the methanol-PBS system reveals periodic features extending up to 0.85 nm away from the surface of HOPG (Figure 5.8c). The associated solvation structure is remarkably intricate with a lateral pattern changing dramatically at different distances from the surface (Figure 5.8d). The transition from the 2D monolayers observed in the 50:50 mixtures of methanol and PBS to the 3D structures observed in the 5:95 mixture may be in part explained by comparisons with the hydrogen bonding behaviour of methanol-water mixtures described in Chapter 4. To re-cap: at low methanol concentration, three-dimensional hydrogen bonded structures dominate due to the tetrahedral coordination of water. In contrast, one- and two-dimensional hydrogen bonded structures such as chains and rings dominate at higher methanol concentrations. Here this could explain why three-dimensional solvation structures develop from the interface at low methanol concentration (Figure 5.8c, d) whereas linear features in the basic methanol-water monolayer are predominant at higher alcohol concentrations (Section 5.3). The exact effect of the PBS is harder to pinpoint. No visible hydration layers were observed above the interfacial structures developing when PBS is present (Figure 5.6), suggesting a higher degree of similarity with the two-dimensional assemblies. It should be pointed out that possible tip effects on the 3D-SFM measurements cannot be ruled out, but such effects would be similar on all 3D results. Yet, there still remains clear solvation differences between the 5:95 and 50:50 methanol-aqueous solution mixtures as well as in the presence of PBS (Figure 5.6c and e, and 5.8c).

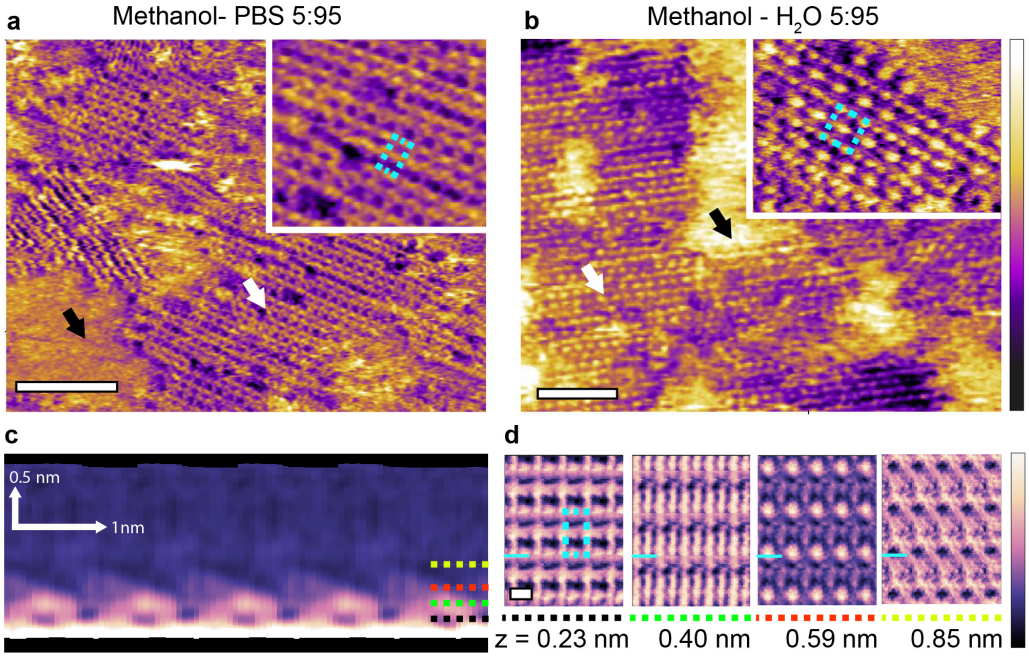

Fig. 5.8: AFM imaging of the unique structures produced in a 5:95 mixture of methanol with the PBS solution on HOPG. Two types of domains are visible (a) (black and white arrows). The inset shows a magnified view of the fine structured region (white arrow), indicating a unit cell of 0.90 ± 0.05 nm by 0.82 ± 0.05 nm (blue dashed line). For comparison, images acquired in a 5:95 mixture of methanol and ultrapure water (b) also show some fine structure across ordered (white arrow) and disordered (black arrow) regions, but with a different unit cell (inset, blue dashed line). A 3D-SFM cross-section taken perpendicularly to the features denoted by the white arrow in (a) reveals complex 3D motifs that extend up to 0.85 nm in the vertical (z) direction (yellow dashed line) (c). These motifs are best visualised by taking horizontal cross sections parallel to the HOPG surface at different heights (d). In all cross sections, the blue line indicates the position where the vertical cross section shown in (c) was taken. The rectangular unit cell from (a) is overlaid on the lowest of the four horizontal cross sections. Images in (c) and (d) have been processed with an average filtering process that uses a pattern matching algorithm. Details of the procedure are described in ref. [14]. The raw data is given in the methods section at the end of this chapter. The scale bars are 10 nm in (a) and (b) and 1 nm in (d). The purple-yellow colour scale bar represents a height variation of 0.2 nm in (a) and the inset, 0.8 nm in (b) and 0.5 nm in the inset. The purple-white scale bar represents a frequency shift variation of 0.8 kHz in (c) and 0.1 kHz in (d).

5.4 Tuning of surface interactions through the length of the alcohol backbone

These last results confirm that influencers and the ratio of alcohol to water can both affect the interactions between the different liquid molecules at the interface and hence the resulting supramolecular structures. There exists a third, more fundamental route to influence the self-assembly process: the strength of the interaction between the assembling molecules and the substrate. To enable self-assembly by group effect, this interaction must remain relatively weak compared to thermal fluctuations. Stronger interactions will tend to bring the system back to the traditional two-step self-assembly regime. If the interaction strength can be tuned, the relative importance of inter-molecular forces and substrate effects can be controlled. In water-alcohol mixtures, this is tuned by the length of the alcohol's alkyl backbone: the longer the carbon backbone, the stronger the attraction to HOPG. To systematically investigate this effect, comparisons were made between the interfacial structures formed in binary mixtures of ultrapure water with alcohols presenting increasingly longer carbon chains, such as ethanol and propanol. Primary alcohols were initially chosen due to their topological similarity to methanol, which allows for a direct comparison with the water-methanol monolayers.

5.4.1 Ethanol

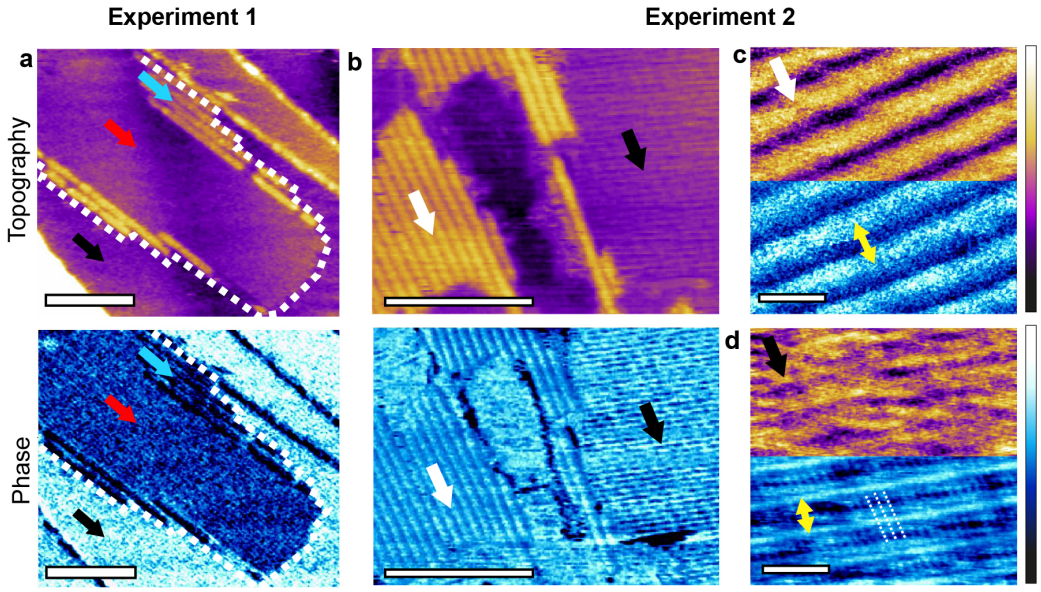

Fig. 5.9: Impact of the backbone length of primary alcohols on interfacial self-assembly on HOPG. In a 50:50 ethanol:water mixture (a), two organised layers are visible both in topography and in the phase where it is more pronounced, outlined by a white dashed line (blue and red arrows). The self-assembled layers appear darker in the phase than the directly exposed graphite (black arrow). The lower layer shows few resolvable features and is bordered by wide rows that have a separation of 5.89 ± 0.28 nm. Repeat experiments,(b), show co-existence of two types of ordered monolayers (black and white arrows). Higher magnification of the area highlighted with the white arrow in (b) reveals a basic structure with a periodicity of 5.40 ± 0.10 nm, (c), but with no sub-features. In contrast, details of the area highlighted with the black arrow in (b) reveals a periodicity of 3.87 ± 0.10 nm with finer features (white dashed lines) running perpendicular to the main rows and spaced by 1.05 ± 0.10 nm, (d). The scale bars are: (a) 100 nm, (b) 50 nm and (c-d) 7 nm. The purple colour scale bar represents a height variation of: (a-b) 1 nm, (c) 0.5 nm and (d) 0.2 nm. The blue scale bar represents a phase variation of (a,c) 1.5^o, (b) 6^o and (d) 4^o.

It is immediately clear that more complicated linear structures can form in the presence of longer alcohols. In a 50:50 mixture of ethanol and water two different types of molecular arrangements are visible (Figure 5.9a). A uniform layer (red arrow) with a height of 0.24 ± 0.05 nm above the HOPG surface is partially covered by a second layer 0.62 ± 0.05 nm high and composed of row-like structures. A clear phase difference is visible between the structures and the HOPG, confirming distinct molecular arrangements. Unlike the previously discussed cases, repeat experiments in the ethanol-water mixture revealed a variance in types of structure produced,

often with periodic row-like features exhibiting sharp domain edges that are uncommon in methanol-water mixtures (Figure 5.9b). The two domains types presented in Figure 5.9b have different row periodicities and present differing resolutions when imaged with the AFM (Figure 5.9c-d). The difference between the structures observed in ethanol-water systems indicates a high degree of polymorphism with more configurations being energetically stable, potentially due to the increased surface interactions. As discussed in Chapter 2, the attainable resolution using dynamic mode AFM is linked to the presence of strong hydration sites on the interface being imaged. Thus the increased resolution on one of the ethanol-water assemblies indicates the larger alcohol structures preferring to have hydrogen bonding group facing away from the interface, consistent with results presented in Chapter 4.

5.4.2 1-Propanol and 2-Propanol

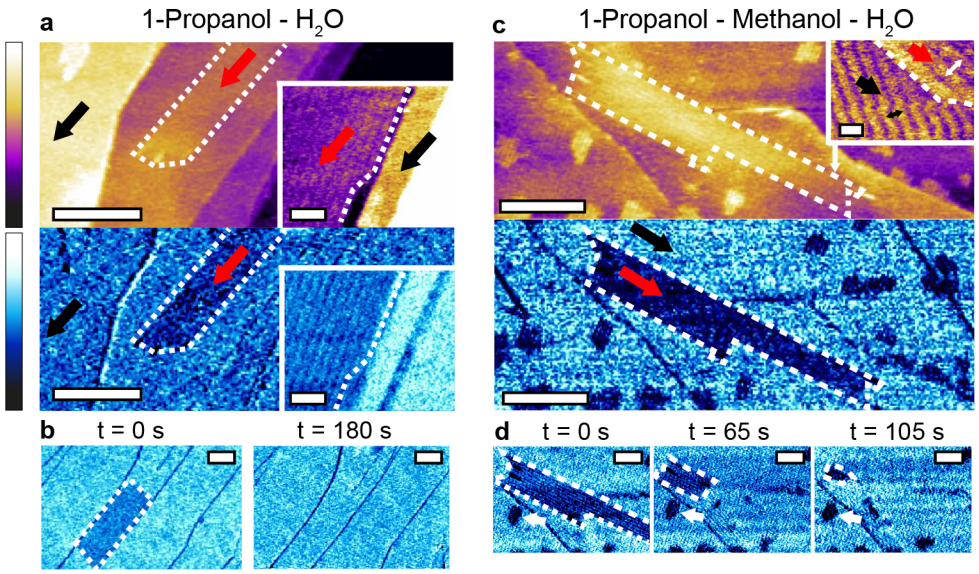

Fig. 5.10: Comparison between the interfacial supramolecular assemblies occurring in a binary 1-propanol-water mixture and a ternary 1-propanol-methanol-water mixture. The unique structures formed in a 50:50 1-propanol:water mixture (red arrows, periodicity 5.86 ± 0.25 nm) exhibit similar properties to those formed in a 10:45:45 1-propanol-methanol-water mixture (red arrow, periodicity 7.21 ± 0.05 nm). The geometry of the structures in the binary mixture (a) strongly resemble that of certain motifs formed in the ternary mixture (c) and both motifs are unstable under imaging (b and d). Unlike the binary mixture, the presence of high quantities of methanol in the ternary mixture causes the rest of the surface to be covered in multi-layered structures resembling the basic methanol-water monolayers (periodicity 5.26 ± 0.05 nm), indicating we have a co-existence of methanol and 1-propanol induced features. The scale bars represent 100 nm in (a-c) main images, 20 nm and 10 nm in the insets of (a) and (c) respectively, and 50 nm in (d). The purple scale bar represents a height variation of 3 nm in (a) (0.6 nm in the inset) and 2 nm in (c) (0.4 nm in the inset). The blue scale bar represents a variation of 4^o in (b) and 1.5^o in (c) and (d).

Increasing the carbon backbone length further and using 1-propanol-water mixtures induces a novel type of structural domain (Figure 5.10a) which also exhibits straight edges, similar to those formed in ethanol-water mixtures (see Figure 5.11 for a comparison). These highly linear domains are unstable under imaging conditions and disassemble within minutes (see Figure 5.10b) indicating the size of the assembling molecules is starting to hinder their ability to form extended hydrogen bonded networks. Interestingly, combining 1-propanol with methanol and water in a ternary

mixture of 10:45:45 creates two domain types, each of which displays characteristics of the two alcohol components. The methanol induced structures cover the surface, display multilayers with non-linear edges and are stable under imaging. Whereas the 1-propanol induced structures are highly linear and are unstable under imaging.

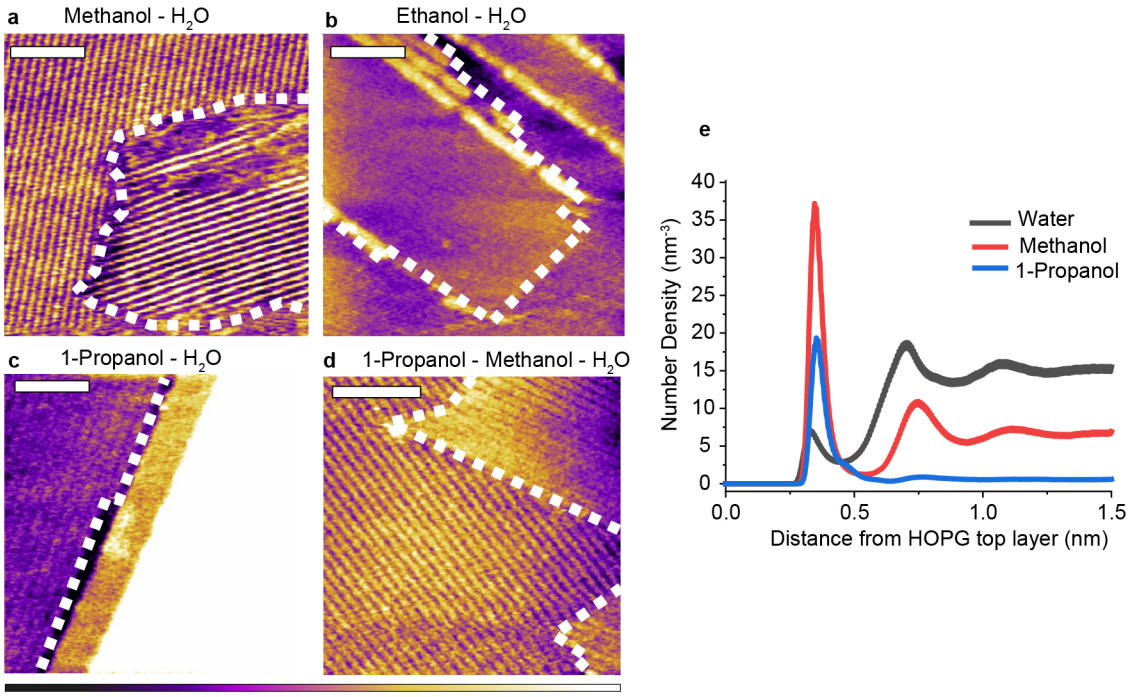

Fig. 5.11: Comparison between the interfacial supramolecular assemblies occurring in different mixtures of water and primary alcohols. The basic monolayer arrangement is visible in the 50:50 methanol-water mixture (a). In contrast, new domains with different periodicities, appearance and clear geometrical edges are formed in the 50:50 ethanol-water (b), 50:50 1-propanol-water (c) and 10:45:45 1-propanol-methanol (d) mixtures. This indicates that a different assembly has taken place. (e) shows linear density plots from a MD simulation of the ternary mixture. As can be seen from this plot, all three molecules are present in the interfacial layer, although the alcohol molecules dominate, consistent with the linear nature of the features observed (as discussed in Chapter 4). Furthermore, methanol still appears to be mixed with the water in the bulk, while 1-propanol demonstrates a clear preference for the surface. The scale bars are 45 nm. The colour scale bar represents a height variation of 0.5 nm in (a), (c) and (d) and 0.8 nm in (b).

Generally, the more elongated, sharp-edged domains observed with larger primary alcohols suggest a stronger epitaxial effect, consistent with the marginally increased alcohol-graphite interaction. This is most obvious for the 1-propanol-water mixture. The fact that only linear structures are observed indicates a predominant role of the one-dimensional molecular chains associated with primary alcohols [18–20]

(discussed in Chapter 4). Indeed, structures become less linear when 1-propanol is replaced with 2-propanol (Figure 5.12), where two novel competing ordered domains appear, exhibiting more frayed and rounded boundaries. The results in 2-propanol also highlights the flexibility of the interfacial hydrogen bonded network, including their ability to incorporate molecules with differing shapes and structures.

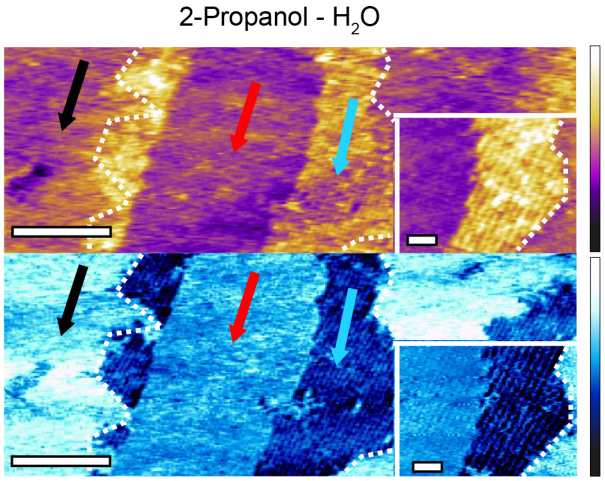

Fig. 5.12: Further variance is seen in a 50:50 2-propanol:water mixture where two types of domains form (red and blue arrows), both demonstrating a clear phase contrast with the graphite surface (black arrow). The domains have longitudinal rows with periodicities of 6.10 ± 0.35 nm (blue arrow) and 4.91 ± 0.45 nm (red arrow). Unlike for 1-propanol, higher resolution of the row (inset) shows the structures have non-linear edges. The scale bars 100 nm in the main image and 20 nm in the inset. The purple colour scale bar represents a height variation of 1 nm in the main image and 0.5 nm in the inset. The blue scale bar represents a phase variation of 15^{o}.

5.4.3 1-Hexanol

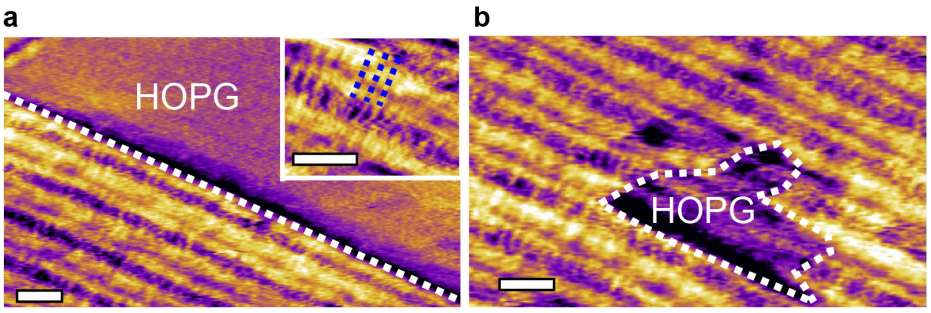

Fig. 5.13: Structures formed in a 1-hexanol-water mixture. In (a) rows with clean edges are visible (outlined by dashed white line) that exhibit a perpendicular substructure with periodicity of 0.89± 0.08 nm (blue dashed lines in inset). When repeatedly scanning the same area the AFM tip creates gaps within the monolayer (b) (white dashed line), exposing the HOPG surface below. The scale bars are 5 nm. The purple colour scale bar represents a height variation of 1 nm.

The largest primary alcohol still able to mix with water is 1-hexanol ($C_6H_{14}O$) with a solubility limit of around 0.7% in ultrapure water. With a carbon backbone twice as long as 1-propanol, the interaction between 1-hexanol and the HOPG surface is significantly stronger in water, thereby offering an ideal system to test the limit of hydrogen bond-based group stabilisation as opposed to traditional surface bound self-assembly. Pure n-hexanol naturally forms ordered structure at the surface of HOPG (from vapour) at temperatures below -10 ^{o}C [21] whereas shorter alcohols require significantly lower temperatures to form ordered structures in similar experiments (e.g. -130 ^{o}C for methanol [20]).

When at its solubility limit in water, 1-hexanol forms self-assembled structure with several different features that can be resolved with molecular resolution. An example structure can be seen in Figure 5.13a which retains a structure comparable in shape and size to the basic methanol-water monolayer. Given the low concentration of hexanol, the small amounts of methanol naturally produced by water catalysis (Chapter 3) may be responsible for creating basic monolayers. However, the presence of hexanol appears to destabilise these structures which can easily be removed from the surface with the AFM tip to expose the HOPG underneath (Figure 5.13b). This is an unusual behaviour for the basic methanol-water monolayers and suggests that the system is being disrupted by the addition of 1-hexanol, to

the point where the intermolecular hydrogen bonds are no longer sufficient to stabilise the monolayers. The system appears to have finally reached the point where direct molecule-substrate interactions can seriously compete with hydrogen bonded molecular networks to drive and control the self-assembly.

This conclusion is also backed by a MD simulation of the water-hexanol system. The simulation was performed for a system consisting of a 10:45:45 hexanol-methanol-water mixture at the interface with 16 layers of graphite in a super-cell geometry. The total number of atoms is approximately 22,000 and the simulation covered 16 ns (Figure 5.14a, see methods for more details). The relatively high concentration of hexanol was chosen to reflect its expected increased concentration at the interface with HOPG when compared to bulk concentrations [4, 22, 23], as discussed in Chapter 4. The presence of methanol accounts for the small quantities of methanol present at the interface due to the *in situ* catalysis of water (see Chapter 3), which may play a role here due to the relatively low hexanol bulk concentration at saturation (0.7%).

The simulation shows the formation of a self-assembled solid-like layer of molecules dominated by the hexanol (Figure 5.14b and c). The most common arrangement consists of hydrogen-bonded parallel chevrons of hexanol molecules (Figure 5.14b), a result previously observed both experimentally and computationally [21, 24, 25]. Within this molecular layer, the oxygen groups of each chevron are separated by an average distance of 1.52 ± 0.01 nm. Interestingly, this computationally obtained molecular arrangement coincided with features observed experimentally, Figure 5.14d. This remarkable agreement validates both the experimental and computational results, bearing in mind the differences in hexanol concentration between experiments and theory. The simulations represent an extreme case where the hexanol concentration is far larger than the 0.7% experimental bulk concentration. This is needed to compensate for the limited time and size of the simulation box. Therefore the experimental observations are not expected to match the simulations over the whole interface due to other possible arrangements and kinetic traps at lower hexanol and methanol concentrations. Indeed, simulations show that water and methanol molecules (green and pink circle Fig. 5.14c) are involved in the hydrogen bonded networks. They can remain hydrogen bonded to hexanol molecules within the structured layer for up to 10 ns, with some methanol molecules remaining indefinitely embedded in the network. The involvement of both methanol and water

also supports the idea of the interfacial molecular assemblies being stabilised by an extended hydrogen bonded network.

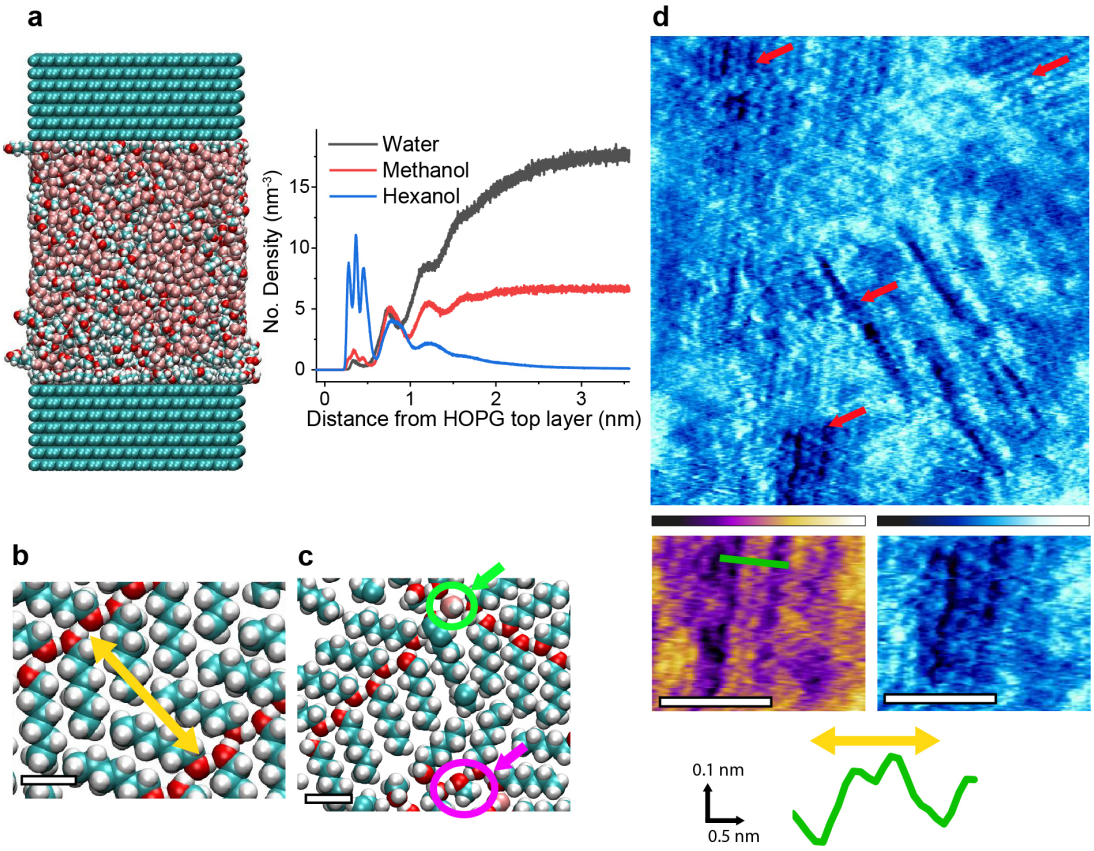

Fig. 5.14: Molecular assemblies forming at the surface of HOPG in water-hexanol mixtures. MD-simulations of the system were carried out using a box of 10.07 nm × 5.53 nm × 11.3 nm with periodic boundary conditions (a). The solution comprises 8,000 molecules composing a 10:45:45 hexanol:methanol:water mixture. Linear number density plots of the molecules indicate the interfacial layer is dominated by hexanol, although both methanol and water are still present. Snapshots of the interfacial molecular arrangement (b, c) taken within 0.6 nm of the HOPG surface reveal a hexanol self-assembled monolayer with a periodicity of 1.52 ± 0.01 nm ((b), yellow arrow). Water molecules (green circle) and methanol (pink circle) are also present in the assembly (c). (d) High-resolution AFM images in a water solution containing 0.7% hexanol (saturation) also reveal multiple different features (red arrows). Some of the features (inset below (d)) exhibit a periodicity of 1.55 ± 0.05 nm (yellow arrow on green profile). The scale bars are: (b-c) 1 nm and (d) 5 nm. The purple colour scale bar represents a height variation of 0.8 nm. The blue scale bar represents a phase bar represents a phase variation of 15^o.

The simulations also reveal an important point: direct molecular-substrate interactions can modulate the formation timescale of supramolecular structures. In Chapter 4, the MD simulations of the aqueous methanol, ethanol and 1-propanol mixtures

were not able to access the long timescales associated with group nucleation events. In contrast, the stronger interaction between hexanol and HOPG considerably increases its residence time at the interface, as well as introducing additional entropic effects which may facilitate molecular adsorption, rendering the nucleation of ordered structures computationally accessible using the present direct MD simulations.

5.5 Assemblies on other hydrophobic surfaces

Overall, the flexibility of interfacial self-assembly through group-effects hinges on the weak interactions between individual molecules and the surface of the solid, so as to prioritise group interactions between assembling molecules. Thus far, HOPG has been used as the solid of choice. HOPG is hydrophobic, inert, uniformly flat apart from step edges and therefore interacts very weakly with the monolayer. These weak interactions between individual molecules and the surface of the solid are key in promoting the group interactions between assembling molecules which determines the resulting supramolecular structure. Hence the HOPG serves more as a solid interface, which reduces the conformational entropy and encourages monolayer formation, rather than being the key stabilising factor. Therefore in principle, the results with HOPG can be extended to any hydrophobic region flat enough to enable self-assembly. In this final section, two different surfaces shall be considered; the amphiphilic graphene oxide (GrO) and the highly ordered hydrophobic molybdenum disulfide (MoS_2).

5.5.1 Graphene Oxide

Graphite oxide (GrO) is the name given to the heterogeneous material whose chemical structure generally contains sheets of graphite with additional function groups such as epoxies and hydroxy groups across the graphite planes and carboxyl groups at the edges [26]. Since the successful preparation and verification of mechanically exfoliated single layers of graphite (graphene) [27] research in carbon related materials has grown exponentially. This interest has been extended to GrO, which retains some of the unique electronic properties of graphene, but the presence of hydrophilic groups make GrO soluble in water, opening new avenues for applications in water

fliltration [28] and ion sieving [29] along with molecular sensing [30].

Due to the presence of the hydrophilic groups on its surface, GrO has a distribution of hydrophilic and hydrophobic regions. Furthermore it is possible to isolate individual GrO flakes on substrates for use with AM-AFM. Here, single GrO flakes have been deposited onto a HOPG substrate so as to offer a clear comparison with the basic monolayer visible on HOPG (Figure 5.15a, yellow arrow).

Larger row-like structures can be observed on GrO in water-methanol mixtures (Figure 5.15 a-c). However, the GrO surface still has topological and chemical inhomogeneity at the nanoscale [26] which precludes the formation of highly regular structures. Instead the rows on GrO exhibit some variability in width and periodicity and are not visible everywhere on the surface. Figures 5.15 d-e show the same experiment for just ultra-pure water. Here the exposed HOPG surface is bare as expected and the GrO flake shows no clear regular pattern (Figure 5.15f).

The additional hydrophilic epoxy, hydroxyl and carboxyl groups randomly distributed across the surface [26] renders the GrO hydrophilic at the macroscale, but this does not exclude nanoscale hydrophobic graphene domains able to template the monolayer self-assembly. Indeed, selective intercalation of GrO sheets has been reported in water-methanol mixtures, consistent with the presence of a specific molecular arrangement of the liquid [31]. The fact that stable structures are able to form suggests that the hydrophilic groups may be simply localised enough to allow the assembly to bridge between hydrophobic nanodomains [32, 33]. Confirming this would involve knowing the specific distribution of hydrophilic groups on the GrO, a task beyond this study.

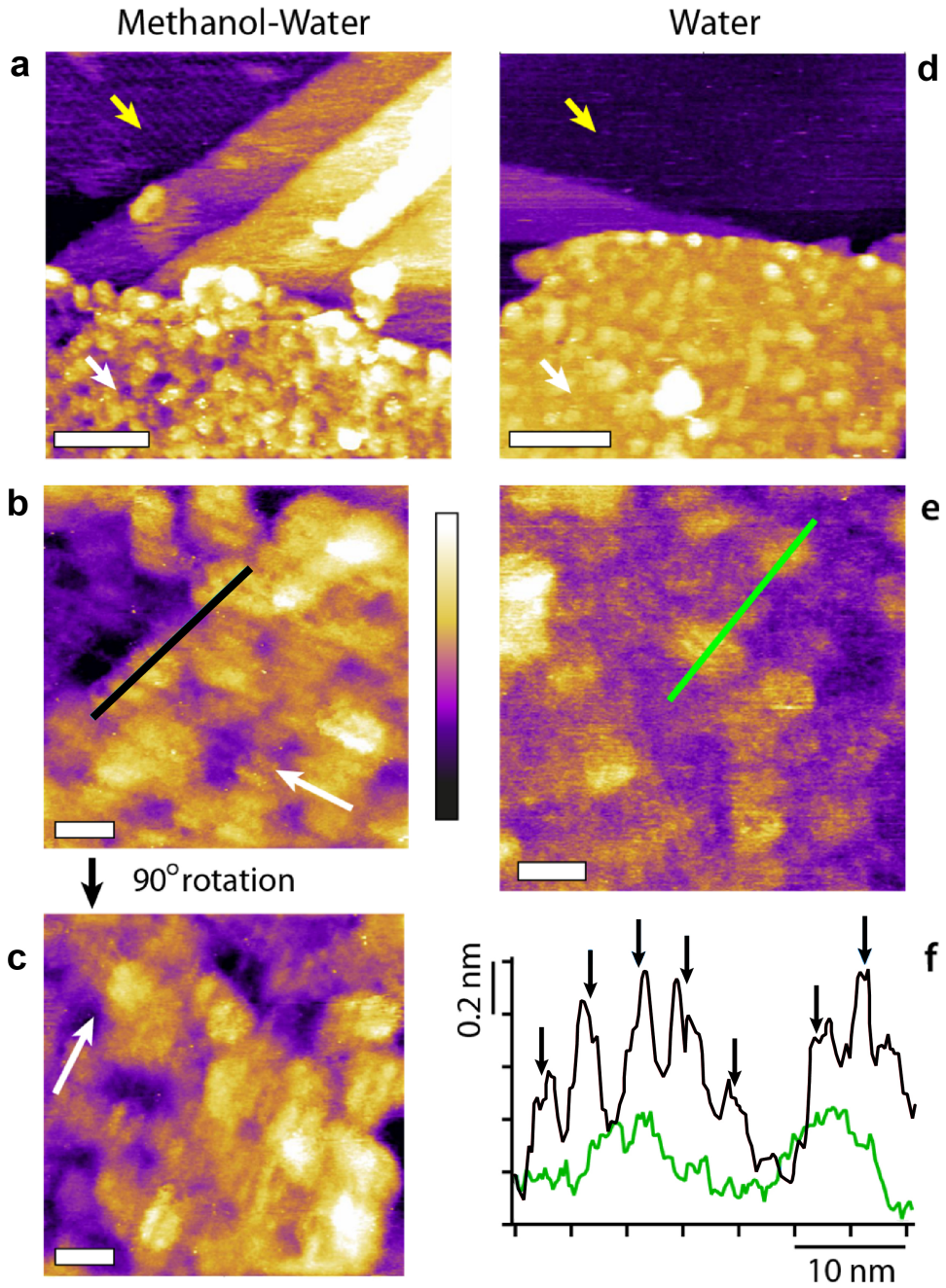

Fig. 5.15: (a) Self-assembly on a flake of GrO in a 50:50 methanol-water mixture. The assembly is less obvious due to the intrinsic roughness of the GrO (a, white arrow) compared to the underlying HOPG substrate where rows are clearly visible (a, yellow arrow). Longitudinal features are however visible at high magnification which remain when the sample is rotated, indicating they are not an imaging artefact (b-c). (d-e) show the same experiment performed in ultrapure water. Here the yellow arrow denotes the bare graphite surface. (f) shows line profiles taken on top of the GrO flake in (b) and (e). No clear periodic features are seen for the ultrapure water case (green line). However, equidistant features are seen in the mixture; corresponding to average separation of 4.5 ± 0.5 nm. The scale bars are 50 nm (a) and(d) and 10 nm (b), (c) and (e). The colour scale bar is 2 nm in all except (e) where it is 0.8 nm.

5.5.2 *Molybdenum disulfide*

The nanoscale disordered GrO surface cannot stabilise large areas of uniform structures, despite clear small areas of alcohol-water assemblies having formed. This is consistent with the well known importance of flat surfaces and regular nanoscale periodicity for supporting self-assembly, as discussed in the Chapter 1. MoS_2 shares many similarities with HOPG such as its hydrophobicity and ability to be cleaved so as to form large, atomically flat areas suitable for assisting self-assembly. This makes MoS_2 a perfect system to demonstrate that alcohol-water monolayers are not surface specific and can in principle form on any atomically flat substrate.

When a freshly cleaved MoS_2 surface is immersed into a 50:50 mixture of methanol and water, highly ordered domains composed of row-like structures immediately appear (Figure 5.16a). The direction of the domains are orientated at 120^o with respect to each other (Figure 5.16b and c) indicating an epitaxial influence like that seen for the structures on HOPG. Furthermore, the row pattern itself is similar to that observed on HOPG, with a periodicity of 5.45 $\pm$ 0.05 nm. MoS_2 has a lattice parameter which is very close to that of HOPG. Considering the fact that the supramolecular pattern produced depends on the substrate lattice parameter [4], this similar row periodicity suggests a molecular level arrangement on MoS_2 that shares some characteristics with those forming on HOPG. Indeed, the computational simulations described in Chapter 1 indicate that the monolayers formed in mixtures of water and methanol are likely composed of repeating stable units, or building blocks, such as the square motifs of two methanol and two water molecules.

Nonetheless, using MoS_2 as the supporting surface impresses unique properties on the supramolecular structures and their kinetics. For instance, the molecular domains prefer an elongated growth with single row progressing longitudinally (Figure 5.16b and c). This characteristic elongated growth of self-assembled monolayers on MoS_2 was also observed in a study using peptides [34]. In this study they also investigated the impact of swapping MoS_2 for HOPG and found that on HOPG, the peptide monolayers gradually drifted across the surface, indicating they are less strongly bound. This may explain the elongated features seen in our experiments. If the structures are more strongly bound to the MoS_2 surface, the epitaxial effect will be greater, giving the structures an energetic gain when following one of the substrates axis of symmetry. This idea is supported by the slow growth rates seen

for the structures on MoS_2 (Figure 5.16d and e); since growth is preferred along a substrate axis, it is inevitably limited by the number of configurations allowing it, resulting in a slower average growth rate.

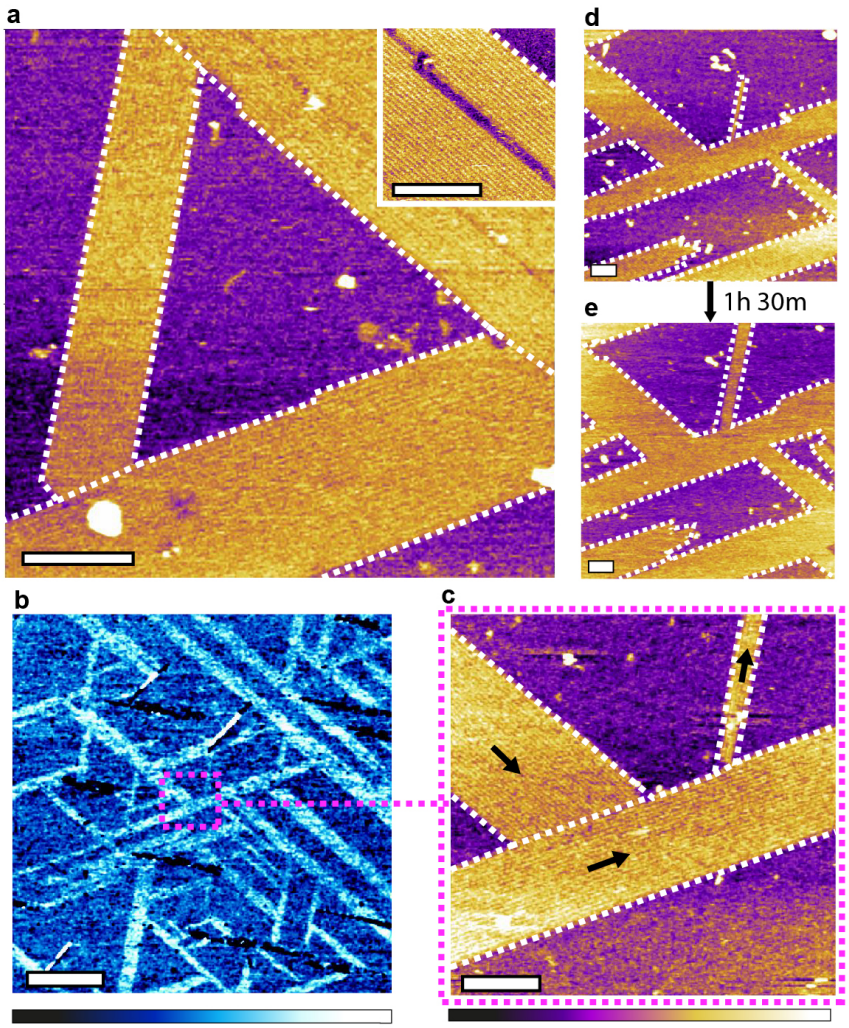

Fig. 5.16: Molecular assemblies forming on MoS_2 in a 50:50 methanol-water mixture. (a) Shows self-assembled domains composed of row patterns developing epitaxially (white dashed line outline) and orientated at 120^o with respect to each other. The rows are clearly defined (inset) with a spacing of 5.45 ± 0.05 nm. (b) shows a phase image of the structures (lighter colours) which tend to form elongated linear domains. The direction of growth is highly influenced by the hexagon symmetry of the substrate resulting in three clear growth directions as can be seen in the topographic image (c). Here three domains have come into contact causing them to stop growing along their main axis. The row structures grow only by 24.6 ± 0.10 % over 1 h 30 min (d and e) though a 'fingering' mechanism where existing rows tend to elongate longitudinally. The surface would have been fully covered over the same time period with HOPG. The scale bars in all the images represent 100 nm other than in (b) where it represents 1 μm. The purple colour scale bars represent a variation of 1 nm in the main images and 0.5 nm in the inset. The blue scale bar represents a phase variation of 3^o.

Control experimenters were also conducted with pure water deposited on MoS_2. No structures are observed, even after several hours of imaging (Figure 5.17 a and b). This not only confirms that the features observed are unique to the alcohol-water mixtures, it also corroborates with the results presented in Chapter 3 where HOPG is shown to act as a catalyst for the production of methanol in water droplets.

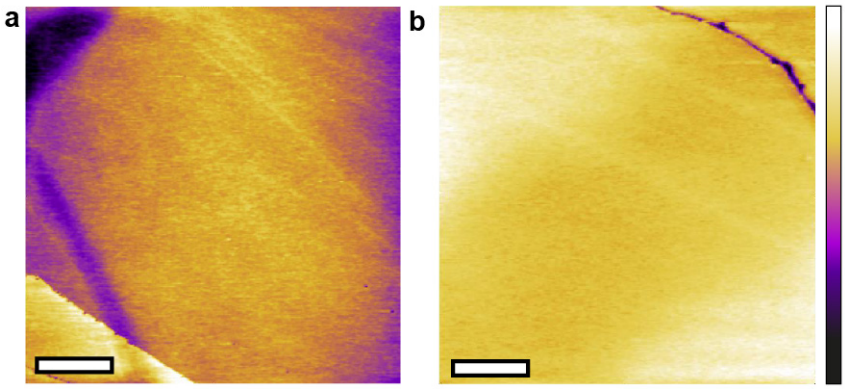

Fig. 5.17: AFM topographic images of MoS_2 in ultrapure water after 2 hours. No structures are visible at low (a) and high resolution (b) in the absence of added alcohol. The sample was imaged for a further 6 hours during which no features were observed. The scale bars represent 500 nm (a) and 100 nm (b). The purple scale bar represents a height variation of 1.5 nm in both.

5.6 Discussion

The results presented in this chapter are investigations into the self-assembly of small molecules at interfaces through group effect, without relying on specific or covalent bonds. Group-based self-assembly of small molecules can be achieved using simple systems (here water and alcohol) where the interactions between molecules in the bulk solution is strong enough to enable their self-assembly into supramolecular structures once stabilised at an interface. The self-assembly can be significantly influenced through external stimuli, with three main routes available here: (1) the addition of small quantities of influencer molecules such as salts and other small hydrogen bonding molecules to modulate both the morphology of the interfacial assemblies and their interactions with the local environment; (2) varying the ratio of alcohol to the other components within the solution; and (3) altering the alcohol-substrate interactions also provide control on the supramolecular assemblies. These three routes can furthermore function in conjunction with one another. For example, in the ternary 1-propanol-methanol-water mixtures, the nucleation of multiple

well-ordered features characteristic of each component were observed (Figure 5.10). These strategies make it is possible to create certain structures with reproducible features and, to an extent, predictable supramolecular assemblies. The key is to vary the parameters progressively, here using alcohols similar to methanol in molecular structure, symmetry and chemical properties, so as to identify the main evolving trends.

Structures with linear features and well-defined, but varying, periodicities could be consistently created, starting from the basic methanol-water system. For methanol-based mixtures the periodicity of the linear features was consistently ~ 5.3 nm and the height of the linear monolayers was ~ 0.3 nm, both consistent with the previous observations outlined in Chapter 1. The linear periodicity of the ethanol-water, 1-propanol-water and hexanol-water structures structures varied between ~ 3.9 nm (Figure 5.9b) and ~ 7.2 nm (Figure 5.11c) and the monolayer height remained consistently ~ 0.3 nm. The large variation in linear periodicities seen with the larger alcohol structures is consistent with the larger alcohol molecules having multiple energetically favourable configurations at the interface (as seen in Chapter 4) which also makes obtaining reproducible structures for these systems more challenging. There is no clear trend between alcohol size and the periodicity of the features (i.e. ethanol induced features in Figure 5.11a have a smaller periodicity than those observed in methanol-based systems).

The adjunction of influencers tends to induce more dramatic changes, which can often be rationalised considering the molecular structure of the influencer. For example, the right angle symmetry of the sophisticated assembly obtained in presence of phosphate ions is likely due to the tetragonal structure of the ion. The addition of sodium and potassium chloride had a comparable influence on the structures, both tending to reside on top of already existing linear features. Their impact was less than that of the phosphate ions and they did not alter the linear features of the structures due to their inability to directly form hydrogen bonds. These are, however, only plausible explanations and the system is also sensitive to the concentrations of the other molecules able to compete with the influencers for hydrogen bonds. This sensitivity, along with the unknown influence of defects such as step edges and experimental restrictions, such as the balance between AFM scanning speeds and the subsequent attainable resolution, makes performing quantitative analysis of the rate of growth and the domain size of the various structures difficult and will need

to be the focus of future work (as will be discussed in Chapter 6).

The results on MoS_2 and GrO indicate a significant degree of flexibility of the group-based strategy which could be extended to a wide range of surfaces, including macroscopically hydrophilic surfaces provided the surface exhibits sufficient nanoscale hydrophobic domains. Further work is however needed to fully explore this idea; the results on GrO are less clear than on the other substrates, but control experiments conducted in pure water do not show comparable row-like features. The possibility of extending the concept of group-based self-assembly to other hydrogen bonding small molecules will also require systematic investigation, starting with molecular systems such as ketones, amides and aldehydes.

5.7 Conclusion

In this chapter the concept of group-based self-assembly of small molecules is explored at solid-liquid interfaces. The main difference with standard self-assembly is the fact that the molecules do not significantly interact with the solid and would not durably reside at the interface when isolated. Instead, strong intermolecular interactions allow the molecules to work in group, nucleating ordered structures large enough to remain attached to the solid which then stabilised the system. The fact that individual molecules interact weakly with the solid has one key consequence: the resulting supramolecular assembly can be dramatically influenced by small amounts of foreign molecules or simply by changing the molecular ratios between the main assembling molecules to achieve multiple distinct structures. The idea is illustrated here using water-alcohol mixture spiked with common small molecules to create a wide range of stable supramolecular assemblies at the interface with HOPG at room temperature. These structures can in turn modify the solvation properties of the solid on which they assemble.

Given the diminished importance of specific surface-liquid interactions, group-based self-assembly can in principle occur on many hydrophobic surfaces, here exemplified with MoS_2 and GrO. Additionally, the concept may be applied to many other small molecule systems where the molecules are able to form hydrogen bonds and weakly interact with a surface. Further investigations are needed to fully explore the concept's applicability and limitations across different systems and derive a deeper

understanding of the molecular details of the structures created, but the concept's simplicity and the high degree of flexibility opens new research avenues for nanotechnology.

5.8 Additional method details

Sample preparation

Details of the chemicals used can be found in Chapter 2. In a typical experiment, a liquid droplet (around 200 µL) of solution was deposited on a freshly cleaved HOPG or MoS_2 substrate (both from SPI supplies, West Chester, PA, USA) mounted on a stainless steel disk. In all cases the substrates were baked at >120 ^{o}C for 15 minutes to remove any contaminants[35] before immediately depositing the droplet. The graphene oxide used was synthesised from graphite powder using a modified Hummers method [36], presented in detail elsewhere [37]. To settle the flakes on the HOPG surface a droplet of 1 g/L graphene oxide was deposited on the HOPG and left for 5 minutes before being rinsed with ultrapure water. After the rinsing the methanol water droplet was added in a similar manner to the other experiments on HOPG and MoS_2.

Amplitude Modulation Atomic Force Microscopy

All the samples were images at 20.0 ± 0.1 °C except for the results presented in Figures 5.9b and c which were acquired at 30 and 35°C respectively in an attempt to encourage novel molecular assemblies. For full details regarding AM-AFM, the reader is referred to Chapter 2.

Frequency Modulation Atomic Force Microscopy

No temperature control was possible using this system so all samples were at room temperature. For full details regarding FM-AFM and 3D-SFM, the reader is referred to Chapter 2. Figure 5.18 presents details of the filtering and averaging procedure. The procedure is applied here on the set of measurements taken in the 5:95 methanol-PBS mixture and used in Figure 5.8 and was performed by K. Miyazawa from Kanazawa University. Details of the algorithm used are described elsewhere [14].

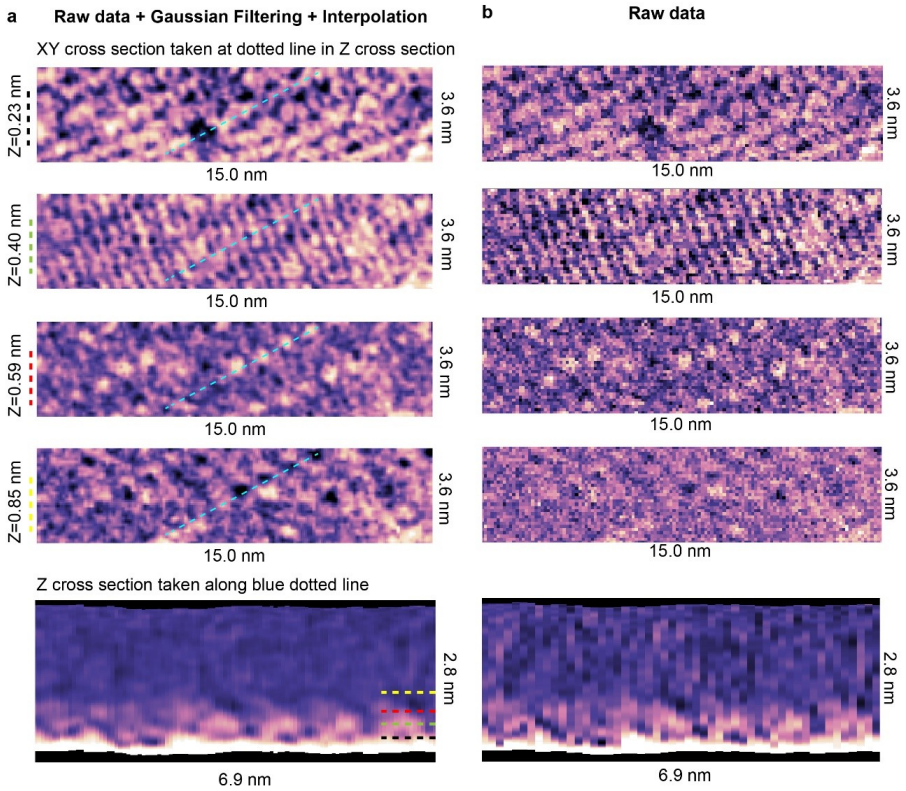

Fig. 5.18: (a) shows the processed data after Gaussian filtering and interpolation procedures have been applied using a home-built software. The raw data is shown for comparison in (b). The images presented in Figure 5.8c and d are then obtained by applying a further average filtering process that uses a pattern matching algorithm [14].

MD Simulations

The methanol molecules, 1-propanol molecules, hexanol molecules, Na^+ ions and HPO_4^{2-} ions were all described by the all atom OPLS force field [38]. The water was described by the TIP4P model [39]. The hexanol and 1-propanol simulations used the same protocol as that described for the other alcohol-water mixtures in Chapter 4. For the phosphate ion simulation, using the OPLS description for a system with Na_2HPO_4 in water with a weight percentage of 30% at 70^{o}C gave a liquid density of 1203 kg m^{-3}, which is within 2.5% of the experimentally observed value (1232 kg m^{-3}) [40]. The system was a NPT ensemble maintained at 298 K and 1 bar using a velocity rescale thermostat [41] and Parrinello-Rahman barostat [42, 43], with coupling times of 0.5 ps and 1 ps, respectively. The simulation was performed with a 0.002 ps timestep and thus all bonds were constrained using the Linear Constraint Solver (LINCS) algorithm [44]. The mixture contained an equal

number of water and methanol molecules as well as Na^+ and HPO_4^{2-} ions corresponding to a weight percentage of 1%. This is higher than would be the case for the 137 mM Na_2HPO_4 mixture studied in the experiments, but can be justified by the limited size and timescale of the simulations. Furthermore, it has been shown that similar molecules tend to cluster together in aqueous solutions and the local concentration hence fluctuates. Prior to analysis, the liquid box was equilibrated for 1 ns. Then, a further 60 ns of simulations were performed during which the behaviour of the Na^+ and HPO_4^{2-} ions was observed. The snapshots in Figure 5.3 were taken 1 ns into the run. As the simulation progressed, the ions gradually became permanently clumped together. At the end of the full 60 ns, all of the charged molecules remained clustered together (Figure 5.19). Therefore the simulation was not extended further. This protocol is similar to previous procedures adopted to simulate processes of nucleation and growth for similar systems [45–47]. However, obtaining a meaningful average cluster size for comparison with the experimental system is beyond computational feasibility due to the size of the simulation box (5 x 5 x 5 nm) and the reported local fluctuations in ion density [9]. The size of the box required to obtain a good comparison is not known at this point. Furthermore, highly charged molecules are reported to be difficult to simulate and can require force fields relying on quantum mechanical derivations [7, 48, 49]. Thus for a better comparison with the experimental data, it is recommended that such a force field be used. Nonetheless, the result obtained here was compared with previously published results obtained for HPO_4^{2-} ions in a calcium diphosphate system, and which uses a force field derived specifically for phosphates [50]. The published study reports a similar effect where the HPO_4^{2-} ions form clusters with the hydroxyl groups facing outwards [9], consistent with the findings reported here.

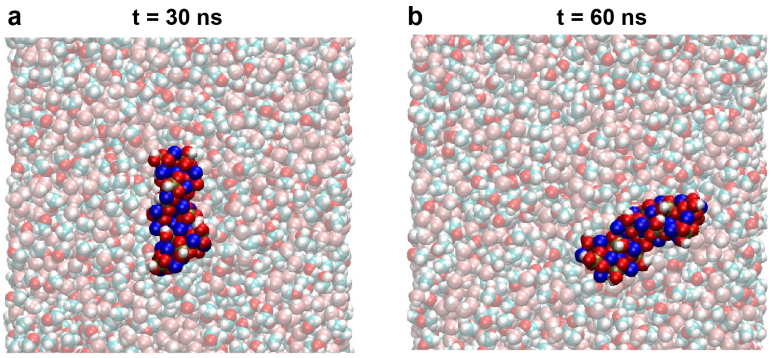

Fig. 5.19: Snapshots of the disodium phosphate simulations taken at (a) t = 30 ns and (b) 60 ns, demonstrating that the phosphate and sodium ions form permanent clusters. All ions in the simulation are shown and the water and methanol molecules have been made partially transparent.

References: Chapter 5

[1] T. D. Li, J. Gao, R. Szoszkiewicz, U. Landman, E. Riedo, "Structured and viscous water in subnanometer gaps", *Physical Review B - Condensed Matter and Materials Physics* **2007**, *75*, 1–6.

[2] D.-Y. Wang, C.-Y. Wei, M.-C. Lin, C.-J. Pan, H.-L. Chou, H.-A. Chen, M. Gong, Y. Wu, C. Yuan, M. Angell, Y.-J. Hsieh, Y.-H. Chen, C.-Y. Wen, C.-W. Chen, B.-J. Hwang, C.-C. Chen, H. Dai, "Advanced rechargeable aluminium ion battery with a high-quality natural graphite cathode", *Nature Communications* **2017**, *8*, 14283.

[3] W. Foster, J. A. Aguilar, H. Kusumaatmaja, K. Voïtchovsky, "In Situ Molecular-Level Observation of Methanol Catalysis at the Water-Graphite Interface", *ACS Applied Materials and Interfaces* **2018**, *10*, 34265–34271.

[4] K. Voitchovsky, D. Giofrè, J. J. Segura, F. Stellacci, M. Ceriotti, "Thermally-nucleated self-assembly of water and alcohol into stable structures at hydrophobic interfaces", *Nature Communications* **2016**, *7*, 13064.

[5] M. Nagasaka, K. Mochizuki, V. Leloup, N. Kosugi, "Local structures of methanol-water binary solutions studied by soft X-ray absorption spectroscopy", *Journal of Physical Chemistry B* **2014**, *118*, 4388–4396.

[6] R. Thiruvengadathan, V. Korampally, A. Ghosh, N. Chanda, K. Gangopadhyay, S. Gangopadhyay, "Nanomaterial processing using self-assembly-bottom-up chemical and biological approaches", *Reports on Progress in Physics* **2013**, *76*.

[7] R. Qi, Z. Jing, C. Liu, J. P. Piquemal, K. N. Dalby, P. Ren, "Elucidating the Phosphate Binding Mode of Phosphate-Binding Protein: The Critical Effect of Buffer Solution", *Journal of Physical Chemistry B* **2018**, *122*, 6371–6376.

[8] R. Pérez, R. García, *Dynamic atomic force microscopy methods - Surface Science Reports.pdf*, *Vol. 47*, **2002**, pp. 197–301.

[9] G. Mancardi, C. E. Hernandez Tamargo, D. Di Tommaso, N. H. De Leeuw, "Detection of Posner's clusters during calcium phosphate nucleation: A molecular dynamics study", *Journal of Materials Chemistry B* **2017**, *5*, 7274–7284.

[10] M. Ricci, W. Trewby, C. Cafolla, K. Voïtchovsky, "Direct observation of the dynamics of single metal ions at the interface with solids in aqueous solutions", *Scientific Reports* **2017**, *7*, 1–12.

[11] W. Trewby, J. Faraudo, K. Voïtchovsky, "Long-lived ionic nano-domains can modulate the stiffness of soft interfaces", *Nanoscale* **2019**, *11*, 4376–4384.

[12] M. Cruz Sanchez, J. Gujt, S. Sokolowski, O. Pizio, "Effects of ion concentration and solvent composition on the properties of water-methanol solutions of NaCl. NPT molecular dynamics computer simulation results", *Condensed Matter Physics* **2018**, *21*, 1–17.

[13] T. Fukuma, Y. Ueda, S. Yoshioka, H. Asakawa, "Atomic-Scale distribution of water molecules at the mica-Water interface visualized by three-Dimensional scanning force microscopy", *Physical Review Letters* **2010**, *104*, 2–5.

[14] K. Miyazawa, N. Kobayashi, M. Watkins, A. L. Shluger, K. I. Amano, T. Fukuma, "A relationship between three-dimensional surface hydration structures and force distribution measured by atomic force microscopy", *Nanoscale* **2016**, *8*, 7334–7342.

[15] T. Fukuma, "Water distribution at solid/liquid interfaces visualized by frequency modulation atomic force microscopy", *Science and Technology of Advanced Materials* **2010**, *11*, 033003.

[16] I. Schlesinger, U. Sivan, "Three-Dimensional Characterization of Layers of Condensed Gas Molecules Forming Universally on Hydrophobic Surfaces", *Journal of the American Chemical Society* **2018**, *140*, 10473–10481.

[17] M. R. Uhlig, D. Martin-Jimenez, R. Garcia, "Atomic-scale mapping of hydrophobic layers on graphene and few-layer MoS2 and WSe2 in water", *Nature Communications* **2019**, *10*, 2606.

[18] T. Takamuku, H. Maruyama, K. Watanabe, T. Yamaguchi, "Structure of 1-propanol-water mixtures investigated by large-angle X-ray scattering technique", *Journal of Solution Chemistry* **2004**, *33*, 641–660.

[19] E. J. W. Wensink, A. C. Hoffmann, P. J. Van Maaren, D. Van Der Spoel, "Dynamic properties of water/alcohol mixtures studied by computer simulation", *Journal of Chemical Physics* **2003**, *119*, 7308–7317.

[20] K. Morishige, K. Kawamura, A. Kose, "X-ray diffraction study of the structure of a monolayer methanol film adsorbed on graphite", *The Journal of Chemical Physics* **1990**, *93*, 5267–5270.

[21] K. Morishige, T. Kato, "Chain-length dependence of melting of n-alcohol monolayers adsorbed on graphite: n-hexanol, n-heptanol, n-octanol, and n-nonanol", *Journal of Chemical Physics* **1999**, *111*, 7095–7102.

[22] J. Sung, K. Park, D. Kim, "Surfaces of Alcohol-Water Mixtures Studied by Sum-Frequency Generation Vibrational Spectroscopy", *The Journal of Physical Chemistry B* **2005**, *109*, 18507–18514.

[23] M. Lundgren, N. L. Allan, T. Cosgrove, "Wetting of water and water/ethanol Droplets on a non polar surface: A Molecular Dynamics Study.", *Langmuir* **2002**, *18*, 10462–10466.

[24] T. Yang, S. Berber, J. F. Liu, G. P. Miller, D. Tománek, "Self-assembly of long chain alkanes and their derivatives on graphite", *Journal of Chemical Physics* **2008**, *128*.

[25] L. Wang, Y. Song, B. Zhang, E. Wang, "Adsorption behaviors of methanol, ethanol, n-butanol, n-hexanol and n-octanol on mica surface studied by atomic force microscopy", *Thin Solid Films* **2004**, *458*, 197–202.

[26] W. Gao, "The chemistry of graphene oxide", *Graphene Oxide: Reduction Recipes Spectroscopy and Applications* **2015**, 61–95.

[27] K. S. Novoselov, A. K. Geim, S. V. Morozov, Y. Z. D. Jiang, S. V. Dubonos, I. V. Grigorieva, A. A. Firsov, "Electric Field Effect in Atomically Thin Carbon Films", **2013**, *666*, 666–669.

[28] A. V. Talyzin, S. M. Luzan, "Pressure-induced insertion of liquid acetone into the graphite oxide structure", *Journal of Physical Chemistry C* **2010**, *114*, 7004–7006.

[29] B. Mi, "Graphene Oxide Membranes for Ionic and Molecular Sieving", *Science* **2014**, *343*, 740–742.

[30] J. T. Robinson, F. K. Perkins, E. S. Snow, Z. Wei, P. E. Sheehan, "Reduced graphene oxide molecular sensors", *Nano Letters* **2008**, *8*, 3137–3140.

[31] S. You, J. Yu, B. Sundqvist, L. A. Belyaeva, N. V. Avramenko, M. V. Korobov, A. V. Talyzin, "Selective intercalation of graphite oxide by methanol in water/methanol mixtures", *Journal of Physical Chemistry C* **2013**, *117*, 1963–1968.

[32] J. J. Kuna, K. Voïtchovsky, C. Singh, H. Jiang, S. Mwenifumbo, P. K. Ghorai, M. M. Stevens, S. C. Glotzer, F. Stellacci, "The effect of nanometre-scale structure on interfacial energy", *Nature Materials* **2009**, *8*, 837–842.

[33] N. Giovambattista, P. G. Debenedetti, P. J. Rossky, "Hydration behavior under confinement by nanoscale surfaces with patterned hydrophobicity and hydrophilicity", *Journal of Physical Chemistry C* **2007**, *111*, 1323–1332.

[34] J. Chen, J. J. De Yoreo, S. Zhang, E. Zhu, Y. Huang, J. Liu, H. Heinz, Z. Lin, X. Duan, "Building two-dimensional materials one row at a time: Avoiding the nucleation barrier", *Science* **2018**, *362*, 1135–1139.

[35] D. Martinez-Martin, R. Longuinhos, J. G. Izquierdo, A. Marele, S. S. Alexandre, M. Jaafar, J. M. Gómez-Rodríguez, L. Bañares, J. M. Soler, J. Gomez-Herrero, "Atmospheric contaminants on graphitic surfaces", *Carbon* **2013**, *61*, 33–39.

[36] W. S. Hummers, R. E. Offeman, "Preparation of Graphitic Oxide", *Journal of the American Chemical Society* **1958**, *80*, 1339.

[37] G. X. Zhou, J. Zhong, H. Zhang, X. Hu, J. Wu, N. Koratkar, X. Shi, "Influence of releasing graphene oxide into a clayey sand: physical and mechanical properties", *RSC Advances* **2017**, *7*, 18060–18067.

[38] W. L. Jorgensen, D. S. Maxwell, J. Tirado-Rives, "Development and testing of the OPLS all-atom force field on conformational energetics and properties of organic liquids", *Journal of the American Chemical Society* **1996**, *118*, 11225–11236.

[39] J. L. Abascal, C. Vega, "A general purpose model for the condensed phases of water: TIP4P/2005.", *The Journal of chemical physics* **2005**, *123*, 234505.

[40] M. I. Nikandrov, Y. I. Mikhailov, "Density and viscosity of sodium phosphate solutions", *Russian Journal of Applied Chemistry* **2005**, *78*, 1538–1539.

[41] G. Bussi, D. Donadio, M. Parrinello, "Canonical sampling through velocity rescaling", *Journal of Chemical Physics* **2007**, *126*.

[42] M. Parrinello, A. Rahman, "Polymorphic transitions in single crystals: A new molecular dynamics method", *Journal of Applied Physics* **1981**, *52*, 7182–7190.

[43] S. Nosé, M. L. Klein, "Constant pressure molecular dynamics for molecular systems", *Molecular Physics* **1983**, *50*, 1055–1076.

[44] B. Hess, H. Bekker, H. J. Berendsen, J. G. Fraaije, "LINCS: A Linear Constraint Solver for molecular simulations", *Journal of Computational Chemistry* **1997**, *18*, 1463–1472.

[45] J. Ma, "A molecular dynamics study on the nucleation of calcium phosphate regulated by collagen", *Journal of Materials Science* **2014**, *49*, 3099–3106.

[46] N. H. De Leeuw, S. C. Parker, "Surface structure and morphology of calcium carbonate polymorphs calcite, aragonite, and vaterite: An atomistic approach", *Journal of Physical Chemistry B* **1998**, *102*, 2914–2922.

[47] N. Almora-Barrios, N. H. De Leeuw, "Molecular dynamics simulation of the early stages of nucleation of hydroxyapatite at a collagen template", *Crystal Growth and Design* **2012**, *12*, 756–763.

[48] L. Rao, Q. Cui, X. Xu, "Electronic properties and desolvation penalties of metal ions plus protein electrostatics dictate the metal binding affinity and selectivity in the copper efflux regulator", *Journal of the American Chemical Society* **2010**, *132*, 18092–18102.

[49] T. Dudev, C. Lim, "Competition among metal ions for protein binding sites: Determinants of metal ion selectivity in proteins", *Chemical Reviews* **2014**, *114*, 538–556.

[50] R. I. Ainsworth, D. D. Tommaso, J. K. Christie, N. H. De Leeuw, "Polarizable force field development and molecular dynamics study of phosphate-based glasses", *Journal of Chem. Phys.* **2012**, *137*.

6.0 Chapter 6: Conclusion and Outlook

6.1 Summary

In this thesis I have investigated the self-assembly of small hydrogen bonding molecules at hydrophobic interfaces in ambient conditions using a base system of alcohol-water mixtures and highly oriented pyrolytic graphite (HOPG). These molecules self-assemble through a group-effect mechanism using extended hydrogen bonded networks between the molecules. The system was investigated using a joint approach of atomic force microscopy (AFM) and molecular dynamics simulations (MD), which enabled the structure and behaviour of the interfaces to be mapped at the molecular scale. In this chapter I will start by outlining the key results from the thesis before discussing the significance of the key results in more detail and then finally introducing what should be addressed in future work. The key results from this work are as follows:

- Micromolar quantities of methanol are catalytically produced at the HOPG-water interface.
  - The most likely reagents for this reaction are water and carbon dioxide from the air.
  - The exact catalysis mechanism is not entirely clear, although the results suggest the most plausible cause is photocatalysis.
  - Applying electric fields enhances the rate of catalysis.
- Aqueous mixtures of methanol, ethanol, 1-propanol, 2-propanol and 1-hexanol are all capable of forming self-assembled monolayers on HOPG through a group-effect mechanism.

- Increasing the size of the hydrophobic group of the alcohol component, and hence the strength of the hydrophobic interaction, enables the formation of multiple stable assemblies for the same alcohol-water system.
  - These structures exhibit sharper edges, potentially due to the increased surface interactions allowing greater surface templating.
  - Assemblies involving 1-propanol and 1-hexanol are less stable than their methanol and ethanol counterparts due to their large hydrophobic groups disrupting hydrogen bond networks.
  - In contrast to the smaller alcohols, features observed experimentally in aqueous 1-hexanol mixtures could also be observed using MD simulations.
- The reliance of methanol-water mixtures on a group-effect mechanism to self-assemble means the subsequent features of the assembly can be altered by the addition of small quantities of hydrogen bonding and non-hydrogen bonding ions, as well as changes in the methanol-water ratio.
  - Adding hydrogen bonding ions results in the formation of small regions of features which are significantly less ordered than those in the pure methanol-water mixtures.
  - The non-hydrogen bonding ions tend to sit on top of the methanol-water structures, which retain their lateral order.
  - Having both hydrogen bonding and non-hydrogen bonding ions present results in the most significant change with the formation of large domains of less ordered features which can co-exist alongside the ordered methanol-water structures.
  - Structures formed at lower methanol concentrations with both the hydrogen bonding and non-hydrogen bonding ions present exhibit a complex solvation landscape, consistent with the dominance of three-dimensional hydrogen bonded networks (see next point).
- The molecular organization of aqueous methanol, ethanol and 1-propanol solutions at the interface with HOPG has a dependence on the alcohol concentration and is linked to the nature of the local hydrogen bond networks. Three regimes were observed as the alcohol concentration increase:
  - Initially the alcohol molecules prefer to stand upright in order to hydrogen bond with water molecules away from the interface.
  - Past a first transition, the alcohol molecules begin to interact with each other at the interface, progressively reducing the concentration of stand-

ing molecules interacting with the bulk hydrogen bond networks.
  - A second transition marks the concentration beyond which the interface is dominated by 1D/2D alcohol networks lying primarily flat on the solid's surface.
- Group-effect self-assembly of small hydrogen bonding molecules is not limited to HOPG and can in principle occur on other atomically flat hydrophobic interfaces (e.g. molybdenum disulphide) as well as non-atomically flat partially hydrophobic interfaces (e.g. graphene oxide).

6.2 General Discussion

From the outset it was predicted that the weak surface interactions and the need for a group-effect would make the small molecule assemblies more sensitive to external influences than traditional self-assembly, which relies on strong surface interactions. This sensitivity, and the fact that the self-assembly of small molecules at interfaces through a group-effect is a recent and relatively unexplored concept, meant it was essential to have a comprehensive understanding of the base system. To this end, a significant portion of this thesis has been dedicated to the study of the general behaviour of alcohol-water mixtures at graphitic interfaces. Specifically, investigations have been performed into the local chemical composition of the water-graphite interface (Chapter 3) and the nature of the alcohol-water interfacial hydrogen bonded networks (Chapter 4). This approach has been justified by the observations made in the final results section (Chapter 5), where I demonstrated that small changes to the base system have a significant impact on the nature of alcohol-water assemblies. This section will further discuss the key results of this thesis along with indicating their wider significance. However, before this discussion, it is also important to reflect on the choice of methods used within this work.

Methods used

Throughout this thesis, the assembled structures were investigated *in situ* using multiple atomic force microscopy (AFM) modes. AFM is generally well suited to surface investigations (as outlined in Chapters 1 and 2) and its versatility proved to be highly beneficial for mapping the local solvation properties of the monolayers using three-dimensional scanning force microscopy (3D-SFM). Furthermore, the

soft imaging conditions of the dynamic amplitude modulation and frequency modulation AFM modes allowed minimal perturbation to the assemblies, whose features were generally independent of tip-effects. However, the information obtainable from AFM did have limitations, especially relating to mapping the chemical composition of the interface. Therefore for a clearer picture, spectroscopic techniques were required (^{1}H NMR in Chapter 3), as were comparisons with molecular dynamics (MD) simulations.

As discussed in Chapter 1, simulating the formation of group-effect stabilised structures using techniques such as MD is highly difficult due to the weak interactions at play, which make the nucleation time-scales inaccessible ($\sim$ minutes) [1]. Nonetheless, MD results regarding concentration-dependant hydrogen bonded networks formed in methanol-water mixtures at the interface with highly orientated pyrolytic graphite (HOPG) provided a reasonable explanation for the concentration dependant assemblies observed with AFM. Moreover, simulations of phosphate ions in a methanol-water mixture indicated the ions preference to form clumps with exposed hydrogen bonding groups, a configuration which has similarities with the experimental observations. Interestingly, for the largest soluble primary alcohol, 1-hexanol, MD simulations were able to capture the formation of self-assembled features observed experimentally. Furthermore, both methanol and water molecules were observed to be embedded at small concentrations within the computationally obtained hexanol structure. This indicates that it may be possible to access the self-assembly of smaller alcohols mixed with water if the system is encouraged towards structure formation, thereby reducing the long time-scales associated with group-effect nucleation events. Structural observations made with high resolution dynamic mode AFM could be used to define the nature of this encouragement, based on the expected final configuration. A computational picture of the assemblies would provide a good foundation for further understanding the nature of the group-effect stabilisation and its response to external stimuli.

Catalytic production of methanol at the HOPG interface from water and volatile organics

In Chapter 5 I demonstrated that when HOPG was swapped with the structurally similar, but chemically distinct, molybdenum disulfide (MoS_2), the production of methanol did not occur (Figure 5.17). This indicates that the catalytic process presented in Chapter 3 is reliant on the chemical composition of HOPG, and thus

this research may impact the development of novel carbon-based catalytic materials [2]. Furthermore, while the catalysis mechanism may not be fully understood, many applications involve water at graphite/graphene interfaces, and thus the resulting self-assembly of the water and methanol molecules is likely to impact their function. It also indicates that future studies into group-effect self-assembly may benefit from using substrates such as MoS_2 to prevent methanol contamination, especially when long periods of liquid-solid contact is required.

The amount of methanol produced is modest in comparison to industrial catalysis techniques. However, the mechanism appears to rely on surface singularities. Therefore, in principle, this can be scaled up through the addition of defects to HOPG, which is currently a expanding field of research [3]. Furthermore, the experiments in Chapter 3 show that the application of an external electric potential enhanced the catalysis rate. Even small surface potentials comparable to that of a silicon nitride AFM tip had a noticeable effect on the amount of methanol present. This observation raises questions about the influence of the probe in scanning probe techniques on the system being studied. Indeed, within this thesis, the subsequent self-assembly of the produced methanol with the water may have caused anomalous results had the source of the methanol not been known.

Impact of local hydrogen bonding behaviour on group-effect self-assembly

In Chapter 4, I presented a computational investigation into the concentration dependent structure of small alcohol-water mixtures at hydrophobic interfaces. The structure of the molecules at the interface was shown to be intrinsically linked to the nature of the local hydrogen bonded networks, which themselves are dependent on the alcohol-water ratio. The nature of the hydrogen bonding networks formed at the interface will likely impact molecular exchange. Therefore this observation will be of wider interest to applications where molecular exchange is pivotal to device function, such as fuel cells [4], separation processes [5], and catalysis [6].

The computational observations of the concentration dependent interfacial organisation of the liquid matched well with experimentally observed features of the methanol-water assemblies on HOPG. Assemblies forming at low methanol concentrations exhibited tetrahedral-like features, and those forming at higher methanol concentrations had linear features. In Chapter 5, three dimensional scanning force microscopy (3D-SFM) demonstrated that the self-assembled structures forming at

low alcohol concentrations have a hydration structure which extends away from the interface, consistent with the description presented in Chapter 4. Similarly, 3D-SFM measurements showed that the linear monolayers associated with higher methanol concentrations did not have any clear hydration layers, consistent with the alcohol molecules preferring to hydrogen bond parallel to the surface. This demonstrates a direct link between the nature of local hydrogen bonded networks present at the interface prior to nucleation, and those of the resulting self-assembly. A search of previous literature revealed no reports of this phenomenon, indicating that it may be unique to self-assembly relying on a the group-effect mechanism.

Impact of molecular hydrophobic backbone on group-effect self-assembly

The impact of marginally increasing the strength of the interactions with the surface was explored in Chapter 5 by replacing methanol with alcohols possessing incrementally longer carbon backbones. For these larger alcohols, the additional surface support enabled the formation of more complicated assemblies than those observed in the methanol-water system. Generally these assemblies exhibited more linear features which is consistent with the increased surface support. As seen in Chapter 4, the transition to alcohol-dominated molecular chains occurs at a lower molar fraction for ethanol and 1-propanol than for methanol, which may also be the reason for the formation of these linear features. Indeed, when an alcohol was used which was unable to pack as efficiently as primary alcohols due to steric restrictions (2-propanol), the structures formed were less linear, consistent with this hypothesis. Interestingly, when a ternary mixture of water with multiple alcohols (methanol and 1-propanol) was used, two co-existing structures were observed, each with features characteristic of the respective alcohol-water binary mixture. This indicates a preference for the assemblies to consist of only one type of alcohol and water, rather than hydrogen bonded networks of mixed alcohols and water molecules, which may have consequences for separation processes [5, 7] and thus merits further investigation.

The increased hydrophobic interactions between the alcohols and the surface also hindered the extended hydrogen bonded networks within the assemblies. For example, regions of monolayers involving the largest soluble alcohol, 1-hexanol, could be destroyed with the tip, exposing the HOPG below. This is significant because it indicates that despite the increase in direct molecule-substrate interactions, the overall assembly is weaker because of a reduction in the group-effect. This supports the idea that a group-effect is essential for the self-assembly of small molecules at in-

terfaces. From here it follows that group-effect self-assembly will not be possible for molecules without directional intermolecular interactions, such as hydrogen bonds, or those unable to form extended hydrogen bonded networks, due to possessing bulky side groups.

Importance of studies into group-effect self-assembly

To achieve self-assembly-based nanotechnology, the process used needs to consistently produce highly ordered assemblies. Group-effect self-assembly does exhibit a high degree of order at the nanoscale, especially considering the size of the assembling components. The supramolecular row patterns produced by structures from methanol-water mixtures can be highly linear over micron-scale areas. Furthermore, in systems containing larger alcohols, well-defined edges can form that appear perfectly straight within the limit of the AFM resolution. However, the weak interactions do mean that multiple variations in structure types can occur within the same system, which would be problematic if a consistent end product is desired. Solutions for this may be found by investigating hydrophobic substrates capable of supporting group-effect self-assembly other than HOPG. For instance, MoS_2 has marginally stronger interactions with the assembling molecules than HOPG [8] and thus induces a more epitaxial driven growth, as demonstrated in Chapter 5. This slight increase in surface interactions should in principle reduce the polymorphism observed on HOPG, while retaining the benefits of a group-effect self-assembly such as the use of smaller molecular units, which would allow greater control over the resulting architectural motifs.

More generally, investigations into group-effect self-assembly are likely to have consequences beyond uses in functional bottom-up processes. It is expected that the principle of group-effect self-assembly could be applied to many systems of small hydrogen bonding molecules. The only thing that is required is the ability to form extended hydrogen bonded networks, a trait inherent in commonly used solvents such as ketones, amides and aldehydes. Furthermore, the results obtained using graphene oxide (GrO) in Chapter 5 indicate that group-effect self-assembly may play a role in the interfacial liquid behaviour at partially hydrophobic surfaces, as well as at non-atomically flat interfaces, such as those found in most real systems. Interestingly, this suggests that group-effect self-assembly may already be influencing interfacial processes in a wide variety of systems. This could include charge exchange at electrodes [9], molecular adsorption to surfaces [10], friction and lubrication [11]

as well as in biological processes where mixtures of water and other small hydrogen bonding molecules at hydrophobic interfaces are common [12].

6.3 Further Work

Whilst the present work provides significant novel insights into the self assembly of small hydrogen bonding molecules at hydrophobic interfaces via a group-effect, it relies on a basic model system and many aspects of the phenomenon remain to be explored. Hereafter is an authoritative list of the most pressing questions and experiments to be addressed in future work. It will begin with the basic next-step experiments which should be performed, before going into more detail about how to address two key topics, namely the increasing of our understanding of the group-effect mechanism and the nucleation and growth properties of the monolayers.

Future investigations

- In Chapter 3, I demonstrated that the surface of HOPG spontaneously catalyses a reaction converting water and organic volatiles into methanol. The experiments suggest that carbon dioxide (CO_2) is the most likely source of the carbon for the reaction. The underlying molecular mechanism of the catalysis, however, remains unclear. The logical next step to further investigate the catalysis mechanism would be to combine regulating the amount of incident light with analysis from high-resolution ^{1}H NMR. An environmental chamber may also be utilised to either vary the amount of CO_2 present, or introduce CO_2 with carbon isotopes, which would confirm atmospheric CO_2 as a reagent following subsequent analysis.
- As previously discussed, changes to the hydrogen bond networks present prior to assembly nucleation may explain the structural variations observed when metallic salts were added to the system (e.g. the raised patches in Chapter 5). This could be confirmed by an experiment where metallic salt ions are added to the system after the HOPG surface is covered in alcohol-water assemblies. Furthermore, MD simulations of the system would provide molecule details regarding the impact of metallic salt ions on the hydrogen bond networks in alcohol-water mixture at hydrophobic interfaces, which may be used for comparison.

- In ethanol-water mixtures it was observed that multiple row-like assemblies could co-exist where only one domain exhibited high resolution features (sub-rows). As discussed in Chapter 2, the attainable resolution using dynamic mode AFM is linked to the presence of strong hydration sites on the interface being imaged. Thus the increased resolution on one of the ethanol-water assemblies may be a consequence of the larger alcohols preferring to have hydrogen bonding group facing away from the interface, consistent with results presented in Chapter 4. This indicates that 3D-SFM measurements on assemblies formed in ethanol-water or 1-propanol-water mixtures may provide insight into the chemical composition of the monolayers through their hydration properties.

Further understanding the group-effect mechanism

So far, the systems where group-effect self-assembly has been observed and studied involve mixtures of water and another molecules. Throughout this thesis, the morphology of the alcohol-water assemblies exhibited characteristics which can be linked to the influence of the constituent alcohol molecules (as previously discussed). Water's hydrogen bonding capability and small size makes it ideal to assist the formation of extended hydrogen bonded networks required for group-effect self-assembly. Thus, it is the author's opinion that investigations involving varying the non-water component will be the optimum method of learning more about group-effect self-assembly. Information can then be obtained by linking the features of the structures experimentally observed with the properties of the non-water component.

Methanol has the weakest surface interaction of all the alcohols investigated and benefits the most from the group-effect, and hence was the subject for the investigations into the addition of influencers along with changing the molecular ratios. However, as demonstrated in Chapters 4 and 5, aqueous ethanol and 1-propanol mixtures do not have the same behaviour as aqueous methanol mixtures at hydrophobic interfaces. Therefore they will respond differently to changes in the system, which would be a promising further area of research. Furthermore, so far, only alcohols with one hydrogen bonding group (monohydric) have been considered. However, preliminary results already demonstrate that alcohols with multiple hydrogen bonding groups can also be used (polyhydric).

In Figure 6.1a, structures formed in a 50:50 mixture of propylene glycol ($CH_3CH(OH)$

CH_2OH) and water on HOPG are presented. The first thing to note is that the additional hydrogen bonding capabilities afforded by the extra hydroxyl group makes the structures stable, unlike the ones reported for the monohydric alcohol with the same carbon chain length (1-propanol). The ability to form multiple hydrogen bonds also appears to allow the direction of the assembly to change direction while maintaining a continuous hydrogen bonded network (Figure 6.1a inset), giving the structures the impression of being a patchwork of different row patterns. Repeat experiments of the same propylene glycol-water system showed the structure formed could vary, with two co-existing domains visible (Figure 6.1b). Interestingly, the two domains have the same row periodicity, but the rows alternate in height in one of the domains.

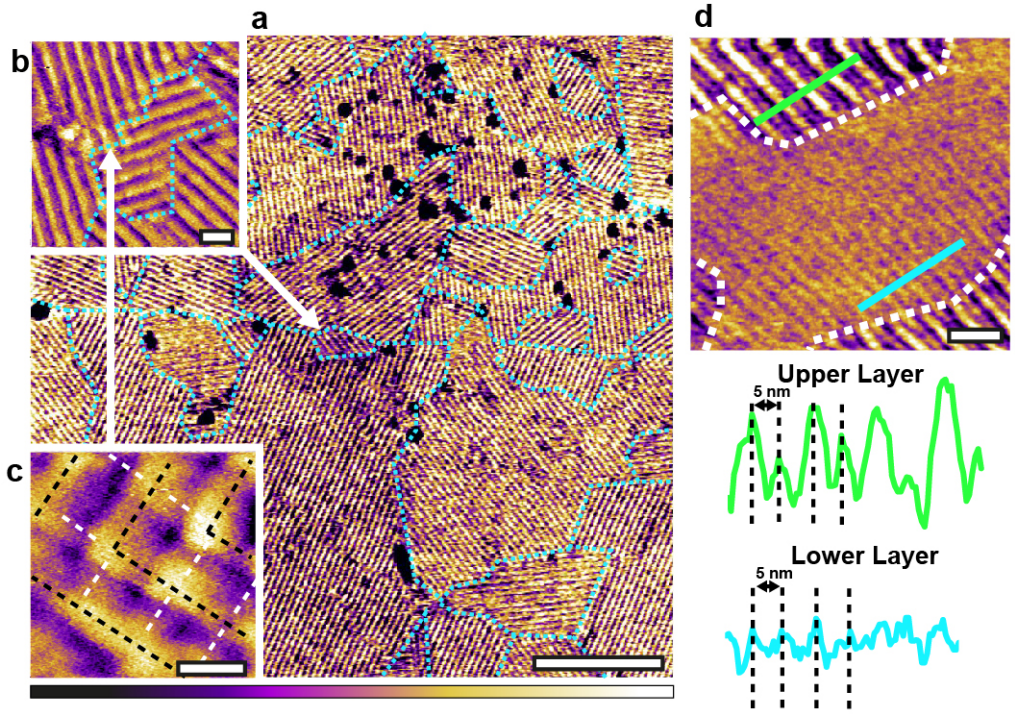

Fig. 6.1: Self-assembled structures on HOPG in a 50:50 mixture of propylene glycol and water. (a) The presence of two hydroxyl groups on the alcohol allows the direction of the supramolecular row pattern to change direction while maintaining a continuous hydrogen bonded network (b-c). In (c) the dashed black line represents the main row pattern which is changing direction. In this region, features other than the main row patterns are also observed, examples of which are highlighted by the white dashed lines. The location at which the rows change direction appears to be somewhat random, making the overall structure give the impression of a patchwork of different row patterns (outlined by blue dashed lines in (a-b)). (d) shows an example structure formed in a repeat of (a-c). Here two domains have formed (boundary shown by white dashed line) which have the same row periodicity, however for one, the height of the structure alternates between rows, as shown by the line profiles taken across the green line and the blue line. The scale bar represents (a) 100 nm (b,d) 10 nm and (c) 5 nm. The purple scale bar represents a height variation of (a-c) 4 nm and (d) 2 nm.

More generally, the observation of structures forming with polyhydric alcohol-water mixtures further strengthens the argument that the principle of group-effect based self-assembly can occur for many different types of molecules. However, they should be small and capable of hydrogen bonding, such as ketones, aldehydes and amines, all of which would be promising candidates for use in further investigations.

Nucleation and growth properties

The impact of factors such as temperature and molecular concentration on the nucleation and growth properties of the alcohol-water assemblies has not been discussed at length in this thesis. The assemblies can take several minutes to nucleate, after which they grow rapidly, often covering the surface faster than can be imaged with the AFM. The delayed nucleation and subsequent fast growth is in part a consequence of the need for a group-effect to stabilise the structures, which introduces an additional factor to the concept of a critical nucleus size (discussed in Chapter 1). The rapid growth of the patches meant that obtaining meaningful data regarding nucleation and growth properties was difficult. A solution for this is to replace the graphite with MoS_2, where slower growth rates were observed (see Chapter 5). However, considerations would need to be made because of the increased epitaxial effects. An alternative approach would be to utilise surface patterning techniques. Molecular groups can be covalently grafted onto graphite via an electrochemical reduction, which would subsequently act as heterogeneous nucleation sites. Thus, when using this approach, the exact location of certain nucleation sites would be known beforehand and therefore the nucleation event and assembly growth could be captured using the AFM.

Preliminary results indicate that further information may be gathered about the assemblies by studying their response to extreme temperature changes. Figure 6.2 shows a monolayer formed in a 50:50 methanol-water mixture on HOPG before and after the temperature was rapidly changed from 25^{o}C to 65^{o}C. Here the rapid temperature change induces a structural reorganisation within the monolayer through the growth of pre-existing pores, as well as a shrinking of the monolayer from the edges. This also indicates that although the hydrogen bonded networks are capable of remaining stable at higher temperatures, they struggle to cope with rapid changes in the size of the thermal fluctuations, or thermal expansion of the HOPG substrate. On the whole, studies into the impact of temperature would elucidate details regarding the energetics of the assemblies and would be important considering the varying

temperatures present in natural systems.

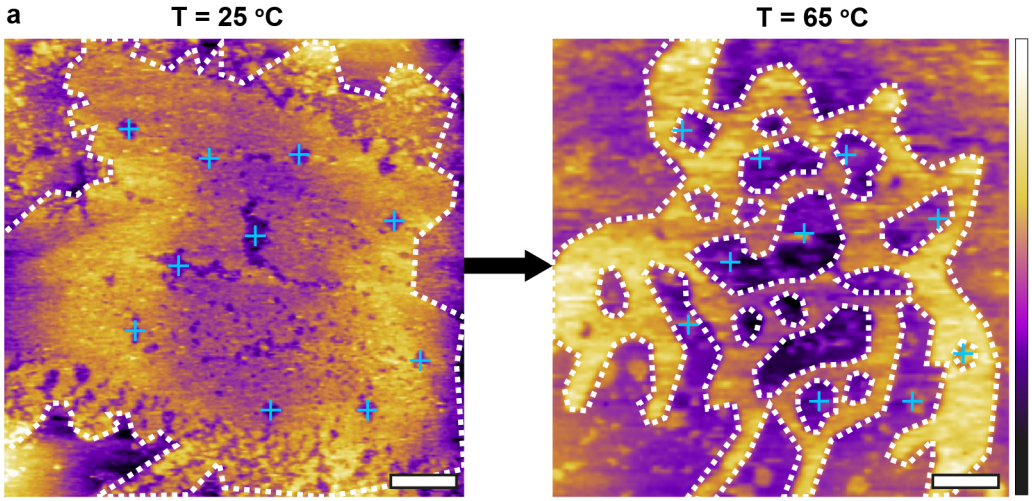

Fig. 6.2: AM-AFM images showing the effect of ramping the temperature from 25^{o}C to 65^{o}C at a rate of 1^{o}C/s on monolayers formed in a 1% methanol-water mixture. (a) The monolayer is initially relatively intact with a few pores represented by the blue crosses. The white dashed line denotes the outline of the monolayer. (b) After the rapid temperature change the monolayer becomes destabilised and the monolayer surface area is reduced. The scale bar represents 1 μm. The purple colour scale bar represents a height variation of 1.5 nm

References: Chapter 6

[1] K. Voitchovsky, D. Giofrè, J. J. Segura, F. Stellacci, M. Ceriotti, "Thermally-nucleated self-assembly of water and alcohol into stable structures at hydrophobic interfaces", *Nature Communications* **2016**, *7*, 13064.

[2] R. L. McCreery, "Advanced carbon electrode materials for molecular electrochemistry", *Chemical Reviews* **2008**, *108*, 2646–2687.

[3] Y. Song, R. Peng, D. K. Hensley, P. V. Bonnesen, L. Liang, Z. Wu, H. M. Meyer, M. Chi, C. Ma, B. G. Sumpter, A. J. Rondinone, "High-Selectivity Electrochemical Conversion of CO2to Ethanol using a Copper Nanoparticle/N-Doped Graphene Electrode", *ChemistrySelect* **2016**, *1*, 6055–6061.

[4] H. Liu, C. Song, L. Zhang, J. Zhang, H. Wang, D. P. Wilkinson, "A review of anode catalysis in the direct methanol fuel cell", *Journal of Power Sources* **2006**, *155*, 95–110.

[5] D. Damasceno Borges, C. F. Woellner, P. A. Autreto, D. S. Galvao, "Insights on the mechanism of water-alcohol separation in multilayer graphene oxide membranes: Entropic versus enthalpic factors", *Carbon* **2018**, *127*, 280–286.

[6] W. Foster, J. A. Aguilar, H. Kusumaatmaja, K. Voïtchovsky, "In Situ Molecular-Level Observation of Methanol Catalysis at the Water-Graphite Interface", *ACS Applied Materials and Interfaces* **2018**, *10*, 34265–34271.

[7] D.-Y. Wang, C.-Y. Wei, M.-C. Lin, C.-J. Pan, H.-L. Chou, H.-A. Chen, M. Gong, Y. Wu, C. Yuan, M. Angell, Y.-J. Hsieh, Y.-H. Chen, C.-Y. Wen, C.-W. Chen, B.-J. Hwang, C.-C. Chen, H. Dai, "Advanced rechargeable aluminium ion battery with a high-quality natural graphite cathode", *Nature Communications* **2017**, *8*, 14283.

[8] J. Chen, J. J. De Yoreo, S. Zhang, E. Zhu, Y. Huang, J. Liu, H. Heinz, Z. Lin, X. Duan, "Building two-dimensional materials one row at a time: Avoiding the nucleation barrier", *Science* **2018**, *362*, 1135–1139.

[9] L. V. Protsailo, W. R. Fawcett, "Studies of electron transfer through self-assembled monolayers using impedance spectroscopy", *Electrochimica Acta* **2000**, *45*, 3497–3505.

[10] W. Beckner, Y. He, J. Pfaendtner, "Chain Flexibility in Self-Assembled Monolayers Affects Protein Adsorption and Surface Hydration: A Molecular Dynamics Study", *The Journal of Physical Chemistry B* **2016**, *120*, 10423–10432.

[11] T. D. Li, E. Riedo, "Nonlinear viscoelastic dynamics of nanoconfined wetting liquids", *Physical Review Letters* **2008**, *100*, 6–9.

[12] J. F. Brandts, L. Hunt, "The Thermodynamics of Protein Denaturation. III. The Denaturation of Ribonuclease in Water and in Aqueous Urea and Aqueous Ethanol Mixtures", *Journal of the American Chemical Society* **1967**, *89*, 4826–4838.